

# Simulation of the Quantum Ising Model in an Ion Trap

Axel Friedenauer



München, März 2010



# Simulation of the Quantum Ising Model in an Ion Trap

Dissertation  
an der Fakultät für Physik  
der Ludwigs-Maximilians-Universität München

von

Axel Friedenauer  
aus Stuttgart

München, März 2010

1. Gutachter: Dr. Tobias Schätz
2. Gutachter: Prof. Dr. Dietrich Habs

Tag der mündlichen Prüfung: 1. Juni 2010

## Abstract

In a proof-of-principle experiment, we simulate the dynamics of a quantum spin system in an ion trap. Following a theoretical proposal by D. Porras and I. Cirac, we use a system of ground state cooled trapped ions to simulate and study the dynamics of a quantum mechanical system, or more precisely, the dynamics of a quantum spin Hamiltonian.

We implement the smallest non-trivial quantum spin Hamiltonian, the quantum Ising model for two spins. Each spin is represented by two hyperfine ground levels of trapped  $^{25}\text{Mg}^+$  ions. The interaction with an external magnetic field is simulated by coherently coupling these hyperfine levels via laser and radiofrequency radiation. The spin-spin interaction is simulated via optical dipole forces, where the effective interaction is mediated by the phonons of the linear ion chain. We demonstrate the adiabatic evolution from a paramagnetically ordered system to ferromagnetic order. The final state of this adiabatic transition is a superposition state of the two degenerate spin configurations of ferromagnetic order  $\Psi_{\text{final}} = 1/\sqrt{2} (|\uparrow\uparrow\rangle + |\downarrow\downarrow\rangle)$  with a quantum magnetisation of 98%. We also show the transition from paramagnetic to antiferromagnetic order with the final state  $\Psi_{\text{final}} = 1/\sqrt{2} (|\uparrow\downarrow\rangle + |\downarrow\uparrow\rangle)$ .

Moreover, we prove that this transition which is to become a quantum phase transition in the thermodynamic limit of infinitely many spins, is driven by quantum fluctuations which dominate the dynamics of such systems at the absolute zero-point of temperature rather than thermal fluctuations which are absent at 0 K. This is verified by the fact that the final state of our adiabatic evolution is entangled, close to a Bell state at a fidelity exceeding 88%.

The set of tools presented in this thesis might serve as a basis for larger scale quantum simulations which might help in gaining insight into many-particle effects that are intractable on classical computers such as spin frustration in triangular lattices or high- $T_c$  superconductivity.



## Zusammenfassung

Mit der vorliegenden Arbeit demonstrieren wir die Realisierbarkeit von Quantensimulationsexperimenten in einer Ionenfalle. Wir setzen hiermit einen experimentellen Vorschlag von D. Porras und I. Cirac um, in dem ein grundzustandsgekühltes System mehrerer Ionen in einer Falle dazu herangezogen wird, quantenmechanische Systeme, genauer gesagt, Quantenspin-Hamilton-Operatoren zu simulieren.

Wir simulieren das einfachste nicht-triviale System, das Quanten-Ising-Modell für zwei Spins. Die Spins werden durch Hyperfeinzustände individueller Magnesiumionen kodiert. Durch kohärente Kopplung mit Hilfe von Laser- und Radiofrequenzfeldern lassen sich externe magnetische Felder simulieren. Die Isingwechselwirkung wird durch optische Dipolkräfte realisiert, die mit Hilfe der Phononen der Spinkette in eine zustandsabhängige Kraft übersetzt werden. Wir zeigen den Übergang von einem paramagnetisch geordneten System zweier Spins zu einem Ferromagneten. Der Endzustand dieser adiabatischen Simulation ist durch eine kohärente Überlagerung der beiden entarteten ferromagnetischen Ausrichtungen der Spins  $\Psi_{\text{final}} = 1/\sqrt{2} (|\uparrow\uparrow\rangle + |\downarrow\downarrow\rangle)$  gegeben, wobei wir eine Quantenmagnetisierung des Systems von 98% erreichen. Desweiteren zeigen wir den Übergang vom selben Ausgangszustand zur antiferromagnetischen Phase  $\Psi_{\text{final}} = 1/\sqrt{2} (|\uparrow\downarrow\rangle + |\downarrow\uparrow\rangle)$ .

Durch die Tatsache, daß der Endzustand nach der Simulation in hohem Maße deterministisch verschränkt ist, verifizieren wir, daß dieser Übergang allein durch Quantenfluktuationen und nicht durch thermische Fluktuationen getrieben wird. Im thermodynamischen Limes unendlich vieler Teilchen wird dieser Übergang zu einem Quantenphasenübergang.

Man erhofft, durch derartige Experimente, ein tieferes Verständnis für Vielteilchen-Quantensysteme, die mit klassischen Computern nicht lösbar sind, zu gewinnen, und damit Effekte wie Spin-Frustration in Dreiecks-Gittern oder Hochtemperatursupraleitung und deren Dynamik besser zu verstehen.



# Contents

<b>I. Introduction</b>	<b>1</b>
1. Quantum Simulations	3
<b>II. Apparatus</b>	<b>9</b>
<b>2. Trapping Ions</b>	<b>11</b>
2.1. Theory of trapping . . . . .	11
2.2. Trap and electrification . . . . .	17
2.3. Vacuum and photochemical reactions . . . . .	19
2.4. Quantisation fields . . . . .	21
2.5. Atom ovens . . . . .	21
2.6. Imaging optics . . . . .	24
<b>3. <math>^{25}\text{Mg}^+</math>: Level structure and transitions</b>	<b>27</b>
3.1. The choice of our spin system . . . . .	27
3.2. Electronic structure of $^{25}\text{Mg}^+$ . . . . .	28
3.3. Initialisation and detection of the spin system . . . . .	29
3.4. Coherent coupling of spin states . . . . .	31
<b>4. Laser apparatus</b>	<b>39</b>
4.1. Fibre lasers . . . . .	39
4.2. First frequency doubling stage (1120 nm $\rightarrow$ 560 nm) . . . . .	46
4.3. Second frequency doubling stage (560 nm $\rightarrow$ 280 nm) . . . . .	53
4.4. Frequency stabilisation of lasers . . . . .	58
4.5. Acousto-optic modulators . . . . .	60
4.6. Laser setups . . . . .	63
4.6.1. Blue Doppler setup . . . . .	63
4.6.2. Red Doppler setup . . . . .	66
4.6.3. Raman setup . . . . .	66
4.6.4. Photoionisation laser . . . . .	71

4.7. Radio-frequency setup . . . . .	72
<b>5. Experimental control</b>	<b>75</b>
5.1. Introduction . . . . .	75
5.2. Hardware . . . . .	76
5.2.1. Data acquisition and digital-analog interface . . . . .	76
5.2.2. Pulse sequencer . . . . .	76
5.3. Flocke software . . . . .	78
<b>III. Experimental tools</b>	<b>83</b>
<b>6. Basic Experiments and Optimisation</b>	<b>85</b>
6.1. Loading ions . . . . .	85
6.2. Transferring ions to the experimental zone . . . . .	85
6.3. Compensation of micromotion . . . . .	86
6.4. Basic experiments . . . . .	87
6.4.1. Frequency scan . . . . .	87
6.4.2. Rabi flopping . . . . .	88
6.4.3. Ramsey spectroscopy . . . . .	89
6.5. Optimisation . . . . .	92
<b>7. Motional ground state cooling</b>	<b>97</b>
7.1. Doppler cooling basics . . . . .	97
7.2. Resolved sideband cooling basics . . . . .	99
7.3. Experimental implementation of ground state cooling . . . . .	101
7.3.1. Doppler cooling . . . . .	101
7.3.2. First sideband cooling . . . . .	103
7.3.3. Second sideband cooling . . . . .	105
7.4. Motional heating rate . . . . .	107
7.5. Sideband cooling of two ions . . . . .	107
<b>8. Simulating spin-spin interactions</b>	<b>111</b>
8.1. Derivation of the Raman Rabi rate . . . . .	111
8.2. Derivation of a state dependent AC-Stark shift . . . . .	114
8.3. Derivation of the spin-spin interaction . . . . .	117
8.4. Walking standing wave . . . . .	119
<b>9. State-sensitive detection</b>	<b>121</b>
9.1. State-sensitive detection of two ions . . . . .	121
9.2. Scattering from dark to bright state . . . . .	122

9.3. Reference histograms . . . . .	123
<b>IV. Experiments</b>	<b>127</b>
<b>10. Experiments</b>	<b>129</b>
10.1. Conditional two qubit geometric phase gate . . . . .	129
10.2. Adiabatic simulation of quantum spin Hamiltonians . . . . .	135
10.2.1. Quantum Ising model . . . . .	136
10.2.2. Implementation . . . . .	138
10.3. Summary: Quantum gates versus quantum simulations . . . . .	147
<b>Conclusion and Outlook</b>	<b>149</b>
<b>A. Derivation of an entanglement witness</b>	<b>153</b>
<b>B. List of Publications</b>	<b>155</b>
<b>Bibliography</b>	<b>165</b>
<b>Danksagung</b>	<b>175</b>
<b>Curriculum vitae</b>	<b>177</b>

x

**Part I.**  
**Introduction**



# 1. Quantum Simulations

*“... we are to be even more ridiculous later and consider bits written on one atom instead of the present  $10^{11}$  atoms. Such nonsense is very entertaining to professors like me. I hope you will find it interesting and entertaining also.”*  
R. P. Feynman in 1985

The idea of the quantum computer is usually ascribed to R. P. Feynman who used the phrase in his famous keynote speech [35] in 1982. But he was not the first one to think about computers based on the principles of quantum mechanics. In 1980, P. Benioff tried to address the, at that time, open question, if it was possible to construct computers which do not dissipate energy [7, 8] and examined spin-lattice systems to work as Turing machines.

Contrary to his colleagues, Feynman posed further reaching questions and conjectured that quantum computers might be able to solve certain tasks more efficiently than classical computers. He turned out to be right [74, 118, 48, 20]. Yet one might argue, that classical computers become faster and faster, so where is the need for a quantum computer. According to Moore's law stated in 1965, computing power and memory capacity of computers double every 18 months. Thus complex tasks should be tractable using classical computers some day. But to illustrate the limitations let us take a look at two aspects. The first one being that building faster processors is accompanied by miniaturising circuit structures. Today's processor's structure sizes are of the order of AIDS viruses, the widths of circuit paths solely consist of few hundreds of atoms. Extrapolating this downsizing, the electrical charges encoding logical zeros or ones in today's computers will soon be constituted of single electrons and the circuit paths will consist of single atoms. Processes on this tiny scales are no longer mainly governed by laws of classical physics, but rather must be described by quantum mechanical means. The electron is no longer confined to a well-defined point in space due to its wave-like behaviour, yet tunnelling phenomena come into play. Stored information is smeared out leading to superpositions of zeros and ones. There is a natural boundary given by the size of the atoms which constitute an upper bound for computational power based on current technologies.

The second point is the inability of classical computers to solve quantum mechanical tasks efficiently. The same aspects which limit the advancement of classical computers are the ones classical computers cannot cope with. Quantum mechanical particularities

## 1. Quantum Simulations

such as tunnelling processes, superposition states or entanglement are not efficiently translatable into the language of classical computers. To predict the behaviour of a quantum mechanical system consisting of 40 spin-1/2 particles, which can take on one out of two spin states, we need  $2^{40}$  (about  $10^{12}$ ) parameters. For calculating its dynamics we have to formulate a matrix consisting of  $2^{40} \times 2^{40}$  (about  $10^{24}$ ) entries. Even state-of-the-art classical computers are doomed to failure in describing systems comprising more than 32 spin-1/2 particles. Even hoping for Moore's law cannot raise any hope with respect to this issue. A doubling of computational power solely allows for simulating one additional particle, the operating expense also grows exponentially with the number of particles. Describing the state of a system of 300 quantum particles would require as many parameters as the estimated amount of protons in our universe ( $2^{300}$ ).

The quantum computer envisioned by Richard Feynman in 1982 could accomplish this task. We would not have to intricately translate the above mentioned quantum mechanical particularities into the language of classical computers, i.e. bits, subsequently referred to as zero and one. Instead of that, a quantum system itself would serve as a computer, in which the laws of quantum mechanics are taken account of naturally and efficiently. To illustrate this let us take a look at the counter-intuitive example of 300 electrons which concurrently occupy the two classically exclusive states zero *and* one. Apparently, this is hard to formulate in terms of classical zeros and ones and involves a lot of parameters. On the other hand, a quantum mechanical system consisting of 300 particles in principle suffices to describe the state or even to simulate the dynamics of 300 quantum particles.

Let us take a closer look at the quantum computer [91, 30]. The common bit of a classical computer, representing zero and one, is replaced by a quantum bit (qubit), which can take on arbitrary superpositions of zero and one. How these qubits will be implemented in the future is a yet unresolved question. Presently there are a lot of competing approaches. During the past decade a lot of different physical systems have been investigated regarding their suitability of becoming the building blocks of a quantum computer, such as solid state systems like quantum dots [16, 75], superconducting circuits (SQUIDs) [22, 79], atoms in optical lattices [47, 15, 80], optical cavities [123, 83], or nuclear magnetic resonance (NMR) quantum computing. Among the technically most advanced candidates which allow for scaling to a larger number of quantum bits are systems of trapped ions [24, 25, 127, 63]. Short quantum algorithms have been realised in setups of up to 8 ions [73, 50]. These constitute important building blocks of a future universal quantum Turing machine. Though there seem to be no greater objections why a universal quantum computer based on these concepts should not be realisable, the scaling up to  $10^5$  logical qubits requiring at least  $5 \times 10^5$  physical qubits for error correction [117, 119, 44] and the realisation of gates exhibiting error rates two order of magnitude lower than today's [106, 4, 91], is a technical challenge

which will not be overcome during another decade, optimistically rated.

R. Feynman did not speculate about a future universal quantum computer, however he launched the concept of an *analogue* quantum simulator. His vision was based on the idea of utilising a quantum system to simulate a different quantum system which is governed by an identical Hamiltonian. His idea is further illustrated and explained in Fig. 1.1.

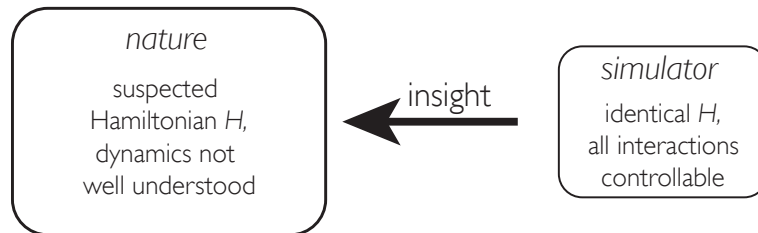


Figure 1.1. – Idea of Quantum Simulation: Assume a quantum mechanical system which we will call *nature* for obvious reasons. We believe to know its Hamiltonian  $H$ , however, due to its size and complexity, we cannot understand important dynamical effects. Now assume we prepare a (not necessarily small) modelling system called *simulator* whose Hamiltonian can be identical to the assumed Hamiltonian of *nature* or simplified. Assume that for the *simulator* system we can vary all parameters and coupling strengths independently and can measure all relevant quantities sufficiently well. With these tools we might obtain a better understanding of the complex dynamics of the simulated system and gain deeper insight into nature.

Following this idea towards realising such a device we may benefit from the advances in quantum computation. We can adapt methods and tools to our specific needs. A system of trapped ions is an ideal candidate serving as a simulator for quantum spin systems. Located in an ultra-high vacuum (UHV), they are close to perfectly decoupled from the (decohering) environment. Hyperfine ground state levels of an appropriate ion species with natural lifetimes of thousands of years form an almost ideal two- or even multilevel system which can serve as a spin to be simulated.

Following the proposal for the realisation of a universal quantum computer [24] in an ion trap in 1995, Diego Porras and Ignacio Cirac proposed an *analogue* quantum simulator based on trapped ions [103] in 2004. It is not intended to solve universal tasks, but specialised in the simulation of quantum spin models. In a linear chain of ions, two hyperfine ground states of each ion represent a spin-1/2 system. These simulated spins can take up arbitrary superpositions of states like real spins. External magnetic fields acting on the spins are simulated via a coherent coupling of the hyperfine ground states. Couplings between spins are proposed to be achieved by applying state-dependent optical dipole forces [26] to the ions. In combination with the non-linear

## 1. Quantum Simulations

nature of the Coulomb potential this leads to an effective spin-spin interaction. Using different beam geometries various kinds of spin-models can be simulated. The simplest model exhibiting interesting dynamics is the quantum Ising model. With the same experimental tools other spin models like the XY-model and the Heisenberg model can be simulated. Systems of this kind could allow for addressing a variety of presently not well understood systems like quantum magnets, high temperature superconductivity [94], Kondo problems [40] or the quantum Hall effect. Other Hamiltonians addressable with quantum simulations using trapped ions include the Bose-Hubbard model [102] and the spin-boson model [104].

But there are also systems which do not apparently exhibit interconnections to a string of ions. For example one can simulate the creation of particles in the early expanding universe [113] by non-adiabatically varying the trapping potential of a single ion which thereby is supposed to end up in a squeezed state of motion. In this case the phonons of the ion simulate particles. Or another subject to be simulated is the quantum walk. Tossing a coin is encoded by rotating the ion's internal state to a coherent superposition state. This information coded in the internal state of the ion is transferred to the motional states of the ion by applying a state dependent displacement pulse by an optical dipole force. Carrying out this process repeatedly leads to interference of different paths.

In this thesis we will focus on the simplest non-trivial quantum spin Hamiltonian, the quantum Ising model for two spins. This model shows critical phenomena already for one dimension, since quantum spin models in  $D$  dimensions behave like classical spin models of  $D + 1$  dimensions [108]. This correspondence can in fact be interpreted in terms of the second spatial dimension of the classical model forming an imaginary time axis of the quantum Ising model.

The simulation consists of an adiabatic passage during which the system is transferred from the ground state of one part of the Hamiltonian to the ground state of the other part of the Hamiltonian. Let us consider the Hamiltonian

$$\begin{aligned}
 H_{\text{Ising}} &= H_{\text{B}} + H_{\text{J}} \\
 &= \underbrace{-B^x \sum_i \sigma_i^x}_{\text{magnetic field}} - \underbrace{\sum_{i>j} J_{ij} \sigma_i^z \sigma_j^z}_{\text{spin-spin coupling}}.
 \end{aligned} \tag{1.1}$$

The first term  $H_{\text{B}}$  describes the interaction of each individual spin with a magnetic field, whereas the second term introduces a spin-spin coupling. We begin the simulation with the system initialised in the ground state of the Hamiltonian on the left hand side ( $J_{ij} = 0$ ), that is, the spins are aligned with the simulated magnetic field, the spins point in  $x$ -direction. The spins are paramagnetically ordered. Now we adiabatically

increase the spin-spin coupling  $J_{ij}$ . The system will remain in its ground state. For  $|J_{ij}| \gg B^x$  the term on the right hand side will dominate. During the adiabatic evolution, the system evolves to the ground state of the spin-spin coupled part of the Hamiltonian  $H_J$ . For this ground state we have to differentiate between two cases: For  $J > 0$  the ground state corresponds to a ferromagnetic order and for  $J < 0$  the system will evolve to an antiferromagnetically ordered state. In the thermodynamic limit of infinitely many spins, a quantum phase transitions between the paramagnetic and one of the two aforementioned ground states of the spin-spin coupled system is predicted to take place at  $|J_{ij}| = B^x$ .

The experiment described within this thesis can be seen as a feasibility study, or demonstration of the building blocks of quantum simulations of spin Hamiltonians in an ion trap architecture. We restrict the experiment to two spins. The observed magnetic transition is smooth and deterministic. Extending this scheme to several particles one would be able to observe critical phenomena, for the quantum Ising model this would be a second-order phase transition. Simulations of more than 30 spins would exceed the power of today's computers. The system could further be scaled to two-dimensional trap arrays. With  $10 \times 10$  ions for example, one could study phenomena far beyond the simulation capabilities of classical computers addressing questions of solid state physics, for example spin frustration in triangular lattices.

Most of the experimental techniques used for this work rely on the pioneering work of the quantum information and computation groups at NIST, Boulder (refs. [127, 87, 72]) and the University of Innsbruck (refs. [34, 107]). In the following, we will take a closer look at our specific spin system and sketch the outline of this thesis. In the second part we explain the experimental apparatus. This part is subdivided into four chapters shedding light on the different thematic blocks constituting the hardware of the experiment. The first chapter provides a short description of ion trapping theory and comments on the specific trap we designed and built for our experiments. For a more detailed description please refer to Hector Schmitz's thesis [111]. We describe the photo-ionisation of a thermal beam of magnesium-25 atoms and how we capture  $^{25}\text{Mg}^+$  ions in a quadrupole Paul trap. Our ion trap is subdivided into several distinct trapping zones. One of these serves for loading purposes with an approximately an order of magnitude larger trapping volume compared to the so-called "experimental zone" which exhibits a stiffer potential to carry out experiments.

The next chapter explains the electronic level scheme of  $^{25}\text{Mg}^+$  ions which resembles the level scheme of alkaline metal atoms possessing a single outer shell electron. Its closed transition gives us the opportunity to perform Doppler cooling and state sensitive detection of the ions. For sideband cooling and simulating interactions we introduce two-photon stimulated Raman transitions. We can also couple the two spin states using resonant radiofrequency transitions. We will consider the initialisation of our spin states, coherent coupling between these states, coupling of the internal states of the

## 1. Quantum Simulations

ions to the motional degrees of freedom which will be needed for ground state cooling and how to analyse the outcome of experiments.

During the next chapter we will concentrate on the laser apparatus, we will in detail consider the four ultraviolet laser sources we need for photo-ionisation, controlling, manipulating, and measuring the states of the ions. Three of these laser systems are based on ytterbium fibre lasers operating in the infrared (near 1118 nm). Each of these lasers is quadrupled in frequency by two subsequent homebuilt second harmonic generation cavities, respectively, to obtain laser radiation at a wavelength of roughly 280 nm. We achieved continuous wave output powers of more than 350 mW with this solid state laser system (publication attached in the appendix, ref. [37]), which is a major prerequisite for scaling up quantum simulation experiments to larger spin systems.

The last chapter of this part shortly highlights the experimental control. We will sketch how a computer together with two field-programmable gate array (FPGA) devices controls trap electrode voltages, triggers the photomultiplier, and controls laser pulses down to time scales of nanoseconds.

The third part of the thesis deals with the experimental tools required to carry out basic quantum simulation experiments. This part is subdivided into four chapters. In the first one we experimentally access the coupling of the *internal* hyperfine states which serve as spin states via Rabi flopping and Ramsey experiments. The following chapter concentrates on the coupling of the *internal* states with the *external* or motional states of the ions. This coupling serves as basis for motional ground state cooling of the ions. We cool the ions to their crystalline phase via a stage of Doppler cooling [34, 84], subsequently, an iterative scheme of resolved sideband cooling [87] brings the ions close to the motional ground state. In the next chapter, we detail the theoretical basis of couplings and interactions and how we implement these. In the last chapter of this part, we analyse state sensitive detection of multiple-ion-experiments.

The fourth part finally discusses the experiments. We begin with calibrating our experimental tools by implementing a geometric phase gate [72]. We achieve a Bell state fidelity of the final state of larger 94%. Then, we continue with the simulation of the quantum Ising model for two ions. We experimentally simulate the adiabatic evolution of the smallest non-trivial spin system from paramagnetic into ferromagnetic order with a quantum magnetisation for two spins of 98%. We prove, that the transition is not driven by thermal fluctuations but is of quantum-mechanical origin (analogous to quantum fluctuations in quantum phase transitions). We observe a final superposition state of the two degenerate spin configurations for the ferromagnetic order, corresponding to deterministic entanglement achieved with 88% fidelity. This method should allow for scaling to a higher number of coupled spins, enabling implementation of simulations that are intractable on conventional computers. The related publication in Nature Physics (ref. [38]) is also attached in the appendix.

**Part II.**  
**Apparatus**



## 2. Trapping Ions

We pursue the goal of carrying out an adiabatic quantum simulation. As the word *adiabatic* anticipates, the duration of the simulation is rather long compared to stroboscopic gate operations, in fact for two ions with our experimental parameters of the order of a hundred microseconds, for more ions we have to increase this duration to remain within the adiabatic regime (see section 10.2.2). We require a trapping apparatus which allows for long coherence times, but nevertheless provides sufficiently strong confinement to support efficient ground state cooling of a linear chain of several ions (see chapter 7) and allows for strong spin-spin interactions (see chapter 8). We discuss the mentioned requirements in the following.

- We need an ultra high vacuum (UHV) of the order of  $10^{-11}$  mbar to minimise the collision rate with background gas particles.
- We need a low motional heating rates (see section 7.4) of the ions confined in the trap. This rate scales as the inverse distance between the ions and the electrodes to the power of four [124].
- For efficient ground state cooling of a linear chain of ions (see chapter 7), we aim for a stiff confinement in all spatial directions. An axial frequency of the order of  $2\pi \times 2$  MHz would be desirable, the radial frequency has to be sufficiently<sup>1</sup> larger for allowing several ions to arrange in linear chain. The achievable radial confinement scales with the inverse square of the ion-electrode distance (see Eq. 2.4).

We have to trade off the heating rate against a strong confinement. It has been my colleague Hector Schmitz's role to design the ion trap. Detailed considerations can be found in his thesis [111]. For the sake of completeness, we will shortly sketch important expressions of ion trapping technology and facts about our specific trap.

### 2.1. Theory of trapping

We learn from Earnshaw's theorem, that it is not possible to trap charged particles in a stationary stable configuration in free space using static electric fields [33]. We can

---

<sup>1</sup>The required ratio between radial and axial confinement depends on the number of ions and will be discussed in section 2.1

## 2. Trapping Ions

only create “saddle”-shaped potentials. Using time-dependent electric fields applied to linear rods, this “saddle”-shaped potential oscillates and on average forms a stable trap in two dimensions. Depending on the frequency of the oscillating electric fields, ions of distinct charge over mass ratio are radially confined. This is the basic working principle of a quadrupole mass spectrometer. By applying static potentials (dc-voltages) at the boundaries of the rods in addition, which give rise to an axial confinement, we obtain the linear radio-frequency (rf) Paul trap [98, 27]. The working principles are illustrated in Figure 2.1.

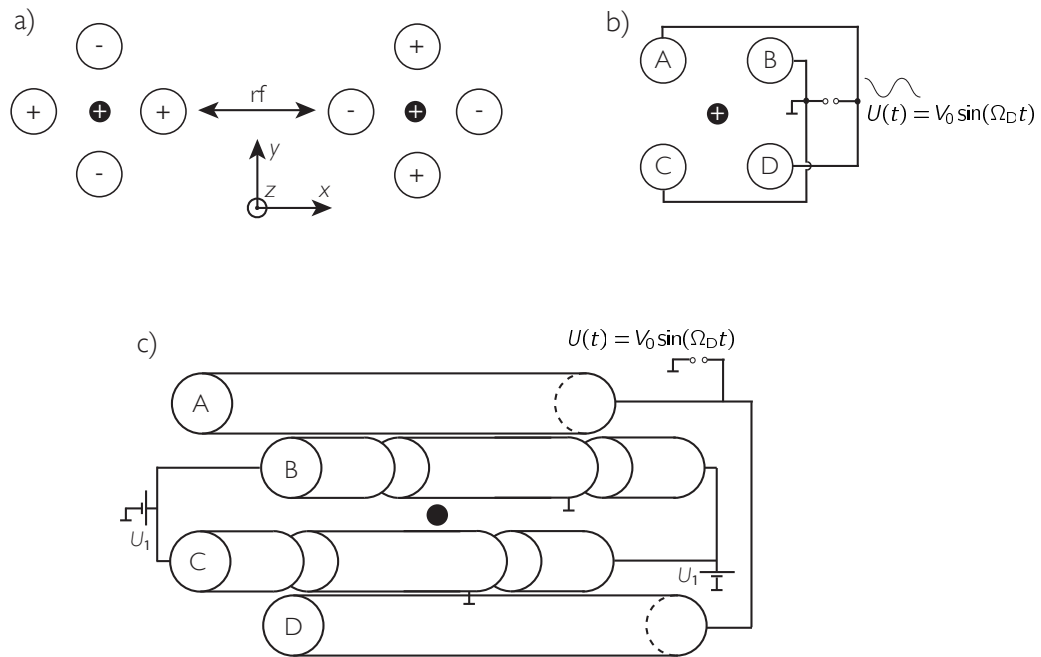


Figure 2.1. – Principles of a Paul trap: A positively charged ion (black) is located in between four electrodes (we see cuts through the  $x$ - $y$  plane of infinitely long rods). a) On the left hand side a slightly displaced ion is refocussed in direction of  $y$  and defocussed in direction of  $x$ . On the right hand side the trapping and repelling directions are reversed. By toggling between both configurations sufficiently fast, ions of distinct charge over mass ratio are on average confined to the centre. b) It is electrically equivalent to ground one opposing pair of electrodes (B&C) and apply a radio frequency potential to the other two electrodes (A&D). c) Axial confinement: The two grounded electrodes from configuration b) are segmented and additional dc voltages are applied to the end segments and provide axial confinement for the ions.

Exact mathematical treatments of the rf quadrupole trap can be found in references

## 2.1. Theory of trapping

[65, 42]. We only recapitulate important expressions here. Radial confinement within the trap is achieved by applying a radio frequency (rf) potential  $V_0 \cos(\Omega_D t)$  with rf drive frequency  $\Omega_D$  to one diagonally opposing pair of electrodes and grounding the other two with respect to the rf. This gives rise to a potential of the form

$$\Phi_{\text{RF}} = \frac{1}{2} \kappa_{\text{RF}} V_0 \cos \Omega_D t \left( 1 + \frac{x^2 - y^2}{r_0^2} \right), \quad (2.1)$$

where  $r_0 = \sqrt{x^2 + y^2}$  is the minimal distance between the surface of the electrodes and the trap axis and  $\kappa_{\text{RF}}$  is a factor accounting for the trap geometry of the order of unity. This potential creates ponderomotive forces in  $x$  and  $y$  directions. In addition we create a barrier for the ions in  $z$  direction by applying dc-voltages  $U_1$  to the end segments of the rf-grounded rods. This leads to a static harmonic well in  $z$ -direction. Taylor expanding this potential along the  $z$ -axis leads to [70]

$$\Phi_S \cong \frac{\kappa_{\text{dc}} U_1}{Z_0^2} \left[ z^2 - \frac{1}{2} \epsilon_{\text{dc}} x^2 - \frac{1}{2} (2 - \epsilon_{\text{dc}}) y^2 \right], \quad (2.2)$$

where  $Z_0$  is the length of the middle segment of the trap and  $\epsilon_{\text{dc}}$  and  $\kappa_{\text{dc}}$  are geometric factors similar to  $\kappa_{\text{RF}}$ . These two potentials are lowest order terms of a multipole expansion [70] about the trapping axis  $z$ . It is appropriate to restrict to the lowest order terms, since the ion is spatially confined tightly in the vicinity of its equilibrium position (order of tens of nm) compared to trap segment sizes of the order of hundreds of  $\mu\text{m}$ .

One can derive the equations of motion for an ion of mass  $m$  and charge  $e$  using  $\ddot{x}_i = -\frac{e}{m} \frac{\partial}{\partial x_i} (\Phi_{\text{RF}} + \Phi_S)$  for  $x_i \in \{x, y, z\}$ .

The (classical) equations of motion are given by homogenous differential equations of the Mathieu type

$$\begin{aligned} \frac{d^2 x}{d\zeta^2} + (a_x - 2q_x \cos 2\zeta) x &= 0 \\ \frac{d^2 y}{d\zeta^2} + (a_y - 2q_y \cos 2\zeta) y &= 0 \end{aligned} \quad (2.3)$$

with  $\zeta = \Omega_D t/2$ ,  $a_x = -4q_x/m\Omega_D^2 \frac{\kappa_{\text{dc}} U_1}{Z_0^2} \epsilon_{\text{dc}}$ ,  $a_y = -4q_y/m\Omega_D^2 \frac{\kappa_{\text{dc}} U_1}{Z_0^2} (2 - \epsilon_{\text{dc}})$ , and  $q_x = q_y = \frac{2e\kappa_{\text{RF}} V_0}{m r_0^2 \Omega_D^2}$ . The motion in axial direction ( $z$ ) is a simple harmonic motion of frequency  $\omega_z = \sqrt{\frac{2e\kappa_{\text{dc}} U_1}{m Z_0^2}}$ .

Under the condition  $|a_{x,y}| < q_{x,y}^2 \ll 1$ , one can perform the so-called *pseudo potential approximation* [78, 42] which separates the ion's motion into a slow component which we will call macromotion or secular motion and a fast modulation on top of it, to which we will refer to as *micromotion*. Fig. 2.2 illustrates the two oscillatory components. By averaging over one RF cycle, one finds a harmonic pseudo-potential in radial

## 2. Trapping Ions

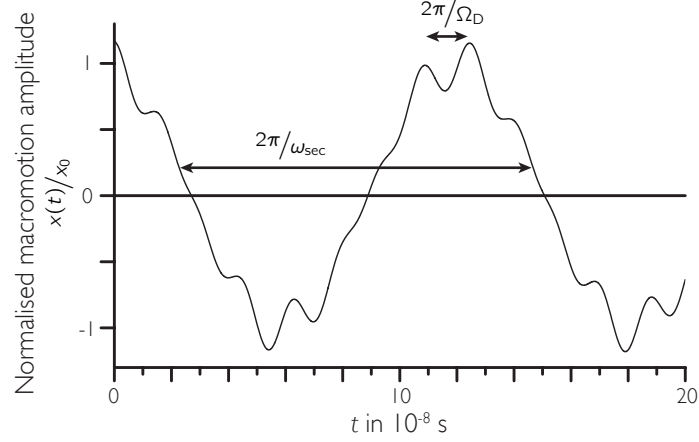


Figure 2.2. – The radial trajectory (here in  $x$ -direction) of an ion in the trap consists of two components, a slow component at the secular frequency  $\omega_{\text{sec}}$  and a fast component at the trap drive frequency  $\Omega_D$  called micromotion. The amplitude of the micromotion depends on the radial position of the ion. In the centre of the trap it is zero and increases with the distance from the trap centre. The depicted simulation has been carried out by Lutz Petersen [99] with parameters  $\Omega_D = 2\pi \times 56$  MHz,  $U_1 = 10$  V,  $V_0 = 1$  kV. Therefore, we obtain  $a_x = 7.78 \cdot 10^{-3}$  and  $q_x = 0.389$ . The macromotion amplitude  $x_0$  of a laser cooled ion amounts to  $x_0 < 100$  nm.

direction of frequency  $\beta_{x,y} = \sqrt{a_{x,y} + 1/2 q_{x,y}^2}$ . For much stronger radial than axial confinement, we can approximate the radial secular frequency

$$\omega_{\text{rad},x,y} \cong \frac{|q_{x,y}|}{\sqrt{8}} \Omega_D = \frac{e\kappa_{\text{RF}}V_0}{\sqrt{2}m\Omega_D r_0^2}. \quad (2.4)$$

This solution is only valid within the above given limit of small  $a_{x,y}$  and  $q_{x,y}^2$ . A more general solution can be obtained by solving the Mathieu equation using the *Floquet solutions* [1]

$$u_1(\zeta) = e^{\mu\zeta} \phi_1(\zeta) \quad , \quad u_2(\zeta) = e^{-\mu\zeta} \phi_2(\zeta) \quad , \quad (2.5)$$

where  $\phi_i(\zeta)$  are periodic functions with the same periodicity as  $u_i(\zeta)$ . For a general solution we may thus write

$$u(\zeta) = Ae^{\mu\zeta} \phi_1(\zeta) + Be^{-\mu\zeta} \phi_2(\zeta) \quad , \quad (2.6)$$

where  $A$  and  $B$  are integration constants depending on initial conditions. Since we are looking for bounded solutions we can deduce that  $\mu = \alpha + i\beta$  has to be purely imaginary, since  $e^{\mu(\alpha+i\beta)}$  diverges for  $\alpha \neq 0$ , and express the  $\phi_i(\zeta)$  in a Fourier expansion [42]

$$u(\zeta) = A \sum_{n=-\infty}^{\infty} C_{2n} e^{i(2n+\beta)\zeta} + B \sum_{n=-\infty}^{\infty} C_{2n} e^{-i(2n+\beta)\zeta} \quad , \quad (2.7)$$

## 2.1. Theory of trapping

where  $C_{2n}$  are the Fourier coefficients. However, this solution is not stable for all values of  $\beta$ , it has to be non-integer. For obtaining general solutions the Ansatz is put back into the Mathieu equation and leads to a recursive relation

$$C_{2n+2} - D_{2n}C_{2n} + C_{2n-2} = 0, \quad (2.8)$$

where  $D_{2n} = (a - (2n + \beta)^2) / q$  relates the coefficients  $a$ ,  $q$ , and  $\beta$ . This leads to a continued fraction

$$C_{2n} = \frac{C_{2n-2}}{D_{2n} - \frac{1}{D_{2n-2} - \frac{1}{\dots}}} \quad (2.9)$$

and similar expressions for  $C_{2n-2}$  and  $\beta^2$ . Numerical values can be obtained by appropriate truncating when sufficient accuracy is reached.

Due to its micromotion, the ion sees laser light modulated and therefore experiences micromotion sidebands. For our trap, the RF drive frequency ( $\Omega_D = 2\pi \times 56$  MHz) is comparable to the linewidth ( $\Gamma = 2\pi \times 42.7$  MHz) of our Doppler cooling transitions of  $^{25}\text{Mg}^+$ , therefore we have to be careful: A laser beam being red detuned with respect to a transition, is blue detuned with respect to the first micromotion sideband and might heat the ion's motion in presence of micromotion. The radiofrequency source providing the trapping voltage has to be sufficiently spectrally pure and should not have components near frequencies where micromotion can occur. Other mechanisms like stray fields can also couple the ion's motion to the rf drive, or electrical noise on the rf signal can parametrically drive the motion of the ion. Various sources are discussed in the literature [127, 70]. By applying additional voltages to electrodes outside of the trap, one can push the ion back into the centre of the rf-trapping potential and therefore compensate this additional micromotion<sup>2</sup>. We will consider this method in chapter 6.3.

**Multiple ions** A single ion occupying the centre of the trap ideally experiences a static harmonic potential. Several ions arrange in a linear chain, given that  $\omega_{rad}$  is sufficiently

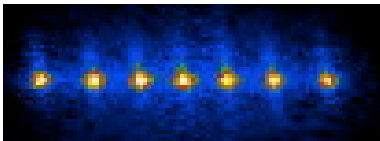


Figure 2.3. – A linear chain of seven ions giving us the idea that the distance between the outermost ions and their neighbours is larger than the distance between the ions located in the center.

higher than  $\omega_z$ , depending on the number of ions. For two ions  $\omega_r/\omega_z > 1$  is sufficient, whereas for three ions we have to choose [127]  $\omega_r > 1.55\omega_z$ . The mutual distances between the ions are governed by the axial confinement  $\omega_z$  and the repulsion between the ions. Starting with four ions the spacing between adjacent ions at the boundaries

<sup>2</sup>However, it is not possible to cancel the micromotion related to the macromotion of the ion.

## 2. Trapping Ions

of the crystal becomes larger, see Fig. 2.3. In addition to the trapping potential, the inner ions are pushed towards each other by the charge of the outer ions, whereas the outer ions experience the sum of the Coulomb repulsion of all the inner ions. Inter-ion distances in crystals are in detail discussed in reference [56].

**Quantisation of the ion's motion and normal modes** In this paragraph, we will introduce an advantageous coordinate system [28] and quantise the motion of the ions. A linear chain of ions confined in a harmonic potential experiences a trapping potential that can be described classically as

$$V = \frac{1}{2}m \sum_j (\omega_x^2 x_j^2 + \omega_y^2 y_j^2 + \omega_z^2 z_j^2) + \sum_{j>i} \frac{e^2}{\sqrt{(x_i - x_j)^2 + (y_i - y_j)^2 + (z_i - z_j)^2}}, \quad (2.10)$$

where  $x$  and  $y$  represent the two radial and  $z$  the axial spatial coordinates, the first term describes the kinetic energy of the ions, whereas the second term describes the Coulomb repulsion between the ions. The sum is carried out over the number of ions. For small displacements around their equilibrium positions in the harmonic potential we may express the position of the ions in the form  $q_j^\alpha = x_j^\alpha - x_j^{\alpha,0}$ , where  $x^\alpha \in \{x, y, z\}$  and  $x_j^{\alpha,0}$  represents the equilibrium position of ion  $j$  in spatial direction  $x^\alpha$ . With this definition we can rephrase  $V$  as

$$V = \frac{1}{2}m \sum_{\alpha,i,j} \mathcal{K}_{i,j}^\alpha q_i^\alpha q_j^\alpha \quad (2.11)$$

with

$$\mathcal{K}_{i,j}^\alpha = \begin{cases} \omega_\alpha^2 - c_\alpha \sum_{j' \neq i} \frac{e^2}{m |z_i^0 - z_{j'}^0|^3} & i = j \\ c_\alpha \sum_{j' \neq i} \frac{e^2}{m |z_i^0 - z_{j'}^0|^3} & i \neq j \end{cases}, \quad (2.12)$$

with constants  $c_{x,y} = 1$  and  $c_z = -2$ . The matrices  $\mathcal{K}_{i,j}^\alpha$  are diagonalised by the the matrices  $\mathcal{M}^\alpha$ :

$$\sum_{i,j} \mathcal{M}_{i,n}^\alpha \mathcal{K}_{i,j}^\alpha \mathcal{M}_{j,m}^\alpha = \omega_{\alpha,n}^2 \delta_{n,m} \quad (2.13)$$

with the eigenvalues  $\omega_{\alpha,n}$  representing the frequencies of the normal modes. Using this diagonalisation, we may quantise the harmonic motion by introducing creation and annihilation operators  $a_{\alpha,n}^\dagger$  and  $a_{\alpha,n}$  and express the local coordinates in terms of these:

$$q_i^\alpha = \sum_n \frac{\mathcal{M}_{i,n}^\alpha}{\sqrt{2m\omega_{\alpha,n}}} (a_{\alpha,n}^\dagger + a_{\alpha,n}). \quad (2.14)$$

## 2.2. Trap and electrification

With the canonic conjugated momenta  $p_i^\alpha$  we can rephrase the vibronic Hamiltonian as

$$H_{\text{vib}} = \frac{m}{2} \sum_{\alpha,i,j} \mathcal{K}_{i,j}^\alpha q_i^\alpha q_j^\alpha + \sum_{\alpha,i} \frac{p_i^2}{2m} = \sum_n \hbar \omega_{\alpha,n} a_{\alpha,n}^\dagger a_{\alpha,n}. \quad (2.15)$$

# of ions	(additional) mode	frequency
1	com	$\omega_z$
2	stretch	$\sqrt{3} \omega_z$
3	egyptian	$\sqrt{29/5} \omega_z$
4		$\sqrt{9.1} \omega_z$

Table 2.1. – Axial normal modes of an ion crystal: The frequency is given in multiples of the axial trap frequency  $\omega_z$ . Starting from 4 ions there is no analytical solution for the frequency of the mode. Taking into account more than 5 ions the frequencies of the lower modes also change slightly [56].

Throughout this thesis, we will only use the axial modes of the ion crystal. For each added ion one additional motional mode comes into play. The normal modes form a complete orthogonal basis. For one ion we solely have the center-of-mass mode (com) whose frequency is determined by the axial frequency  $\omega_z$ . For two ions the 180°-out-of-phase, stretch (str), or breathing mode accounts for differential motion between the ions. Table 2.1 summarises the motional modes and frequencies [56] for up to 4 ions. The frequencies of these modes will be important for ground state cooling (see chapter 7).

## 2.2. Trap and electrification

In this section, we comment on our specific ion trap. It vaguely resembles the rod model, depicted in Fig. 2.1, except that the rods are replaced by sharp copper prisms (see Fig. 2.4) coated by a thin layer of gold (few micrometers thick) to optimise conductance and (chemical) resistance during assembly. We subdivide the trap into two trapping zones of different measures by segmenting the dc electrodes. For loading ions, it is convenient to use a shallow potential within a large trapping volume (see chapter 6.1). However, for experimenting we need a strong confinement in both radial and axial directions (see chapter 7). Three segments of the dc electrodes form the loading zone of the trap characterised by the distance between the trap center and the surface of the electrodes of  $r_0 = 800 \mu\text{m}$ . The three remaining segments constitute the experimental zone of the trap, where  $r_0 = 400 \mu\text{m}$ . The experimental zone allows for a four times tighter confinement in the radial directions (see Eq. 2.4). All of this trap's components

## 2. Trapping Ions

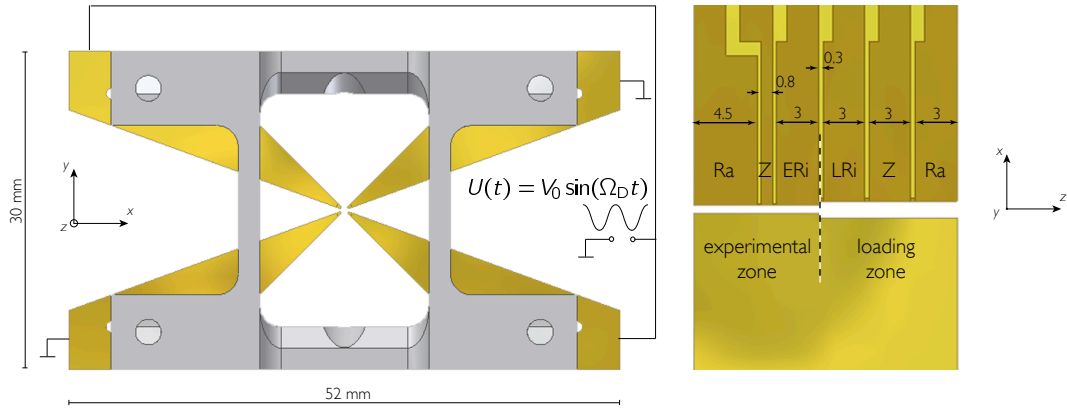


Figure 2.4. – View along the  $z$ -axis of our quadrupole Paul trap and top view (rotated) of the electrode structure. Rf-voltages are applied to one opposing pair of electrodes. The other opposing pair is rf-grounded. The segmentation of the rf-grounded electrode (upper right hand side) allows for applying additional dc voltages for the axial confinement. All measures are given in mm. The electrodes Ra, Z, and ERi compose the experimental zone, and the electrodes LRi, Z, and Ra form the loading zone of the trap. The central segment of the experimental zone (Z) is only 0.8 mm wide and allows for a stiff axial confinement.

have been built in the machine-shop of our institute. Schematic views of the trap are depicted in Fig. 2.4. The electrode structure in total measures  $52 \times 30 \times 18 \text{ mm}^3$ , the widths of single electrode segments ranges between 0.8 mm and 4.5 mm with inter-segment gaps of  $300 \mu\text{m}$ . The absolute fabrication accuracy is down to  $10 \mu\text{m}$ .

**Radial confinement** For the radial confinement we use an analog oscillator (*Hewlett-Packard HP8640B*) connected to a rf-amplifier (gain of 42 dB, *Amplifier Research 10W1000*). The output signal of the rf-amplifier is further enhanced via a high- $Q$ -helical resonator [58] which is explained in detail in Hector Schmitz's thesis [111]. The amplified signal is coupled into the vacuum chamber via an electrical rf-feed-through and applied to the rf-electrodes of the trap. The combined system of the tank circuit and the trap has a resonance frequency of  $\Omega_D \approx 2\pi \times 56 \text{ MHz}$ , the resonator quality factor  $Q$  of the system which is defined as the fraction between stored power and dissipated power amounts to  $Q \approx 90$ . We reach effective voltages of about 850 V at the trap electrodes allowing for radial trapping frequencies of the order of  $\omega_{\text{rad},x,y} = 2\pi \times 6 \text{ MHz}$  (see Eq. 2.4). Operating the system at higher rf-power levels, the electrodes considerably warm up due to resistive losses and noticeably degrade the vacuum pressure.

## 2.3. Vacuum and photochemical reactions

**Axial confinement** To provide axial confinement for the ions, we apply additional dc-voltages to the segmented rf-grounded electrodes. We do not have to apply independent dc-voltages to each of the electrodes' segments. Five independent voltage sources suffice for transferring ions from the loading zone to the experimental zone, e.g. both Ra segments and both Z-segments (see Fig. 2.4) are coupled and connected to the same source. These dc-trapping-voltages are generated by a *Jäger Meßtechnik, ADwin Gold* controller, a digital signal processor providing various analogue and digital in- and output signals. It is controlled by our measurement computer via Ethernet (see chapter 5.1). We enhance the maximum output voltage of +10 V out of this controller by home-built low noise voltage amplifiers to reach up to +100 V. These voltage multipliers are based on *PA-85* operational amplifiers. The supplying voltages are generated by low noise power supply sources (*Kniel, low emission series*). Electrical noise on the outputs of these amplifiers is further reduced by low-pass filters with cut-off frequencies of 100 Hz.

In the experimental zone, we apply the following voltages to the respective electrode segments  $U_{\text{Ra}} = 62\text{ V}$ ,  $U_{\text{Z}} = 0\text{ V}$  and  $U_{\text{ERi}} = 44\text{ V}$ . Via the experimentally measured trapping frequency  $\omega_z = 2\pi \times 2.11\text{ MHz}$ , we can determine the geometric parameter  $\kappa_{\text{dc}}$  in Eq. 2.1 and obtain  $\kappa_{\text{dc}} \approx 0.32$ . The reason for the asymmetric voltages for the Ra and the ERi electrodes is an additional axial contribution of the radial potential. This contribution is orders of magnitude smaller than the axial potential caused by the applied dc-voltages. Nevertheless, we may not neglect it, as it gives rise to differential micromotion between the ions. The above given voltages are chosen such that the two axial potential minima coincide.

If the ions are not located in the centre of the rf trapping potential, they are exposed to micromotion (see Fig. 2.2). We use two more electrodes for pushing the ions back into the centre of the harmonic potential, where the ions are free of micromotion. These micromotion compensation electrodes are located outside of the trap. Due to the shielding of the trap electrodes we need high voltages to achieve an impact on the ions<sup>3</sup>. With our current setup we cannot work with an axial confinement larger than  $\omega_z = 2\pi \times 2.5\text{ MHz}$ , since we would have to exceed the maximum voltage rating for our electrical feed-through of 1000 V to compensate for micromotion (see section 6.3).

## 2.3. Vacuum and photochemical reactions

We provide an ultra-high vacuum (UHV) to minimise collisions with background gas particles which can result in ion loss, cause decoherence by scattering, or lead to

---

<sup>3</sup>One of these compensation electrodes has negligible effect on the ions (the one in the tangential plane of the trap), therefore we differentially apply voltages to the pair of Z-electrodes to compensate for micromotion in this spatial direction. As seen from the trap centre (position of the ions), the electrodes enclose an angle of approximately 35° with the tangential plane which couples the degrees of freedom and we have to iterate the compensation of the spatial directions

## 2. Trapping Ions

(photo)chemical reactions in combination with laser fields. A vacuum pressure of the order of  $10^{-11}$  mbar allows for lifetimes of the ions of many hours or even days.

To achieve vacuum pressures of the order of  $10^{-11}$  mbar, we first carefully cleaned the vacuum chamber and all parts of the trap apparatus and assembled the trap in a clean environment. We evacuated the vacuum chamber using an oil-free scrollpump and an oil-free molecular turbo pump (*Pfeiffer Vacuum*) for about 24 h. Thereby, we reached a pressure of the order of  $10^{-7}$  mbar. We baked out the whole vacuum apparatus at a temperature of about  $150^{\circ}\text{C}$ . To provide a uniform temperature distribution among the whole apparatus, we built a brick oven around the system. We had some issues with vacuum laser viewports which became leaky and had to be exchanged, so that the baking process altogether took about four weeks. After slowly cooling down the setup to prevent mechanical stress, we employed an ion getter pump and a titanium sublimation pump (*Varian*) and finally achieved a vacuum pressure of approximately  $6 \times 10^{-11}$  mbar at room temperature measured by an ion gauge (*Granville-Phillips model 350*). This ion gauge has been calibrated with nitrogen, but since the constitution of the residual gas in our chamber certainly differs from pure nitrogen, and furthermore, the ion gauge is operated at its sensitivity limit, this number has to be taken with care. A more relevant measure for the quality of the vacuum is the lifetime of the ions. Typically, we are able to keep strings of ten ions over night without loss.

However, there is a process which occurs more frequently than the process that ions are being kicked out of the trap due to collisions, that is a photochemical reaction. The reaction



leaves us with a dark molecular ion. In principle this reaction is reversible, but there are two dissociation channels [59],  $\text{MgH}^+ \longrightarrow \text{Mg}^+ + \text{H}$  or  $\text{Mg} + \text{H}^+$ . In the latter reaction both the Magnesium atom and the proton would be lost from the trap. The two decay channels could be deterministically controlled [59] by shining in two laser pulses at wavelengths  $\lambda_1 = 280.89$  nm and  $\lambda_2 = 620$  nm. Yet we have not pursued this possibility. However, it happened up to several times a day that dark molecular ions became bright again on time scales ranging between minutes and few hours. The interpretation that one of the ions was kicked out of a crystal and circulated on a high orbit and was cooled back to the crystal does not hold, since we were able to provoke changes in place between the constituents of the crystal by heating and re-cooling the ion crystal. This proves that a dark ion was actually part of the ion crystal. Working with longer linear chains of ions, the probability that one of the ions undergoes a photochemical reaction increases, so for future work one could think about incorporating the above mentioned scheme [59]. To achieve an even better vacuum, we might also consider to incorporate cryogenic trap technology in the future.

## 2.4. Quantisation fields

In order to be able to manipulate the electronic population of the Zeeman sublevels of the  $^2S_{1/2}$   $F = 3$  and  $F = 2$  manifolds, we break the degeneracy of these manifolds by introducing a quantisation magnetic field  $B_{\text{quant}}$ . Further, this field provides a quantisation axis for the ions and defines the polarisation of laser beams interacting with the ions. The main contribution to this quantisation field is generated by two magnetic field coils on opposite sides of the vacuum chamber with their axes collinear with the detection laser beam (see chapter 4). The geometry of our recipient does not allow for Helmholtz's configuration where the radius of the coils  $r_{\text{coil}}$  corresponds to the distance between these  $d_{\text{coils}}$ . In our case this ratio is  $d_{\text{coils}}/r_{\text{coil}} \approx 5$ . The geometry of the field coils is depicted in Fig. 2.5. Nevertheless, we obtain a sufficiently homogenous magnetic field for several ions [99]. We use a home-built current stabilisation circuit to supply the field coils with currents of  $I = 6$  A (accuracy  $\frac{\Delta I}{I} < 10^{-5}$ ). We achieve a magnetic field of  $B = 5.5$  G leading to a Zeeman splitting of adjacent levels of  $\Delta\omega = 2\pi \times 2.74$  MHz. The coils get considerably warm ( $T \approx 60^\circ\text{C}$ ) and it takes hours until they reach a steady state condition, but we avoid water cooling to minimise vibrations.

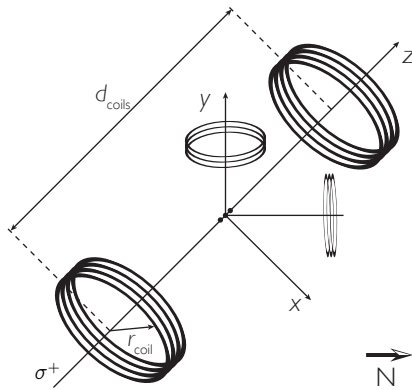


Figure 2.5. – Geometry of magnetic field coils generating the quantisation magnetic field. The axis of the two large coils coincides with the  $\mathbf{k}$ -vector of the detection laser beam (see chapter 4). The two (smaller) compensation coils, one of them pointing in the vertical direction, the other one in the horizontal plane enclose an angle of  $45^\circ$  with the quantisation axis and allow us to maximise the fluorescence count rate by fine-tuning the collinearity of the laser beam and the  $\mathbf{B}$ -field axis.

We fine-tune the direction of the quantisation axis to match the  $\mathbf{k}$ -vector of the detection beam via two additional transverse compensation coils, as is depicted in Fig. 2.5. In practise, we optimise the fluorescence count rate from the ions by adjusting the current of these coils (see chapter 6.5).

## 2.5. Atom ovens

We photoionise a thermal beam of magnesium atoms within the trapping region of the loading zone of our trap. The atom ovens generating the atomic beam are depicted in Fig. 2.6. The ovens are made of tantalum tubes filled with a granulate of magnesium. This tantalum tubes are held in place and heated by two tantalum wires each. One of

## 2. Trapping Ions

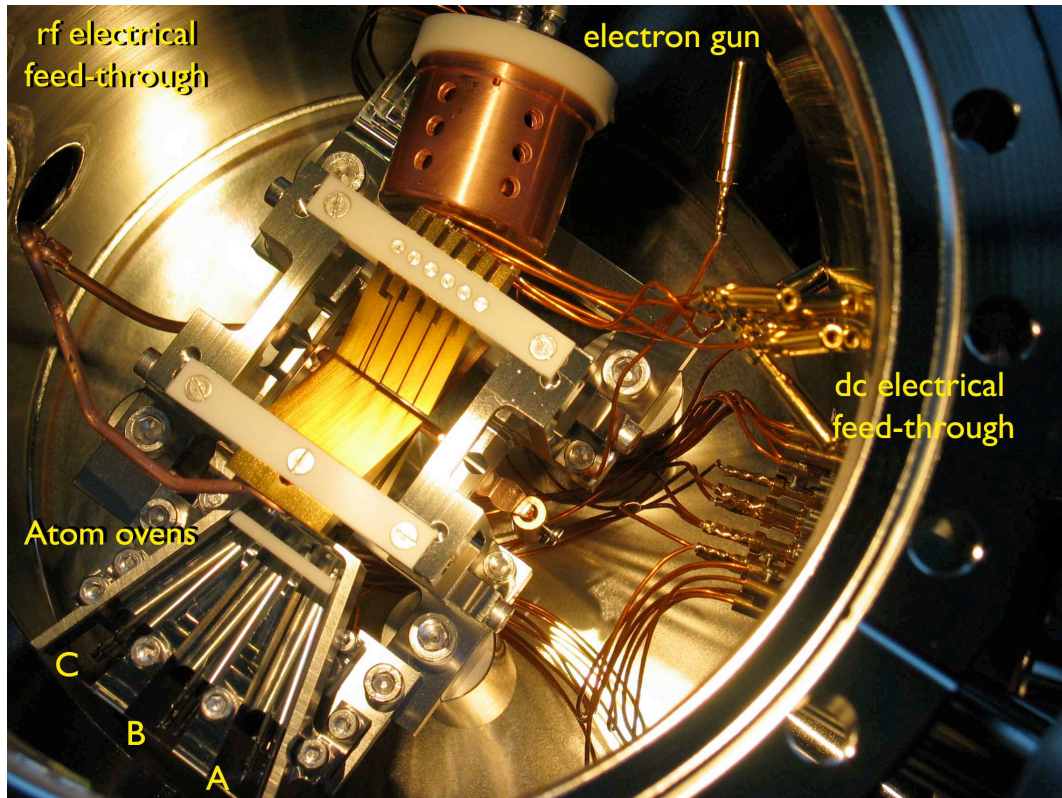


Figure 2.6. – Top view of the recipient with the ion trap in the centre, the three atom ovens pointing to the loading region of the trap in the lower left and the emergency electron gun in the upper middle. Further one can see the gold coated trap electrodes (compare to Fig. 2.4). The trap electrodes and atom ovens are connected to the dc vacuum feed-through via insulated *capton* wires. The rf electrodes are supplied by the two thick copper conductors ending in the upper left at the rf feed-through.

the ovens is filled with natural abundant magnesium isotopes (Oven A, 79%  $^{24}\text{Mg}$ , 10%  $^{25}\text{Mg}$ , and 11%  $^{26}\text{Mg}$ ), the other two ovens contain isotopically enriched  $^{25}\text{Mg}$  atoms (Oven B and C, 99.9%  $^{25}\text{Mg}$ ). Due to the isotope shifts (for  $^2\text{S}_{1/2} \rightarrow ^2\text{P}_{3/2}$  transition  $\Delta\nu(^{24}\text{Mg}^+, ^{25}\text{Mg}^+) \approx 2.23 \text{ GHz}$ ,  $\Delta\nu(^{24}\text{Mg}^+, ^{26}\text{Mg}^+) \approx 3.05 \text{ GHz}$  [11]) we can selectively load different isotopes of magnesium by appropriately tuning the wavelengths of the photoionisation and cooling laser. The ovens are all pointing towards the center of the loading zone of the trap from slightly different directions. Oven B is perpendicular to the trap axis, whereas oven A and C are tilted by  $\pm 15^\circ$  to both sides of oven B and one has to take into account Doppler shifts when choosing the appropriate frequency for the photoionisation laser. We deduce oven temperatures on the order 600 K at typical currents of  $(2.2 \pm 0.1) \text{ A}$ . With these parameters, it takes about a minute for

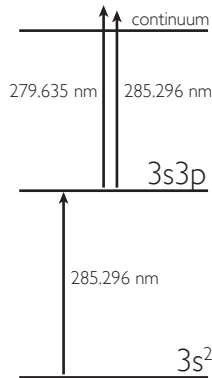


Figure 2.7. – Level scheme of atomic Magnesium. Magnesium has the electronic configuration  $[\text{Ne}] 3s^2$ . We photoionise via a resonant two step process. The atom is resonantly excited to the electronic state  $3s3p$  by the photoionisation laser of wavelength  $\lambda_{\text{photo}} = 285.296 \text{ nm}$ . The excited atom may either absorb another photon out of the photoionisation beam or a photon out of the cooling laser beam (see next chapter). Both absorption process bring it to the continuum.

the oven to heat up.

Photoionisation of magnesium atoms can be accomplished in a two step process. In a first step, a magnesium atom with a valence electron configuration  $3s^2$  resonantly absorbs a photon of wavelength  $\lambda = 285.296 \text{ nm}$ , we resonantly drive the atomic transition<sup>4</sup>  $3s^2 \rightarrow 3s3p^1P_1$ . From this excited state, the atom can either absorb another photon from the same laser or absorb a photon from the cooling laser (see Fig. 2.7 for the corresponding level scheme). Both processes further excite the electron to the continuum, leaving us with a singly ionised magnesium ion.

We also included an electron gun in our setup which can be seen in Fig. 2.6. We call it “emergency electron gun” as it was only included in case we did not succeed in photoionisation. Compared to photoionisation, electron bombardment has several drawbacks:

- Electron bombardment is less efficient than photo-ionisation.
- Due to the heat of the photo cathode the vacuum pressure suffers.
- The insulators within the apparatus become charged and influence the position of the ions which might result in micromotion and changing overlap of the ions with the laser beams.
- Isotope-selectively loading of ions with the electron gun is not possible.

<sup>4</sup>Shining in the photo-ionisation laser beam at a laser beam power  $> 1 \text{ mW}$  with a corresponding beam waist of roughly  $w_0 \approx 70 \mu\text{m}$ , we are able to observe fluorescence light from the excited Mg atoms of the atomic beam, this eases the initial alignment of the overlap between the atomic beam and the photoionisation laser beam.

## 2. Trapping Ions

### 2.6. Imaging optics

To be able to collect fluorescence light from the ions, we use a diffraction limited  $f/1$  high-quality four lens objective built by *B. Halle Nachfl, Berlin*. It has a focal length  $f = 19.3$  mm and is optimised for a magnification factor of 50. All surfaces of this objective are anti-reflective coated for 280 nm. We observe the fluorescence light emitted from the ions in vertical direction. The dipole characteristics of the emission of  $\sigma^\pm$  polarised light is given by

$$P(\theta) = 1 + \cos^2(\theta) \quad (2.17)$$

in polar coordinates, where  $\theta = 0$  is pointing along the quantisation axis. Thus, in the particular direction we observe ( $\theta = \pi/2$ ), the ion has its emission minimum. Nevertheless, the objective captures 4.7% of the fluorescence light due to its large aperture. An inverted window equipped with a sapphire single crystal, antireflective (AR) coated for 280 nm, serves as observation port. The objective is inserted into a metal tube for shielding stray light and mounted on a 3D linear translation stage. This assembly is mounted to the recipient with three fine adjustment screws, allowing for tip/tilt adjustment of the objective. More details about this adjustment procedure can be found in refs. [99, 111]. As illustrated in Fig. 2.8, the fluorescence light is reflected by a  $45^\circ$  mirror of 50 mm diameter and propagates horizontally for almost two more meters to a optically sealed box which contains an electron multiplying charge coupled device (EMCCD) camera (*Andor, iXon*) and a photomultiplier tube (PMT, *Hamamatsu*). The EMCCD camera is back-illuminated and features an inherent signal amplification mechanism. The chip contains a gain register which enhances the signal on the chip, thereby suppressing read out noise. The chip is cooled down to temperatures of the order of  $-90^\circ\text{C}$  to further reduce the noise level. We apply water-cooling to the heat sink of the camera to achieve temperatures below  $-80^\circ\text{C}$ . To optimise the fluorescence count rate of the PMT, we have to slightly de-focus the incoming light to avoid locally saturating the PMT. To toggle between the camera and the PMT, we use a motorised flip mirror mount. Both the camera and the PMT are equipped with AR coated *Schott UG5* glass filters to absorb visible straylight (1 mm thick, transmission of 88% at 280 nm). All components are carefully shielded against ambient light using laser safety curtain wrappings or metal housings.

The total fluorescence count rate of an irradiated ion is given by

$$R_{\text{fl}} = \frac{s \cdot \Gamma/2}{1 + s + (2\delta/\Gamma)^2}, \quad (2.18)$$

where  $s \equiv I/I_0$  is the on-resonance saturation parameter which is the fraction between applied intensity  $I$  and saturation intensity  $I_0$  of the ion which is given by  $I_0 = 255 \text{ mW/cm}^2$ . At a beam waist of the BD beam of  $30 \mu\text{m}$ , half the saturation

## 2.6. Imaging optics

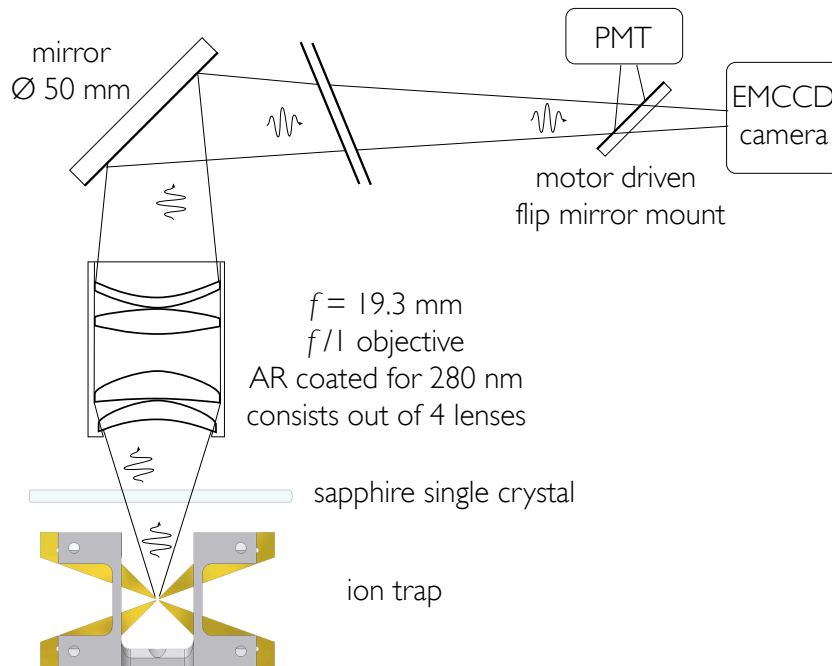


Figure 2.8. – Schematic of imaging optics (not to scale): the total length of the beam path amounts to roughly 2 m. A fraction of the fluorescence light emitted by an ion leaves the vacuum chamber in vertical direction via an inverted view port. The light is focussed by a diffraction limited objective and propagates for about two meters, being reflected by one or two mirrors on its way, depending on the position of the flip mirror in front of the camera, until reaching the EMCCD chip or the PMT.

intensity amounts to  $1.6 \mu\text{W}$ ,  $\delta$  represents the detuning of the laser frequency from the resonance and  $\Gamma = 2\pi \times 42.7 \text{ MHz}$  is the natural linewidth of the transition. For the case of zero detuning at half of the saturation intensity we obtain  $R_{\text{fl}} \approx 45 \text{ MHz}$ . As stated above, we collect 4.7% of the emitted photons due to the limited solid angle, loose 14% due to the *Schott* glass filter and mirror imperfections. The quantum efficiency of our PMT at  $\lambda = 280 \text{ nm}$  is 14%. Hence, we detect 5.6‰ of the total number of emitted photons. This leads to a fluorescence count rate of the order of  $R_{\text{count}} \approx 250 \text{ kHz}$ . This analysis is in good agreement with experimentally observed count rates ( $\delta = 0$ ,  $I = \frac{I_0}{2}$ ).

## 2. *Trapping Ions*

## 3. $^{25}\text{Mg}^+$ : Level structure and transitions

### 3.1. The choice of our spin system

One crucial decision one has to reach, when designing an ion trap experiment, is the species of ion to choose. To obtain a simple electronic level scheme similar to that of alkaline atoms used for experiments with neutral atoms, we take into consideration earth alkaline atoms (Be, Mg, Ca, Sr, Ba), Lanthanides (Yb) or transition elements (Al, In, Hg). We formulate the following requirements to be met by the ion:

1. a lightweight ion for strong spin-motion coupling (for motional ground state cooling, see chapter 7), and stiff confinement<sup>1</sup>
2. long life time of the qubit/spin system
3. available lasers meeting certain specifications (linewidth, power, reliability) to address transitions
4. number of laser systems as low as possible
5. being able to use photoionisation

We opted for magnesium-25 ions for the following reasons: It is comparably lightweight and its electronic D-levels do not fall in between the S and P levels, which renders repumper lasers for the D-levels unnecessary. To ensure long life times of the internal states, we chose two hyperfine ground states to simulate spin states (natural lifetime  $\tau$  of hundreds of years), instead of using one ground state and one “long-lived” excited state (e.g. calcium, metastable  $D_{5/2}$  state with  $\tau \approx 1$  s). The latter scheme requires the stabilisation of the corresponding laser linewidth to sub-Hertz. Rainer Blatt’s group in Innsbruck follows this approach [107]. David Wineland’s group at NIST uses hyperfine ground states of beryllium [127] which has similar properties as magnesium-25.

For efficient ground state cooling (see chapter 7) and achieving strong spin-spin coupling (see chapter 8) we use two-photon stimulated Raman (TPSR) transitions via a detuned virtual level (see section 3.4). The two beams required to achieve this coupling have to be phase-coherent. We use one<sup>2</sup> laser for generating these two beams

---

<sup>1</sup>Lightweight ions experience a stronger confinement in future shallow surface traps.

<sup>2</sup>One can also use two self-reliant laser systems which are stabilised in phase. We disregard this possibility for now due to pecuniary aspects.

### 3. $^{25}\text{Mg}^+$ : Level structure and transitions

and use AOMs (see section 4.5) to bridge the frequency gap determined by the ground state splitting  $\omega_0$  (see Fig. 3.2).

Although the  $^2\text{S}_{1/2} - ^2\text{P}_{3/2}$  transition of magnesium ions near 280 nm (see next section) lies deeper in the ultraviolet than the corresponding transition of beryllium at 313 nm<sup>3</sup>, however they are more convenient to address. To accomplish this, we developed a laser system [37] comprising a diode pumped ytterbium fibre laser and two second harmonic generation cavities (SHG, see chapter 4). This system is cheaper by approximately a factor of three than the previously used dye laser system including pump laser and one second harmonic generation cavity. We achieve more laser beam power at lower linewidth and less beam power fluctuations which is advantageous for far detuned two-photon stimulated Raman transitions (see section 3.4). However, we are still experiencing reliability issues with the ytterbium fibre lasers.

## 3.2. Electronic structure of $^{25}\text{Mg}^+$

There are three stable magnesium isotopes<sup>4</sup>: magnesium-24, and magnesium-26 which do not exhibit a nuclear magnetic momentum and hence lack hyperfine structure and magnesium-25 which has a nuclear magnetic spin of  $I = 5/2$ . After singly ionising magnesium-25, it has a single valence  $3s$ -electron. We recapitulate the spectroscopic notation  $^{2S+1}L_J$ , where  $S$  is the spin quantum number,  $L$  the angular magnetic momentum, and  $J = L + S$  the total orbital angular momentum. The angular magnetic momentum  $L$  takes on the values labelled  $S = 0$ ,  $P = 1$ ,  $D = 2$ ,  $\dots$ . We will only consider the ground  $S$  orbital and the lowest excited state, the  $P$  orbital, since the  $D$  levels do not fall in between the  $S$  and  $P$  levels, are not populated and can thus be neglected in this work. The coupling of spin ( $S$ ) and angular momentum ( $L$ ) of the electron leads to the fine-structure splitting of the  $^2\text{P}$  level into lower lying  $^2\text{P}_{1/2}$  and higher lying  $^2\text{P}_{3/2}$  levels in terms of energy. These are separated by  $\omega_{FS} = 2\pi \times 2.74$  THz (see Fig. 3.1).

The nuclear magnetic momentum  $I$  couples to the total angular momentum  $J$  of the electron and gives rise to a hyperfine structure splitting of  $\omega_0 = 2\pi \times 1.77$  GHz for the ground state  $^2\text{S}_{1/2}$ . The two resulting manifolds carry the quantum numbers  $F = I \pm J$ . We break the degeneracy of the Zeeman sub-levels by applying a magnetic quantisation field of the order of 5.5 G (see section 2.4). The energy shift is given by  $\Delta E = -\mu_B g_F m_F B$  with the Bohr magneton  $\mu_B$ , the Landé factor  $g_F$  which takes the values  $g_F = \pm 1/2$  for  $F = 3$  (upper sign) and  $F = 2$  (lower sign).  $B$  is the magnetic

<sup>3</sup>The NIST group is now adapting a new laser setup consisting of two fibre lasers, one erbium doped near 1530 nm and one ytterbium doped near 1060 nm. They employ sum frequency generation (SFG) to obtain  $\lambda = 626$  nm which they further double in frequency to finally reach radiation near 313 nm. The scheme is elaborate but promises to achieve higher output power and lower maintenance compared to the dye lasers in use up to now.

<sup>4</sup>For natural abundances see section 2.5

### 3.3. Initialisation and detection of the spin system

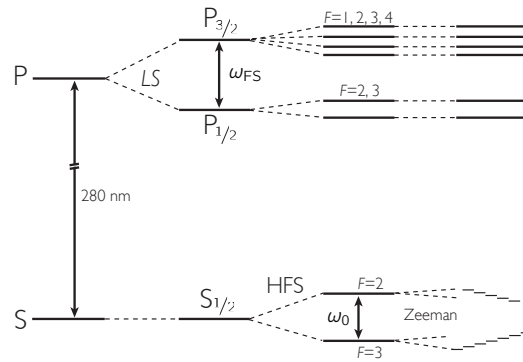


Figure 3.1. – On the left hand side we depicted the two lowest states of angular momentum  $L = 0$  called S and  $L = 1$  called P orbitals. The spin orbit coupling ( $LS$ ) gives rise to a fine-structure splitting of the excited state. The coupling between nuclear magnetic momentum  $I$  and total orbital angular momentum  $J$  leads to a hyperfine structure. The hyperfine ground state splitting  $\omega_0$  amounts to  $\omega_0 = 2\pi \times 1.77$  GHz and will be of importance throughout this thesis, as  $\hbar\omega_0$  is the energy difference between our spin states. The Zeeman effect, induced by our quantisation magnetic field, lifts the degeneracy between the sublevels. The hyperfine structure of the excited P states is negligibly small compared to  $\omega_0$ .

field and  $\hbar m_F$  corresponds to the projection of the ion's total angular momentum onto the axis of the quantisation field  $B$  with  $\hbar$  being Planck's constant  $h$  divided by  $2\pi$ . The electronic level scheme is illustrated in Fig. 3.1

### 3.3. Initialisation and detection of the spin system

Starting an experiment, the electronic population is equally distributed over all Zeeman sublevels of the  $^2S_{1/2}$  ground state. We optically pump [54] the ion to the state  $^2S_{1/2} |F = 3, m_F = +3\rangle$  by shining in a  $\sigma^+$  polarised laser beam tuned to the transition  $^2S_{1/2} F = 3 \rightarrow ^2P_{3/2}$  from now on referred to as Blue Doppler (BD). In addition, we have to repump<sup>5</sup> electrons decaying to the state  $^2S_{1/2} F = 2$  with the so-called Red Doppler (RD) beam addressing the transition  $^2S_{1/2} F = 2 \rightarrow ^2P_{1/2}$ . We label the state  $^2S_{1/2} |F = 3, m_F = +3\rangle \equiv |\downarrow\rangle$  and call this process initialisation of the spin state. We further define the state  $^2S_{1/2} |F = 2, m_F = +2\rangle$  as  $|\uparrow\rangle$  state, together, these two states shall represent a spin-1/2 system.

<sup>5</sup>This task can also be accomplished by a further red detuned BD beam of correspondingly higher intensity, which we will refer to as Blue Doppler detuned (BDdet) and mainly serves for pre-cooling, see chapter 7.

### 3. $^{25}\text{Mg}^+$ : Level structure and transitions

For state sensitive fluorescence detection [90, 128] (see section 3.3 and chapter 9), we require a closed electronic transition. After initialising the spin system to the state  $|\downarrow\rangle$ , we shine in  $\sigma^+$  polarised light with respect to the ion. The valence electron is taken to the state  $^2\text{P}_{3/2} |F = 4, m_F = +4\rangle$ . This level has a natural lifetime of  $\tau = 3.7$  ns. The corresponding linewidth of its decay by spontaneous emission amounts to  $\Gamma = 2\pi \times 42.7$  MHz. This excited state will inevitably decay to the state  $|\downarrow\rangle$  (since there is no other level with  $m_F \geq +3$ ) emitting a  $\sigma^+$ -polarised photon. Being prepared in state

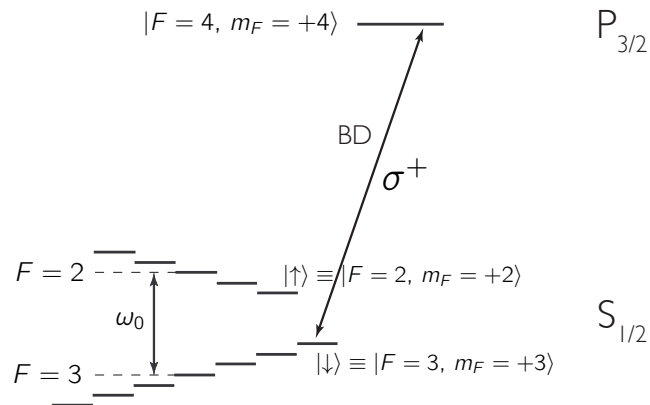


Figure 3.2. – In this reduced level scheme we define the spin-1/2 system  $|\downarrow\rangle$  and  $|\uparrow\rangle$ . Furthermore we illustrated the cycling BD transition coupling the  $|\downarrow\rangle$  state with the  $^2\text{P}_{3/2} |F = 4, m_F = +4\rangle$  state and serving as system initialisation, Doppler cooling and state detection laser. The other hyperfine levels of the  $^2\text{P}_{3/2}$  are omitted for clarity. The ground state splitting  $\omega_0$  amounts to  $\omega_0 = 2\pi \times 1.77$  GHz. The degeneracy of the Zeeman sublevels is lifted by a quantisation magnetic field of  $B_{\text{quant}} = 5.5$  G giving rise to a splitting of  $\Delta = 2\pi \times 2.74$  MHz between adjacent levels.

$|\downarrow\rangle$ , the ion is able to resonantly scatter hundreds of millions of photons during one second, whereas being in the state  $|\uparrow\rangle \equiv ^2\text{S}_{1/2} |F = 2, m_F = +2\rangle$ , it will in first order not be excited and therefore remain dark during detection. For long detection intervals ( $t_{\text{det}} > 50 \mu\text{s}$ ), this does not hold true any more (see chapter 9). Fig. 3.2 depicts the ground state hyperfine levels including the two levels spanning our spin-1/2 system and the BD transition<sup>6</sup>.

<sup>6</sup>More subtleties about the BD transitions and the technical implementation of the beams are discussed in section 7.3.1 and section 4.6.1

### 3.4. Coherent coupling of spin states

**Single ion state detection** After having carried out an experiment, we want to be able to measure the outcome which might be an arbitrary superposition or mixture of states  $|\uparrow\rangle$  and  $|\downarrow\rangle$ . By shining in the detection laser we project the ion into our measurement basis  $\sigma^z$  with the two eigenstates  $|\uparrow\rangle$  and  $|\downarrow\rangle$ . The ion will either be projected into the bright state or into the dark state with probabilities given by the amplitudes of the given state. For a single ion in an arbitrary state  $|\Psi\rangle$

$$|\Psi\rangle = c_1 |\downarrow\rangle + c_2 |\uparrow\rangle \quad (3.1)$$

with complex amplitudes  $c_i$  which obey the condition  $|c_1|^2 + |c_2|^2 = 1$ , the fluorescence count rate  $S_{\text{tot}}$  is given by

$$S_{\text{tot}} = |c_1|^2 S_0, \quad (3.2)$$

where  $S_0$  is the fluorescence count rate for one ion in state  $|\downarrow\rangle$  (for a numerical analysis of this fluorescent count rate see section 2.6). The analysis of the outcome of experiments with several ions is discussed in chapter 9.

### 3.4. Coherent coupling of spin states

We can choose between two possible ways of driving coherent transitions between the states  $|\downarrow\rangle$  and  $|\uparrow\rangle$ : resonant radio-frequency transitions and two-photon stimulated Raman (TPSR) transitions which are subdivided into transitions driven by collinear and orthogonal beams. Radio-frequency and TPSR transitions with collinear beams are not sensitive to the motion of the ion in the harmonic oscillator potential of the trap. Yet, they differ in the type of transition, the employed TPSR transitions are electric dipole transitions (E1), whereas the radio-frequency transitions are magnetic dipole transitions (M2). During M2 transitions, the nuclear magnetic spin may be flipped. Laser induced transitions via detuned “virtual” levels suffer from the possibility of spontaneous emission after off-resonantly populating a “real” level. This is a source of decoherence (see chapter 6.4.2). In addition, it has to be made sure that the spatial overlap between laser beams and the position of the ions is optimised and the ions are equally irradiated<sup>7</sup>. As an advantage, in principle, it allows for single ion addressing which we did not pursue in this work. Driving radio-frequency transitions in some respects provides advantages over collinear TPSR transitions. With radio-frequency transitions, unequal irradiation of different ions is mitigated, since the wavelength of the radio-frequency is orders of magnitude larger than the inter-ion distance and length of the spin chain.

TPSR transitions driven by mutually orthogonal beams transfer momentum to the ion and, therefore, allow to couple the internal (electronic) states with the external (motional) states of the ions confined in the harmonic trapping potential. By choosing

<sup>7</sup>In our case for two ions the Gaussian beam waist  $w_0$  is much larger than the length of the ion chain  $w_0 \approx 45 \mu\text{m} \gg l_{\text{chain}} \approx 4 \mu\text{m}$

### 3. $^{25}\text{Mg}^+$ : Level structure and transitions

an appropriate beam geometry, we can determine which modes to address, the axial, or the radial vibrational modes. During this thesis, we solely address the axial modes (see Fig. 3.3). In the following, we move to a more formal description of the interaction between atoms and laser fields and explain the theoretical framework for laser-induced transitions.

**Reduction to a two-level system** As can be deduced from the quantum numbers, the  $^2\text{S}_{1/2}$  ground state consists of 12 Zeeman sub-levels (see Fig. 3.1). Since we apply an external magnetic field to lift the degeneracy of the sublevels, it is appropriate to restrict our consideration to solely two out of these 12 levels. The frequencies of the laser beams for coupling the internal levels are applied close-to-resonance ( $\delta \approx 0$ ,  $\Delta_R$  large) and the intensities such that the corresponding Rabi frequency describing the coupling strength is much smaller than the detuning relative to off-resonant transitions [71].

Mathematically, a two-level system is equivalent to a spin-1/2 system [36], thus, we may map our system onto the spin-1/2 operator basis, enabling us to formulate the Hamiltonian in the following form

$$H_{\text{el}} = \frac{\hbar\omega_0}{2} \hat{\sigma}^z, \quad (3.3)$$

where we suppressed a state-independent energy contribution [71]. As we do not want to obscure matters by using different notations for basis states, we express the Pauli matrices in terms of our basis states  $|\uparrow\rangle$  and  $|\downarrow\rangle$ . They take the following form:

$$\begin{aligned} \hat{\sigma}^z &\equiv |\uparrow\rangle\langle\uparrow| - |\downarrow\rangle\langle\downarrow| & \hat{I} &\equiv |\uparrow\rangle\langle\uparrow| + |\downarrow\rangle\langle\downarrow| \\ \hat{\sigma}^x &\equiv |\downarrow\rangle\langle\uparrow| + |\uparrow\rangle\langle\downarrow| & \hat{\sigma}^y &\equiv i(|\downarrow\rangle\langle\uparrow| - |\uparrow\rangle\langle\downarrow|) \\ \hat{\sigma}^+ &\equiv |\uparrow\rangle\langle\downarrow| & \hat{\sigma}^- &\equiv |\downarrow\rangle\langle\uparrow| \end{aligned} \quad (3.4)$$

The Hamiltonian describing a chain of ions confined in a harmonic axial potential can be expressed as

$$\begin{aligned} H_0 &= H_{\text{el}} + H_{\text{vib}} \\ &= \frac{\hbar\omega_0}{2} \sum_{j=1}^n \hat{\sigma}_j^z + \hbar \sum_i \omega_{z,i} \hat{a}_i^\dagger \hat{a}_i, \end{aligned} \quad (3.5)$$

where the summation in the first term is carried out over the number of ions  $n$  and the summation in the second term over  $n$  axial normal modes  $\omega_{z,i}$  (see Eq. 2.1).

**Coupling to a light field** We can relate a fictitious magnetic moment  $\hat{\boldsymbol{\mu}} = \mu_M \hat{\mathbf{S}}$  to this spin-1/2-system, where  $\hat{\mathbf{S}} = \frac{\hbar}{2} \hat{\boldsymbol{\sigma}}$  represents the spin operator. The interaction of the spin-1/2-system with a light field can be described in terms of a magnetic field

### 3.4. Coherent coupling of spin states

$\mathbf{B}(z, t)$  interacting with this magnetic moment. Assuming a travelling-wave magnetic field, polarised in  $x$ -direction, propagating in  $z$ -direction with effective wavevector  $k$  (in section 3.4 we will comment in more detail on this wavevector), we obtain

$$\begin{aligned} H_I &= -\boldsymbol{\mu} \cdot \mathbf{B}(z, t) \\ &= -\mu_M \hat{\mathbf{S}} \cdot \hat{x} B_x \cos(kz - \omega t + \phi) \\ &= \hbar\Omega(\sigma^+ + \sigma^-) \left( e^{i(kz - \omega t + \phi)} + e^{-i(kz - \omega t + \phi)} \right), \end{aligned} \quad (3.6)$$

where  $\hat{\sigma}^+ \equiv \hat{\sigma}_x + i\hat{\sigma}_y$ ,  $\hat{\sigma}^- \equiv \hat{\sigma}_x - i\hat{\sigma}_y$ ,  $\hat{x}$  is the unit vector in  $x$ -direction and we introduced  $\Omega \equiv -\mu_M B_x/4$ . It is convenient to canonically transform this expression to the interaction picture, where we can simplify the interaction by applying the *rotating wave approximation* [76] (RWA, neglecting terms oscillating at optical frequencies  $e^{\pm i(\omega + \omega_0)t}$ ). This transformation is given by

$$H'_I = e^{i\frac{H_0}{\hbar}t} H_I e^{-i\frac{H_0}{\hbar}t} \quad (3.7)$$

with  $H_0 = H_{\text{el}} + H_{\text{vib}}$ .

The wavefunction in the interaction picture can be expressed as

$$\psi = \sum_{s=\uparrow, \downarrow} \sum_{n=0}^{\infty} C_{s,n}(t) |s\rangle |n\rangle, \quad (3.8)$$

where  $s$  and  $n$  are the internal and the motional eigenstates, respectively, which are time-independent in the interaction picture. The interaction picture representation of the Hamiltonian for one motional mode is given by [127]

$$H'_I = \hbar\Omega \sigma^+ \exp(i[\eta(\hat{a} e^{-i\omega_z t} + \hat{a}^\dagger e^{i\omega_z t}) - \delta t + \phi]) + \text{h.c.}, \quad (3.9)$$

where we expressed the ion's motion in terms of normal modes (see section 2.1) using  $z = z_0(\hat{a}^\dagger + \hat{a})$ ,  $\delta \equiv \omega - \omega_0 = \omega_z(n' - n)$ , and  $\eta \equiv kz_0$  denominates the Lamb-Dicke parameter, which is proportional to the coupling strength between internal and motional states of the ion. Its square represents the fraction between the recoil energy experienced by the ion upon absorption or emission of a photon and the energy of a vibrational quantum.

The interaction Hamiltonian couples the internal and vibrational degrees of freedom of the ion. The coupling arises from the oscillatory motion of the ion in the harmonic potential. As perceived by the ion in its rest frame, the laser field is modulated in frequency, therefore, the ion experiences sidebands separated by the trapping frequency  $\omega_z$ . Due to the principle of energy conservation, the motional state of the ion changes upon absorption or emission of a photon on a sideband. By tuning the laser resonantly to a (sideband) transition, one can coherently drive transitions between the states  $|\downarrow, n\rangle$  and  $|\uparrow, n'\rangle$ .

### 3. $^{25}\text{Mg}^+$ : Level structure and transitions

Inserting our wavefunction ansatz (Eq. 3.8) into Schrödinger's equation

$$i\hbar \frac{\partial}{\partial t} \Psi = H'_1 \Psi, \quad (3.10)$$

we can solve for the coefficients  $C_{s,n}(t)$  and obtain a coupled set of equations

$$\dot{C}_{\uparrow,n'} = -i^{(1+|n'-n|)} e^{i\phi} \Omega_{n',n} C_{\downarrow,n}, \quad (3.11)$$

$$\dot{C}_{\downarrow,n} = -i^{(1-|n'-n|)} e^{-i\phi} \Omega_{n',n} C_{\uparrow,n'}, \quad (3.12)$$

where  $\Omega_{n',n}$ , the Rabi frequency, is given by [127]

$$\Omega_{n',n} \equiv \Omega \left| \langle n' | e^{i\eta(\hat{a} + \hat{a}^\dagger)} | n \rangle \right| \quad (3.13)$$

$$= \Omega e^{-\eta^2/2} \sqrt{\frac{n_{<}!}{n_{>}!}} \eta^{|n'-n|} L_{n_{<}}^{|n'-n|}(\eta^2), \quad (3.14)$$

and  $n_{<}$  ( $n_{>}$ ) is the lesser (greater) of  $n'$  and  $n$  and  $L_n^\alpha$  is the generalised Laguerre polynomial

$$L_n^\alpha(X) = \sum_{m=0}^n (-1)^m \binom{n+\alpha}{n-m} \frac{X^m}{m!}. \quad (3.15)$$

Eq. 3.13 will be important for resolved sideband cooling, which will in detail be described in chapter 7.

The time evolution of the wavefunction describing a resonant interaction with a light field exhibits sinusoidally oscillating terms

$$\Psi(t) = \begin{pmatrix} \cos \Omega_{n',n} t & -ie^{i(\phi + \frac{\pi}{2}|n'-n|)} \sin \Omega_{n',n} t \\ -ie^{-i(\phi + \frac{\pi}{2}|n'-n|)} \sin \Omega_{n',n} t & \cos \Omega_{n',n} t \end{pmatrix} \Psi(0). \quad (3.16)$$

For a full treatment of the equations of motion including off-resonantly driven systems, please refer to ref. [127].

**Transitions within the Lamb-Dicke regime** In the Lamb-Dicke regime ( $\sqrt{n}\eta \ll 1$ ), a change of the vibrational state is unlikely during a spontaneous emission due to energy conservation [89]. This is essential for efficient sideband cooling (see chapter 7). The Lamb-Dicke criterion is not to be confused with the constraint of a small Lamb-Dicke parameter ( $\eta \ll 1$ ). It is a more severe criterion and allows us to simplify the above equations. In the Lamb-Dicke regime we may expand the exponential function in Eq.(3.9) to lowest order in  $\eta$  obtaining

$$H'_1 = \hbar\Omega\sigma^+ [1 + i\eta(\hat{a}e^{-i\omega_z t} + \hat{a}^\dagger e^{i\omega_z t})] e^{i(\phi - \delta t)} + h.c.. \quad (3.17)$$

### 3.4. Coherent coupling of spin states

Applying radiation at the carrier frequency ( $\delta = \omega_z(n' - n) = 0$ ) we obtain the so-called *carrier transition* which takes the form

$$H_c = \hbar\Omega(\sigma^+ + \sigma^-) \quad (3.18)$$

(for  $\phi = 0$ ). For  $n' = n = 0$  the *Rabi frequency*  $\Omega_{n',n}$  simplifies to  $\Omega_{0,0} = \Omega e^{-\frac{\eta^2}{2}}$  with the Debye-Waller factor  $e^{-\frac{\eta^2}{2}}$  [126, 127]. This transition couples  $|\uparrow\rangle$  and  $|\downarrow\rangle$  without affecting the motional state  $|n\rangle$  of the system.

Tuning the frequency of the light field to the first red sideband ( $\delta = -\omega_z$ ), we obtain the following Hamiltonian

$$H_{\text{rsb}} = \hbar\Omega\eta(\sigma^+\hat{a} + \sigma^-\hat{a}^\dagger), \quad (3.19)$$

which is identical to the ‘‘Jaynes-Cummings’’-Hamiltonian [57] describing the coupling of a two-level system to a single mode of a radiation field. In our context it expresses that upon a transition from state  $|\downarrow\rangle$  to state  $|\uparrow\rangle$ , the corresponding vibrational mode is de-excited by one motional quantum or phonon, a vibrational quasi-particle. The Rabi frequency of this *red sideband transition* is given by

$$\Omega_{n,n-1} = \sqrt{n}\eta\Omega_{0,0}. \quad (3.20)$$

The red sideband transition is the main ingredient for resolved sideband cooling (see chapter 7).

For  $\delta = +\omega_z$  we obtain the *blue sideband transition*

$$H_{\text{bsb}} = \hbar\Omega\eta(\sigma^+\hat{a}^\dagger + \sigma^-\hat{a}) \quad (3.21)$$

(choosing  $\phi = -\pi/2$ ) with Rabi frequency

$$\Omega_{n,n+1} = \sqrt{n+1}\eta\Omega_{0,0}. \quad (3.22)$$

For the blue sideband transition the transition from state  $|\downarrow\rangle$  to state  $|\uparrow\rangle$  is accompanied by the creation of a phonon. This coupling is also called *anti-Jaynes-Cummings* coupling, because it has no counterpart in cavity-QED. Note that for both red and blue sideband transitions one creates entanglement between the internal and motional states for pulse lengths of  $t \neq k\pi/\Omega_{n,n\pm 1}$ , where  $k$  is an integer.

**Two-photon stimulated Raman transitions** The fact, that the dynamics of one system depends on the state of another system, is the basis for quantum logic [127, 86]. In this simplified description, the reason for the coupling between the internal and the motional states lies in the nature of the magnetic field  $\mathbf{B}(z, t)$ . Expanding  $\mathbf{B}(z, t)$  in Eq.(3.6) in a Taylor series,

$$\mathbf{B}(z, t) = \mathbf{B}(0, t) + \frac{\partial}{\partial z}\mathbf{B}(z, t)\Big|_{z=0}z + \frac{1}{2}\frac{\partial^2}{\partial z^2}\mathbf{B}(z, t)\Big|_{z=0}z^2 + \dots, \quad (3.23)$$

### 3. $^{25}\text{Mg}^+$ : Level structure and transitions

we focus our attention on the gradient term of the expansion  $\frac{\partial}{\partial z}\mathbf{B}(z, t)$ . The oscillatory motion of the ion at frequency  $\omega_z$  can be seen as a modulation of the magnetic field in the rest frame of the ion. And this modulation gives rise to spin-flip transitions.

Now we can take a closer look at the wavevector  $\mathbf{k}$  in Eq.(3.6): The ground state splitting of  $^{25}\text{Mg}^+$  accounts to  $\omega_0 = 2\pi \times 1.77$  GHz. This corresponds to a very long wavelength in the order of 170 mm and therefore the wavevector  $\mathbf{k}$  is very small resulting in a negligible coupling between internal and motional states which is proportional to  $\frac{\partial}{\partial z} \cos kz = -k \sin kz$ . However, there is a way to achieve a strong coupling despite using optical transitions: the *two-photon stimulated Raman transition* (TPSR). The idea is to introduce a third *virtual* level which is far detuned from a resonant transition (see Fig. 3.3). The related Hamiltonian is given by

$$H_{\text{int}} = \hbar\Omega(\sigma^+ + \sigma^-) \left( e^{i((k-k')z - (\omega-\omega')t + \phi)} + h.c. \right). \quad (3.24)$$

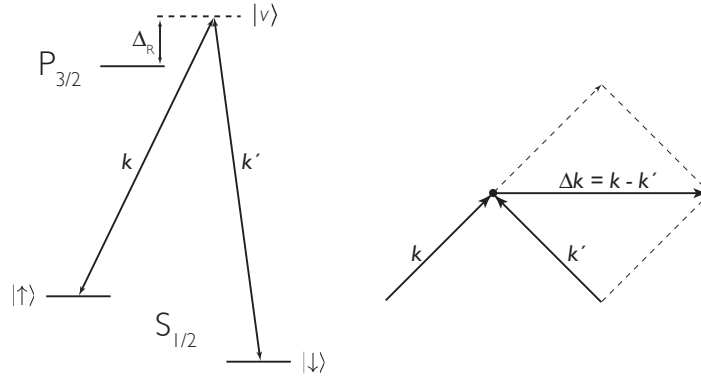


Figure 3.3. – Schematic of the two-photon stimulated Raman process: On the left one can see the two previously defined spin states  $|\uparrow\rangle$  and  $|\downarrow\rangle$ . These two states are coupled to a virtual level  $|v\rangle$  which is blue detuned from the  $^2\text{P}_{3/2}$  by  $\Delta_R = 2\pi \times 80$  GHz by two Raman laser beams of wavevectors  $\mathbf{k}$  and  $\mathbf{k}'$ . Tuning the frequency difference of these two beams to the ground state splitting of  $^{25}\text{Mg}^+$  we can drive *two-photon stimulated Raman carrier transitions* between  $|\uparrow\rangle$  and  $|\downarrow\rangle$ .

On the right hand side the wavevectors  $\mathbf{k}$  and  $\mathbf{k}'$  of the Raman laser beams shining on the ion are illustrated. The ion absorbs a photon out of the left beam and emits a photon into the right beam, therefore experiencing a momentum transfer of  $\Delta\mathbf{p} = \hbar(\mathbf{k} - \mathbf{k}')$ . We can choose the laser beam geometry such that the direction of momentum transfer coincides with the trap axis. For the given beam geometry and under the approximation  $\mathbf{k} = \mathbf{k}'$  the effective wavevector corresponds to  $|\Delta\mathbf{k}| = \sqrt{2}|\mathbf{k}|$ .

We abbreviate the wavevector difference  $\Delta\mathbf{k} = \mathbf{k} - \mathbf{k}'$ . By choosing an appropriate beam geometry, one can vary the wavevector difference  $\Delta\mathbf{k}$ . Choosing collinear beams

### 3.4. Coherent coupling of spin states

( $\Delta \mathbf{k} \approx 0$ ) leads to transitions which are insensitive to motion. In mathematical terms, one does not need to expand the exponential of Eq. 3.9, since the Lamb-Dicke parameter  $\eta$  is so small, that the coupling between internal and motional states is negligible. For this type of transitions, the Rabi frequency  $\Omega$  does not depend on the motional state  $n$ . We will refer to this kind of transitions as **collinear transitions**.

The second possibility is choosing orthogonal beams with the wavevector difference pointing along the trap axis. This situation is depicted in Fig. 3.3. With this setup we are only sensitive to motion in direction of the trap axis  $z$ . The motional sidebands are detuned by the axial trap frequency  $\omega_z$ , respectively. We will refer to this setup as to **orthogonal transitions**. Furthermore one can align the wavevector difference pointing perpendicular to the trap axis. With this setup one addresses the radial motional modes of the ions in the trapping potential. In a linear Paul trap there are two radial directions, thus one has to deal with two motional sideband transitions with detunings with respect to the carrier transition corresponding to the radial trap frequencies  $\omega_x$  and  $\omega_y$ . In this thesis we are only concerned with the axial motional modes and will refer to the axial direction when talking about orthogonal two-photon stimulated Raman transitions.

The detuning  $\Delta_R$  from the resonant transition  ${}^2S_{1/2} \rightarrow {}^2P_{3/2}$  is much larger than the ground state splitting, which allows us to adiabatically eliminate the virtual level  $|v\rangle$ . The whole theoretical derivation is beautifully described in ref. [64]. Following this scheme, we can attain high field gradients utilising different directions for the Raman beams despite the small ground state splitting. We also benefit from the fact, that we solely have to adjust the frequency difference between the two Raman beams and not their absolute frequencies. This frequency difference is precisely controlled via radio-frequency oscillators serving as AOM driver sources (see section 4.5) which are accurate down to the Hz level (see chapter 5.1).

In the above mentioned approximation  $\Delta_R \gg \omega_0$ , the Rabi frequency for a two-photon stimulated Raman transitions can be described by

$$\Omega \propto \frac{g_r g_b}{\Delta_R}, \quad (3.25)$$

where  $g_r$  and  $g_b$  are the resonant single-photon Rabi frequencies of the Raman beams  $b$  and  $r$ , which scale proportionally with the corresponding beam intensity  $I_i$ .  $b$  and  $r$  represent the blue and red Raman beams coupling the states  $|\downarrow\rangle$  and  $|\uparrow\rangle$  to the virtual level  $|v\rangle$ , respectively.  $\Delta_R$  is the detuning of the virtual level  $|v\rangle$ . An exact numerical evaluation of the Raman Rabi rate is carried out in section 8.1.

One severe drawback of TPSR is off-resonant spontaneous emission (SE) which is a source of decoherence. The rate of SE scales as

$$\gamma_{SE} \propto \frac{\Gamma g_r g_b}{\Delta_R^2}, \quad (3.26)$$

where  $\Gamma$  is the natural linewidth of the resonant transition. We want to be able to drive TPSR transitions efficiently, while minimising the rate of spontaneous emission.

### 3. $^{25}\text{Mg}^+$ : Level structure and transitions

Therefore, we evaluate the ratio  $\xi_{\text{SR}}$  between the spontaneous emission rate and the Rabi frequency, the single-photon Rabi frequencies  $g_i$  cancel

$$\xi_{\text{SR}} = \frac{\gamma_{\text{SE}}}{g_b g_t / \Delta_{\text{R}}} = \frac{\Gamma}{\Delta_{\text{R}}} . \quad (3.27)$$

The ratio is linearly decreasing with increasing detuning of the virtual level  $\Delta_{\text{R}}$ . However, we have to correspondingly increase the Raman beam powers (see Eq. 3.25) to maintain a constant Raman Rabi rate. Practically, we are limited by the availability of laser beam intensity for the TPSR transition. A quantitative analysis of SE for different ion species can be found in ref. [128].

**AC-Stark shifts** Off-resonant laser beams interacting with ions cause AC-Stark shifts [61] of electronic levels. The energy shift of an electronic level can be approximated by

$$\Delta E = \hbar \frac{g_i^2}{\Delta_{\text{R}}} . \quad (3.28)$$

If, during a transition, both spin states are shifted by an equal amount, the net shift is zero. But in case of differing shifts, it has to be accounted for. By adjusting relative polarisation and intensities of laser beams, AC-Stark shifts can be compensated (see chapter 7 and section 6.5 for compensation of differential AC-Stark shifts).

On the other hand, AC-Stark shifts can be useful in tailoring interactions: By appropriately adjusting the polarisation of the Raman beams, one can generate spin-dependent forces and simulate an effective spin-spin interaction (see chapter 8).

## 4. Laser apparatus

Our Laser apparatus consists of four laser systems, including seven second harmonic generation (SHG) cavities, generating nine different beams entering the recipient enclosing our trap from five different directions. Fig. 4.1 illustrates our vacuum chamber with all entering laser beams.

We address electronic transitions of  $^{25}\text{Mg}^+$  in the deep ultraviolet (UV) near 280 nm. These transitions with respective wavelengths are illustrated in Fig. 4.2. Except for the Raman laser, all transitions are addressed close-to-resonance. Thus, we only need beam intensities of the order of the saturation intensity<sup>1</sup>. But except for the photoionisation laser, all laser systems generate several laser beams of different frequencies. We accomplish these frequency shifts using acousto-optical modulators (AOMs). Although these AOMs are highly efficient (see section 4.5), the losses introduced by each diffraction sum up and thus it is desirable to have UV beam powers of at least 10 mW for each laser at our disposal. The situation for the Raman laser is different, this laser system drives coherent transitions between our spin states  $|\downarrow\rangle$  and  $|\uparrow\rangle$  via a far detuned virtual level  $|\nu\rangle$ . The required beam power for constant Raman transition rates (see chapter 8.1) scales linearly with the detuning of the virtual level  $|\nu\rangle$ . For the adiabatic simulation experiments which for two ions already take of the order of 100  $\mu\text{s}$  we have to minimise decoherence effects due to spontaneous emission (see section 3.4). This can be achieved by increasing the detuning  $\Delta_R$  which reduces the probability for off-resonant excitation of the  $^2\text{P}_{3/2}$  levels. Yet we have to achieve a strong coupling between motional and internal states by inducing high field gradients acting on the ions which is essential for the simulations of interactions. During this chapter we will in detail consider our four laser systems, frequency stabilisation, frequency shifting and switching of beams.

### 4.1. Fibre lasers

The BD, RD and Raman laser beams are provided by three frequency-quadrupled Ytterbium fibre lasers in the wavelength range between 1118 nm and 1121 nm with output powers ranging between 1 W and 2 W. To achieve narrow linewidths, these systems are set up as master oscillator fibre amplifier (MOFA) systems. They were manufactured

---

<sup>1</sup>The saturation intensity for  $^{25}\text{Mg}^+$  amounts to  $I_{\text{sat}} \approx 255 \text{ mW/cm}^2$ . With beam waists of the order of 30  $\mu\text{m}$  the saturation intensity roughly corresponds to 3  $\mu\text{W}$ .

#### 4. Laser apparatus

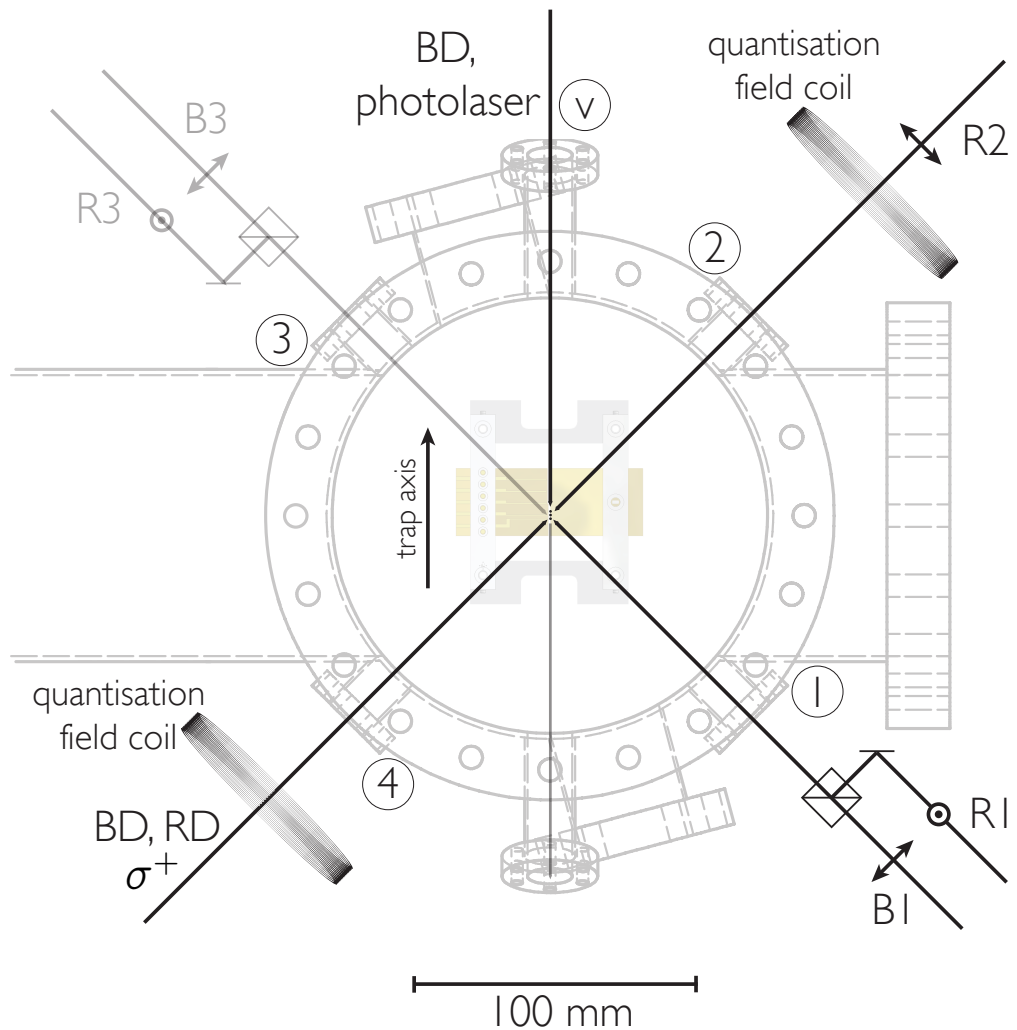


Figure 4.1. – Vacuum chamber and laser beam geometry: The vacuum chamber is outlined with its four main laser ports labelled with arabic numbers. Two magnetic quantisation field coils are located next to laser ports 2 and 4. Collinear to this quantisation field axis, the Blue Doppler and Red Doppler beams enter the chamber via laser port 4. Raman beams R1 & B1 enter the chamber through laser port 1. They are orthogonal in polarisation with respect to each other. The “orthogonal” Raman beam R2 enters the recipient via port 2 and encloses a right angle with both B1 and R1 and is polarised orthogonal with respect to beam R1. Loading ions into the trap is carried out using laser beams BD and photolaser entering the chamber via port v, which encloses an angle of  $22^\circ$  with respect to the optical table (descending).

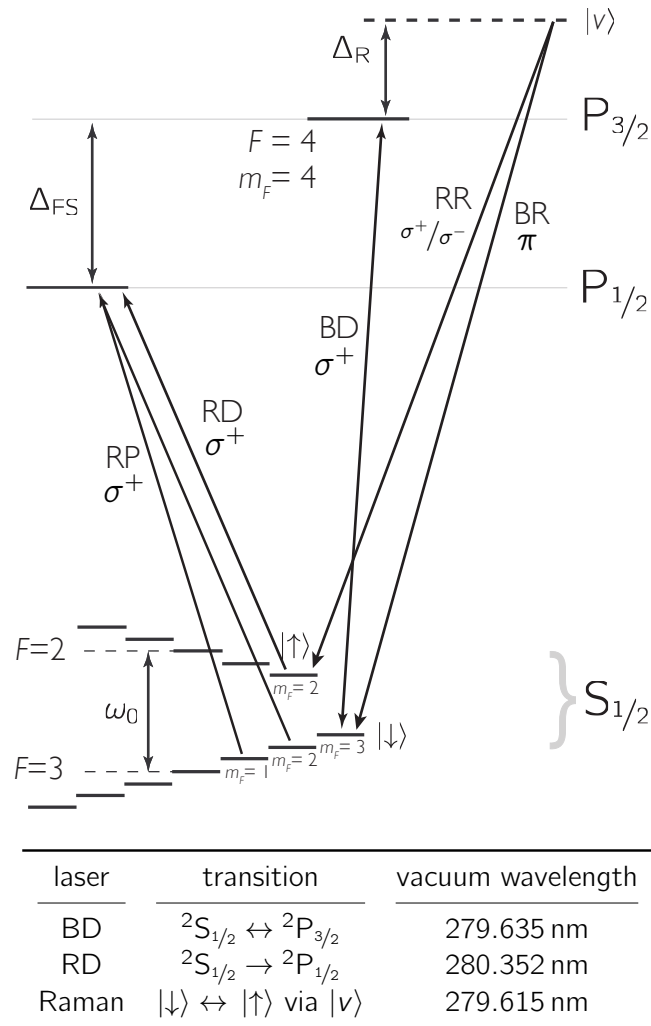


Figure 4.2. – In the above table and figure the main laser-induced transitions of  $^{25}\text{Mg}^+$  are summarised including the polarisation of respective laser beams. The schematic is not to scale and we omitted higher excited states and excited state hyperfine splittings. The S and P-levels are separated by an optical frequency corresponding to a wavelength of the order of 280 nm, the fine structure splitting of the P levels amounts to  $\Delta_{FS} = 2\pi \times 2.74$  THz, and the hyperfine structure splitting of the ground state amounts to  $\omega_0 = 2\pi \times 1.77$  GHz. The Blue Doppler (BD) acts as Doppler-cooling and detection laser. The BD beams are circular polarised and couple levels of extremal  $m_F$  numbers of  $F = 3$  and  $F = 4$  manifolds. The Red Doppler laser system provides two beams (RD&RP) and serves as a repumping laser for  $F = 2$ , and  $F = 3$  manifolds, respectively. The Raman laser system used for two-photon stimulated Raman transition via the virtual level  $|\nu\rangle$  is blue detuned from the  $^2P_{3/2}$  level by  $\Delta_R \approx 80$  GHz, and generates two sets of beams, the red Raman (RR) and the blue Raman (BR) beams.

#### 4. Laser apparatus

by *Koheras* and feature spectral linewidths of below 100 kHz. The fibres constituting the master oscillator are mounted on ceramic/aluminium substrates which are actively temperature controlled to adjust the emission wavelengths (slow tuning). In addition the output wavelength is tunable by a piezo of 20 kHz bandwidth and a tuning range of several GHz. Specifications of distinct lasers are summarised in Table 4.1.

laser	output power	ASE	$\lambda_{\text{central}}$	$\delta\nu(T)$	$\Delta\nu(U)$	$T_{\text{op}}$
BD	1.44 W	660 mW	1118.52 nm	80 GHz	9 GHz	36.6 °C
RD	1.27 W	820 mW	1121.44 nm	85 GHz	9 GHz	32.3 °C
Raman	1.9 W	900 mW	1118.43 nm	73 GHz	60 GHz	39.4 °C
Raman II	900 mW	600 mW	1118.536 nm	163 GHz	9 GHz	35.2 °C

Table 4.1. – Overview of fibre laser specifications: The columns denote name/function of the respective laser, output power in the signal excluding amplified spontaneous emission (ASE), ASE power, emission wavelength at a fibre laser temperature of 35 °C, temperature tuning range  $\delta\nu(T)$ , the piezo tuning range  $\Delta\nu(U)$  (both frequencies in the IR), usual set temperatures for addressing the respective transition. Raman II laser is equipped with an aluminium substrate (wider tuning range) on which the master oscillator fibre is mounted compared to the others with ceramic substrates. The Raman laser contains a monopolar piezo which allows for a larger tuning range.

The fibre lasers belong to two generations. All of our fibre lasers feature three amplifier sections: two preamplifier sections and a power amplifier. Since there is no preferred direction of amplification in the power amplifier and light passing through in opposite direction is also amplified and can destroy the master oscillator or the preamplifier, the power amplifier contains an emergency shut-down circuit which switches off the power amplifier, if back-reflected light exceeds a certain threshold. A schematic of a fibre amplifier is depicted in Fig. 4.3. The fibre lasers of the first generation had a fragile preamplifier section built in a core-pumped single-clad fibre configuration. The therein used wavelength division multiplexers (WDM) were operated near their maximum power rating which lead to a few failures of the preamplifier. In addition, we had failures of optical isolators, and oscillator pump diodes. We had to ship the lasers back to the manufacturer 9 times altogether.

The youngest laser (Raman II) features a completely new designed preamplifier section employing a double-clad fibre configuration (core-doped, cladding-pumped ytterbium fibre). When we received the laser initially, it was built in a co-propagating signal-pump configuration which was supposed to have the advantage of reduced amplified spontaneous emission (ASE). In this configuration, the ASE generated at the beginning of the fibre is reabsorbed within the amplifier. The laser emitted 1.80 W of total output power out of which only 50 mW amounted to ASE (1.75 W of useful output power at 1118 nm). Unfortunately, this configuration lead to a photo-darkening of the fibre

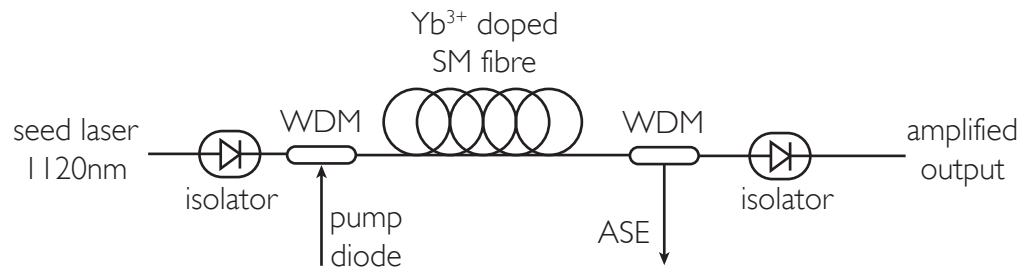


Figure 4.3. – The schematic shows a fibre amplifier in co-propagating signal-pump configuration: The seed laser signal passes an optical isolator to avoid optical feedback to the preceding section of the laser. Subsequently it is superimposed with the pump laser light via a wavelength division multiplexer (WDM). The pump light excites the  $\text{Yb}^{3+}$  ions in the doped gain fibre which amplify the seed laser signal by stimulated emission. The following WDM filters out (amplified) spontaneously emitted photons at the gain maximum of Yb, which is near 1060 nm (see Fig. 4.4, suppression of amplified spontaneous emission, ASE). The optical isolator at the end also prevents optical feedback and the onset of stimulated Brillouin scattering.

[81, 82]. We had to return the laser to *Koheras* after only three weeks of operation. They changed the layout of the amplifier section to a counter-propagating signal-pump configuration. With this configuration the laser currently runs stable, yet with a larger fraction of ASE. The total output power of the system now amounts to 1.7 W with slightly less than 1 W in the signal.

The fibre lasers are designed to be mounted in a 19" rack, but since these lasers are based on non-polarisation maintaining fibres, we have to ensure that the single-mode fibre pigtailed to the laser is neither bent nor stressed. Our optical tables feature active suspension damping, thus, we have to keep the lasers fixed with respect to the optical tables. We mount the lasers beneath the optical tables and fix the fibre waveguides to its sides and protect them with a half cylinder of acrylic glass on their way to the first frequency doubler stage.

**Collimation and isolation of fibre laser output** We use collimators by *Schäfter und Kirchhoff* to couple the infrared light out of the single-mode fibres. These allow to adjust the distance between the tilted<sup>2</sup> end facet of the fibre and the collimating lens. As delivered from the company, these collimators are equipped with an eccentric mechanism to shift the lens. This mechanism turned out to be not reproducible. A

<sup>2</sup>All fibres used throughout this thesis are FC/APC-type fibres, that is, their end facets are polished at an angle of  $8^\circ$  with respect to the normal to minimise back reflections.

#### 4. Laser apparatus

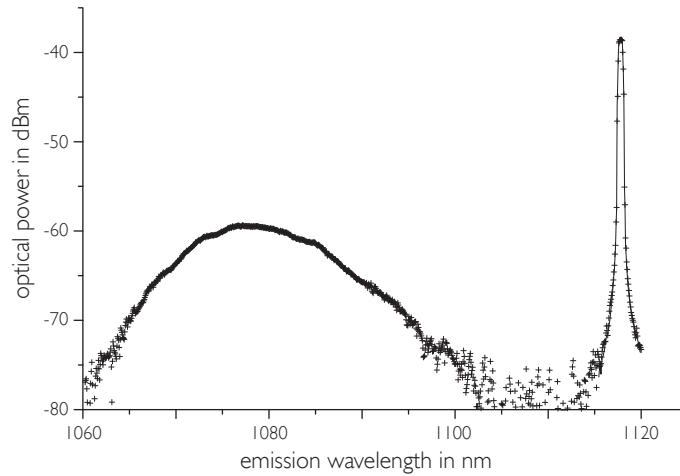


Figure 4.4. – Frequency spectrum of fibre laser output: The spectral power level (logarithmically in dBm, arbitrary values) is plotted versus the emission wavelength. The wide peak is due to amplified spontaneous emission (ASE) near the gain maximum of Yb. The ASE spectrum depicted here differs from the actual gain spectrum of ytterbium which has a maximum near 1064 nm due to various spectral filters (WDMs) within the amplifier. The sharp peak at 1118 nm ( $< 100$  kHz linewidth) is broadened due to the limited resolution ( $> 0.06$  nm) of the optical spectrum analyser and contains 85.5% of the total output power. This spectrum has been recorded with the Raman laser cooled to  $18^{\circ}\text{C}$ . The total output power amounts to 2.35 W of which 2.01 W are in the signal. The ratio between the power in the signal and ASE given here differs from the values in table 4.1, which were recorded without cooling, as further cooling reduces the amount of ASE.

technician from the MPQ has improved this shifting mechanism allowing for a precise collimation of the laser beam. We use collimators of focal lengths  $f = 4.5$  mm. With the numerical aperture  $\text{NA} = 0.13$  of our single mode fibres (*Nufern 460-HP*), the resulting collimated beam has a Gaussian beam waist of  $w \approx 480$   $\mu\text{m}$ . We glue<sup>3</sup> the collimator into an adapter ring to be able to mount it using stable mirror mounts. For all important beam lines and coupling into resonators we use *Maier S3* mirror mounts.

The laser beam leaving the fibre is arbitrarily polarised. We adjust the output polarisation to match the input polarisation of a polarisation dependent optical isolator using a quarter- and a half-waveplate. We use optical isolators by *OFR* designed for a wavelength of  $\lambda = 1064$  nm. We optimise the performance of the isolators at a wavelength of 1120 nm by adjusting of the output polariser of the isolator. We have to trade off

<sup>3</sup>We prefer gluing over screwing in order to avoid stress inducing birefringence of the lens.

attenuation against isolation. At a level of isolation of about 32 dB the laser operates stably and we achieve a corresponding transmission of 90% at 1120 nm.

**Adjustment of the optical isolator** To adjust the level of isolation, we send the laser beam through the optical isolator in reverse direction. The power amplifier of the laser should be switched off<sup>4</sup>. Reverting the isolator one has to make sure, that the beam passes undisturbed through the isolator which has a small aperture (diameter of the input aperture of 2.5 mm). One rotates the output polariser of the reverted device (now input polariser) to achieve optimum transmission (>92%). Then one adjusts for the desired level of isolation by rotating the output polariser.

We have also tried to use polarisation independent optical isolators by *OFR, IO-3-1064-HP* (specified isolation >38 dB and transmission >93% at 1064 nm), but these isolators only provided an isolation of 28 dB at 1120 nm, which resulted in repeated emergency shutdowns of the power amplifier at full power.

**Compensation of polarisation drifts** We manually adjust the output polarisation after the fibre laser to match the input polariser of the polarisation dependent optical isolator using a quarter- and a half wave plate. However, varying ambient temperature leads to a change of the state of polarisation of the beam emitted by the fibre laser which deteriorates the transmission through the optical isolator. In the beginning, we had an insufficient air-conditioning systems allowing for oscillations of the temperature of the air in the laboratory of 2 K amplitude within a period of 20 minutes. This resulted in fluctuations of laser output power after frequency-quadrupling to the ultraviolet of about 10%. We circumvented this by actively stabilising the temperature of the heat sink of the fibre laser. The large heat capacity of the heat sink lead to an inert feedback control loop (time constant of the servo loop of the order of 30 min) and it took about 90 minutes to reach a steady state. We even gained more output power out of the laser by cooling it down to lower temperatures. By stabilising the heat sink temperature to  $T \approx 15^\circ\text{C}$ , we achieved a spectral output power of 2.18 W compared to 1.90 W without cooling. However, the increased output power was accompanied by square-shaped modulations of the output power of the laser with an amplitude of 4% and a frequency of several kHz. So we increased the temperature to 20°C to abandon this modulation and obtained a stable spectral output power of 2.01 W. We cooled the laser using a direct-to-liquid cooler (*Telemeter, DL-120-24-00*, cooling power 120 W) and a

---

<sup>4</sup>The un-amplified output power of the master oscillator amounts to roughly 1 mW and is free of ASE, which is unpolarised and has a broad frequency spectrum. The spectrum of the laser may be analysed with an optical spectrum analyser, but one should be careful not to use the monitor output of the laser, since this spectrum differs from the spectrum of the actual output (see Fig. 4.4). Without exactly knowing the output spectrum of the laser and the (wavelength-)characteristics of the faraday rotator used in the optical isolator, one cannot reliably predict its isolation and transmission.

#### 4. Laser apparatus

temperature stabilised water chiller. The signal of a *AD590* temperature sensor was fed to a proportional-integral servo which controlled the current of the Peltier element of the direct-to-liquid cooler.

After upgrading our air-conditioning system, which allows for a regulated cooling power instead of the on-off mechanism of the former model, the laboratory temperature is kept within  $\pm 0.5K$  and the temperature stabilisation of the lasers became superfluous.

### 4.2. First frequency doubling stage (1120 nm $\rightarrow$ 560 nm)

For wavelengths close to 1120 nm there exist various schemes for efficient cavity enhanced second harmonic generation (SHG) employing type II phase-matched sodium titanyl phosphate (KTP) crystals achieving efficiencies of 85% at 1080 nm [95] or resonators featuring magnesium doped lithium niobate ( $MgO:LiNbO_3$ ) crystals achieving 82% doubling efficiency at 1060 nm [97]. Though our wavelength of 1120 nm is close, we cannot adopt those schemes. Either the crystal does not allow for phase-matching at our required wavelength (KTP) or non-critical phase-matching temperatures are above  $300^\circ C$  ( $MgO:LiNbO_3$ ). Although the effective non-linear coefficient  $d_{eff} = 0.82 \text{ pm/V}$  of lithium triborate (LBO) [93] crystals can by far not compete with the specifications of the above mentioned crystals, we are able to build very efficient SHG cavities. We report doubling efficiencies of up to 79% [37] for this first SHG stage. LBO crystals are of superb optical quality and therefore have an extremely low linear absorption ( $\alpha = 3.5 \times 10^{-4} \text{ 1/cm}$  measured at 1064 nm [93], we deduce  $\alpha = (2.0 \pm 0.5) \times 10^{-4} \text{ 1/cm}$  at 1120 nm) which contributes to a low passive loss of the cavity. As additional benefit we are not affected by problems as grey-tracking [13], green-induced infrared absorption (GRIIRA) [39] or low damage thresholds (LBO has the largest damage threshold of all known nonlinear optical crystals, threshold intensity  $> 6 \times 10^9 \text{ W/m}^2$  [129]) which is a major concern with crystals of high non-linear coefficients (especially niobate crystals).

We embed the type I non-critically phase-matched LBO crystal within an external bow-tie cavity for frequency doubling the output of the fibre laser at 1118 nm to 559 nm. For non-critical phase-matching, the conversion efficiency  $\kappa = \frac{P_{\text{harmonic}}}{P_{\text{fundamental}}^2}$  of the doubling cavity does not critically depend on the length of the crystal. However, it is advantageous to choose a long crystal, because of the increased ratio between active loss and passive losses in the resonator. The related lower Finesse and larger beam waists inside the cavity decrease the sensitivity to dust particles on the optics. We chose a crystal size of  $3 \times 3 \times 18 \text{ mm}^3$ . We purchase these from *Castech, China*. Previously, we tried crystals manufactured by *Crystals of Siberia, Russia* since they were cheaper than the *Castech* crystals. Switching to *Castech* LBO crystals, we gained an increase of harmonic beam power at 560 nm of about 20% using *Castech* crystals which is mainly due to better AR-coatings and a lower linear absorption coefficient.

The crystal is placed inside a home-built oven (depicted in Fig. 4.5) made of copper

#### 4.2. First frequency doubling stage (1120 nm → 560 nm)

to ensure the optimum phase matching temperature without Pointing vector walkoff of 89°C. The 90°-cut LBO crystal is antireflective (AR) coated for both fundamental and harmonic wave using ion beam sputtering (IBS) coating technique. The cavity consists of two concavely curved mirrors ( $f = -25$  mm) and two plane mirrors whose specifications are summarised in the table below Fig. 4.6. The high reflectivity mirrors inside the cavity are coated using the ion beam sputtering (IBS) technique by *Layertec* (specified reflectivity above 99.98% at 1120 nm). The output coupler of the cavity, which has to be dichroic (highly reflective at 1120 nm and highly transmissive for 560 nm), is coated via standard electron beam coating technique, which is preferential for this mirror. We have to impedance match the cavity losses including the conversion loss via the the plane incoupling mirror. For the Raman laser (2 W at 1120 nm) we use an incoupling mirror of  $R = 97.5\%$  reflectivity, whereas for the other fibre lasers (1 W at 1120 nm) we use incoupling mirrors of  $R = 98.4\%$ , since for lower fundamental input power the conversion is not as efficient and therefore the active cavity loss is smaller. The other plane mirror, which is glued onto a piezo (*Thorlabs AE0203D04*,  $\nu_{\text{res}} > 18$  kHz with mirror attached to it), we diminished in size by the help of a diamond saw ( $3 \times 3 \times 2$  mm<sup>3</sup>) to ensure a large servo bandwidth. All the mirrors are mounted on replicas of *Lees* mounts manufactured by *Radiant Dyes* equipped with high precision fine thread screws (pitch 0.15 mm).

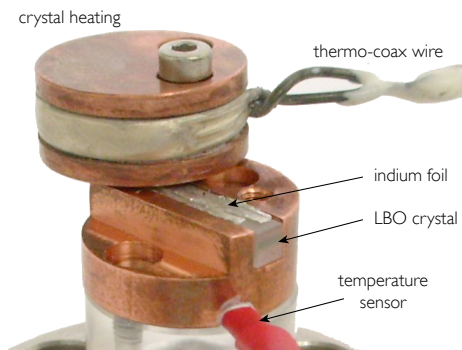


Figure 4.5. – Opened home-built crystal oven with LBO crystal inside wrapped in a 100 μm thick indium foil. The heating consisting of a copper cylinder with hard-soldered thermo-coax wire is partially removed. For temperature stabilisation to an accuracy of 10 mK a thermal sensor *AD 590* is placed within the oven beneath the crystal.

Since it is not possible to build a ring cavity without tilted incidence angles on curved mirrors, we have to minimise astigmatism within this cavity. We accomplish this by choosing a bow-tie resonator design which allows for small cavity folding angles. We choose an angle of incidence of 6° on the curved mirrors. The related astigmatism is negligible, yet the small angle of incidence poses restrictions on the dimensions of the crystal oven which has to be narrow on one side, so the laser beams can pass undisturbed, and yet avoid thermal gradients within the crystal. Astigmatism could also be compensated via using a Brewster-cut crystal and choosing the cavity folding angle such that the astigmatism caused by the crystal is compensated by the tilted incidence on the mirrors. However, one loses roughly 20% of harmonic power due to Fresnel

#### 4. Laser apparatus

losses at the end facet of the crystal, since the harmonic beam (extraordinary beam) is orthogonal in polarisation with respect to the fundamental beam (ordinary beam). Since AR coatings of LBO crystals in this spectral region do not show degradation at high power levels (different for BBO see section 4.3), we discard this possibility and use an AR-coated crystal.

Optimising the output power of this cavity while preventing pointing vector walkoff is done by ensuring collinearity between the designated optical axis<sup>5</sup> and the fundamental beam. This can be achieved by overlapping the incoming beam with the backreflection of the crystal surface, given that the cutting angles of the crystal are correct ( $\theta = 90^\circ$ ,  $\phi = 0^\circ$ ). However, the backreflected beam is quite divergent due to tight focussing into the crystal. This alignment procedure can be simplified by using a glass substrate instead of the incoupling mirror to increase the intensity of the fundamental beam<sup>6</sup>. We find a phase-matching temperatures of  $94.5^\circ\text{C}$  measured with a *AD590* sensor (see Fig. 4.5). The possible calibration error of the used temperature sensor is up to 10 K, so the difference between the calculated phase-matching temperature ( $89^\circ\text{C}$ ) and the measured value lies within the calibration uncertainty. The accuracy of the temperature control loop is better than 10 mK. We optimise the heat contact between the oven and the crystal by wrapping the crystal in a  $100\ \mu\text{m}$  thick indium foil. The aforementioned aligning method minimises pointing vector walk-off resulting in a non-astigmatic beam after the cavity and eases the crystal phase-matching. After having optimised the phase-matching of the crystal, one completes the cavity round trip solely using mirrors M4 and M1. We apply a triangular voltage ramp to the cavity piezo scanning the cavity length. We observe harmonic transmissions fringes of the cavity at the resonance condition via a photodiode (length of the cavity equals an integer multiple of the wavelength). We maximise the harmonic output of the cavity using all cavity mirrors. Finally, we end up with a cavity solely resonant for the Gaussian  $\text{TEM}_{00}$  mode. For modematching of the fundamental input beam to the cavity mode please refer to Fig. 4.10 and the next section.

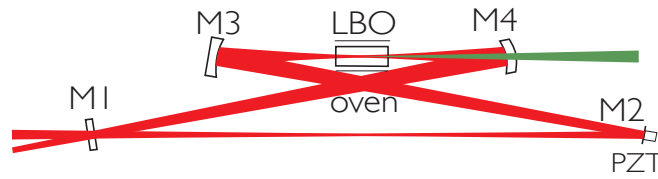
**Stabilisation of the cavity length** To achieve constructive interference between the light which has undergone one or more cavity roundtrips and the incoupling beam, we have to make sure that the length of the cavity equals an integer of the fundamental wavelength. The length of the cavity is adjusted by a mirror (M2) mounted on a piezoelectric element. The error signal which determines the necessary displacement to fulfil this condition is generated using the scheme of Hänsch Couillaud [52]. A small fraction of the incoupling beam which is reflected at the incoupling mirror (M1, see

---

<sup>5</sup>For non-critical type I phase matching in the negative bi-axial LBO crystal the pointing direction of the fundamental beam must be collinear with the crystallographic  $x$ -axis.

<sup>6</sup>By removing the input coupler the beam is displaced. The glass substrate comes up for this displacement

#### 4.2. First frequency doubling stage (1120 nm → 560 nm)



mirror #	substrate	coating
M1	plane	$R = 97.5\%$ and AR@1120 nm outside
M2	plane	$HR \geq 99.98\%$ @1120 nm
M3	$f = -25$ mm	$HR \geq 99.98\%$ @1120 nm
M4	$f = \mp 25$ mm	$HR \geq 99.8\%$ @1120 nm $\wedge$ $HT \geq 94\%$ @560 nm and AR@560 nm outside

Figure 4.6. – Mirrors of the LBO frequency doubling cavity: M1 is the incoupling mirror which features a rather low reflectivity for impedance matching and an AR-coating on its outside for the fundamental beam. Its transmission corresponds to the active (conversion) and passive (absorption, imperfections of mirrors) losses inside the cavity. M2, which is mounted onto a piezo, and M3 and the LBO crystal are coated using the ion beam sputtering (IBS) technique. M4 is a zero-lens with the concave side facing the crystal. Its backside is AR coated for the harmonic wavelength. All the mirror substrates are made of fused silica and have diameters of 12.5 mm and are 6.25 mm thick, except for the piezo mirror which we cut down to  $3 \times 3 \times 2$  mm<sup>3</sup> using a diamond saw.

Fig. 4.6 and Fig. 4.10) is superimposed and interferes with the light which has undergone a cavity roundtrip and leaves the cavity through the same mirror having passed the crystal which serves as a polariser<sup>7</sup>. If the cavity fulfils the resonance condition, destructive interference takes place and attenuates the reflected beam, which is linearly polarised. If the length of the cavity changes, the light which has undergone a cavity roundtrip gets shifted in phase with respect to the directly reflected light, resulting in elliptically polarised light. The handedness of the ellipse encodes the direction of the phase shift and by analysing this handedness, we gain an error signal which we feed back to the cavity piezo to adjust the cavity length. In practise, a quarter wave plate and a polarising beam cube decompose the beam of elliptical polarisation into two beams of orthogonal linear polarisation which are detected by a home-built difference photo diode amplifier (see Fig. 4.10).

For the LBO crystal, we non-critically phase-match the fundamental beam with the

<sup>7</sup>The reflected beam has experienced a phase shift of  $\pi$ , whereas the beam having undergone a cavity round trip has experienced a shift of  $3\pi$ . Thus, they have the same phases.

#### 4. Laser apparatus

harmonic beam, this implies that the fundamental beam propagates along one optical axis of the crystal. The two polarisation directions therefore experience no walk-off and propagate through the crystal on the identical path but with different phase velocities. Hence both polarisation directions can be resonant in the enhancement cavity. Taking a closer look at the error signal one observes two phase-shifted dispersive resonances within one free spectral range of the cavity. An oscilloscope trace of the error signal of the LBO SHG cavity is depicted in Fig. 4.7. The resonance corresponding to the extraordinary beam (no harmonic transmission fringes) has inverted phase compared to the one originating from the ordinary beam.

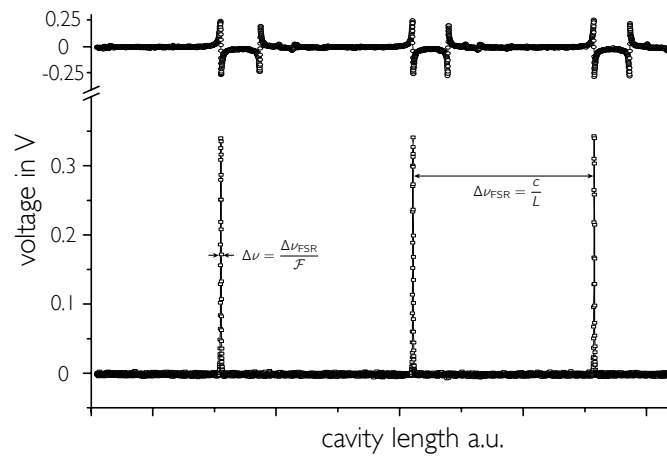


Figure 4.7. – Harmonic transmission spectrum of LBO SHG cavity (lower trace) and corresponding error signal (upper trace): The transmission fringes are separated by the free spectral range  $\Delta\nu_{\text{FSR}} = c/l_{\text{cav}}$ , where  $l_{\text{cav}}$  is the length of the cavity (here  $\Delta\nu_{\text{FSR}} \approx 2\pi \times 650$  MHz). The acceptance bandwidth  $\Delta\nu$  of the cavity, which determines how narrow the linewidth of a laser has to be for being coupled into the cavity efficiently, is given by the free spectral range divided by the cavity Finesse  $\mathcal{F}$ . The Finesse  $\mathcal{F}$  is mainly determined by the conversion efficiency of the crystal. We have a cavity Finesse of about  $\mathcal{F} \approx 150$ , leading to an acceptance bandwidth of about  $\Delta = \Delta\nu_{\text{FSR}}/\mathcal{F} \approx 2\pi \times 4.3$  MHz. The linewidth of less than  $2\pi \times 100$  kHz for our fibre lasers is well within the acceptance bandwidth of the cavities. The upper trace shows the corresponding Hänsch-Couillaud error signal with the additional resonance of opposite polarisation (see text for details).

**Technical details of the cavity length stabilisation** We have two generations of photo diode difference amplifiers in use, the older one employs two *Hamamatsu S1336-18BK* silicon photodiodes, two *OPA847* operational amplifiers as trans-impedance amplifiers and an instrumentation amplifier *INA111* subtracting the two generated voltages from each other. We etch and solder circuit boards in surface mount design (SMD).

#### 4.2. First frequency doubling stage (1120 nm → 560 nm)

Since the high-speed OPA847 requires  $\pm 6\text{ V}$  for operation whereas the photodiodes can maximally be biased with  $5\text{ V}$ , there are 3 voltage regulators on the board, which is circumstantial. The redesigned amplifier employs two silicon PIN photo diodes *Hama-matsu S5821-01* which feature focussing lenses in front of the active area and allow bias voltages of up to  $20\text{ V}$ . In addition, we simplified the circuit design. The two biased photo diodes act as a voltage divider and the signal tapped in between is amplified using a single *AD829* chip. This chip requires operating voltages of  $\pm 15\text{ V}$ , the voltage regulators are abandoned, and the lenses mounted to the photodiodes ease aligning.

The typical photodiode signal, which has an amplitude of the order of  $50\text{ mV}$  peak-to-peak, is fed to a proportional-integral-differential (PID) controller designed by Helmut Brückner, a local electronic technician. At the monitor output of this so-called *lockbox* we measure signal amplitudes of about  $1\text{ V}$  peak-to-peak for optimised gain adjustment. We can toggle between a *dither*-mode which scans the cavity and a *lock*-mode where the cavity length is stabilised. The signal is passed on to a high-voltage (HV) amplifier employing *PA85* operational amplifiers. We use two different kinds of HV amplifiers, one we purchased from NIST, Boulder, the other type from Helmut Brückner. The NIST amplifier generates symmetric ( $\pm 200\text{ V}$ ) output voltages, whereas the Brückner amplifier is monopolar, so we have to make sure the piezos do not receive negative voltages which would depolarise them. The output voltage between ( $0\text{--}170\text{ V}$ ) is fed to the piezo and a resistor ( $10\text{ k}\Omega$ ) in series as a low-pass filter.

**Challenges with LBO crystals** We found two wavelength regions in which the LBO crystals show anomalous behaviour.

The first anomaly appears between  $\lambda = 1121.430\text{ nm}$  and  $\lambda = 1121.306\text{ nm}$  and affects the wavelength of the RD laser ( $\lambda_{\text{RD}} = 1121.408\text{ nm}$ ). Tuning the emission wavelength of the laser to values outside of this range and aligning the SHG cavity, we measure harmonic output powers of the cavity of  $520\text{ mW}$  (measured with *Coherent Fieldmaster* with an InGaAs detector and a 1000:1 attenuator), when stabilising the cavity length to an integer multiple of the wavelength. Now changing the output wavelength of the fibre laser by either temperature or piezo tuning into the  $28\text{ GHz}$  (IR) wide range given above, provides the identical peak power (detected with a photodiode), when scanning the cavity length with the piezo. However, when stabilising the cavity length, the output power only reaches a fraction of the peak power depending on the frequency. The efficiency reaches its minimum at  $\lambda = 1121.369\text{ nm}$  where the harmonic output power amounts to  $24\text{ mW}$ . At the wavelength of the RD transition we obtain 45% of the maximal output power. Further analysing this behaviour shows that we can reduce the IR pump power to the value at which the peak power of the cavity corresponds to the output power of the stabilised cavity without reducing the amount of harmonic power. The crystal does not emit higher power levels in this spectral region. Thermal lensing effects are not known for LBO crystals and it is unlikely that they occur

#### 4. Laser apparatus

only within narrow frequency ranges. The effect appeared with several crystals from different manufacturers. The RD transition lies 3 GHz (IR) from the red border inside this range. Detuning the laser to a wavelength outside this region and shifting the harmonic output, we would have to shift the visible light by 6 GHz. This could be done using an electro-optic modulator, which would also reduce the available power by roughly the same amount. The achieved output power of 235 mW suffices for us to work successfully, so we did not further investigate this phenomenon.

The second feature appears in a 14 GHz (IR) wide spectral region of the Raman laser between  $\lambda = 1118.339$  nm and  $\lambda = 1118.409$  nm. Within this range the cavity scan peaks are broadened or narrowed when scanning the length of the cavity in one or the other direction. Oscilloscope traces of this phenomenon are depicted in Fig. 4.8. We deduce an intensity dependent change of the refractive index of the crystal. As the

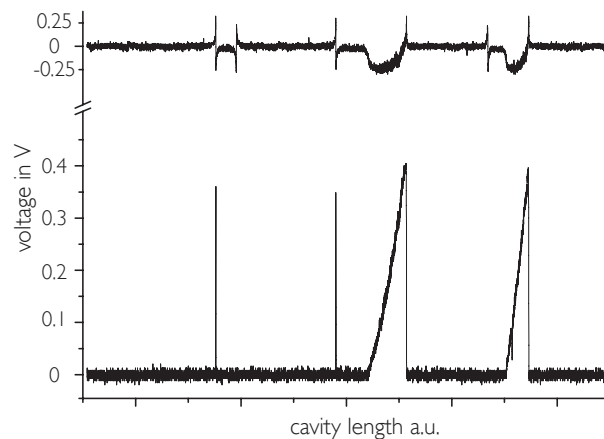


Figure 4.8. – This plot, similarly to Fig. 4.7, shows the harmonic transmission spectrum of an LBO SHG cavity monitored with a photodiode. We tuned the laser into the critical wavelength region given in the text, where the refractive index of the crystal changes dependent on the laser beam intensity. One can see the broadened, or narrowed harmonic cavity fringes, respectively, which depend on the direction of the cavity length variation. The upper trace shows the corresponding Hänsch-Couillaud error signal (see text for details).

cavity length approaches a resonance, scanning the cavity piezo in direction of a shorter cavity length, the intensity inside the crystal rises. The refractive index of the crystal and, therefore, the optical path length of the crystal becomes larger. The cavity length compensates for the displacement of the piezo until the intensity in the crystal reaches a maximum and the refractive index cannot change further. Shortening the cavity length,

### 4.3. Second frequency doubling stage (560 nm → 280 nm)

the harmonic transmission fringes are broadened, whereas when increasing the length of the cavity the phenomenon is reversed and the change of the refractive index narrows the transmission fringes. This effect might be due to resonances of OH<sup>-</sup> impurity complexes found in niobate and borate crystals [66]. Resonances of similar width but located at different wavelengths have previously been observed in LBO crystals [67].

Since we use the Raman laser for two-photon stimulated Raman transitions via a virtual level far detuned to the higher frequency side of the  ${}^2S_{1/2} \leftrightarrow {}^2P_{3/2}$  transition, this imposes restrictions on the detuning. Thus, we cannot work with detunings of the virtual level between  $2\pi \times 124$  GHz and  $2\pi \times 180$  GHz with respect to the resonant transition in the ultraviolet.

### 4.3. Second frequency doubling stage (560 nm → 280 nm)

To achieve the required wavelengths near 280 nm, we further double the light at 560 nm from the LBO cavity or the output of a dye laser, respectively, to the ultraviolet spectral region using a(nother) SHG cavity. In this spectral region Beta Barium Borate (BBO) [92] surpasses all other nonlinear crystals with its effective nonlinearity  $d_{\text{eff}} = 1.62$  pm/V. We critically phase match the negative uni-axial crystal (cutting angles  $\theta = 44.4^\circ$ ,  $\phi = 0$ ). The angular acceptance bandwidth of BBO is extremely small ( $\Delta\theta = 0.8$  mrad cm) and its walk-off angle [69] large ( $\rho = 84.5$  mrad). These two properties limit the effective interaction length and force us to use a short crystal length.

We will first focus on the single pass conversion efficiency of a crystal with given length  $l$ , which can be determined using the Boyd-Kleinman phase matching integral for circular Gaussian beams [14]

$$\kappa_0 = \frac{2\omega^2 d_{\text{eff}}^2}{\epsilon_0 n_1^2 n_2 c^3 \pi} l k_1 h(\sigma, B, \xi) \quad (4.1)$$

with

$$h(\sigma, B, \xi) = \frac{1}{4\xi} \int_{-\xi}^{\xi} \int_{-\xi}^{\xi} \frac{e^{i\sigma(\tau-\tau')} e^{-\frac{B^2(\tau-\tau')^2}{\xi}}}{(1+i\tau)(1-i\tau')} d\tau d\tau', \quad (4.2)$$

where  $\omega$  is the frequency and  $k$  the wavevector of the fundamental laser beam, and  $n_1$  and  $n_2$  the refractive indexes of the fundamental and the harmonic light of the crystal, respectively. The integral depends on the phase matching parameter  $\sigma$ , the walk-off parameter  $B$  and the focus strength  $\xi$ . We numerically optimise this phase matching integral with respect to these three parameters and obtains the optimum focus parameter of the laser beam leading to maximum conversion efficiency.

This expression is derived by dividing the crystal into infinitesimally thin slices perpendicular to the  $\mathbf{k}$ -vector of the laser beam. The interaction of the fundamental laser beam with the nonlinear crystal generates second harmonic light in each slice. These

#### 4. Laser apparatus

contribution have to be coherently added. However, the birefringent pointing vector walk-off of the harmonic (extraordinary) beam has to be taken in account. This results in a spatial displacement of the harmonic light generated in different slices within the crystal. We obtain an interference pattern consisting of fringes perpendicular to the optical axis of the crystal.

With Boyd Kleinman's calculus we determine the optimum focus parameter and the single pass efficiency of a given crystal, it does not provide us with the optimum crystal length for achieving a high total conversion efficiency of the SHG cavity. The total harmonic output power  $P_{\text{out}}$  can be described by the following equation

$$P_{\text{out}} = \frac{P_{\text{inc}}}{\left(X_{\text{FOM}}^2 + \sqrt{X_{\text{FOM}}^2 + 1}\right)^2}, \quad (4.3)$$

where  $P_{\text{out}}$  is a function of the incoupled power  $P_{\text{inc}}$  which is given by the fundamental pump power times the incoupling efficiency of the resonator.  $X_{\text{FOM}}$  is a figure of merit giving a relation between passive loss  $L_{\text{pass}}$  and active loss in the resonator

$$X_{\text{FOM}}^2 = \frac{L_{\text{pass}}^2}{4\kappa_0 P_{\text{inc}}} \quad (4.4)$$

with  $\kappa_0$  the single pass conversion efficiency of the crystal which one obeys following Boyd-Kleinman [14] calculus (see Eq. 4.2). The figure of merit  $X_{\text{FOM}}$  is to be minimised in order to achieve a high total conversion efficiency. The passive loss  $L_{\text{pass}}$  scales linearly with the length of the crystal  $l$ . The "active loss", which is the harmonic gain, is determined by  $\kappa_0$ , and the incoupled power  $P_{\text{inc}}$ . The dependence of  $\kappa_0$  on the crystal length can for small crystal lengths be approximated as  $\kappa_0 \propto \sqrt{l}$ . Simulations predict, that for our parameters the total output power of the cavity  $P_{\text{out}}$  reaches its maximum at a crystal length of  $l = 6$  mm.

The shorter the crystal, the smaller are both the active and passive losses of the resonator leading to a higher power enhancement factor and cavity Finesse. However, Boyd-Kleinman calculus demands tighter focusing for shorter crystals. Both factors lead to higher intensities both of the beam focus in the crystal and on its surfaces. These might lead to thermal instabilities and damage of the crystal's surfaces, respectively. To ease aligning, we mount the crystal on a 3-D rotational stage and on a linear translation table for parallelly displacing the crystal and thus shift the location of the laser beam spot on the crystal surface. Rotational mounts of decent stability define a certain minimum distances between crystal surfaces and curved focussing mirrors. Tighter focussing demands a higher curvature of the focussing mirrors, thus they have to be placed closer to the crystal. Increasing the crystal length to  $l = 10$  mm, we solely loose 3% of harmonic power and can fulfil the other requirements.

A critical point to address is the decision between anti-reflective coated crystals and Brewster cut crystals. The advantages of AR-coated compared to Brewster cut

### 4.3. Second frequency doubling stage (560 nm → 280 nm)

crystals being that one loses about 20% of the harmonic output beam due to the “wrong” polarisation with respect to the Brewster cut. The surface of an AR-coated crystal is harder and less susceptible with respect to damage and can more easily be cleaned. However, anti-reflective coatings on BBO crystals are critical with respect to degradation or damage at high ultraviolet laser beam intensities. Benefits of the Brewster cut crystals are that the residual reflections are smaller compared to AR-coatings and they allow to compensate the astigmatism originating from the tilted incidence angles of the beams on the focussing mirrors of the cavity. Due to the AR-coating issue, we chose to build astigmatism compensated cavities with Brewster cut crystals.

Numerically optimising Boyd-Kleinman’s phase matching integral for optimum conversion efficiency leads to a beam waist within the centre of the crystal of  $w_0 = 19.4 \mu\text{m}$ . Simulating the cavity round trip for both tangential and sagittal plane, we optimise the distances between focussing mirrors and the angle of incidence on these aiming for optimum overlap of the stability region of the optical resonator. We deduce an optimum distance between the crystal surface and the curved mirror of  $d = 24.6 \text{ mm}$  and an astigmatism compensation angle of  $13.7^\circ$  (angle between incident beam and normal). To achieve the above mentioned crystal focus, we adjust the cavity length to  $l_{\text{cav}} = 470 \text{ mm}$ .

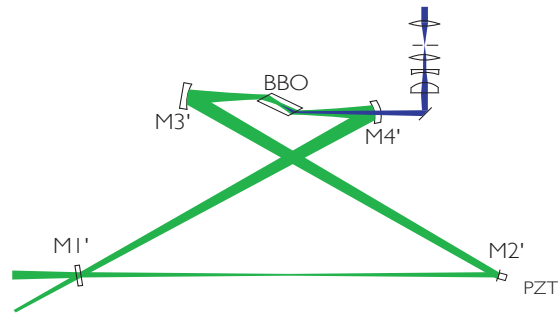
Due to the tilted angle of incidence on the curved mirrors we end up with an elliptical (not astigmatic) cavity mode in the crystal. We could have taken advantage from this fact by implementing the theory of SHG with elliptical Gaussian beams [120]. It states, that one can gain in conversion efficiency by loosening the focus in the direction of the optical axis therefore decreasing the intensity in the crystal reducing of thermal effects. Unfortunately this theory requires elliptical beams perpendicular to the ellipticity present in our setup. The simulated crystal focus for our resonator in the sagittal plane amounts to a beam waist of  $w_{\text{sag}} \approx 18 \mu\text{m}$  and for the tangential plane  $w_{\text{tan}} \approx 28 \mu\text{m}$ . With AR-coated crystals one would have been able to rotate the crystal by  $90^\circ$  so that the crystal axis would lie in the tangential plane. With Brewster-cut crystals, this would lead to non-planar ring cavities. Related disadvantages include a rotation of polarisation within one cavity round trip, custom designed posts for the mirror mounts, and mechanical stability issues due to long posts.

We purchase BBO crystals measuring  $4 \times 4 \times 10 \text{ mm}^3$  from *Castech*. We place the crystals in home-built mounts made of copper including a crystal heating to prevent the slightly hygroscopic crystal from moisture ( $T \approx 50^\circ\text{C}$ ). To ensure optimised heat contact and prevent the crystal from moving within the mount we wrapped it in a  $100 \mu\text{m}$  thick indium foil. The crystal mount is placed on a rotational mount<sup>8</sup> (*Newport PO-32N*) installed on top of a linear translational stage (*Newport S-DS-40*). For

---

<sup>8</sup>The angular tolerance of BBO crystals is about an order of magnitude smaller than the one of LBO crystal, making the alignment more critical.

#### 4. Laser apparatus



mirror #	substrate	coating
M1'	plane	$R = 98.5\%$ and $AR@560\text{ nm}$ outside
M2'	plane	$HR \geq 99.93\% @ 560\text{ nm}$
M3'	$f = -25\text{ mm}$	$HR \geq 99.93\% @ 560\text{ nm}$
M4'	$f = \mp 25\text{ mm}$	$HR \geq 99.8\% @ 560\text{ nm} \wedge HT \geq 90\% @ 280\text{ nm}$ and $AR @ 280\text{ nm}$ outside

Figure 4.9. – BBO cavity mirrors: The mirrors used for the BBO cavity are similar to the LBO cavity mirrors (Fig. 4.6), only the reflectivities are slightly lower due to the shorter wavelength: The IBS coating is specified to be  $HR \geq 99.93\%$ . For the input coupler M1 we need a higher reflectivity since the conversion efficiency of the BBO crystal is lower than the one of LBO. Also take notice of the larger angles used for astigmatism compensation and the need of a cylindrical telescope behind the resonator (see below) for correcting the astigmatism given rise by interferences due to critical phase-matching within the BBO crystal.

the Raman laser, we occasionally need to vary the detuning of the virtual level (see section 3.4), thus we change the frequency of the fundamental beam by several tens of GHz. With the rotational stage we can subsequently optimise the harmonic output of the BBO cavity by solely tilting the crystal (changing the angle between the optical axis and the  $\mathbf{k}$  vector of the fundamental beam) without having to realign the cavity.

The mirrors were coated at the *Laserzentrum Hannover*. The specifications of the used mirrors are summarised in the table within Fig. 4.9. We use the same mirror mounts as for the LBO resonator.

The procedure for initially aligning the BBO SHG cavity can be simplified by removing the incoupling mirror and replacing it by a glass substrate providing the same parallel displacement of the beam as the incoupling mirror. We adjust the polarisation of the beam to match the resonator plane and align the beam in such a way that it hits all mirrors in their centres. We rotate the crystal about the vertical axis to minimise

### 4.3. Second frequency doubling stage (560 nm → 280 nm)

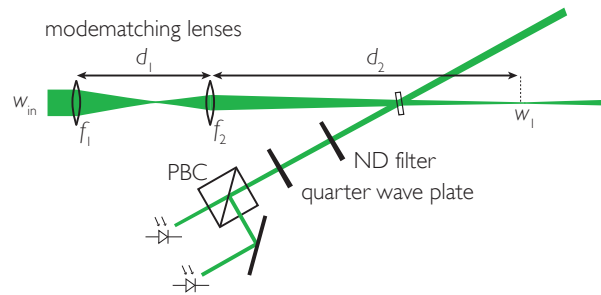


Figure 4.10. – Schematic of in-coupling telescope for longitudinal modematching the cavity mode. Measures for the telescope are given in the text. In addition we included the optical setup for generating the Hänsch-Couillaud error signal consisting of an optical attenuator, a quarter wave plate, a polarising beam cube and a difference photo diode (see chapter 4.2).

residual reflections at the Brewster cut surfaces. To be able to see the harmonic light generated in the crystal, we use dichroic mirrors (HR@280 nm and HT@560 nm) to filter out the green light passing through the output coupler. With a sufficient amount of fundamental beam power (above 400 mW at  $\lambda = 560$  nm), we try to achieve phase matching by tilting the crystal about the horizontal axes. When the phase matching condition is fulfilled, we are able to see a blue shimmering spot on a white card, since the UV light is converted to the visible by optical brighteners used in white paper. We complete the cavity round trip after installing the in-coupling mirror via mirrors M4' and M1' (see Fig. 4.9). We do not adjust mirrors M2' and M3', otherwise the phase-matching condition might be deteriorated. Subsequently, we can see twinkling blue light on the white card. We apply a triangular voltage ramp to the piezo which periodically changes the cavity length and observe the harmonic cavity spectrum on an oscilloscope using a UV-sensitive photodiode (for example *Hamamatsu S1336-18 BQ*). We choose the amplitude of the voltage ramp such that we see a repeating fringe pattern within one flank of the ramp. That is, we scan over more than a free spectral range of the cavity and thus see the full spectrum of cavity modes (see Fig. 4.7). We maximise the amplitude of the harmonic fringes of the cavity using all degrees of freedom of the mirrors and finally achieve a cavity solely resonant with a Gaussian TEM<sub>00</sub> mode.

**Longitudinal modematching** The in-coupling beam also has to be longitudinally overlapped with the resonator mode. The focal length of the curved cavity mirrors and the geometry of the resonator define a cavity mode. This cavity mode has two foci, the smaller one ( $w_0 = 19.4 \mu\text{m}$ , see optimisation of the Boyd-Kleinman phase-matching integral above) within the crystal and the in-coupling focus ( $w_1 = 180 \mu\text{m}$ , deduced by simulating the cavity round trip using Gaussian beam propagation ray matrices) half way

#### 4. Laser apparatus

between the mirrors M1' and M2' of the symmetric cavity (see Fig. 4.9). We use an incoupling telescope consisting of two plane-convex lenses to match this cavity mode. We mount these lenses on linear translation stages for finetuning the mode-matching by maximising the amplitude of the harmonic transmission fringes of the cavity monitored with a photodiode.

**Spatial filtering** The second harmonic laser beam is not of Gaussian shape, but an interference pattern of the harmonic light generated in different slices of the crystal which is coherently added (see above). The interference leads to an astigmatic UV-beam. The beam characterised 66 mm behind the outcoupling mirror<sup>9</sup> has the following beam parameters:

	tangential	sagittal
beam waist $w$	0.57 mm	0.52 mm
radius of curvature	82 mm	-1500 mm

The UV beam is convergent in the sagittal plane and has a strong divergence in the tangential plane. We use a cylindrical telescope for adapting the beam parameters of the divergent tangential plane to the convergent beam parameters of the sagittal plane. It is composed out of two plane-konvex lenses of focal lengths  $f = 70$  mm. The first one is placed at a distance  $d = 112$  mm from the reflecting side (inside) of the outcoupling mirror and the second one at a distance of  $d = 340$  mm measured the same way.

Behind the cylindrical telescope we use a spherical mode-cleaning telescope to abandon the interference fringes due to critical phasematching in the BBO crystal, collimating the UV beam, and adapting the beam waist to  $w = 0.75$  mm. With this beam waist the 220 MHz UV AOMs diffract the beam most efficiently (see section 4.5). The first lens of the spherical telescope has a focal length  $f = 76$  mm and the second lens  $f = 150$  mm. We use a pinhole in the telescope's focus of  $75 \mu\text{m}$  diameter. The choice of the lenses and pinholes depends on the distance the telescope is placed with respect to the resonator.

### 4.4. Frequency stabilisation of lasers

To prevent thermal frequency drifts of our lasers we stabilise three out of four laser systems to appropriate iodine transitions via Doppler-free saturation spectroscopy. The Raman laser does not require frequency stabilisation, since the transition depends on the relative frequency difference between two Raman beams, which is controlled by rf

---

<sup>9</sup>Zero-lenses focus the transmitted beam, the focal length is given by  $f = \frac{6r^2}{t}$ , where  $r$  is the radius of curvature of the lens and  $t$  is the thickness of the substrate. With  $r = 50$  mm and  $t = 6.35$  mm the focal length amounts to  $f = 2.34$  m.

#### 4.4. Frequency stabilisation of lasers

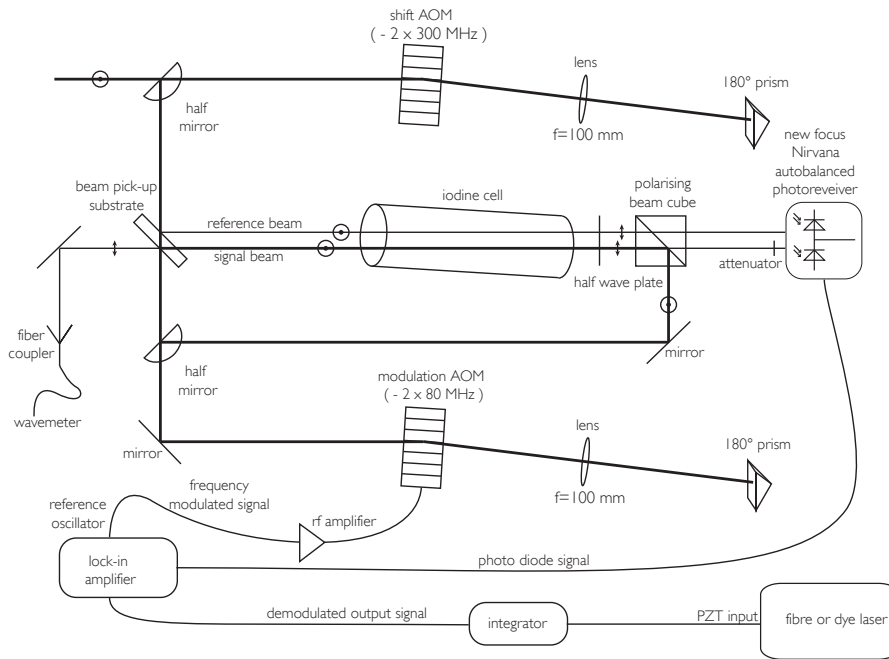


Figure 4.11. – Doppler-free absorption spectroscopy of the BD laser light: The green laser beam enters the setup s-polarised in the upper left corner and is red-shifted (to the lower frequency side) using a double-pass AOM operated at 269 MHz for reaching an appropriate iodine transition. The frequency-shifted beam then passes an uncoated glass substrate which reflects  $\approx 10\%$  of the beam on both sides thereby generating a signal and a reference beam. These two beams pass a slightly tilted iodine cell, a half wave plate and are transmitted by a PBC. The signal beam is attenuated (factor of  $\approx 1/2$ ) by a *Schott* glass filter for improved performance of a *New Focus Nirvana* auto-balanced photo-receiver. The pump beam transmitted at the glass substrate is double-passed through another AOM, modulated in frequency by the reference oscillator of a lock-in amplifier (NIST, Boulder). The frequency modulated beam passes the iodine cell counter-propagating superimposed with the signal beam. The difference signal from the *Nirvana* is demodulated by the lock-in amplifier. This error signal is integrated and fed back to the piezo tuning input of the fibre laser.

AOMs to the Hz level, and the detuning of the virtual level  $\Delta_R$  is large compared to thermal frequency drifts of the laser.

We will exemplarily explain the scheme for the BD setup here<sup>10</sup> (see Fig. 4.11 for

<sup>10</sup>The BD setup is identical to the stabilisation of the other lasers, however, it includes an additional double-pass AOM for bridging the frequency gap between the magnesium transition and the iodine transition. Working with magnesium-24 ions this is considerably easier since there is an iodine transition close to the  $^2S_{1/2} \leftrightarrow ^2P_{3/2}$  transition.

#### 4. Laser apparatus

the experimental setup). The stabilisation is carried out in the green spectral region (first harmonic for the fibre laser systems). The cycling transition for our magnesium

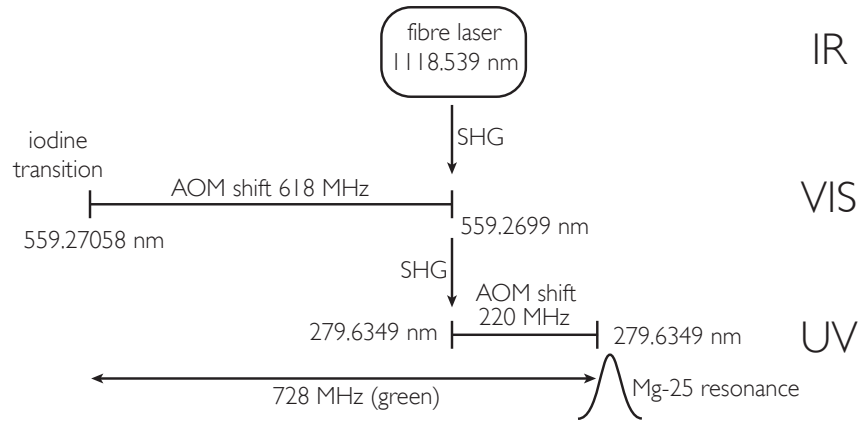


Figure 4.12. – Adjustment of the frequency of the BD: The fibre laser emits radiation at  $\lambda = 1118.539$  nm. A fraction ( $\approx 10$  mW) of the frequency doubled light is red-shifted to match an appropriate iodine transition at  $\lambda = 559.2716$  nm. The laser is stabilised in frequency to this transition. The larger part of the green light is further doubled in frequency to the UV, where it is shifted to the higher frequency side to address the  $^{25}\text{Mg}^+$  resonance. In the figure, the BD beam addresses the resonance at a detuning of  $\Gamma/2 = 2\pi \times 42.7/2$  MHz.

isotope  $^{25}\text{Mg}^+$  lies at a wavelength of  $\lambda_{\text{BD}} = 279.63492$  nm whereas the nearest iodine transition is at a wavelength of  $\lambda_{\text{iod}} = 2 \times 279.63581$  nm. We bridge the corresponding frequency gap of about 728 MHz (frequency difference in the green) via AOMs partly in the UV and partly in the visible (details in Fig. 4.13). The largest part of the shift is done by a double-passed 300 MHz AOM (see section 4.5) in the visible driven by a voltage controlled oscillator (VCO, *minicircuits, ZX95-400*) and a rf-amplifier (*minicircuits, ZHL-1-2W*). The use of a double-pass AOM is convenient, since changing its frequency does not vary the pointing direction of the frequency-shifted beam. This allows to change the detuning between iodine transition and laser frequency whilst the stabilisation is active, without having to realign the iodine spectroscopy. An experimentally recorded iodine spectrum is depicted in Fig. 4.13.

#### 4.5. Acousto-optic modulators

In our present beamline assembly, we use 18 acousto-optic modulators (AOM) for laser beam switching and frequency shifting. All of these were supplied by *Intraaction*. Four out of these are designed for the green spectral region and use tellurium dioxide ( $\text{TeO}_2$ ) as interaction medium and lithium niobate piezoelectric transducers operating

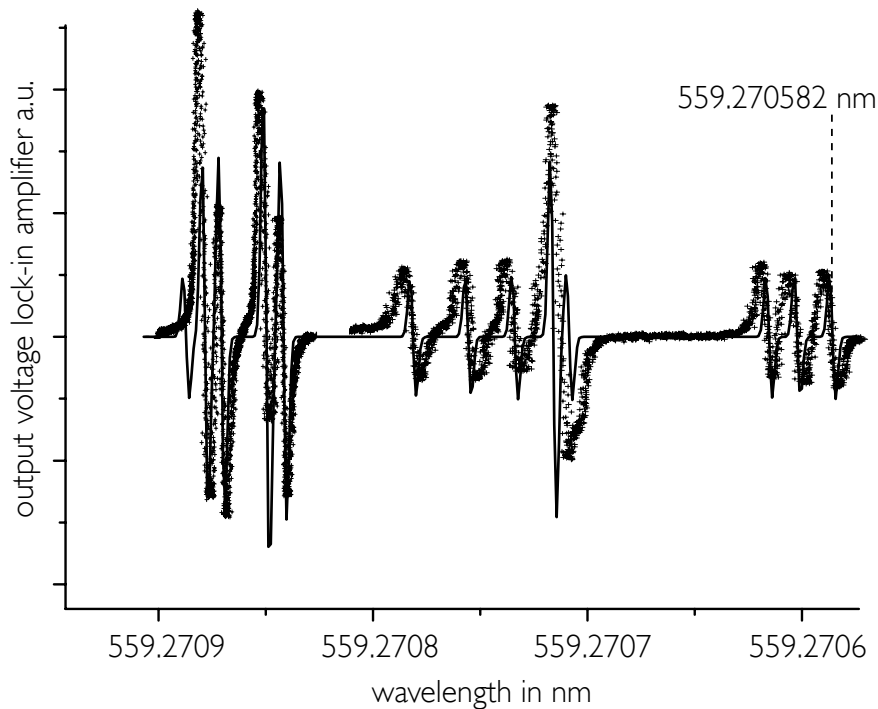


Figure 4.13. – Experimentally recorded iodine spectrum of the BD setup. This plot consists of two oscilloscope traces of experimentally recorded iodine spectra embedded in a calculated transition spectrum taken from *Iodinespec* [122]. We stabilise our laser to the bluest transition line of the spectrum. The exact wavelength of the transition is noted. The resolution of the spectroscopy is not high enough to resolve close doublets e.g. fourth and fifth line from the right hand side.

between 80 MHz and 300 MHz. These AOMs feature apertures of 1 mm and achieve diffraction efficiencies between 80% and 85% for collimated beams with beam waists of 0.4 mm. The required rf-drive-power level amounts to 0.5 W. The crystals' surfaces are coated with dielectric broadband anti-reflective coatings.

The other 14 AOMs are designed to work with UV laser beams and are based on fused silica crystals. They are polarisation dependent (higher diffraction efficiency for s-polarised light) which has to be taken into account for double-passing (see section 4.5). Twelve of the AOMs are operated at  $\approx 220$  MHz, in addition, there is one 120 MHz model which is part of the Raman intensity stabilisation (see section 4.5) and one AOM for 450 MHz, which is part of the Red Doppler setup (see section 4.6.2). The 220 MHz models feature vertical apertures of 2 mm, horizontal apertures of 25 mm and achieve 85% diffraction efficiency into the first order at a rf drive power of 2 W for collimated beams of 0.75 mm beam waist. The single 450 MHz AOM is not as efficient compared

#### 4. Laser apparatus

to the others, it diffracts about 50% of the incoming beam power. Furthermore, it demands a beam waist of 0.25 mm for optimum diffraction. If this AOM had worked more efficiently one could have used it to simplify the beamline of the Raman laser (see section 4.6.3). We used this AOM for the RD setup, where the requirements for efficiency are still met. The 120 MHz AOM used for intensity stabilisation in the Raman setup only needs to diffract 30% of the incident beam power to the first order (see section 4.5).

**Double passing of UV AOMs** For the Raman laser and for the Red Doppler, we have to bridge frequency gaps of roughly 1.8 GHz, hence, we operate most of the highly efficient 220 MHz AOMs in double pass configuration, where the diffracted beam is retro-reflected and undergoes another diffraction process. Therefore, we achieve twice the frequency shift. The other advantage is the avoidance of beam pointing when tuning the frequency of the AOM. Since the UV AOMs rely on vertically polarised (s-pol) light, we cannot use the common scheme [31] based on a polarising beam cube, a quarter wave plate and a mirror. In this scheme the incident and the superimposed outgoing beam are separated by a rotation of the polarisation of the returning beam. We have to spatially separate the two paths through the AOM: The two beams intersect in the centre of the AOM at an angle of  $<2^\circ$  in the vertical plane. The incoming beam enters the AOM from one side and approximately 85% of the beam power is diffracted into the first blue order. After a distance of 100 mm, a lens of focal length  $f = 100$  mm follows. The distance between the AOM and the lens exactly has to match the focal length of the lens to ensure that an angular deviation, caused by a change of the AOM driving frequency, is translated into a parallel displacement. The zeroth and first order beams are still spatially overlapping when passing the lens. However, since both beams are focussed down while keeping their relative distance, one can place a beam dump exclusively for the zeroth order before the beam foci. In the focus we place a  $180^\circ$  prism which displaces the first order beam vertically. On its way back the beam is collimated by the lens (the lens and the prism form a 1:1 telescope) and its parallel displacement is translated back to the required angular deviation. The beam crosses the incoming beam in the center of the AOM. Taking the first blue diffraction order of the returning beam again one has to separate the returning beam from the incoming using a half mirror. The trick of separation in the focus does not work for the collimated beam, so one has to let the beams propagate until they are spatially separated (15-20 cm). The intersection angle of the beams have to be compromised, smaller angle means higher efficiency, whereas a larger angle leads to better resolvable separation of the beams at the half mirror. We achieve double pass efficiencies of the order of 65% using this method.

**Intensity stabilisation** We need to provide both long- and short term stable UV output power levels of the fibre and dye laser systems<sup>11</sup>. For the Blue Doppler setup (see section 4.14), the main reason concerns the detection process, where intensity fluctuations influence the photon counting rate and reduce the fidelity of the state-sensitive detection scheme (see chapter 9). For the Raman laser (see section 4.6.3), intensity fluctuations deteriorate the fidelity of pulses e.g. leading to less efficient motional ground state cooling (see section 7).

To detect the output power, we reflect a small amount of UV light via a fused silica substrate inserted close to Brewster's angle<sup>12</sup>. We direct this light onto a fast gallium phosphide (GaP) photodiode for the UV (*Thorlabs, PDA25K-EC*) which features bandwidth of up to 7.5 MHz depending on the switchable gain. We previously employed self-built photo diode amplifiers using silicon carbide (SiC) photodiodes (*IFW Jena, JEC 0.1 S*) with the limitation that the active size of the detector was solely 0.1 mm<sup>2</sup> and we had to amplify the photo current considerably to get enough signal thereby reducing servo bandwidth.

To stabilise the output power, we feed the 50  $\Omega$  output of the photodiode amplifier to a commercial servo electronics circuit (*TEM Meßtechnik, miniNE*) comprising a pre-amplifier stage and a PID servo which provides an output signal proportional to the detected power above an externally set threshold. Laser beam power above this threshold is diffracted to the first order of the noise eater AOM and dumped. The servo output signal controls the amplitude of a voltage controlled oscillator (VCO) via a rf-modulator. Subsequently, the output signal of the VCO is amplified and fed to the noise eater AOM. In practise, one adjusts the threshold power to about 85% of the laser beam power depending on the fluctuations of the laser source. We end up with an intensity stabilised beam of slightly reduced power. The noise eater setup is illustrated in the upper right of Fig. 4.14.

## 4.6. Laser setups

### 4.6.1. Blue Doppler setup

The UV output of the Blue Doppler SHG cavity is split into three physical beams. These three beams fulfil four different tasks summarised in Table 4.2. All these beams address the  $^2S_{1/2} \leftrightarrow ^2P_{3/2}$  cycling transition and differ by detuning and power. The

<sup>11</sup>Drifts of the ambient temperature rotate the state of polarisation of the non polarisation maintaining fibre lasers leading to reduced transmission of the optical isolator. The dye lasers are sensitive with respect to misalignment due to their long optical resonators. In addition, the resonator and especially the dye jet are sensitive with respect to environmental disturbances such as air turbulences, mechanical influences and acoustic vibrations leading to fast fluctuations up to several kHz bandwidth.

<sup>12</sup>We try to minimise this fraction in order to have more UV light for the subsequent beamline.

#### 4. Laser apparatus

functions of the individual beams are discussed in section 7.3.1 and chapter 9. In this

beam	beam power	detuning	TTL channel
BD	$1.6 \mu\text{W}$	$\approx 2\pi \times 21 \text{ MHz}$	1
$\text{BD}_{\text{loading}}$	$> 400 \mu\text{W}$	$\approx 2\pi \times 500 \text{ MHz}$	1
BDdet	$80 \mu\text{W}$	$\approx 2\pi \times 440 \text{ MHz}$	2
BDX	$1.6 \mu\text{W}$	0	10

Table 4.2. – Parameters of Blue Doppler beams: The first column labels the different functions of the beams: the Blue Doppler (BD), the  $\text{BD}_{\text{loading}}$  beam, the Blue Doppler detuned (BDdet) and the Blue Doppler detection beam (BDX). The second column shows the required beam powers, the third column states the red-detuning from the resonance frequency of  $^{25}\text{Mg}^+$ , and the last column gives the TTL channels by which they are controlled.

section we will address their technical realisation. The BD beam is used twofold with

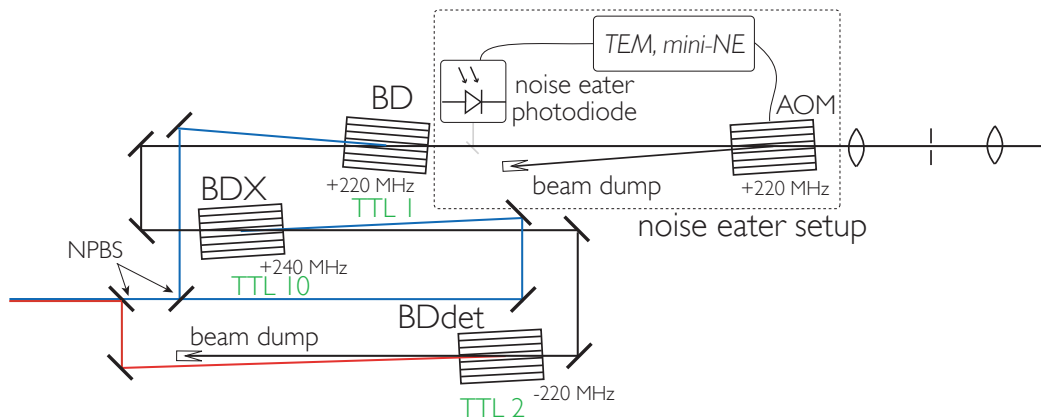


Figure 4.14. – Schematic BD beamline and AOM setup: The beam coming from the BBO SHG cavity passes a mode-cleaning telescope. The dashed box depicts the intensity stabilisation (*noise eater*, see section 4.5). The beam subsequently passes three AOMs generating three independent beams: BD, BDX and BDdet which are superimposed via non-polarising beam splitters (NPBS, *Laseroptik*). The switching electronics is explained in Fig. 4.15. Since we do not use BD and BDX at the same time, the variation of power when switching on the BD AOM does not matter. The small amount of power used for the BD beam during experiments ( $1.6 \mu\text{W}$ ) does not significantly change the power of the BDdet beam ( $80 \mu\text{W}$ ).

two different sets of properties, for loading ions (see sections 2.5 and 6.1) we prefer a beam power above  $400 \mu\text{W}$  and a detuning of about  $2\pi \times 500 \text{ MHz}$  red with respect

#### 4.6. Laser setups

to the  ${}^2S_{1/2} \leftrightarrow {}^2P_{3/2}$  transition (for loading we do not stabilise the laser in frequency), whereas for experimenting we used it for Doppler cooling at a beam power of  $1.6 \mu\text{W}$  which corresponds to half the saturation intensity of the transition. During experiments we have to independently switch the three laser beams BD, BDdet, and BDX via AOMs. To overlap the beams with identical polarisation we use non-polarising beam splitters.

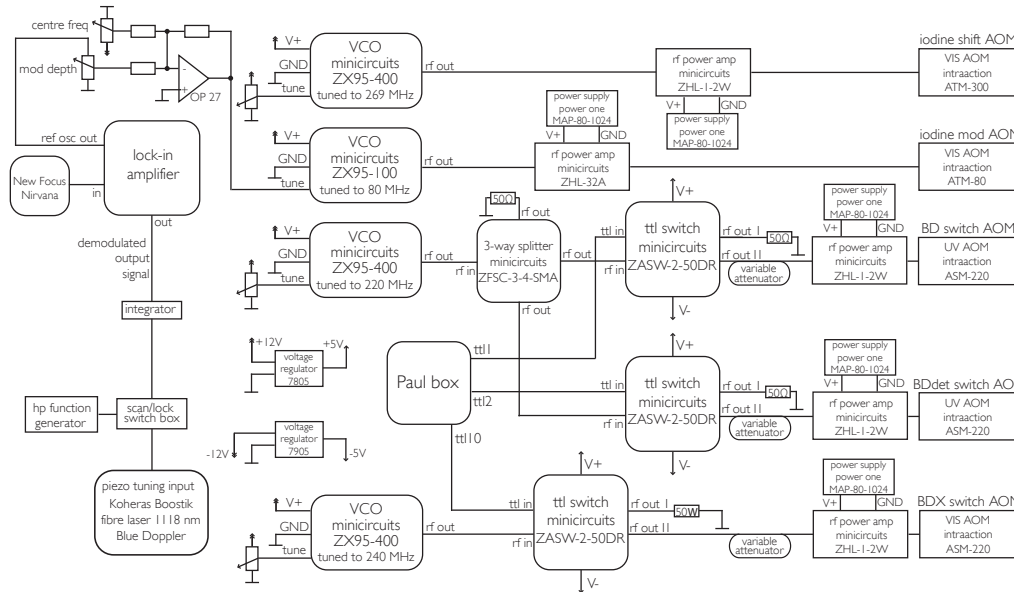


Figure 4.15. – Schematic of Blue Doppler electronics: All rf-signals for the AOMs are generated by voltage controlled oscillators (VCO, *minicircuits ZX95-x00*). The two upper rows are part of the frequency stabilisation of the laser (see section 4.4). The AOM in the upper right runs at constant frequency. In the second row we generate a frequency modulated drive signal by adding the reference oscillator output of a lock-in amplifier to a constant voltage using an operational amplifier (*OP27*). The modulated signal is fed to a VCO. The centre frequency (80 MHz) and modulation depth (2–3 MHz) are adjusted by potentiometers, whereas the modulation frequency (10 kHz) is set with the lock-in amplifier. The three lower rows represent the switching electronics for the UV AOMs. Two of them are driven by a single VCO tuned to 220 MHz and the remaining one is driven by another VCO tuned to 240 MHz. Each of the signals is independently switched (*minicircuits ZASW-2-50DR*) using TTL logic controlled by the Paul box (see chapter 5.1). The output signals can be variably attenuated to adjust laser beam powers. Each signal is amplified to up to 2W (*minicircuits ZHL-1-2W*) and fed to an AOM (*intraaction, ASM-220*, see section 4.5).

After the intensity stabilisation (see section 4.5), the beam subsequently passes three AOMs: the BD AOM tuned to 220 MHz diffracting the incoming beam to the first blue order generating the Doppler cooling beam BD (detuned from the BD resonance by

#### 4. Laser apparatus

$\Gamma/2 = 2\pi \times 21.5$  MHz); the BDX AOM tuned to  $\approx 240$  MHz diffracting the beam to the first blue order generating the detection beam BDX which is resonant with our cycling transition, and finally the BDdet AOM (220 MHz) which diffracts the beam to the first red order generating a beam red-shifted by 440 MHz with respect to the BD beam. This beam provides recoiling of ions which have accidentally become warm. The beamline setup is depicted in Fig. 4.14. All AOMs used in this setup are *Intraaction ATM-220*. A schematic of the switching and iodine stabilisation electronics is depicted in Fig. 4.15

##### 4.6.2. Red Doppler setup

The Red Doppler laser system provides two beams addressing the  $^2S_{1/2} \rightarrow ^2P_{1/2}$  transition. The beam of lower frequency addresses the  $F = 2$  manifold of the  $^2S_{1/2}$  level and is referred to as RD. The so-called Repumper beam (RP) addresses the transition  $^2S_{1/2} |F = 3, m_F = +1, +2\rangle \rightarrow ^2P_{1/2}$  level (see Fig. 4.2). The  $|\downarrow\rangle$  is a dark state with respect to these transitions, since both beams are polarised  $\sigma^+$  and there are no  $m_F = +4$ -levels in the  $^2P_{1/2}$  manifold.

The frequency difference of the RD and RP beams equals the hyperfine ground state splitting  $\omega_0$  of the  $^2S_{1/2}$  level and is approximately  $2\pi \times 1.77$  GHz. The frequency of the RD laser system is stabilised to a suitable iodine transition which ensures that the frequency in the UV is centred between the  $^2S_{1/2} F = 3 \rightarrow ^2P_{1/2}$  and the  $^2S_{1/2} F = 2 \rightarrow ^2P_{1/2}$  transitions. The UV output beam is frequency shifted via three AOMs. The AOM schematic is depicted in Fig. 4.16.

##### 4.6.3. Raman setup

In principle the Raman laser setup does not differ greatly from the RD setup. It also generates beams separated in frequency by the hyperfine ground state splitting of the  $^2S_{1/2}$  level. But whereas resonant repumping carried out by the RD requires just a few microwatts of beam power, the coupling between these states using two-photon stimulated Raman transitions via a far detuned virtual level is more demanding. The Raman laser couples our spin states  $|\uparrow\rangle$  and  $|\downarrow\rangle$ , enabling us to coherently transfer population between these levels (Rabi flopping), couples the internal states to the motional states of the ions confined in the harmonic potential, therefore enabling us e.g. to accomplish motional ground-state cooling (see chapter 7). Furthermore, it generates optical dipole forces for conditionally coupling the states of several ions and lets us simulate effective spin-spin interactions as needed for simulating quantum Ising-type interactions (see chapter 8). The Raman laser can be considered as the “heart of the experiment”. The ultraviolet beam line setup employs seven acousto-optic modulators, three of them double-passed. Three of these AOMs are controlled by direct digital synthesis (DDS) boards controlling frequency, phase and amplitudes of the laser beams shining on the ions (see chapter 5.1 for details).

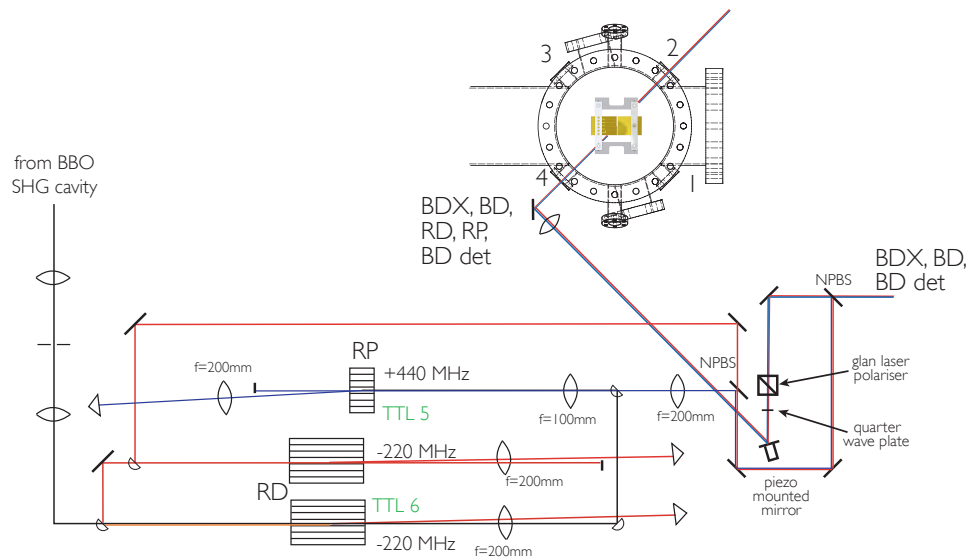


Figure 4.16. – Red Doppler beamline: The beam coming from the BBO resonator enters from the left and passes a mode cleaning telescope. The beam is double-passed (see section 4.5) twice using two 220 MHz AOMs. The resulting beam, shifted by  $-4 \cdot 2\pi \times 220$  MHz, is labelled RD beam. The zeroth order of the first RD AOM is recycled and double-passed by a 450 MHz AOM. We include a 2 : 1 telescope before the AOM to match the required beam waist of 0.25 mm. The RP beam shifted by approximately  $+2 \cdot 2\pi \times 440$  MHz passes a 1 : 2 telescope and is superimposed with the RD beam on a 50 : 50 non polarising beam splitter (NPBS). The RD and RP beams are superimposed with the three BD beams entering from the right. The beams enter the vacuum chamber via laser port 4 parallel to the quantisation magnetic field. We achieve  $\sigma^+$  polarisation by using a glan laser polariser (polarisation  $10^5 : 1$ ,  $\alpha$ -BBO, AR-coated, *Lasercomponents*) and a zero-order quarter wave plate (*B. Halle*). The wave plate is mounted on a 3D rotational mount to fine-tune the polarisation of the beams.

**Efficiency** The Raman fibre laser has an infrared output power of about 1.8 W at the wavelength 1118.460 nm excluding ASE (see section 4.1). About 90% of this power pass the optical isolator providing us with 1.62 W of pump power for the first frequency doubling stage. Out of this LBO resonator we get 1.27 W of green light in a Gaussian TEM<sub>00</sub> mode which corresponds to a conversion efficiency of 78%. This light is directly mode matched into the BBO resonator and generates 365 mW of ultraviolet light at about 280 nm, this corresponds to a conversion efficiency of 28.7% or an overall conversion efficiency from the infrared to the ultraviolet of 22.5%.

#### 4. Laser apparatus

**Beam line** The UV beamline of the Raman laser setup is illustrated in Fig. 4.17. Following after the BBO SHG cavity, we use a cylindrical telescope to eliminate the astigmatism resulting from critical phase matching in the BBO crystal. We took utmost care to achieve a circular non-astigmatic beam since the beamline of the Raman lasers is about 7 m meters long and astigmatism reduces the diffraction efficiency of the AOMs, the beam intensity on the ions as well as cause straylight in the vacuum chamber. After the cylindrical telescope, we use a mode-cleaning telescope with a pinhole in its focus to adjust the beam waist to 0.75 mm for optimum diffraction efficiency in the AOMs. A noise eater follows stabilising the power of the beam (see 4.5).

Subsequently, the beam passes the “Raman splitter” AOM which divides the Raman beam into its red branch (zeroth order of the AOM) generating the red Raman beams (R1 and R2) and the blue Raman beam (B1, first blue order of the AOM). Since the AOMs cause an interference pattern in the zeroth order beam at maximum diffraction efficiency, it is important to note, that this AOM is driven at moderate radio frequency power and, therefore, only diffracts a small fraction of the light into the blue branch, whereas the beam used for the red Raman beams passes with little disturbance. This part of the beam is divided into two equal parts via a polarising beam cube (PBC, *Halle Nfl.*) which is optically contacted. Power levels of more than 200 mW at the wavelength of 280 nm might degrade the kit used for conventional PBCs. The two resulting beams are both diffracted to the first red order of two AOMs (labelled R1 and R2), which are driven by DDS boards controlled in frequency, amplitude and phase, respectively. The resulting beams R1 and R2 enter the vacuum chamber via laser port 1 and 2, respectively. The R1 beam is polarised in the sagittal plane and superimposed with beam B1 by the help of a PBC. The R2 beam passes a half wave plate and a glan laser polariser followed by a quarter wave plate under approximately zero degrees (the polarisation as seen by the ions corresponds to  $\sigma^+ - \sigma^-$ , by rotating the  $\lambda/4$  waveplate we can (im-)balance the two contributions, see chapter 6.5). Therefore the R2 beam is polarised in the parallel plane and perpendicular to the R1 beam. We will now continue with the blue branch of the Raman setup. After being diffracted to the first blue order of the Raman splitter AOM the beam passes three additional double pass AOMs.

The first two double-pass AOMs are labelled blueshifter I and blueshifter II, respectively, and are always driven at maximum power ( $P \approx 2\text{W}$ ) and at a fixed frequency of 222.83 MHz (see Table 4.3). This frequency value is chosen such that the following AOM B1 operates at optimum diffraction efficiency and the diffracted beam power upon varying its driving frequency does not change considerably. The two blueshifter AOMs are driven by a Hewlett Packard oscillator stabilised in phase to the master oscillator serving as a clock for the DDS boards (see chapter 5.1). The third double pass AOM is called “frequency shifter” and is the only AOM which is changed in frequency during experimentation. It also acts as a switch for the beam B1 which enters the chamber through laser port 1. The polarisation of the B1 beam lies within the horizontal plane



#### 4. Laser apparatus

AOM	single pass / double pass	frequency shifts
R1 / R2	single pass	-220 MHz
splitter	single pass	+222.83 MHz
blueshifter I	double pass	+2 × 222.83 MHz
blueshifter II	double pass	+2 × 222.83 MHz
B1	double pass	+2 × 220 ± 5 MHz
		$\Sigma$ 1774.15±10 MHz

Table 4.3. – AOMs used in the beamline of Raman setup and corresponding frequencies

and the beam is superimposed with the R1 beam using a PBC. These two beams are perpendicular to the quantisation axis, therefore, the beam B1 is  $\pi$  polarised and the beam R1 is  $\sigma^+ + \sigma^-$  polarised. The last mirrors before the PBC are mounted on piezo-driven mirror mounts to be able to maximise the beam overlap with the ions very sensitively. All Raman beams are focussed to about 45  $\mu\text{m}$  beam waist into the centre of the experimental trap via lenses of focal lengths  $f = 200$  mm.

One might wonder, why we chose to setup the beam line asymmetrically, that is, the largest part of frequency shifting is carried out by the blue Raman branch which generates the B1 beam. This is due to the fact, that the requirements in power for the respective beams are also asymmetric: The red Raman beams are used to generate optical dipole forces to simulate spin-spin interactions, demanding high intensities in order to achieve strong enough coupling strengths, whereas the blue Raman beam B1 is solely used for ground state cooling. In order to avoid difficulties with respect to temporal synchronisation as well as switching flanks becoming important, it is preferential to keep the beam powers for ground state cooling on the order of few milliwatts at a typical detuning of  $\Delta_R = 2\pi \times 80$  GHz of the virtual level.

We split the power asymmetrically to give the majority of power to the red branch (this beam is splitted up into two equal parts and both parts undergo just one AOM diffraction), therefore, loosing less absolute power compared to a symmetric setup. Assuming, we split up the power to two equal parts and both parts undergo 4 AOM diffractions with realistic diffraction efficiencies of 80%, we loose 60% of the total power. In our setup, which splits the power in a ratio 1:9 (blue branch : red branch) and the blue branch undergoes 7 diffractions compared to a single diffraction for the red branch, we only loose 26% of the total power.

**Beamline change to address the radial modes** With the current laser beam line setup, as described here, we are only able to address the axial modes of motion. For the easiest way to modify the laser beamlines to address the radial modes, refer to Fig. 4.1. We could also let the two Raman beams R1 and B1 enter the chamber on

the opposite side through laser port 3. However, we want to minimise beam distortions by longer propagation distances for the Raman beams. In addition, the available space on the opposite side is limited due to the vacuum pump. An alternative way would be to superimpose beam R2 with the BD and RD beams, but we would lose half of the power in both beams and lack the possibility of AC-Stark shift compensation of the Raman beams which will become important in chapter 8 (the BD and RD beams rely on purely  $\sigma^+$  polarised light). The best way to accomplish is exchanging port 2 and 4, i.e. letting the Raman beam R2 enter through port 4 and the BD and RD beams through port 2. This leaves the propagation distance of the Raman beam almost unchanged, the BD beam line is even shortened, only the RD beam line becomes longer which is of minor importance.

### 4.6.4. Photoionisation laser

In section 2.5, we discussed the process of resonant two-photon photoionisation [77] and the need for a laser source at a wavelength of  $\lambda = 285.296$  nm. Narrow linewidth ytterbium fibre lasers at 1140 nm are difficult to build and not commercially available, and solid state materials like quantum well structures do not offer enough power yet, to obtain sufficient frequency-quadrupled laser beam power in the UV. One possibility to obtain the required wavelength is to use a frequency doubled dye laser operated at  $\lambda = 570.592$  nm. We use a *Coherent 899* dye laser pumped by a *Coherent Verdi V10*. The output of the *Verdi* is split into two equal parts by a half wave plate and a polarising beam cube (PBC). We can use the *Verdi* for pumping two dye lasers with up to 5 W each. We dissolve 1 g of Rhodamin-19 dye in 1400 ml ethylene glycol. To be able to use higher pressures and for increasing the lifetime of the dye we cool the solution down to about 12°C. With fresh dye the ring laser emits more than 500 mW of light at a wavelength of  $\lambda = 570.592$  nm for 4 W of pump light at  $\lambda = 532$  nm. With a fresh dye solution we can work for about 6 weeks. The rough control of the wavelength is carried out by the help of a *Burleigh* wavelength meter. To precisely adjust the frequency of the laser, we use an iodine saturation spectroscopy setup (see section 4.4). Subsequently, the yellow light is coupled into an optical fibre waveguide and guided to our “experiment” table. The dye lasers are located on a different optical table to protect the experiment from vibrations due to the dye pumps and cooling water circulation for the pump laser. To couple visible light into the fibre waveguide (*Thorlabs hp460* with FC/APC connectors), we use a *Toptica Fiberdock* fibre coupler which features solid state flexures and allows for very precise and reproducible adjustment. We achieve coupling efficiencies of up to 86% at power levels of 10 mW. For higher input power levels of the order of 500 mW, the coupling efficiency and the transmission through the fibre deteriorate to of the order of 65%. After the SHG cavity, which contains identical crystal and mirrors as the cavities for 560 nm, the beam is focussed into the trapping

#### 4. *Laser apparatus*

volume, where it has a beam waist of  $w \approx 70 \mu\text{m}$ .

### 4.7. Radio-frequency setup

Strictly speaking, radio-frequency transitions do not really match into this laser section, but in practise, we use radio-frequency and laser induced transitions between our spin states interchangeably. As an alternative to TPSR transitions with collinear laser beams we can also resonantly couple our spin states  $|\downarrow\rangle$  and  $|\uparrow\rangle$  by addressing the M1 transition using radio-frequency. We superimpose the radiofrequency with the trapping rf-drive via a self-built  $\lambda/4$  copper antenna in proximity to the massive copper conductor which connects the tank circuit with the rf electrical feed-through.

The electronic setup is depicted in Fig 4.18. The source for our radiofrequency signal is a *Rohde & Schwarz* 2 GHz oscillator and a DDS-board of the Paulbox (see section 5.1). There are two reasons why we cannot solely use the oscillator: the first one being that for experiments where we want to rapidly change the frequency of the oscillator the *Rohde & Schwarz*, which uses a General Purpose Interface Bus (GPIB) for communication, is too slow. This protocol has been designed for communication on the timescale of seconds, not for microsecond time scale switching. Employing this protocol would considerably slow down our experiments. But the more important drawback related to this oscillator is that we lack phase control. For our experiments we need to control the phases between subsequent pulses on the microsecond level. Thus, we use the *Rohde & Schwarz* oscillator to generate a radiofrequency signal 200 MHz detuned from our transition. With a radiofrequency mixer we modulate sidebands on top of this signal via a DDS-board, which we are able to control on timescales of tens of nanoseconds both in frequency and phase (see chapter 5.1). Subsequently, we use an interdigital filter of 50 MHz bandwidth (*H. Reichel*) to filter out the carrier and the red sideband, we solely use the blue sideband at frequency 1774 MHz, the frequency of our spin-flip transition. We use an additional preamplifier (*Minicircuits ZX-4016E-S*) to match the required input power level of a radio-frequency amplifier (5 W, *D. Fischer Elektronik*).

Then the signal is splitted, attenuated in one path and recombined to be able to vary the intensity of the rf-signal. The setup is illustrated in Fig. 4.18, a truth table of the switching logic can be found in Table 4.4.

#### 4.7. Radio-frequency setup

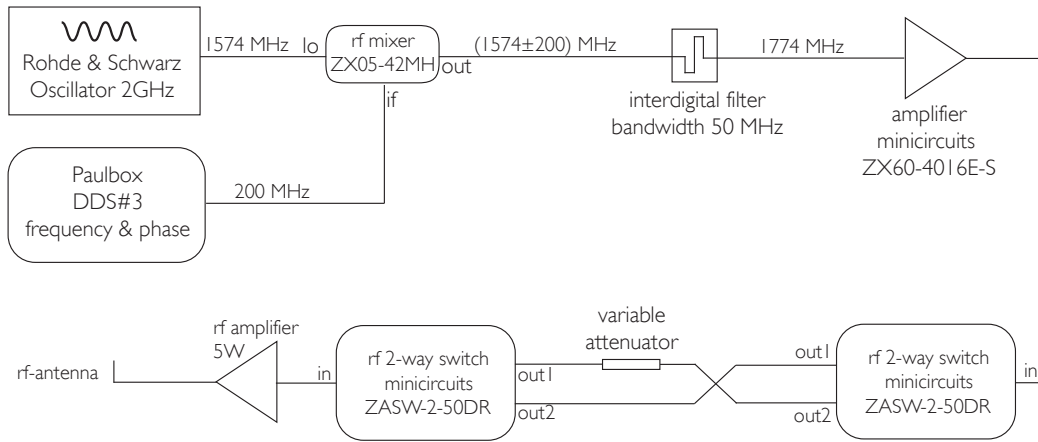


Figure 4.18. – Schematic of radiofrequency control: On the left hand side the *Rohde & Schwarz* oscillator generates a signal at a frequency of 1574 MHz and a power level of +10 dBm. This signal enters the lower frequency input of a rf-mixer *Minicircuits ZX05-42MH*. To the intermediate frequency (if) input of the mixer we feed the output signal of a DDS board controlled by the *Paulbox* which will be detailed in chapter 5.1. Only the first blue sideband of the output signal of the mixer passes an interdigital filter of 50 MHz bandwidth. The output signal after the mixer now is centered at 1774 MHz and adjustable both in frequency and phase due to the DDS board. This signal is divided into two signals and recombined by two rf-switches (*Minicircuits ZASW-2-50DR*) where one branch incorporates a manually switchable attenuator. The second switch is used in reverse direction. This setup gives us the possibility of using the rf at two distinct power levels. The output after recombination is amplified by a 5W rf-amplifier (*D. Fischer Elektronik*) and fed to a  $\lambda/4$  antenna which couples the signal onto the rf electrodes of our ion trap.

TTL 13	TTL 14	signal
0	0	none
0	1	full signal
1	0	attenuated signal
1	1	none

Table 4.4. – Truth table for the two-switch configuration used for toggling between full rf- and attenuated rf-signal. The two switches are controlled by the Paulbox TTL outputs 13, and 14, respectively.

#### 4. *Laser apparatus*

## 5. Experimental control

### 5.1. Introduction

We have an elaborate experimental control and data acquisition system which meets the following requirements: It is able to generate laser pulses adjustable with respect to frequency, phase, and amplitude at a time resolution of down to 10 ns. It provides a language which allows us to compose programs to control experiments consisting of hundreds of individual  $\mu\text{s}$ -long laser pulses. These typically milliseconds-long programs can be repeated thousands of times with varying parameter sets. It counts TTL pulses from the photomultiplier and writes the experiment outcomes to disk. The experimen-

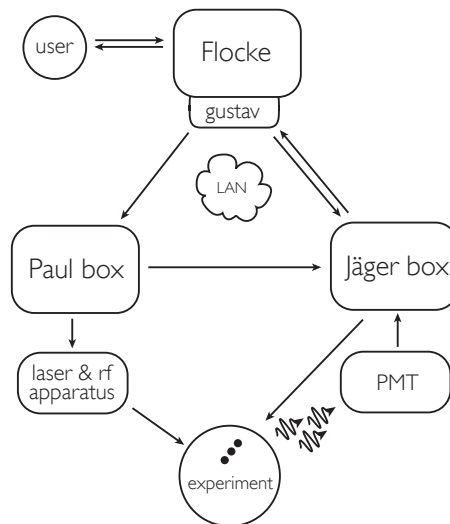


Figure 5.1. – Schematic of experimental control: The user gives commands, starts measurements and receives experiment results via the Flocke software running on the measurement computer gustav. Gustav communicates with the Paul box and the Jäger box via a local area network (LAN). The Paul box controls all laser beams acting on the ions depicted as little circles. The photo multiplier tube (PMT) captures fluorescence photons from the ions and sends TTL pulses to the Jäger box for counting. The recorded number of photons is returned to the Flocke software for analysis.

tal control is a threefold interplay of a pulse sequencer, the so-called *Paul box*, a digital

## 5. Experimental control

signal processor with programmable in- and outputs aka *Jägerbox*, and the *Flocke* software running on the measurement computer *Gustav*. The Paul box contains a field programmable gate arrays (FPGA) and controls four direct digital synthesis (DDS) boards which act as sources for AOMs and provides TTL signals to switch AOMs and trigger the photomultiplier. The *Jäger* box, based on a digital signal processor provides dc-voltages for the trap electrodes and counts TTL pulses from the photomultiplier.

The diagram in Fig. 5.1 visualises all interactions of the components constituting the experiment control. A short overview is given during the next sections, more detailed considerations can be found in Hector Schmitz's [111] and Lutz Petersen's thesis [99].

## 5.2. Hardware

### 5.2.1. Data acquisition and digital-analog interface

The *Jäger* box is a commercial product by *Jäger Meßtechnik, ADWin Gold*. It has six analog outputs and 32 configurable digital inputs and outputs and an event input which allows for external triggering. Five analogue outputs, amplified to up to 100 V by home-built HV amplifiers (see section 2.2), control the dc-voltages of the trap. The outputs have a resolution of 16 bits and can be adjusted on microsecond time scales. Within this thesis, we keep these voltages fixed during experiments, they are varied for loading ions, transferring ions from the loading zone to the experimental zone, for micromotion compensation, or changing inter-ion distances. During the detection process of an experiment, it counts TTL pulses generated by the photomultiplier upon detection of fluorescence photons. The number of detected photons is passed on to the measurement computer which analyses and displays the results of the experiments.

### 5.2.2. Pulse sequencer

The Paul box takes in an even more important role in the experimental control. It controls all laser beams and rf-fields acting on the ions, switches them on and off and for some of the Raman laser beams it controls frequencies, amplitudes and phases. Paul Pham who used to be a master's student from the group of Ike Chuang built this box for us, thus the name of the device. It is based on a FPGA (*Altera, Cyclone*) clocked at 100 MHz and able to execute commands on a 10 ns time scale. Simple commands as TTL switching is actually carried out on that time scales, more complex tasks such as changing frequencies of laser beam take several clock cycles. It controls 16 TTL output channels which mostly trigger rf-switches controlling AOMs to switch on and off laser beams or radiofrequency pulses. It also triggers the event input of the *Jäger* box to start and stop counting TTL pulses from the photomultiplier.

Its main task is to control four direct digital synthesis (DDS) boards (*Analog devices*

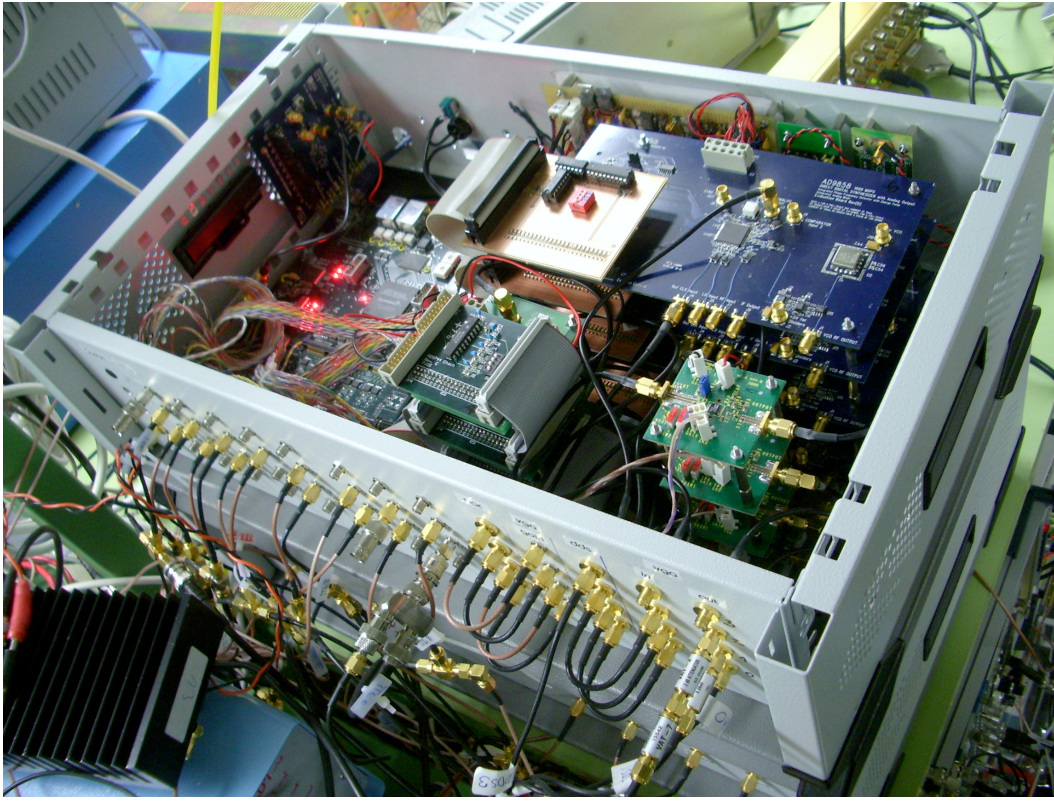


Figure 5.2. – Photograph of the Paulbox: The stacked blue boards in the upper right hand side are the DDS boards, the smaller boards in the lower right hand side contain the variable attenuators and the larger board on the left hand side is the FPGA-board.

9858) serving as oscillators both controllable in frequency and phase. The DDS boards are clocked at 1.1 GHz by a *Rohde und Schwarz* reference oscillator. The clock signal for the Paul box at 100 MHz is also derived from the identical oscillator via a 1:11 signal divider (*Analog devices 9515 evaluation board*) to eliminate phase jitter. The amplitude of the output oscillation of the DDS board is fixed, therefore, we need an additional<sup>1</sup> digital-to-analogue-converter (DAC) which controls a voltage-variable attenuator. For simplicity, we will refer to these two elements as “DAC” for the rest of the thesis. The characteristics of the DACs are plotted in Fig 5.3.

**Software** Paul provided us with a Python compiler which was supposed to translate commands to the binary language of the Pulse Control Processor (PCP) software of the

<sup>1</sup>The DDS board already incorporates a digital-to-analogue-converter in order to generate an analog output signal.

## 5. Experimental control

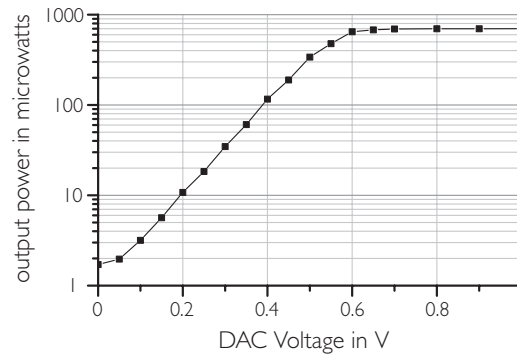


Figure 5.3. – Output power of the voltage-variable attenuator in microwatts plotted versus the applied voltage (supplied by the DAC). The plot shows the exponential amplitude characteristics of the output signal of the DAC with respect to the applied voltage. At a voltage of 0.6 V the output amplitude saturates. The DAC shows a residual signal for zero applied voltage. Therefore, we use an additional rf-switch subsequently to the DAC to be able to completely switch off laser beams.

FPGA. However, it was not sufficiently fast. Lutz Petersen, a former diploma student in our group, implemented a new compiler based on C/C++ language which for large pulse programs led to a speed-up of a factor 2000 compared to Paul's. This compiler processes human-readable intuitive commands, the so-called `1xx` code, see Fig. 5.5 for an example.

### 5.3. Flocke software

The Flocke software has been developed by Hector Schmitz and is named after the german word for snowflake since at the day he started programming the first snowflakes of the year came down. The software is written in *python*, since this was the language the whole Paul box was supposed to work with. The adaptation of a different compiler language took place after the first versions of the software had already existed.

It features a graphical user interface based on GTK and is easily portable to any platform. The software incorporates different sections for loading and shuttling ions, micro-motion compensation, carrying out experiments, and analysing outcomes. A screenshot of the Flocke software is depicted in Fig. 5.4. Experimental subroutines are implemented to simplify the experiment code, for example, for Doppler cooling and sideband cooling, which are used for almost every experiment, one only needs to call the subroutine *cool*. The software displays graphs of measured data and offers fitting routines for further analysing measurements. To discriminate the states of multiple ions it features a histogram section, where photon number distributions are created by binning numbers of

experiments with distinct photon numbers. By fitting reference histograms to the measured curves, we can discriminate between different states of several ions. This process is in detail considered in section 9.

**Example of a pulse program** Each experiment is defined by a pulse program written in python and `1xx` code. The overall structure of a pulse program including loops and subroutines is written in python, whereas the commands which are passed on to the FPGA of the Paul box are formulated in `1xx`. Python commands are written in standard font, whereas `1xx` code is written in typewriter font. We will exemplarily discuss one distinct program to get an idea of the general structure of a pulse program. We will not go into details of distinct commands here, please refer to the aforementioned theses.

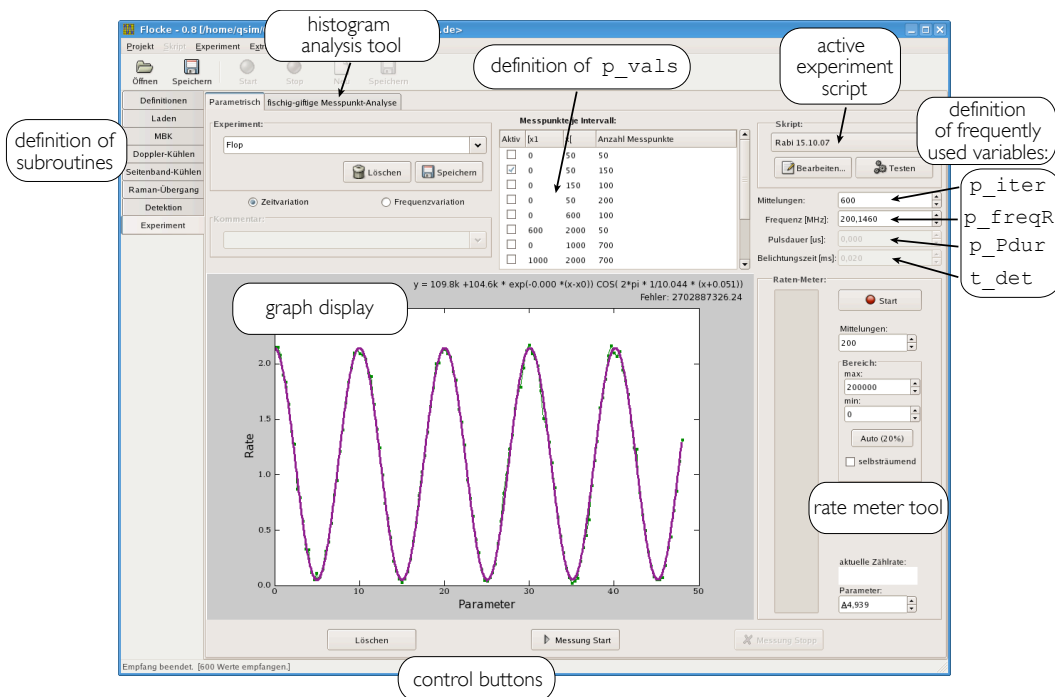


Figure 5.4. – Screenshot of the Flocke software: The display showing recorded measurement data, in this case a radiofrequency flopping curve, takes up the lower half of the program window. Above, starting from the left hand side, there is a register card menu where subroutines are defined. In the next frame a category of experiments is chosen. The next frame shows a set of parameter intervals `p_vals` which can be activated for the running variable `x`. In the next box, one can choose experiment scripts and define frequently used variables such as frequency, pulse duration, or number of experiment iterations. Below, a *real time* rate meter, similar to an analogue indicator, allows for optimisation tasks like increasing overlap of beams with the ions.

## 5. Experimental control

```

#Initialisation ← comment
~Init(pb_dds1f,pb_dds2f,pb_dac0,pb_dac1,pb_dac2) ← invocation of lxx environment,
                                                    variables are passed on to this section
    dds1.frequency=pb_dds1f
    dds2.frequency=pb_dds2f
    ddsX.update()
    dac0=pb_dac0
    dac1=pb_dac1
    dac2=pb_dac2
} ← frequency and DAC values are set
]~ ← end of Init environment

#Experiment part
for x in p_vals: ← repeat experiment for all values defined in array p_vals
    p_PdurHalf=p_Pdur/2 ← definition of variables
    t_wait=15 us
    ~[(p_iter,p_freqR,t_wait) ← invocation of lxx environment
      loop(p_iter){ ← repeat experiment p_iter times
        #preparation
        cool() ← invoke cool subroutine

        #experiment
        dds3.phase=0 ← initialise phase of subsequent pulse
        dds3.update()

        RamanPulse(p_freqR,p_PdurHalf) ← invoke RamanPulse subroutine
                                         with given parameters
        wait t_wait ← wait for 15 microseconds

        RamanPulse(p_freqR,p_Pdur) ← invoke RamanPulse subroutine
        wait t_wait ← wait for 15 microseconds

        dds3.phase = x ← change phase to x
        dds3.update()
        RamanPulse(p_freqR,p_PdurHalf) ← invoke RamanPulse subroutine

        #detection ← invoke detection subroutine
        subs det

      } ← close loop
    ]~ ← close lxx environment

```

Figure 5.5. – Example of program code: the actual program code is printed in typewriter font, whereas explanations are written in sans serif. See Fig. 5.4 for the main program window where variables are set. The structure of the program is further explained in the text.

The program code in Fig. 5.5 generates the pulses for a Ramsey experiment including spin-echo (see next chapter). Relevant experimental parameters are set in the Init(ialisation) part which begins with the sequence `~Init[(var)` which is followed by `lxx` code. The variable `var` in round brackets is passed on to the respective section. Changes of frequency or phase of DDS-boards require an update command `ddsX.update()` to

address all DDS-boards, or `dds3.update()` to address DDS-board number 3. Variables used in the Init part, such as frequency and DAC values, are globally defined in an initialisation mask, so that changes affect all programs. The subsequent experimental part consists of two loops: the inner loop repeats the experiment `p_iter` times for each distinct parameter set, whereas the outer loop changes the parameter set within the interval defined by `p_vals` in the main program window. Each experiment starts with a cooling subroutine, which includes Doppler-cooling and sideband-cooling, if activated via a switch in the sideband cooling register.

The actual experiment starts with a  $\pi/2$ -pulse initialising the phase with respect to subsequent Raman pulses (`dds3.phase=0`). After a duration `t_wait`, the spin-echo  $\pi$  pulse at identical frequency but twice the pulse duration follows. After another duration `t_wait`, a  $\pi/2$  pulse shifted in phase with respect to the previous pulses by `x`, finalises the experiment. We vary `x` within the interval `p_vals=[0..2 $\pi$ [` for this experiment. After this sequence of laser pulses, the detection subroutine is invoked. All subroutines are defined and altered in register cards on the main program window on the left hand side of Fig. 5.4. Two important variables, `p_freqR` and `p_Pdur`, which appear in almost every pulse program, can be entered directly via the main program window. All pulse programs are structured similar to this code, mainly differing by laser pulse sequences. The experiment is started by pushing the button *Messung starten* on the main program window. Measured data points are immediately displayed in the graph display. After the end of a measurement, various functions can be fitted to the measured data.

## 5. *Experimental control*

**Part III.**

**Experimental tools**



## 6. Basic Experiments and Optimisation

During this chapter we will take a closer look at basic procedures and experiments which we use to operate and optimise our experiment on daily basis. It starts with the procedure of loading ions, continues with their transfer to the experimental zone and compensation of micromotion. Subsequently, we explain basic experiments to maximise operational fidelities, such as maximising beam overlap, fine-tuning beam polarisation, and optimising detection efficiency.

### 6.1. Loading ions

For successful loading of a single or several ions, we have to provide sufficient radial and axial confinement for the ions. We adjust the radio frequency power level of the ion trap to  $P_{rf} \cong +42$  dBm which corresponds to an effective trap voltage of  $U_{eff} \approx 800$  V. We apply the following dc-voltages to the respective electrode segments  $U_{Ra} = U_{LRi} = 10$  V and  $U_Z = 0$  V and the micromotion compensation electrode  $U_{ou} = 0$  V (see Fig. 2.4 for nomenclatura). These voltages provide an axial confinement of  $\omega_z \approx 2\pi \times 400$  kHz. We apply the photolaser at a wavelength of  $\lambda = 285.296$  nm and a laser beam power of  $P_{photo} > 400$   $\mu$ W. We adjust the frequency of the cooling laser BD, roughly at  $2\pi \times 500$  MHz red detuned with respect the BD resonance at a laser beam power of  $P_{BD} > 100$   $\mu$ W and heat one of the atom ovens at a current of  $I_{oven} \approx 2.2$  A. It typically takes about one minute until the first ion is captured, further ions follow within tens of seconds. As soon as the required number of ions is captured, we quickly shutter the photo-ionisation laser beam and switch off the atom oven.

### 6.2. Transferring ions to the experimental zone

After loading, we transfer the ions from the loading zone to the experimental zone in a fully automated way. By pressing a single button, the Flocke software causes the Jäger box to successively change the dc-voltages applied to the segmented trap electrodes. After 500 infinitesimal voltage steps, the ions arrive in the experimental zone. The process takes about 11 s for a distance of roughly 8 mm. We can also separate strings of ions by decreasing the axial confinement and then ramping up the voltage applied to the central electrodes to cut a string into two parts [111]. One could further extend this scheme by loading a reservoir of ions into the loading zone and transferring a distinct

## 6. Basic Experiments and Optimisation

number of ions to the experimental zone when needed (for example if a photochemical reaction led to a “dark ion,” see section 2.3).

### 6.3. Compensation of micromotion

Once the ions have arrived in the experimental zone, we increase the axial confinement to a desired value, typically  $\omega_z = 2\pi \times 2.1$  MHz, which corresponds to dc-voltages  $U_{\text{Ra}} \approx 62$  V,  $U_{\text{LRi}} \approx 34$  V,  $U_z = 0$  V. Due to the change of confinement, we have to compensate for micromotion, see section 2.1. There are several schemes for compensating the radial micromotion of the ions:

- Changing the radial trap voltages should not displace the ion’s position.
- Tuning the cooling laser to a motional sideband and minimising the fluorescence.
- Minimising the correlation between fluorescence count rate and trapping rf.

Compensation of micromotion is explained in more detail in the theses of my colleagues Hector Schmitz [111] and Lutz Petersen [99], we solely sketch the principles of the last mentioned method. We analyse the correlation between the emission of photons of the ion and the driving rf, known as “cross-correlation” technique [9]. The frequency components of the micromotion are (multiples of) the drive frequency  $\Omega_D$  of the trap, see section 2.1. Due to first-order Doppler shift of the oscillating ion the fluorescence is modulated. This modulation of the photon detection statistics is analysed via a time-to-amplitude converter (TAC). The TAC is triggered upon the detection of a photon and measures the time until the trap drive frequency has a (negative) zero crossing<sup>1</sup>. The measured signal is converted to digital, binned and plotted in a histogram, which shows the modulation of fluorescence over one rf period. We observe a flat histogram, if the ion exhibits no micromotion. Otherwise, we observe a sinusoidal modulation of the count rate. For different spatial directions, we need several beams. We vary the voltages applied to the micromotion compensation electrodes to push the ion into the centre of the trap. To increase sensitivity, we resonantly drive the micromotion by stabilising the frequency of the cooling laser close to a micromotion sideband.

The trapping radiofrequency also has a component which acts in axial direction and affects motional ground state cooling of several ions, see chapter 7. Therefore, the above mentioned dc trap voltages are adjusted in a way, that the ions are located in the axial minimum of the trapping radiofrequency. However, the resulting position does not coincide with the geometric centre of the trap.

---

<sup>1</sup>If we start the TAC with a zero crossing of the drive signal ( $\approx 56$  MHz) the probability that a photon is detected during this cycle is low ( $<200$  kHz).

## 6.4. Basic experiments

### 6.4.1. Frequency scan

The energy difference between the two spin states  $|\downarrow\rangle$  and  $|\uparrow\rangle$  is mainly determined by the hyperfine ground state splitting  $\hbar\omega_0$  of  $^{25}\text{Mg}^+$ . In addition, we have to take into account the quantisation field (see section 2.4) which gives rise to a Zeeman splitting of the sublevels. To allow for high operational fidelities, we have to experimentally determine this energy difference with high accuracy. We apply the so-called *frequency scan*.

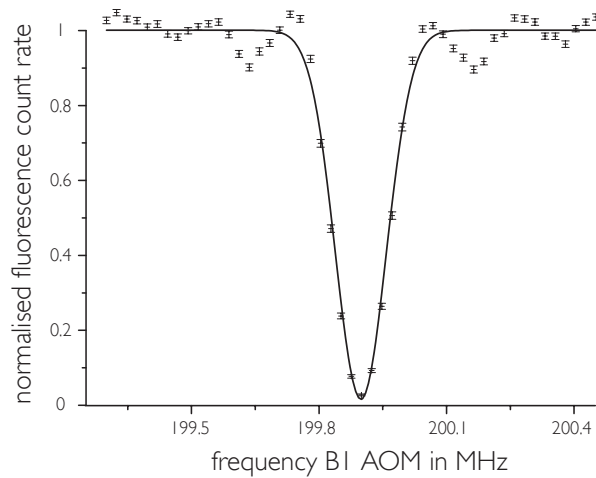


Figure 6.1. – Frequency scan: We plotted the normalised fluorescence after a radiofrequency pulse of constant duration, but variable frequency. At an AOM frequency of  $\nu = 199.90$  MHz the population is resonantly transferred to the state  $|\downarrow\rangle$  with a fidelity of 98%.

We Doppler-cool the ions and optically pump them to state  $|\downarrow\rangle$ . After this initialisation, we apply a laser or radiofrequency pulse of fixed duration<sup>2</sup>  $t_0$  while varying the frequency difference between the Raman beams or the absolute frequency of the rf-transition, respectively, from experiment to experiment. Subsequently, we shine in the detection beam and measure the fluorescence of the ion. Due to the statistical nature of quantum mechanics, we have to repeat each experiment for a few hundreds of times depending on the desired accuracy. We plot the fluorescence count rate versus the frequency of the applied pulse and obtain a constant fluorescence count rate while being off-resonant and a Lorentz-shaped dip in the vicinity of the correct transition

<sup>2</sup>This pulse duration  $t_0$  depends on the laser beam power, beam waist, detuning  $\Delta_R$ , or rf-power level, respectively.

## 6. Basic Experiments and Optimisation

frequency. Fig. 6.1 shows a frequency scan carried out with radiofrequency pulses. We determine the transition frequency by fitting a Lorentzian to the obtained curve. The width of the Lorentzian and therefore the frequency resolution is given by the inverse laser pulse duration:

$$\Delta\nu \propto \frac{1}{t_0} = \frac{\Omega_{n',n}}{2\pi} \propto \frac{\sqrt{I_b I_r}}{\Delta_R}, \quad (6.1)$$

where  $\Omega_{n',n}$  is the Raman Rabi frequency (see section 3.4 and section 8.1) which depends on the intensities of the Raman beams  $I_b$  and  $I_r$  and the detuning of the virtual level  $\Delta_R$ . We can adjust the resolution of a frequency scan by varying the Raman beam intensities. Another way to increase the resolution without changing laser beam powers is discussed in section 6.4.3.

### 6.4.2. Rabi flopping

The supplement to the frequency spectroscopy of the transition is the observation of a coherent transition between the spin states, the so-called Rabi flopping curve. Instead of varying the frequency of the applied pulses, we vary their durations. We ideally obtain a graph of a sinusoidal oscillation between states  $|\downarrow\rangle$  and  $|\uparrow\rangle$ , see Fig. 6.2. The duration

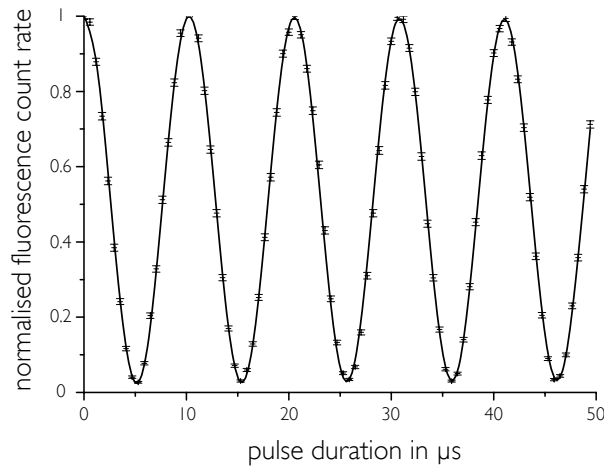


Figure 6.2. – Radiofrequency Rabi flopping curve: The frequency of the applied pulse is kept constant whereas the pulse duration is varied. We see sinusoidal oscillations between the “bright” state  $|\downarrow\rangle$  and the “dark” state  $|\uparrow\rangle$  (see section 3.3). We deduce a  $\pi$ -pulse duration of  $t_\pi = 5.11 \mu\text{s}$ . The contrast of this Rabi flopping curve amounts to 98%.

from the initial fluorescence maximum to the first minimum is labelled  $\pi$ -pulse duration.

### 6.4.3. Ramsey spectroscopy

Ramsey spectroscopy [105] is a versatile tool for diagnostics, optimisation and measurement. The resolution affiliated with spectroscopy using two-photon stimulated Raman transitions is given by Eq. 6.1. Performing e.g. a frequency scan with a  $\pi$ -pulse duration of  $t_\pi = 1 \mu\text{s}$  we obtain a frequency resolution of approximately 1 MHz. We could increase the frequency resolution by lowering the intensity of the Raman beams, thereby increasing the pulse durations. But we can even gain more information by employing Ramsey spectroscopy. We split the  $\pi$  pulse into two “interaction zones” consisting of  $\pi/2$  pulses and introduce a duration  $t_{\text{wait}}$  in between. We obtain a frequency resolution of  $\Delta\nu \propto \frac{1}{t_{\text{wait}}}$  for  $t_{\text{wait}} \gg t_\pi$ .

Before describing the experiment in more detail we express the rotation matrix of Eq. 3.16 in the following way [127]:

$$R(\theta, \phi) = \cos(\theta/2)\hat{I} - i \sin(\theta/2) \cos(\phi)\hat{\sigma}^x - i \sin(\theta/2) \sin(\phi)\hat{\sigma}^y, \quad (6.2)$$

$\hat{I}$  stands for the identity operator and  $\hat{\sigma}^i$  for the Pauli matrices. This rotation matrix describes the evolution of a state vector on the Bloch sphere upon the action of a laser or rf-pulse.  $\phi$  defines the axis of rotation in the x-y plane and  $\theta$  the angle through which the state vector is rotated. In the following, we also use the notation  $R(\theta, \phi)$  when we address two ions instead of  $R_1(\theta, \phi) \otimes R_2(\theta, \phi)$ , since we do not individually address the ions, but the interaction addresses both ions simultaneously.

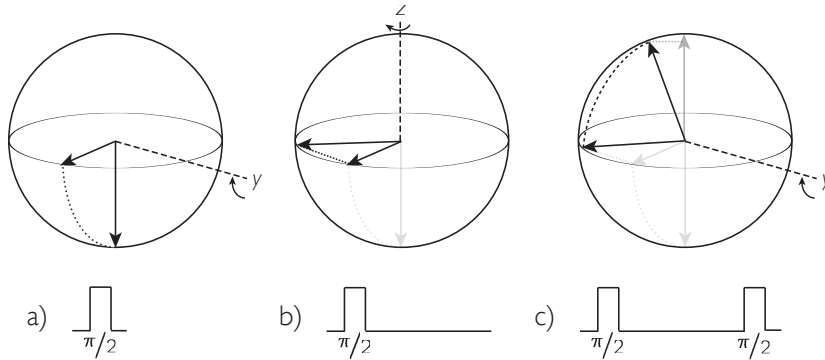


Figure 6.3. – Ramsey experiment visualised on the Bloch sphere: a) The first  $\pi/2$  pulse rotates the state vector from state  $|\downarrow\rangle$  to an equal superposition of  $|\uparrow\rangle$  and  $|\downarrow\rangle$ , leaving the state vector in the equatorial plane. b) In the following duration, the state vector is perturbed due to e.g. magnetic field drifts and rotates about the z-axis. c) The second  $\pi/2$  pulse rotates the state vector about the same axis as the first pulse and cannot return the state vector to the  $|\uparrow\rangle$  state. The loss of contrast is determined from the projection of the final state vector on the  $|\uparrow\rangle$  state.

We apply a resonant  $\pi/2$ -pulse  $R(\pi/2, -\pi/2)$  to a single ion initialised in state  $\begin{pmatrix} 1 \\ 0 \end{pmatrix} \equiv |\downarrow\rangle$

## 6. Basic Experiments and Optimisation

$\begin{pmatrix} 0 \\ 1 \end{pmatrix} \equiv |\uparrow\rangle$ ). The spin system ends up in a superposition of the two spin states  $|\rightarrow\rangle = 1/\sqrt{2}(|\downarrow\rangle + |\uparrow\rangle)$ . During the duration  $t_{\text{wait}}$ , the system oscillates at its own resonance frequency. In the co-rotating reference frame of the Bloch sphere the orientation of the Bloch vector remains constant. The second “interaction zone”, ideally consisting of a pulse identical to the first one, rotates the spin to the state  $|\uparrow\rangle$ . If the resonance frequency of the system varies during an experiment due to fluctuations of magnetic fields or AC-Stark shifts of atomic levels, a phase shift arises between the oscillating spin-1/2 system and the electromagnetic field constituting the second “interaction zone”. In terms of the Bloch sphere picture, the state vector rotates about the z-axis through an angle  $\Delta\phi$ . Thus the final state of the evolution is not  $|\uparrow\rangle$ , but a superposition of  $|\uparrow\rangle$  and  $|\downarrow\rangle$ .

By varying the phase of the second interaction zone we can determine the phase shift  $\phi$  caused by the fluctuation. We can further increase the sensitivity of this method by using the spin-echo technique [5]. If fluctuations act on time scales much shorter than  $t_{\text{wait}}$ , we can refocus the evolution by introducing an additional spin-echo  $\pi$ -pulse at  $t_{\text{wait}}/2$ . This pulse rotates the Bloch vector to the opposite side of the sphere. Now the fluctuation rotates the spin backwards and corrects for the rotation experienced in the first half of the experiment.

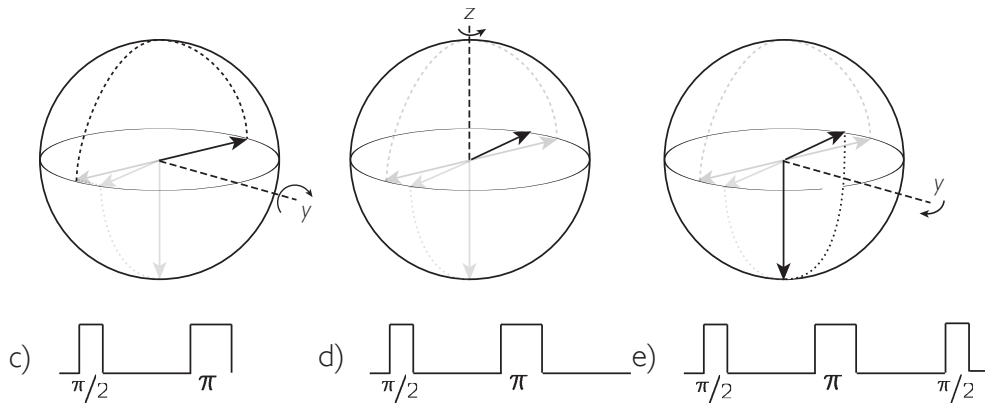


Figure 6.4. – Ramsey experiment including the spin-echo technique: For the first two steps of the evolution refer to Fig. 6.3. c) Differing from the Ramsey experiment we apply an additional  $\pi$ -pulse which rotates the state vector by  $180^\circ$ . d) Given that the perturbation acts on a time scale much slower than our experiment, during the following waiting duration the state vector propagates back along the point-reflected path of b). e) The final interaction zone returns the state vector back to our starting state  $|\downarrow\rangle$ . The error experienced in the first Ramsey “arm” is corrected in the second one.

See Fig. 6.5 for an application of the Ramsey technique in order to increase the sensitivity of a frequency scan. By increasing  $t_{\text{wait}}$ , we obtain more and more narrower

fringes of width  $\Delta\nu = \frac{1}{t_{\text{wait}}}$ , whereas the envelope of the fringe pattern is still given by the inverse of the pulse duration  $t_0$ . To precisely determine the transition frequency, we slightly vary  $t_{\text{wait}}$ , which causes all fringes to shift except for the central fringe of the spectrum.

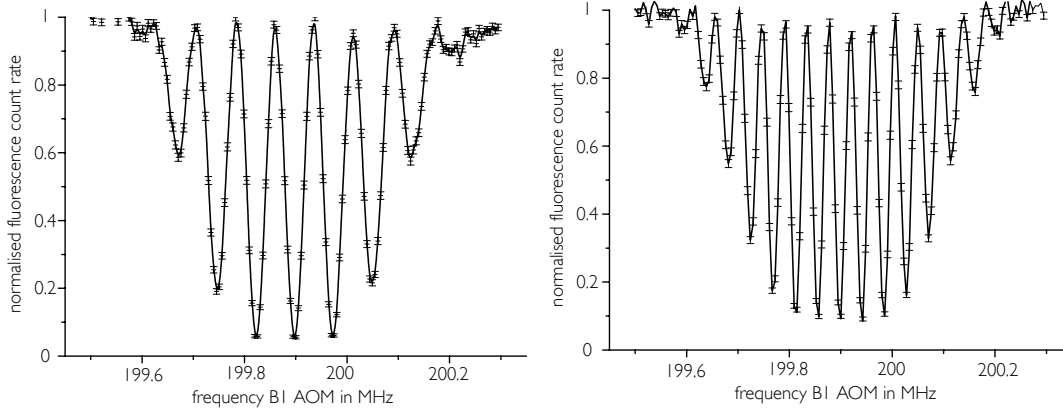


Figure 6.5. – Ramsey frequency scan with spin echo: Similar to Fig. 6.1, these plots show frequency scans recorded with the Ramsey technique including spin-echo for different durations  $t_{\text{wait}} = 20 \mu\text{s}$  and  $t_{\text{wait}} = 40 \mu\text{s}$ , respectively. The Ramsey fringes become sharper with increasing  $t_{\text{wait}}$ . The contrast is mainly limited due to the long detection interval  $t_{\text{det}} = 30 \mu\text{s}$ .

Rabi flopping curves alongside Ramsey spectroscopy can be used as tools for analysing various sources of decoherence, the first three sources are only related to laser-driven transitions:

- Spontaneous emission: in case of two-photon stimulated Raman transitions via the virtual level  $|v\rangle$  which is detuned from the  $^2P_{3/2}$  level by  $\Delta_R$ , there is a probability of *really* populating this state followed by spontaneous emission. This process can lead to a loss of information [96]. Its probability can be reduced by increasing the detuning  $\Delta_R$ . However, we are limited by the available laser beam power in the UV due to the fact that the laser beam intensity has to be increased proportionally with the detuning to achieve comparable couplings.
- Variation of applied laser fields: fluctuations of laser beam power, instabilities of beam pointing and impair irradiation of several ions can lead to varying Raman rates of laser-driven transitions both between different ions and in time. The effect of impair irradiation might also be caused by differential micromotion between ions (see 2.1). Averaging many experiments of different rates, the contrast of the outcome decreases.

## 6. Basic Experiments and Optimisation

- Magnetic field fluctuations can shift atomic levels and related transition frequencies. We actively stabilise the current of our magnetic quantisation field to minimise fluctuations (see section 2.4). Furthermore, we plan to add a circuit to compensate for changes of the ambient magnetic field, e.g. earth magnetic field in the near future [43].

### 6.5. Optimisation

**Fluorescence count rate** After compensating the micromotion, we adjust the beam intensities of the BD, BDX beams to half the saturation intensity (see section 4) and optimise the beam overlap with the position of the ions by maximising the fluorescence count rate detected by the PMT (see section 2.6). In addition, we optimise the polarisation of the beams and finetune the quantisation field via the compensation coils (see section 2.4). The aforementioned beams enter the chamber via the same laser port and therefore pass the same polarisation optics, focussing lens, and last mirrors. We declare the BDX beam, the beam responsible for state-dependent detection (see chapter 9) at the end of the experiment, as “master beam” and finetune its overlap with the ion using a piezo-driven mirror mount which allows more sensitive and reproducible adjustment than the used manual mirror mounts. We optimise the overlap of the other beams (also RD and RP beams, see next paragraph) with the ions for each beam via two mirrors before the respective beamsplitter at which they are superimposed with the BDX beam.

The quarter wave plate, which is used for generating  $\sigma^+$  polarised light out of the linear polarised laser beams has to be adjusted carefully<sup>3</sup>. A contribution of  $\sigma^-$  polarisation allows the electronic population to leave the cycling transition and populate other Zeeman sublevels which are off-resonant with respect to the driven transition. We loose fluorescence count rate and the contrast of Rabi flopping suffers delicately.

**Red Doppler and Repumper beams** For the RD beam we apply the following procedure: we initialise the system in  $|\downarrow\rangle$  and rotate the state vector to the “dark”  $|\uparrow\rangle$  state via a  $\pi$ -pulse. By shining in the RD beam, we resonantly pump the population to the  $^2P_{1/2}$  state, from where it spontaneously decays back to the  $^2S_{1/2}$  state within nanosecond time scales, that is, we optically pump [54] the population to the  $|\downarrow\rangle$  state. We record a series of experiments in which we successively increase the duration  $t_{RD}$  of the RD laser pulse. With increasing repumping duration  $t_{RD}$ , the population is pumped to the  $|\downarrow\rangle$  state, therefore the detected fluorescence signal rises from almost zero to maximum fluorescence. We analyse this “rise time” of the optical pumping process and

---

<sup>3</sup>We have to tilt the quarter wave plate in addition to compensate for manufacturing uncertainties of up to  $\pm 2$  nm of the zero order wave plate in order to achieve maximum fluorescence count rate.

shorten it by optimising the beam overlap with the position of the ion. With optimised beam overlap, 90% of the population should be repumped within less than 500 ns.

To optimise the operation of the RP beam we proceed in a similar way. As before, we apply a  $\pi$ -pulse to prepare the spin system in state  $|\uparrow\rangle$ . Subsequently, we apply another pulse of appropriate frequency and duration to transfer the population to the state  ${}^2S_{1/2} |F = 3, m_F = +1\rangle$ . Shining in the detection beam, the population in this state is also resonantly addressed<sup>4</sup> and we observe bright fluorescence light. We record a series of experiments with stepwise increasing duration  $t_{\text{RP}}$  and optically pump the population to the  ${}^2P_{1/2}$  level, from where it decays to the  $|\downarrow\rangle$  state with a probability of  $\approx 30\%$  or to  ${}^2S_{1/2} |F = 2\rangle$  levels with a probability of  $\approx 70\%$ . In this case, the fluorescence count rate gets reduced from its maximum value to  $\approx 1/3$ . We minimise this “fall time” to optimise the repumping process.

**Stark shift compensation** We also use Ramsey spectroscopy including spin-echo to cancel differential AC-Stark shifts between different Raman beams (see chapter 3.4). Primarily, this is done for mitigating shifts of transition frequencies due to varying Raman beam power levels, which may be caused by fluctuations, but will also be deliberately varied to change effective couplings in chapter 10.2.2.

First, we record a Ramsey experiment without additional pulses for calibration. The related pulse sequence is illustrated in Fig. 6.4. We begin with a  $R(\pi/2, 0)$ -pulse, wait for a duration  $t_{\text{wait}}$ , apply a spin echo pulse, wait for another duration  $t_{\text{wait}}$  and finally apply a final  $R(\pi/2, \phi)$ -pulse of which we vary the phase  $\phi$  within the interval  $[0..2\pi[$ . We obtain an oscillation of the fluorescence count rate in dependence of the phase  $\phi$  of the final pulse. Subsequently, we add two Raman beam pulses with beams R1 and R2, respectively, of equal duration without temporal overlap within one arm of the spin-echo experiment, while we keep the duration  $t_{\text{wait}}$  for both arms constant. In an ideal case, the first pulse rotates the state vector in the co-rotating frame by an angle determined by its beam intensity and polarisation, whereas the second pulse returns the state vector back to its starting point. If there is a differential Stark shift between the beams R1 and R2, the measured curve appears phase-shifted with respect to the calibration curve. We adjust the polarisation of beam R2 with the quarter wave plate in front of the chamber and maximise the overlap with our calibration curve. For fine-tuning we can increase the sensitivity by elongating the Raman pulse durations<sup>5</sup>.

<sup>4</sup>Taking a closer look at this state’s quantum numbers and transition strengths, it should be a “dark” state with respect to the BD transition. The electron has to be scattered several times on weak transitions to get to the  $|\downarrow\rangle$  state. In beryllium, which has a very similar level structure, this property can be used to even better protect electronic population from being off-resonantly pumped out during detection. In experimental contrast, for magnesium the population is scattered out of this state within nanoseconds. The reason for this might be found in a mixing of excited states whose energetic separation is much closer than for beryllium.

<sup>5</sup>To avoid adjusting the phase shift to a multiple of  $2\pi$ , we start with short pulse lengths and step-wise

## 6. Basic Experiments and Optimisation

**Subtleties about measuring trap frequencies** For our experiments, it is important to cancel differential AC-Stark shifts between the Raman beams R1 and R2, which generate dipole forces and give rise to an effective spin-spin coupling (the reason for this will be explained in chapter 8). On the other hand, we need Raman beam R2 together with beam B1 for motional ground state cooling (see chapter 7). Due to technical reasons<sup>6</sup> we cannot compensate differential Stark shifts for both tasks. As a consequence, beam power fluctuations may shift the frequency of transitions and lead to reduced fidelities for ground state cooling. To determine trapping frequencies, we also have to take into account differential AC-Stark shifts. With typical beam intensities on the mW-level and a detuning of the virtual level of  $\Delta_R = 2\pi \times 80$  GHz, transitions appear shifted on the order of  $2\pi \times 50$  kHz. To mitigate this, we determine trapping frequencies with small laser beam intensities (beam powers of the order of 100  $\mu$ W).

**Initial alignment of Raman beams** We can also benefit from the AC-Stark shifts related to the Raman beams for initial alignment of these<sup>7</sup>. Shining in a single Raman beam in a spin-echo experiment with rf-transitions is an extremely sensitive way to detect, if this beam has an overlap with the position of the ion despite its considerable detuning  $\Delta_R = 2\pi \times 80$  GHz from resonance. Contrary to Stark shift compensation, we maximise the AC-Stark shift related to a single Raman beam here by increasing the overlap with the ion.

**Temporal beam overlap and synchronous switching of beams** Both laser pulses constituting a TPSR transition have to impinge the ion at the same time. A single Raman beam irradiating an ion solely causes an AC-Stark shift and can lead to spontaneous emission (see section 3.4). Thus, we have to make sure that the beams are switched on and off synchronously with respect to the position of the ions. The effect of run-time differences of the beams in air is negligible (a difference of 1 m leads a delay of roughly 3 ns) compared to the effect due to the finite speed of the sound wave in the AOM crystals. After switching on an AOM, there is a delay until the laser beam is diffracted to the first order. This delay is proportional to the distance between the piezo-electric transducer and the position of the laser beam traversing the crystal. (for a distance of 5 mm between beam position and transducer the delay  $\Delta t = \frac{5 \text{ mm}}{4.26 \text{ km/s}} = 1.2 \mu\text{s}$  with the speed of sound in the crystal  $v = 4.26 \text{ km/s}$ ). By parallelly displacing the AOMs perpen-

---

increase the spin-echo arm lengths.

<sup>6</sup>In principle, one could employ a UV electro-optical modulator (EOM) into the R2 beamline and compensate AC-Stark shifts dynamically. However, this would lead to additional optical losses and beam quality deterioration.

<sup>7</sup>As we lack an iodine spectroscopy for this laser we are not able to accurately tune the Raman laser close to resonance of the BD transition, furthermore, changing the emission wavelength of the Raman laser to resonance, the beam pointing varies considerably.

pendicular to the beam, we can vary these delays and optimise the temporal beam overlap<sup>8</sup>. Fine-synchronisation can be carried out by introducing waiting durations in the program code of the Flocke software (adjustment possible down to 10 ns, see section 5.1). The same delay occurs when switching off an AOM. Therefore, we implement waiting durations of 2  $\mu\text{s}$  to prevent overlap of laser pulses with rf-pulses which act on the ions within nanoseconds,

**Radio-frequency synchronisation** To carry out experiments with high repetition rates and minimise decoherence during experiments, it is desirable to keep pulses short. On the other hand, we also simulate an effective magnetic field by coherently coupling the states  $|\downarrow\rangle$  and  $|\uparrow\rangle$  and have to be able to vary the amplitude of this coupling (see section 10.2.1). Thus, we use two different radio-frequency power levels realised via a rf-switch setup where the attenuation in one branch is manually variable (see section 4.7). However, the attenuated rf-signal is retarded with respect to the other one, and its retardation depends on the attenuation level. When we use both power levels of rf-pulses within one experiment, we have to determine their relative phase difference. We determine this phase shift via a Ramsey experiment comprising one  $R(\pi/2, 0)$ -pulse with unattenuated signal and one  $R(\pi/2, \phi)$ -pulse of varying phase  $\phi$  with the attenuated signal. At the correct phase difference  $\phi_0$ , the second pulse rotates the Bloch vector to state  $|\uparrow\rangle$ .

---

<sup>8</sup>The UV AOMs feature a horizontal aperture of about 20 mm. The beam should not be too close to the transducer to achieve optimum diffraction efficiency.

## 6. *Basic Experiments and Optimisation*

## 7. Motional ground state cooling

### 7.1. Doppler cooling basics

Employing the mechanical forces of light for cooling atoms or in this case ions has a long history. It was independently proposed by two groups [53, 125] in 1975. There are extensive reviews [34] available, thus, we will not go into theoretical details of Doppler cooling here. The principles are illustrated in Fig. 7.1. We will only comment on our specific

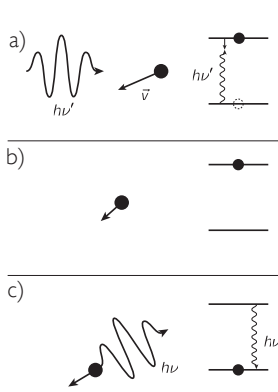


Figure 7.1. – Doppler cooling: a) A photon of energy  $h\nu'$  approaches a two-level system (ion) with a corresponding transition frequency of  $\nu > \nu'$ . The ion is moving towards the photon with velocity  $\vec{v}$ , sees the frequency of the photon Doppler shifted  $\nu'(1 + v/c) = \nu$  and absorbs it, leaving the ion decelerated and in the excited state, as can be seen in b). c) The excited ion decays to the electronic ground state emitting a photon and experiences a recoil with a momentum transfer in opposite direction of emission. The ion loses motional energy by repeatedly absorbing Doppler shifted photons. The additional recoils due to the reemission make the ion undergo a random walk in momentum space.

situation, where the linewidth  $\Gamma$  of our cooling transition  $|\downarrow\rangle \leftrightarrow {}^2P_{3/2} |F = 4, m_F = 4\rangle$  is much larger than the trap frequency  $\omega_z/\Gamma = 0.049 \ll 1$ . This is called the regime of weak confinement. Alternatively, this can also be formulated in terms of time scales: The scattering of a photon takes place much faster than the time the ion requires for an oscillation in the trapping potential. Therefore, the ion can be regarded as *free*. If, otherwise, the trapping frequency was larger than the linewidth of the cooling transition, we could selectively drive motional sideband transitions (see section 3.4) with the Doppler cooling laser and get close to the ground state of motion. We have to include motional sideband cooling in order to reach the motional ground state.

In principle, one needs six cooling laser beams for Doppler cooling a free particle, two counter-propagating beams for each spatial direction. For a trapped particle, the requirements are relaxed and one laser beam which is tilted with respect to all of the trap axes suffices. The minimum reachable *temperature*  $T_{\text{doppler}}$  associated to our ion

## 7. Motional ground state cooling

species amounts to

$$T_{\text{doppler}} \cong \frac{3\hbar\Gamma}{10k_{\text{B}}} \cong 600 \mu\text{K}, \quad (7.1)$$

where  $k_{\text{B}}$  is Boltzmann's constant<sup>1</sup>. We put the term temperature in italics emphasising that we are aware of the problem of speaking of a temperature for a single particle. Assuming a thermal distribution we can relate the ion's *temperature* to a probability of motional state occupation. The stronger the confinement of the trap, the wider is the spacing of the ladder states in the harmonic trapping potential. Refer to Fig. 7.2 for an illustration. Thus the mean motional state  $\bar{n}$  is lower for a steeper trapping

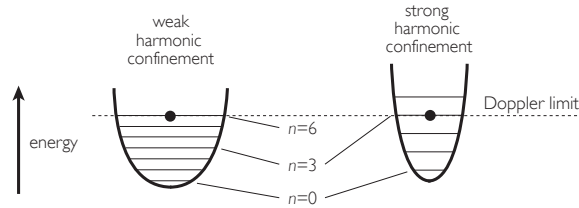


Figure 7.2. – Mean vibrational occupation number of a Doppler cooled ion in two traps of different harmonic confinement. On the right hand side the trapping potential is steeper. This implies, that the secular frequency  $\omega_z$  is larger and so is the spacing between adjacent harmonic oscillator energy levels. Thus for a stronger confinement, the mean motional state  $\bar{n}$  is lower, although both ions have identical *temperatures*.

potential. This results in a smaller amount of required resolved sideband cooling cycles (see section 7.2) to reach the motional ground state. Furthermore, population of motional state  $n > n_0$  is trapped in  $n_0$  and cannot be cooled to the motional ground state. This number  $n_0$  increases with tighter confinement and is discussed in Fig. 7.5.

**Thermal states** The thermal state in which an ion ends up after Doppler cooling is a *classical* mixture of different motional states. It can be characterised by the following density matrix

$$\rho_{nn} = \sum_n P_n |n\rangle \langle n|, \quad (7.2)$$

where  $P_n$  is given by

$$P_n = \frac{\bar{n}}{(\bar{n} + 1)^{n+1}}, \quad (7.3)$$

and  $\bar{n}$  is the mean value of vibrational quanta. Considering an ensemble of  $m$  ions, one will find  $m \times P_n$  ions in the motional state  $n$ , or equivalently, one can consider a single ion on which  $m$  measurements are performed. This differs from a non-classical state

<sup>1</sup>The factor of 3/10 accounts for the dipole emission characteristics [32].

## 7.2. Resolved sideband cooling basics

of motion, where one ion is in a superposition of several motional states, as can be created by e.g. *squeezing* [113, 127].

**Measuring motional states** If an ion is taken down the ladder of vibrational states to the ground state of motion, its red sidebands vanish, whereas the contrasts of the blue sidebands increase. In the motional ground state, which is a Fock state of motion, blue sideband transitions have a well-defined pulse duration and can be driven with high fidelity (section 3.4). We can determine the mean number of vibrational quanta of an ion in a thermal state out of the ratio of contrasts  $c_i$  of the Rabi flopping curves of both red (r) and blue (b) motional sidebands [65]:

$$\bar{n} = \frac{c_r/c_b}{1 - c_r/c_b}. \quad (7.4)$$

## 7.2. Resolved sideband cooling basics

We recall the Hamiltonian discussed in chapter 3.4 which describes red sideband transitions

$$H_{\text{rsb}} = \hbar\Omega\eta(\sigma^+ a + \sigma^- a^\dagger). \quad (7.5)$$

We adjust the frequency difference of the two orthogonal Raman laser beams to  $\delta = -\omega_z$  and apply a  $R(\pi, 0)$ -pulse to an ion initialised in state  $|\downarrow\rangle$ . We observe the following transition

$$|\downarrow\rangle |n\rangle \leftrightarrow |\uparrow\rangle |n-1\rangle. \quad (7.6)$$

The ion ends up in the  $|\uparrow\rangle$  state with the mean phonon number reduced by one. For each motional state  $n$  the Rabi frequency is different, obeying

$$\Omega_{n,n-1} = \sqrt{n}\eta\Omega_{0,0}. \quad (7.7)$$

To complete one cycle of resolved sideband cooling, we optically pump the population back to the  $|\downarrow\rangle$  state on average without affecting the mean motional state. Refer to Fig. 7.3 for an illustration. Within the Lamb-Dicke regime, a change of the vibrational state during a spontaneous emission is unlikely due to energy conservation [89]. However, a Doppler cooled ion trapped in an axial confinement related to an axial frequency  $\omega_z = 2\pi \times 2.1$  MHz is not yet within the Lamb-Dicke regime<sup>2</sup>.

The RD beam (see section 4.6.2) resonantly transfers the electron to the  ${}^2P_{1/2}$  state, from where it spontaneously decays to the  ${}^2S_{1/2}$  state on a nanosecond time scale. Decaying to the  $|\downarrow\rangle$  state, the RD does not address the electron anymore due to its  $\sigma^+$  polarisation and the absence of a  $m_F = +4$  state in the  ${}^2P_{1/2}$  manifold. Only one

<sup>2</sup>The Lamb-Dicke criterion  $\sqrt{\bar{n}}\eta \ll 1$  is not fulfilled,  $\sqrt{\bar{n}}\eta \approx \sqrt{10} \cdot 0.325 \approx 1.03$ .

## 7. Motional ground state cooling

scattering event has occurred. If the electron decays to the  $F = 2$  manifold, it is again transferred to the  ${}^2P_{1/2}$  state and gets another possibility of decaying to the  $F = 3$  manifold. Still, there is a possibility that it decays to the level  ${}^2S_{1/2} |F = 3, m_F = +2\rangle$ .

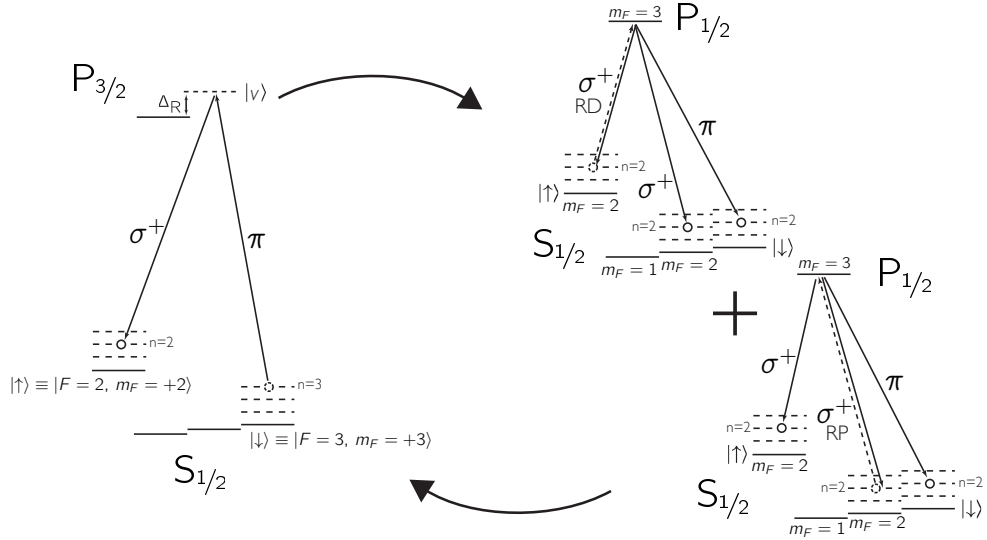


Figure 7.3. – On the left hand side we can see a red sideband transition transferring the population from state  $|\downarrow\rangle |n = 3\rangle$  to  $|\uparrow\rangle |n = 2\rangle$ , reducing the motional state  $n$  of the ion by one. On the right hand side we repump the population to the  $|\downarrow\rangle$  state by the help of the Red Doppler (RD, upper schematic) and repumper (RP, lower schematic) beams. The action of the beams RD and RP are depicted with dashed lines, whereas the possible decay channels are depicted with solid lines. Details about the repumping processes can be found in the text.

The population in the state  ${}^2S_{1/2} |F = 3, m_F = +2\rangle$  would be lost for the next cycle of sideband cooling, if we did not pump it back into our spin system. We use the Repumper beam (RP, see section 4.6.2) which addresses the  ${}^2S_{1/2} |F = 3, m_F = 1, 2\rangle \rightarrow {}^2P_{1/2}$  transition. From there it might again decay to the  $F = 2$  manifold and we need to invoke the RD beam once more. We optically pump the electronic population back to the  $|\downarrow\rangle$  state by iteratively applying pulses of the RD and RP beams. A different realisation is to shine in both beams synchronously.

The complete cycle is repeated and the ion iteratively descends the ladder of harmonic oscillator states. For each red sideband pulse we have to adjust the pulse duration according to Eq. 7.7. Ideally, we reach the recoil limit

$$\bar{n}_{\min} \approx (\gamma_{\text{rad}}/2\omega_z)^2, \quad (7.8)$$

where  $\gamma_{\text{rad}}$  is the radiative line width of our TPSR transition which is given by the

### 7.3. Experimental implementation of ground state cooling

inverse pulse duration. With an axial trap frequency of  $\omega_z = 2\pi \times 2.1$  MHz and a radiative linewidth of the order of  $2\pi \times 1$  MHz for typical Raman beam intensities and detuning, we obtain the numerical value  $\bar{n}_{\min} \approx 0.013$ . However, in reality we have to take into account the heating rate of the ions in the trap (see section 7.4) and end up in a thermal equilibrium.

## 7.3. Experimental implementation of ground state cooling

As a preface for the following chapters which include experimental measurements, we would like to mention, that all measurements within this thesis have been carried out using a frequency doubled Coherent dye laser as source for the Raman laser beams as a replacement for a defective fibre laser. Frequency shifts of the dye laser (for a thorough analysis see ref. [51]) are translated into intensity fluctuations by resonant frequency doubling and negatively affect all measurements. Although we use a noise eater for intensity stabilisation, the laser system exhibits fast intensity fluctuations on the  $\mu\text{s}$ -timescale which we cannot compensate due to limited servo bandwidth. With a fibre laser as a source for the Raman beams, due to its inherently more frequency- and intensity-stable output, the achievable contrasts should be even higher.

### 7.3.1. Doppler cooling

Sufficient Doppler pre-cooling is inevitable for efficient ground state cooling of the motional degrees of freedom as discussed in section 7.1. Optimum Doppler cooling for already pre-cooled ions in our experiment is achieved at a detuning of half a natural linewidth  $\Gamma/2$  ( $\Gamma = 2\pi \times 42.7$  MHz) red of the transition frequency at half of the saturation intensity [127]. If an ion suffers a collision with background gas or electronically excited to some other state and decays to one of the  $^2S_{1/2} |F = 2\rangle$  levels, the electron is lost from the cycling transition, therefore the ion is not cooled anymore. Ions which suffer collisions with background gas for example are in general too hot and have to be efficiently recooled by a further red detuned and accordingly stronger laser beam, the BDdet beam. The BDdet is mainly responsible for cooling hot population to a regime, where the BD beam can further reduce the temperature to reach the Doppler limit. The main characteristics of the involved beams are summarised in Table 7.1.

To initialise an experiment, we shine in the BD and the BDdet beams simultaneously. The ions are cooled efficiently and off-resonantly repumped to the  $F = 3$  manifold due to the high intensity of the BDdet beam. Shining in both beams BD and BDdet also has a negative side effect. The off-resonant BDdet beam induces an AC-Stark shift of the order of  $2\pi \times 10$  MHz depending on the exact power level, which shifts the resonance of the cycling transition to higher frequencies and therefore diminishes the cooling efficiency of the BD beam. To circumvent this, we shine in the beams BDdet

## 7. Motional ground state cooling

beam	intensity	detuning	TTL channel
BD	$1/2 I_{\text{sat}}$	$1/2 \Gamma$	1
BDdet	$(10 - 20) \cdot I_{\text{sat}}$	$10 \Gamma$	2
RD	$1/2 I_{\text{sat}}$	$1/2 \Gamma$	6
RP	$1/2 I_{\text{sat}}$	$1/2 \Gamma$	5

Table 7.1. – Blue Doppler beams: The first column labels the different beams, the second denotes their intensities in multiples or fractions of the saturation intensity  $I_{\text{sat}} = 255 \frac{\text{mW}}{\text{cm}^2}$ , the third column states the detuning from the resonance frequency of  $^{25}\text{Mg}^+$ , and the last column labels the TTL channel by which they are controlled.

and BD for about 2 ms, and finally switch off BDdet and apply the RD beam for 10  $\mu\text{s}$ . The RD beam repumps resonantly and does not give rise to a considerable AC-Stark shift. Fig. 7.4 shows the carrier and motional sideband spectrum of a single Doppler cooled ion.

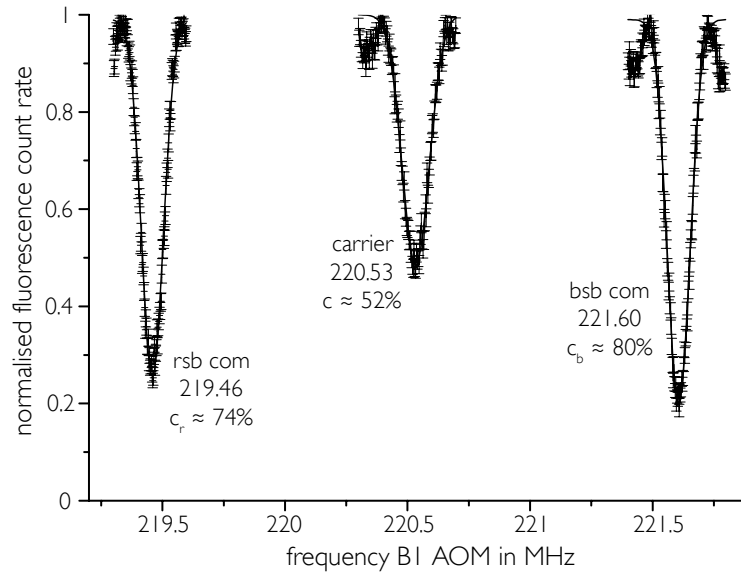


Figure 7.4. – Axial motional sideband frequency spectrum of a single ion. The abscissa shows the frequency of the double-passed frequency shifter AOM B1. To derive the axial trapping frequency  $\omega_z = 2\pi \times 2.14 \text{ MHz}$ , we have to double the frequency difference between carrier and first sidebands. Due to the statistical mixture of states of different  $n$ , the contrasts are limited. From the contrasts of the sidebands, we deduce a mean phonon number for the thermal state of about  $\bar{n} = 12.8 \pm 3.8$ . Each data point represents an average of 500 experiments.

### 7.3.2. First sideband cooling

We measure the frequency of the red sideband transition by performing a frequency scan (see section 6.4.1) in the vicinity of  $\omega_{\text{carrier}} - \omega_z$ . The required pulse durations for addressing different motional states  $n$  are calculated using Eq. 3.13. Relative Rabi frequencies for carrier transitions, first sideband and second sideband transitions for different motional states  $n$  are plotted in Fig. 7.5 for typical experimental conditions. The carrier Rabi rate  $\Omega_{0,0}$  of a ground state cooled ion ( $n = 0$ ) for orthogonal Raman beams is about 5% smaller than for a transition driven with collinear beam (Co-carrier) due to the Debye-Waller factor<sup>3</sup> for the same experimental parameters. The relative

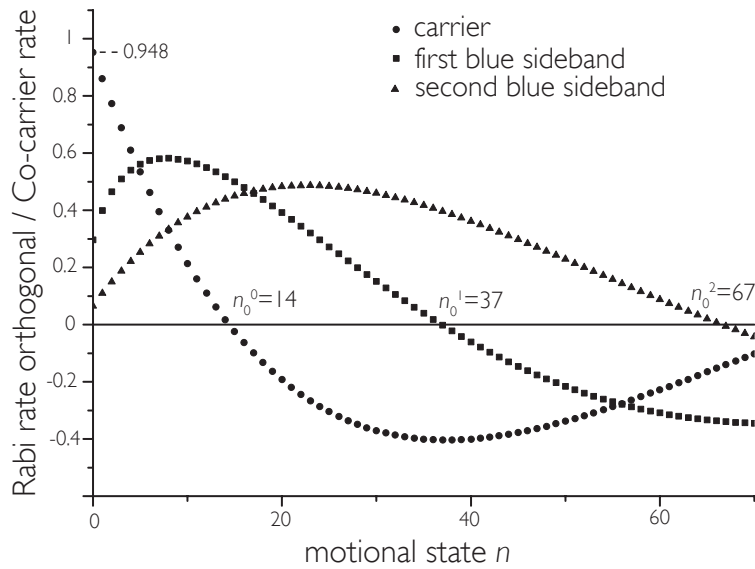


Figure 7.5. – The plot shows the relative Rabi frequencies for orthogonal carrier transitions (depicted as circles), first (squares) and second (triangles) sideband transitions for different motional states  $n$ . The values are calculated for an axial trapping frequency of  $\omega_z = 2\pi \times 2.11$  MHz. For  $n = 0$  the pulse duration for a sideband transition is 3 times longer than the carrier transition. We notice distinct zero-crossings of the Rabi frequencies. See text for details. For higher trap frequencies the zero-crossings shift to higher  $ns$ .

Rabi frequencies for both carrier transition and motional sidebands become zero for a distinct motional state  $n$ . The zero crossing for the first sideband takes place at  $n_0^1 \approx 37$ , implying that the pulse time for  $n = 37$  becomes infinite and we cannot reduce the motional state for the population with  $n > 37$ . This part of the population

<sup>3</sup>see section 3.4,  $\Omega_{0,0} = \Omega e^{-\eta^2/2} = .948$  with a typical value for the Lamb-Dicke parameter  $\eta = 0.32$ .

## 7. Motional ground state cooling

gets trapped in  $n = 37$ . Applying a pulse  $R(\pi, 0)$  on the red sideband with a pulse duration adapted to the transition  $|n = 30\rangle \rightarrow |n = 29\rangle$  does not only transfer the population between the above declared levels. The population in adjacent levels is also partially transferred. A pulse protocol for resolved sideband cooling is depicted in Fig. 7.6. We analyse the results of this cooling scheme and obtain red sideband contrasts

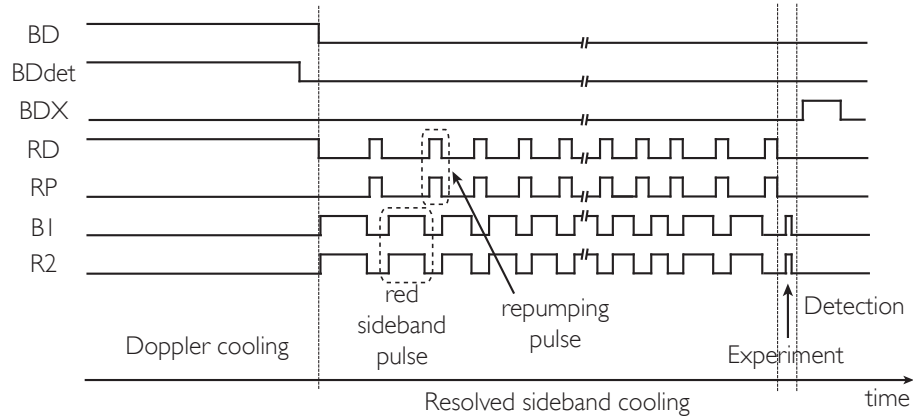


Figure 7.6. – This figure depicts the pulse protocol of a typical experiment including sideband cooling. The time axis is not to scale. We begin with Doppler cooling (see text). A resolved sideband cooling stage follows consisting of red sideband transitions with variable pulse times according to Eq. 3.13 in turn with repumping pulses of  $5\mu\text{s}$  duration (RD and RP synchronously). After the last repumping block a simple experiment follows, in this case a Rabi flop on the orthogonal carrier (the indicated experiment pulse duration is considerably shorter than the sideband transitions). The detection finalises the experiment. The experiment is repeated hundreds of times to obtain sufficient statistics.

of  $c_r < 4\%$  and blue sideband contrasts of above  $c_b > 90\%$  which corresponds to a mean occupation numbers of  $\bar{n} < 0.05$  using Eq. 7.4. However, we notice a residual beating of the Rabi flopping curve of the carrier. The first and third flopping minima show contrasts of about 86% whereas the second and fourth minima show contrasts of about 90%. By increasing numbers of cooling pulses (addressing motional states up to the trapping state  $n_0^1 = 37$ ), repeating each cycle up to three times, increasing repumping durations, or improving beam overlaps with the position of the ion we are not able to overcome this beating. We suppose, that it is due to the motional state population above the trapping state  $n_0^1 = 37$ . We extend our scheme with second sideband cooling.

### 7.3.3. Second sideband cooling

We are able to gain access to higher excited motional states by employing second sideband cooling. The zero-crossing of the relative Rabi frequency for the second motional sideband occurs at  $n_0^2 = 67$  (compared to  $n_0^1 = 37$  for the first motional sideband, see Fig. 7.5). For motional states  $n > 17$  the relative Rabi frequency of the second blue motional sideband becomes larger than that of the first sideband (see Fig. 7.5, this holds true up to  $n = 50$ ). Thus we annihilate two phonons per cooling cycle within a shorter duration compared to one cycle of first sideband cooling. Solely

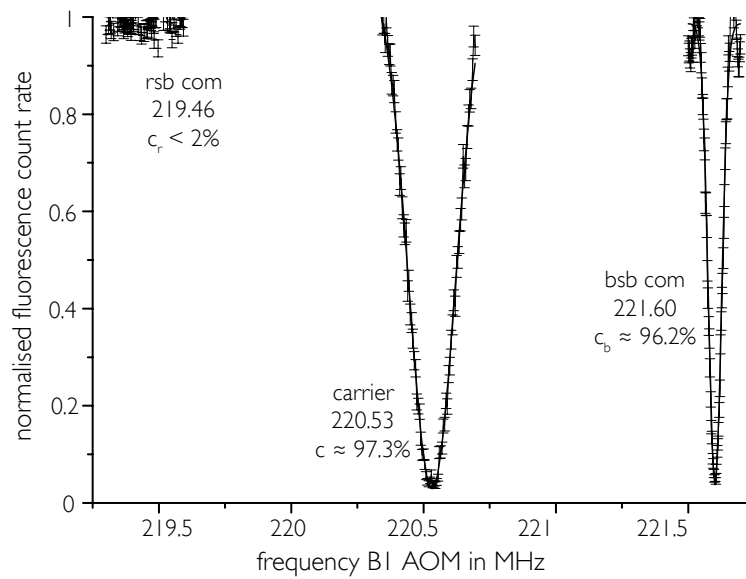


Figure 7.7. – Axial motional sideband frequency spectrum of a ground state cooled single ion. The red sideband vanishes completely and the contrasts of the carrier and the blue sideband are augmented. Due to a factor of three shorter pulse duration, the carrier appears a factor of three wider than the blue sideband. The contrasts amount to 97.3% for the carrier and 96.2% for the blue sideband. We deduce a motional state occupation number of  $\bar{n} < 0.02$ . Each measurement point corresponds to the mean value of 1000 experiments.

applying second sideband pulses we end up with the largest part of the population in the motional ground state  $n = 0$  but in addition a considerable amount in  $n = 1$ , since the population is transferred from the motional states  $4 \rightarrow 2$ ,  $3 \rightarrow 1$ ,  $2 \rightarrow 0$ , but left in motional state  $n = 1$ . We can apply one single additional cycle of first sideband cooling which transfers the population from  $n = 1$  to the motional ground state.

For motional states  $n < 6$  the relative Rabi frequency for the second motional side-

## 7. Motional ground state cooling

band drops below half of the Rabi frequency of the first motional sideband. An efficient scheme is to apply 20 cycles of second sideband cooling, starting with  $n = 27$ , and subsequently  $2 \times 6$  cycles of first sideband cooling starting with  $n = 6$ , where we repeat each cycle. We achieve a mean phonon number of  $\bar{n} \leq 0.02$ . See Fig. 7.8 for an orthogonal carrier Rabi flopping curve. The initial contrast amounts to 95.5% and could be

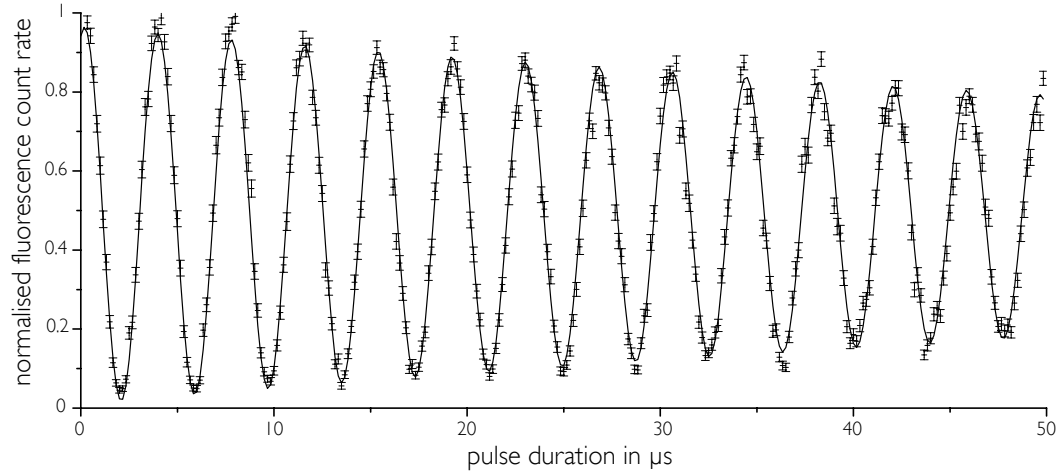


Figure 7.8. – Rabi flopping curve of a single ion cooled to  $\bar{n} < 0.02$  on the orthogonal carrier. The solid line depicts a damped cosine function fitted to the experimental data. The initial contrast amounts to 95.5%. Each data point corresponds to an average of 1000 experiments. Decoherence effect diminishing the flopping contrast are discussed in section 6.4.2.

further increased by reducing the detection interval  $t_{\text{det}} = 20 \mu\text{s}$  (see section 9.2). The decoherence, the reduction of the amplitude, could be further minimised by increasing the detuning  $\Delta_R = 2\pi \times 80 \text{ GHz}$  of the virtual level  $|v\rangle$  (reducing spontaneous emission, see section 3.4), and by compensating the differential AC-Stark shift of the beams B1 and R2 (see section 6.5).

**Continuous sideband cooling** Another viable approach to bring ions to the ground state of motion is to apply continuous sideband-cooling. We shine in the two Raman beams R2 and B1 tuned to the first red sideband and at the same time shine in the RD and RP beams. The population undergoing a red sideband transition ideally gets repumped within tens of nanoseconds, in contrast to the pulsed scheme where we subsequently apply  $\pi$ -pulses on the red sideband of adapted duration and repumping pulses on the order of  $\mu\text{s}$ . We also have to apply first and second sideband cooling stages. We achieve comparable efficiencies as in the pulsed cooling scheme. However,

the potential benefit of shortening the cooling duration does not hold true in practise. The duration of cooling an ion to the motional ground state is about the same as for the pulsed scheme.

## 7.4. Motional heating rate

An important quantity in characterising an ion trap is its motional heating rate. It expresses the average number of motional quanta gained by the secular motion for a specific mode in a given time [124]. We determine the heating rate by cooling an ion to the motional ground state and wait for a certain duration, e.g. 10 ms. Subsequently, we analyse its temperature by measuring the ratio of the motional sidebands (see Eq. 7.4). For an axial trapping frequency of  $\omega_z = 2\pi \times 2.1$  MHz we measure a heating rate for the motional com mode of  $\dot{n} = 0.066 \frac{\text{quanta}}{\text{ms}}$  in our trap.

Several research groups investigate the fundamental mechanisms for this heating process [124, 68, 29]. Experimental data shows, that the heating rate scales with the distance between the electrodes to the power of four [124]. Most probable candidates [127, 124] causing this heating process include fluctuating patch fields, and Johnson noise from the resistance of the trap electrodes.

For several ions, the com mode (eigenmode of lowest frequency, see section 2.1) is more severely affected than modes of higher frequency, since the heating is due to electric fields rather than field gradients [65], furthermore modes of larger frequency have larger motional state energy spacings and, therefore, heat more slowly.

## 7.5. Sideband cooling of two ions

Sideband cooling of several ions is carried out by subsequent cooling of the different modes. After Doppler cooling, we first cool the modes of larger frequency due to their lower heating rates. For two ions, we begin with second sideband cooling of the stretch mode, continue with second sideband cooling of the com mode. Then, we cool the stretch mode to the motional ground state using first sideband cooling. Finally, we first-sideband-cool the com mode.

We apply the identical number of pulses as in the one-ion case to cool the com mode of motion. To cool the stretch mode, we additionally apply 14 cycles of second sideband cooling ( $\delta = -2\omega_{\text{str}}$ ) starting from  $n = 20$  and 6 cycles of first sideband cooling ( $\delta = -\omega_{\text{str}}$ ) starting at  $n = 6$  in the order given above. Orthogonal axial frequency spectra of two Doppler and sideband cooled ions, respectively, are plotted in Fig. 7.9. From the sideband cooled orthogonal frequency spectrum we determine mean occupation numbers of  $\bar{n}_{\text{str}} \approx 0.046$  and  $\bar{n}_{\text{com}} \approx 0.035$  via Eq. 7.4. A Rabi flopping

## 7. Motional ground state cooling

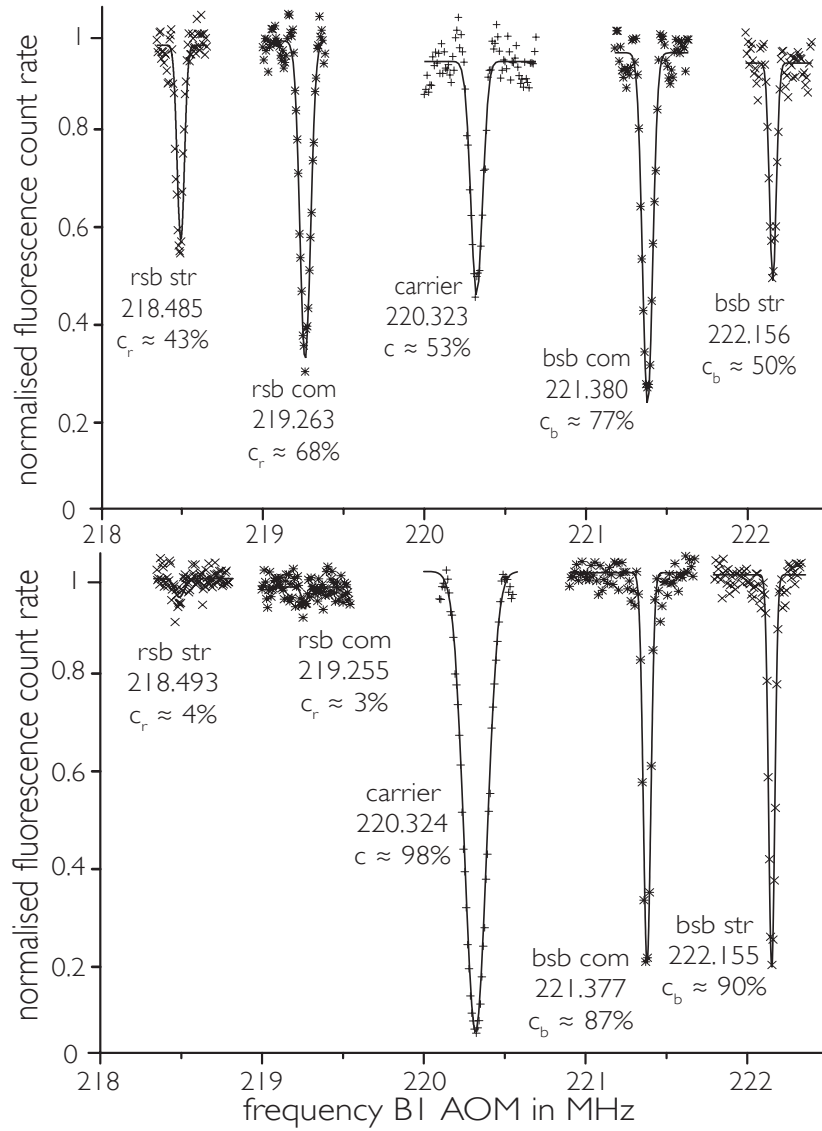


Figure 7.9. – The upper plot shows the orthogonal axial frequency spectrum of two Doppler cooled ions. From left to right we see the first red sidebands of the stretch mode and com mode, the carrier transition and the blue sidebands of com and stretch mode. We deduce a mean number of motional quanta of  $\bar{n}_{\text{str}} \approx 6$  and  $\bar{n}_{\text{com}} \approx 7$  for the Doppler cooled ions. The lower plot shows the orthogonal axial frequency spectrum of two sideband cooled ions. We deduce a mean number of motional quanta of  $\bar{n}_{\text{str}} \approx 0.046$  and  $\bar{n}_{\text{com}} \approx 0.035$ . Each data point corresponds to an average of 500 experiments.

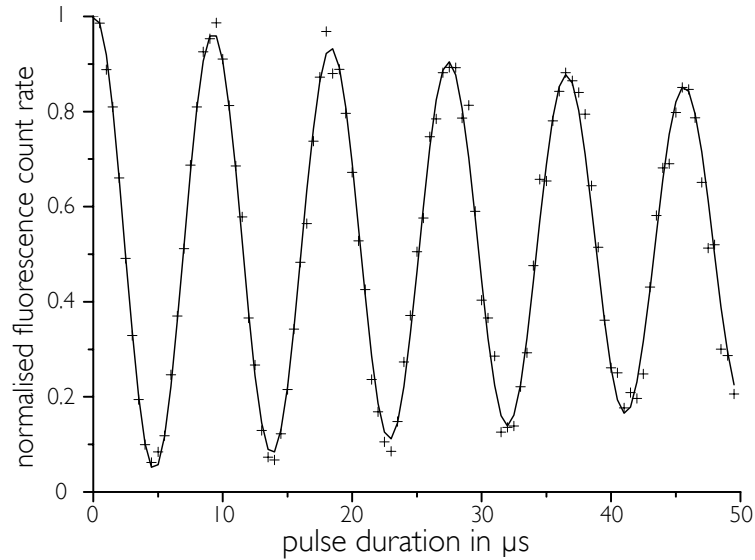


Figure 7.10. – Rabi flopping curve on the orthogonal carrier transition of two sideband cooled ions. Mean motional occupation numbers are analysed in Fig. 7.9. The solid line represents the best fit of a damped cosine function to the data. Each data point corresponds to an average of 1000 experiments.

curve on the orthogonal carrier transition of two ions<sup>4</sup> cooled to the motional ground state is depicted in Fig. 7.10.

If the ions experience different intensities of the Raman beams, we observe different transition durations for different ions and the contrast of a Rabi flopping curve suffers. For two ions, it is straight forward to achieve equal irradiation. For larger numbers of ions, we can mitigate this effect by increasing the beam waists of the laser beams along the trap axis via cylindrical lenses.

<sup>4</sup>Due to the occurrence of differential axial micromotion between the ions (see section 2.2), we observed the following effect: The rf-oscillations of different amplitudes for different ions and the resulting sidebands near the trapping frequency  $\Omega_D$  reduce the laser beam intensities as seen by the ions. Therefore, the pulse duration becomes position-dependent. We have to shift the ions along the trap axis so that the dc-minimum coincides with the axial minimum of the rf-potential to minimise this effect.

## 7. *Motional ground state cooling*

## 8. Simulating spin-spin interactions

In this chapter we derive a state dependent optical dipole force by coupling the spin states  $|\downarrow\rangle$  and  $|\uparrow\rangle$  off-resonantly to the excited state  ${}^2P_{3/2}$ . Without changing the spin states, this coupling induces an AC-Stark shift of these states. This AC-Stark shift is different for the two spin states and depends on the polarisation and the orientation of the  $\mathbf{k}$ -vectors of the used Raman beams. By suitably adjusting parameters we achieve a force acting on the two spin states with different amplitudes and opposite sign, respectively.

The identical force also plays a role in quantum computation: Changing the inter-ion distance conditioned on the mutual state provides the interaction required for universal conditional gates e.g. CNOT [86], or a geometric phase gate [72]. But this force can also be tailored to simulate an effective spin-spin interaction allowing for the simulation of quantum spin Hamiltonians in an ion trap.

Before proceeding with the derivation of the spin-spin coupling, we calculate the Rabi frequency of a two-photon stimulated Raman transition. From this result, we move on to the introduction of a state-dependent optical dipole force by a slight change of laser beam geometry.

### 8.1. Derivation of the Raman Rabi rate

First, we theoretically investigate the coupling of the spin states  $|\downarrow\rangle$  and  $|\uparrow\rangle$  to the  ${}^2P_{3/2}$  manifold for driving two-photon stimulated Raman transitions (see section 3.4) between these states and then alter the setup for simulating the spin-spin interaction.

The Rabi frequency  $\Omega_{nm}$  associated with an off-resonant coupling of a state  $|n\rangle$  to a state  $|m\rangle$  via an intermediate excited level, in our case a virtual level  $|v\rangle$  detuned by  $\Delta_R$  from the  ${}^2P_{3/2}$  levels can be expressed as [127]

$$\Omega_{nm} = -\frac{g_b^* g_r}{\Delta_R} \langle n | e^{i\eta(\hat{a}_z + \hat{a}_z^\dagger)} | m \rangle , \quad (8.1)$$

where  $\eta = kz_0$  is the Lamb-Dicke parameter (see section 3.4) for the two-photon stimulated Raman transition and  $z_0 = \sqrt{\frac{\hbar}{2m\omega_z}}$  the width of the ground state wave function in direction of  $z$ . The amplitude of the wave vector  $k$  is given by  $k = \frac{2\pi}{\lambda_{\text{eff}}} = \frac{2\pi}{\lambda} \sqrt{2}$  (see Fig. 3.3). The coupling strengths of the blue (B1) and red (R2) Raman

## 8. Simulating spin-spin interactions

beams, can be expressed as

$$g_{b/r} = -\frac{eE_{b/r}}{2\hbar} \langle \downarrow / \uparrow | \hat{\epsilon} \cdot \mathbf{r} | \nu \rangle e^{-i\phi_{b/r}} = -\frac{E_{b/r}}{2\hbar} \wp, \quad (8.2)$$

where we introduced  $\wp$ , the component of the matrix element  $e\mathbf{r}$  along  $\mathbf{E} = E\hat{\epsilon}$ .  $\hat{\epsilon}$  is the unit vector of polarisation of the electromagnetic field  $\mathbf{E}$  and  $e$  the elementary charge. We identify the virtual level  $|\nu\rangle$  with the electronic state  ${}^2P_{3/2} |F=3, m_F=+3\rangle$ , see Fig. 8.1. The component  $\wp$  of the dipole matrix element can be determined via the Wigner-Weisskopf approximation of spontaneous emission [115, 85] to be

$$\wp^2 = 4\pi\epsilon_0 \Gamma \frac{3\hbar\lambda^3}{32\pi^3}, \quad (8.3)$$

with the dielectric constant  $\epsilon_0$ , the natural linewidth  $\Gamma$  and the wavelength of the transition  $\lambda$ .

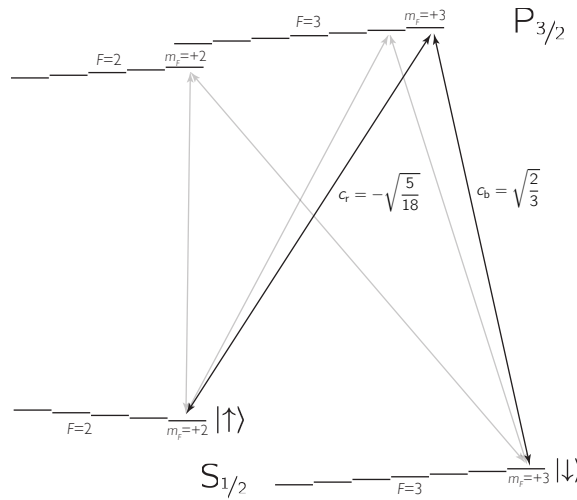


Figure 8.1. – Participating levels for the two-photon stimulated Raman transition: In principle all three illustrated paths would be viable, but due to our laser beam geometry and polarisation the two shaded paths are not possible. The Clebsch-Gordan coefficients are given for the actual transition  $|\downarrow\rangle \rightarrow {}^2P_{3/2} |F=3, m_F=+3\rangle \rightarrow |\uparrow\rangle$ .

Inserting this into the last equation we obtain

$$g_{b/r}^2 = 4\pi\epsilon_0 \frac{E_{b/r}^2}{4\hbar^2} \Gamma \frac{3\hbar\lambda^3}{32\pi^3}. \quad (8.4)$$

### 8.1. Derivation of the Raman Rabi rate

We formulate the electric field  $E_{b/r}$  in terms of laser beam power  $P_{b/r}$  and laser beam waists  $w_b = w_r = w_0$ , use  $I_{b/r} = \frac{2P_{b/r}}{\pi w_0^2}$  and  $I_{b/r} = \frac{c\epsilon_0}{2} |E_{b/r}|^2$  and obtain for the square of the electric field

$$E_{b/r}^2 = \frac{4}{\pi c \epsilon_0} \cdot \frac{P_{b/r}}{w_0^2}, \quad (8.5)$$

and

$$g_{b/r}^2 = \frac{3 P_{b/r} \lambda^3}{8 \pi^3 c \hbar w_0^2} \Gamma. \quad (8.6)$$

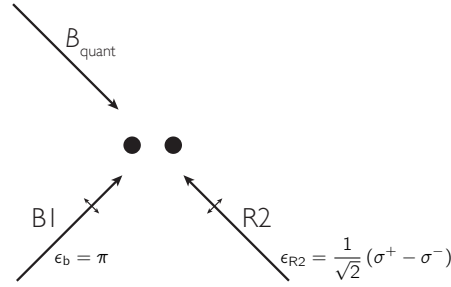


Figure 8.2. – Beam geometry and polarisation for orthogonal Raman transition: The two beams B1 and R2 enclose an angle of  $90^\circ$  and both beams enclose an angle of  $45^\circ$  with respect to the trap axis. Both beams are polarised linearly in the tangential plane (p-polarised). Beam R2 points parallel to the quantisation axis, therefore the ion sees the light as  $\frac{1}{\sqrt{2}}(\sigma^+ - \sigma^-)$  polarised. Beam B1 is orthogonal to the quantisation axis, the light is  $\pi$ -polarised as seen by the ion.

To evaluate the other matrix element in Eq. 8.1, we take into account the laser beam geometry, beam polarisation<sup>1</sup> (see Fig. 8.2) and the Clebsch-Gordan coefficients of the transitions (see Fig. 8.1) and obtain

$$\langle \downarrow | e^{i\mathbf{m}(\hat{a}_z + \hat{a}_z^\dagger)} | \uparrow \rangle = \left( \sqrt{\frac{2}{3}} \cdot (-) \sqrt{\frac{5}{18}} \cdot \frac{1}{\sqrt{2}} \right). \quad (8.7)$$

With typical laser beam powers  $P_{b/r} = 1$  mW, beam waists of  $w_0 = 45$   $\mu\text{m}$ , wavelength  $\lambda = 279.2$  nm, and natural linewidth  $\Gamma = 2\pi \times 42.7$  MHz, we obtain

$$\Omega_{\downarrow\uparrow} \approx 2\pi \times 680 \text{ kHz} \quad (8.8)$$

for the Rabi frequency of a carrier transition between states  $|\downarrow\rangle$  and  $|\uparrow\rangle$ . We neglected couplings to the  $^2P_{1/2}$  levels, since the finestructure splitting between the  $^2P_{1/2}$  and  $^2P_{3/2}$

<sup>1</sup>Due to its polarisation  $\frac{1}{\sqrt{2}}(\sigma^+ - \sigma^-)$ , only half of the beam intensity of the R2 beam contributes to the transition.

## 8. Simulating spin-spin interactions

levels  $\omega_{FS} = 2\pi \times 2.74$  THz is much larger than the detuning of the virtual level  $\Delta_R$  ( $\frac{\Delta_R}{\omega_{FS}} \approx 0.029 \ll 1$ ). The evaluation of this Rabi Raman rate is valid under the following approximations:

$$\omega_{FS} \gg \Delta_R \gg \omega_{HFS} \gg \Omega_{\uparrow\downarrow}, \quad (8.9)$$

a more general derivation can be found in the literature [128].

### 8.2. Derivation of a state dependent AC-Stark shift

Starting from the two-photon stimulated Raman transition between the spin states  $|\downarrow\rangle$  and  $|\uparrow\rangle$  with orthogonal Raman beams, we replace Raman beam B1 by beam R2. This beam enters the identical port, has orthogonal polarisation with respect to both B1 and R2 (see Fig. 8.3), and the same frequency as R2. Shining in these two beams R1 and R2, both atomic states  $|\uparrow\rangle$  and  $|\downarrow\rangle$  have different couplings to the excited states. We show that the generated force can act in opposite direction for opposite spin states.

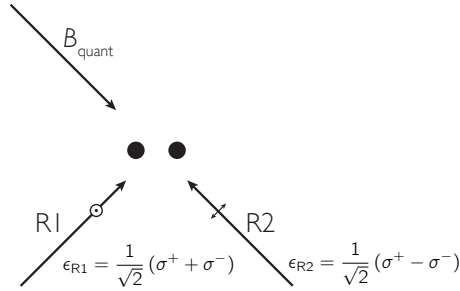


Figure 8.3. – Beam geometry and polarisation for state dependent force: The beam geometry is identical to Fig. 8.2, but beam R1 is s-polarised and has the identical frequency as beam R2 (p-pol). As experienced by the ions, R1 is polarised  $\frac{1}{\sqrt{2}}(\sigma^+ + \sigma^-)$ , and R2  $\frac{1}{\sqrt{2}}(\sigma^+ - \sigma^-)$ .

The form of the electric field pattern on the  $z$ -axis is simulated in Fig. 8.4. The plot shows one oscillation period of the polarisation pattern of effective wavelength  $\lambda_{\text{eff}} = \lambda/\sqrt{2} \approx 197$  nm. The polarisation pattern is similar to a lin  $\perp$  lin scheme employed for polarisation gradient cooling [84].

The polarisation gradients lead to spatially and state dependent AC-Stark shifts  $\Delta E_{\text{Stark}}(z, m_s)$  of the electronic levels resulting in an optical dipole force given by

$$F_z(z, m_s) = -\frac{\partial}{\partial z} \Delta E_{\text{Stark}}(z, m_s). \quad (8.10)$$

The Stark shift  $\Delta E_{\text{Stark}}(z, m_s)$  can be approximated by

$$\Delta E_{\text{Stark}}(z, m_s) = -4\hbar |g(z, m_s)|^2 \quad (8.11)$$

## 8.2. Derivation of a state dependent AC-Stark shift

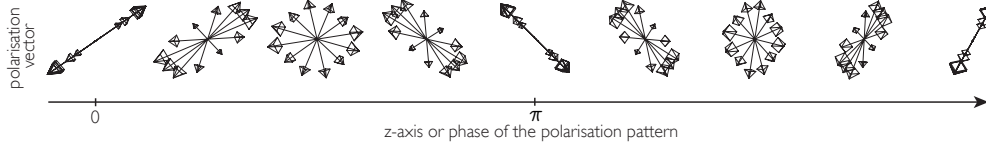


Figure 8.4. – Standing wave polarisation pattern generated by the laser beams seen in Fig. 8.3. The plot depicts the polarisation vector at 9 locations along the z-axis of the trap corresponding to the phases  $n\pi/8$ ,  $n$  integer, depicted at 12 instants during one oscillation period of the electric field. Starting from the left hand side the polarisation alters from linear via elliptical to circular via opposite elliptical to orthogonal linear and so on.

with a coupling constant  $g(z, m_s)$  which depends on the axial coordinate  $z$  and thus on the phase of the polarisation pattern and on the spin state  $m_s$  of the ion. We suppose that the individual ions are located at integer multiples of the effective wavelength  $\lambda_{\text{eff}}$  and therefore experience the same phase of the polarisation pattern  $g(z, m_s) = g(z + n\lambda_{\text{eff}}, m_s)$ . In addition, the gradient of the polarisation shall reach its extremum value at  $z = z_{\text{extr}}$ . With this suppositions, we neglect the spatial dependence and introduce a new coupling constant  $\Omega(m_s)$  solely depending on the spin state of the ion

$$\Omega(m_s) \equiv |g(z_{\text{extr}}, m_s)|^2. \quad (8.12)$$

This new coupling  $\Omega(m_s)$  is given by

$$\Omega(m_s) = \sum_i \frac{\langle m_s | \mathbf{E} \cdot \mathbf{r} | i \rangle \langle i | \mathbf{E} \cdot \mathbf{r} | m_s \rangle}{\Delta_i} \quad (8.13)$$

and includes the dipole matrix elements  $\langle m_s | \mathbf{E} \cdot \mathbf{r} | i \rangle$  which express a coupling between the spin states  $m_s$  and intermediate levels  $|i\rangle$  within the  ${}^2P_{3/2}$  manifold via the electric field  $\mathbf{E}$  of the Raman beams R1 and R2. We have to sum over all participating intermediate levels  $|i\rangle$ , see Fig. 8.5.

Taking into account the geometry and polarisation of the laser beams, the ions are not able to absorb  $\pi$  polarised light and we can expand the electric field for the two Raman beams as  $\mathbf{E}_{R1} = E_{R1}\hat{\mathbf{e}}_{R1} = E_{R1}(1/\sqrt{2}\sigma^+ + 1/\sqrt{2}\sigma^-)$  and  $\mathbf{E}_{R2} = E_{R2}\hat{\mathbf{e}}_{R2} = E_{R2}(1/\sqrt{2}\sigma^+ - 1/\sqrt{2}\sigma^-)$ . Evaluating the matrix elements of the dipole operator is carried out by summing over all couplings to states of the  ${}^2P_{3/2}$  manifold weighted with the squares of the corresponding Clebsch-Gordan coefficients. These are summarised in Fig. 8.5. For the coupling  $\Omega(\downarrow)$  we obtain

$$\Omega(\downarrow) = -\frac{g_{R1}g_{R2}}{\Delta_R} \frac{1}{2} \left( (c_{\downarrow}^{\sigma^+})^2 - (c_{\downarrow}^{\sigma^-})^2 \right) = -\frac{g_{R1}g_{R2}}{2\Delta_R} \left( 1 - \frac{1}{3} \right) = -\frac{g_{R1}g_{R2}}{2\Delta_R} \frac{2}{3}, \quad (8.14)$$

## 8. Simulating spin-spin interactions

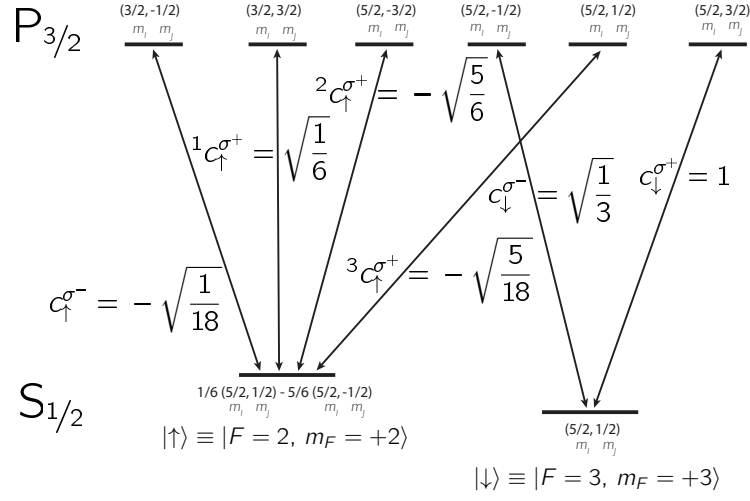


Figure 8.5. – The coupling of the spin states  $|\uparrow\rangle$  and  $|\downarrow\rangle$  (expressed in the basis  $m_l$  and  $m_j$ ) to the excited states of the  ${}^2P_{3/2}$  manifold with polarisation and Clebsch-Gordan coefficients. For clarity we omitted all states not involved.

where the  $c_{\downarrow}^{\sigma^{\pm}}$  represent the Clebsch-Gordan coefficients related to the respective transition from  $|\downarrow\rangle$  in Fig. 8.5, and for the coupling

$$\Omega(\uparrow) = -\frac{g_{R1}g_{R2}}{\Delta_R} \frac{1}{2} \sum_i \left( (i c_{\uparrow}^{\sigma^+})^2 - \sum_i (i c_{\uparrow}^{\sigma^-})^2 \right) = \frac{g_{R1}g_{R2}}{2\Delta_R} \frac{4}{9}, \quad (8.15)$$

where the  $i c_{\uparrow}^{\sigma^{\pm}}$  represent the Clebsch-Gordan coefficients for the transition from the  $|\uparrow\rangle$  level. Thus we conclude

$$\Omega(\downarrow) = -\frac{3}{2}\Omega(\uparrow). \quad (8.16)$$

Using Eq. 8.10, we obtain the following relation between the optical dipole force  $F_z$  and the coupling to the excited states  $\Omega(m_s)$ :

$$F_z \propto \frac{\partial}{\partial z} \Delta E_{\text{Stark}}, \quad (8.17)$$

whereas

$$\Delta E_{\text{Stark}} \propto \Omega(m_s). \quad (8.18)$$

### 8.3. Derivation of the spin-spin interaction

We move to a more formal description of the interaction and express it in form of the following Hamiltonian [103]

$$H_f = -2 \sum_i F_z q_i \left( |\uparrow\rangle \langle \uparrow| - \frac{3}{2} |\downarrow\rangle \langle \downarrow| \right). \quad (8.19)$$

For clarity we will absorb the different amplitudes of the force on the  $|\uparrow\rangle$  and  $|\downarrow\rangle$  states into  $F_z$ , which therefore becomes a matrix  $\tilde{F}_z$ . We reexpress the above Hamiltonian as

$$H_f = -2 \sum_i \tilde{F}_z q_i \hat{\sigma}_i^z, \quad (8.20)$$

with the Pauli matrix  $\hat{\sigma}^z$ . Remembering the introduction of normal coordinates in chapter 2.1, we formulate the spatial displacement of the  $i$ th ion in the following way:

$$q_i = \sum_n \mathcal{M}_{in} \sqrt{\frac{\hbar}{2m\omega_n}} (\hat{a}_n + \hat{a}_n^\dagger) \quad (8.21)$$

The summation is carried out over the different normal modes  $n$  (see chapter 2.1). We omit the spatial index  $z$  for the coordinates  $q_i$  and for the creation and annihilation operators  $\hat{a}_n$  and  $\hat{a}_n^\dagger$ , since we only consider the axial modes of the trap. The matrices  $\mathcal{M}_{in}$  diagonalise the confining potential.

The Hamiltonian for the dipole force in terms of normal modes becomes

$$H_f = -2\tilde{F}_z \sum_{i,n} \mathcal{M}_{in} \sqrt{\frac{\hbar}{2m\omega_n}} (\hat{a}_n + \hat{a}_n^\dagger) \hat{\sigma}_i^z. \quad (8.22)$$

A second term contributing to the Hamiltonian of the system describes the collective modes of vibration

$$H_{\text{vib}} = \sum_n \hbar\omega_n \hat{a}_n^\dagger \hat{a}_n. \quad (8.23)$$

The total Hamiltonian of the system reads

$$\begin{aligned} H &= H_{\text{vib}} + H_f \\ &= \sum_n \hbar\omega_n \hat{a}_n^\dagger \hat{a}_n - 2\tilde{F}_z \sum_{i,n} \mathcal{M}_{in} \sqrt{\frac{\hbar}{2m\omega_n}} (\hat{a}_n + \hat{a}_n^\dagger) \hat{\sigma}_i^z. \end{aligned} \quad (8.24)$$

We transform the latter part describing the optical dipole force using the canonical transformation

$$H_J = e^{-S} H_f e^S \quad (8.25)$$

## 8. Simulating spin-spin interactions

with

$$\mathcal{S} = \sum_{i,n} \zeta_{in} (\hat{a}_n^\dagger - \hat{a}_n) \hat{\sigma}_i^z, \quad (8.26)$$

where  $\zeta$  is given by

$$\zeta_{in} = \tilde{F}_z \frac{\mathcal{M}_{in}}{\hbar \omega_n} \sqrt{\frac{\hbar}{2m\omega_n}}. \quad (8.27)$$

Using the Baker-Hausdorff identity [114]

$$e^A B e^{-A} = B + [A, B] + \frac{1}{2!} [A, [A, B]] + \dots \quad (8.28)$$

and the canonical commutation relations

$$\begin{aligned} [\hat{a}_n, \hat{a}_m^\dagger] &= \delta_{nm}, \\ [\hat{a}_n, \hat{a}_m] &= 0, \quad \text{and} \quad [\hat{a}_n^\dagger, \hat{a}_m^\dagger] = 0, \end{aligned} \quad (8.29)$$

we obtain

$$e^{-\mathcal{S}} H e^{\mathcal{S}} = \underbrace{\sum_n \hbar \omega_n \hat{a}_n^\dagger \hat{a}_n}_{H_{\text{vib}}} + \frac{1}{2} \underbrace{\sum_{i,j} J_{ij} \hat{\sigma}_i^z \hat{\sigma}_j^z}_{H_J}, \quad (8.30)$$

where the latter term  $H_J$  can be interpreted as an effective spin-spin coupling with the coupling constant

$$J_{ij} = - \sum_n \frac{\tilde{F}_z^2}{m \omega_n^2} \mathcal{M}_{in} \mathcal{M}_{jn}. \quad (8.31)$$

The zeroth order of the Taylor operator series cancels with the commutator of  $H_{\text{vib}}$  and  $\mathcal{S}$ . The coupling matrix  $J$  is on the one hand determined by the amplitude of the optical dipole force given by  $\tilde{F}_z$  and on the other hand by the axial trapping potential, i.e. the mutual distance between neighbouring ions. We can express  $J$  as [103]

$$J_{ij} = - \frac{\tilde{F}_z^2}{m} (1/\mathcal{K})_{ij}, \quad (8.32)$$

where  $\mathcal{K}$  is the matrix describing the trapping potential and Coulomb interaction (see chapter 2.1).

According to [103], our experimental conditions are such, that the Coulomb interaction can be considered as a perturbation of the trapping potential, the so-called regime of stiff modes, which is determined by the parameter  $\beta_z$ :

$$\beta_z = \frac{2e^2}{m \omega_z^2 d_0^3} \approx 10^{-10} \ll 1. \quad (8.33)$$

As a result, we obtain a ferromagnetic interaction of dipolar decay for the axial modes.

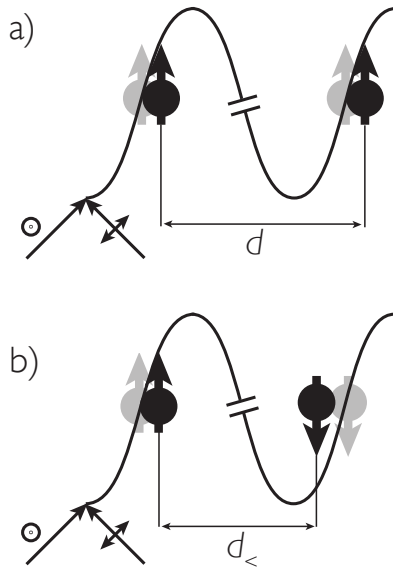


Figure 8.6. – Simulation of spin-spin interaction between the ions: The resulting displacement (black) of two ions under the effect of the state-dependent optical dipole force is illustrated for two cases. a) both ions are prepared in the identical state, the optical dipole force solely displaces the ions without changing the relative distance  $d$  between them. b) If adjacent spins point in opposite directions, switching on the optical dipole force displaces the ions in opposite directions. For this case, the mutual distance  $d_<$  between the ions is reduced and therefore the mutual Coulomb energy increased. The ferromagnetic interaction between the ions is mediated through the Coulomb energy.

The effect of the optical dipole force giving rise to a spin-spin interaction is visualised in Fig. 8.6. Depending on the spin state of the adjacent ion, the mutual distance between the ions is conditionally reduced and therefore the Coulomb energy conditionally increased. The application of the optical dipole force to a string of ions provides a ferromagnetic coupling  $J\sigma^z\sigma^z$ . The energy of the system for both ferromagnetic Ising interaction and Coulomb interaction is minimal for aligned spins, whereas it rises for anti-aligned spins. The coupling matrix  $J$  depends on the square of the amplitude of the applied force (see Eq. 8.31).

## 8.4. Walking standing wave

For the derivation of the optical dipole force (chapter 8.2) we made the assumption, that the ions are exposed to the same phase of the standing wave polarisation pattern. Fluctuations of the length of the different laser beam paths (e.g. by mechanical vibration of optics) cause jittering of the polarisation pattern. This jitter will on average randomise the phase and mitigate the effective spin-spin interaction. This implies, that we would have to stabilise the absolute phase of the polarisation pattern to nanometer accuracy. The generated force is sinusoidally varying in space as  $F(z) = F_0 \cos(kz)$  with an effective wavelength of  $\lambda_{\text{eff}} \approx 197 \text{ nm}$ . The ions have to be located at the position where the gradient of the field takes on its maximum value. In the maxima and minima of the force pattern, the spin-spin interaction vanishes. Moreover, at these phase values, the interaction can be described by the term  $\propto B^2 \hat{\sigma}^z$ . This term can

## 8. Simulating spin-spin interactions

be interpreted as a bias field which determine a preferred direction of alignment. This contribution can be five [101] times larger than the effective spin-spin interaction.

One solution to this challenge is to replace the standing wave by a *walking* standing wave scheme. That is, we detune the frequency of one of the two laser beams R1 and R2 with respect to the frequency of the other one. Thereby, we create a force pattern walking over the ions with a frequency determined by their relative detuning<sup>2</sup>  $\Delta_{\text{walk}}$ . On longer time scales, this dipole force is modulated at the frequency of this detuning  $\Delta_{\text{walk}}$  and if the this detuning  $\Delta_{\text{walk}}$  is adjusted to coincide with a motional mode of the ions, we can resonantly excite the ions' motion [127].

Adjusting the difference frequency of the laser beams to fulfil  $\Delta_{\text{walk}} = \omega_{\text{str}} - \delta$ , we obtain an effective coupling determined by

$$J \propto \frac{\omega_{\text{str}}}{\delta}. \quad (8.34)$$

However, we have to adjust the inter-ion distance to match an integer multiple of the effective wavelength. Therefore, we cool the ion crystal close to the motional ground-state ( $\bar{n}_{\text{str}} \approx \bar{n}_{\text{com}} \approx 0.04$ , see chapter 7) and initialise the ions to the internal state  $|\downarrow\downarrow\rangle$ . Subsequently, we apply a pulse of the optical dipole force resonantly tuned to the frequency of the stretch mode ( $\Delta_{\text{walk}} = \omega_{\text{str}}$ ) and analyse the excitation via a Rabi flopping on the red sideband of the stretch mode. To minimise the differential excitation of the ion crystal, we adjust the dc-voltages altering the axial confinement of the trap (see Eq. 2.1) .

---

<sup>2</sup>The detuning  $\Delta_{\text{walk}}$  has to be large enough to allow for averaging out the above mentioned (now fast oscillating) contributions  $B^z \hat{\sigma}^z$ .

## 9. State-sensitive detection

For experiments with a single ion we can use detection durations of the order of tens of microseconds. By repeating a experiments sufficiently often, we can achieve enough photon count statistics to discriminate between the spin states. For experiments with two or more ions we have to discriminate between two cases: experiments during which we apply collective pulses to the ions and experiments where we introduce couplings between the individual ions such as spin-spin interactions (see chapter 8). For the former type, the above mentioned method of detection still holds true. However, for experiments with two ions including couplings between these, the situation becomes more involved for there are several different quantum mechanical states of two ions leading to identical photon count rates. As an example, we consider the states  $1/\sqrt{2}(|\uparrow\uparrow\rangle + |\downarrow\downarrow\rangle)$  and  $|\uparrow\downarrow\rangle$  which on average lead to the identical global fluorescence count rate. Thus, we need the possibility of discriminating between these. A simplifying fact is that for our experiments, we do not have to discriminate which one out of two ions is bright given the states  $|\uparrow\downarrow\rangle$  or  $|\downarrow\uparrow\rangle$ . We could do this using our CCD-camera, but since the read-out of the CCD chip takes much longer and the CCD chip is less sensitive than the photomultiplier (PMT), we prefer experimenting with the PMT as long as we do not need spatial resolution.

### 9.1. State-sensitive detection of two ions

Let us consider the two states above in more detail and assume that one ion in state  $|\downarrow\rangle$  scatters 5 photons during our detection interval. The entangled state will therefore on average either scatter 10 photons upon being projected to  $|\downarrow\downarrow\rangle$  or none if it is projected to the state  $|\uparrow\uparrow\rangle$ . Both possible projections occur with probabilities of  $P_{\downarrow\downarrow} = P_{\uparrow\uparrow} = 1/2$ . Averaging over all measurements, we would obtain an average count rate of 5 photons per experiment. For the other state  $|\uparrow\downarrow\rangle$ , one ion will on average scatter 5 photons per experiment and the other ion on average none, on average also leading to 5 photons per experiment.

However, instead of averaging the total number of photons of all repetitions of an experiment, we can also determine the photon numbers detected in each experiment and sum up the number of experiments with distinct numbers of captured photons. We plot these photon numbers in a histogram and obtain two distinct peaks for the entangled state, one peak at zero photons detected and another peak for 10 photons

## 9. State-sensitive detection

detected on average. For the other state we obtain only one peak centred at 5 phonons detected on average.

The statistics of scattered photons follows Poissonian statistics, which implies that the width of a photon number distribution is equal to the square root of the number of scattered photons. The number of scattered photons increases linearly with the duration of the detection interval. Ideally, we can minimise the overlap of the distributions for  $|\uparrow\downarrow\rangle$  and  $|\uparrow\uparrow\rangle$  by increasing the detection duration  $t_{\text{det}}$ .

Before continuing with the analysis of state-sensitive detection of two ions, we have to discuss an additional effect which arises when we elongate the detection interval.

### 9.2. Scattering from dark to bright state

For larger detection durations  $t_{\text{det}}$ , the assumption that the ion in the dark state does not scatter any photons does not hold anymore. The probability, that the electron is off-resonantly pumped out of the state  $|\uparrow\rangle$  by the detection laser, increases and from this moment it takes part in the cycling transition. This process has been studied in detail elsewhere [2, 65]. The probability that the ion originally prepared in the dark state is pumped to the bright state can be described by

$$P_{\downarrow}(t) = 1 - e^{-\omega_{\text{leak}} t} \quad (9.1)$$

with decay rate

$$\omega_{\text{leak}} = \frac{\Gamma}{2} \frac{s_0}{1 + s_0 + 4\delta^2/\Gamma^2} c_{\text{BR}}, \quad (9.2)$$

where  $\Gamma$  is the natural linewidth of the transition,  $s_0 = I/I_0$  the on-resonance saturation parameter,  $\delta$  the detuning from resonance, which can be approximated by the ground state splitting  $\delta \approx \omega_0$ , and  $c_{\text{BR}}$  an atomic coupling coefficient for scattering into the bright state. Subsequent to this scattering process follows a time interval  $t = t_{\text{det}} - t_{\text{leak}}$  in which the ion takes part in the cycling transition. To obtain the mean value of scattered photons within the given detection interval, one has to integrate over all possible decay times. One obtains a Poissonian of reduced mean value due to the reduced effective detection duration.

To obtain the coefficient  $c_{\text{BR}}$ , we have to consider couplings from the dark state  $|\uparrow\rangle \equiv {}^2S_{1/2} |F = 2, m_F = +2\rangle$  to the state  ${}^2P_{3/2} |F = 3, m_F = +3\rangle$ , from where the electron can decay to the states  ${}^2S_{1/2} |F = 2, m_F = +2, +3\rangle$ . The coefficient  $c_{\text{BR}}$  can be calculated using

$$c_{\text{BR}} = C(I - 1/2, I + 1/2; I - 1/2, I + 1/2) \sum_{i=I-1/2}^{I+1/2} C(I + 1/2, I + 1/2; I + 1/2, i), \quad (9.3)$$

### 9.3. Reference histograms

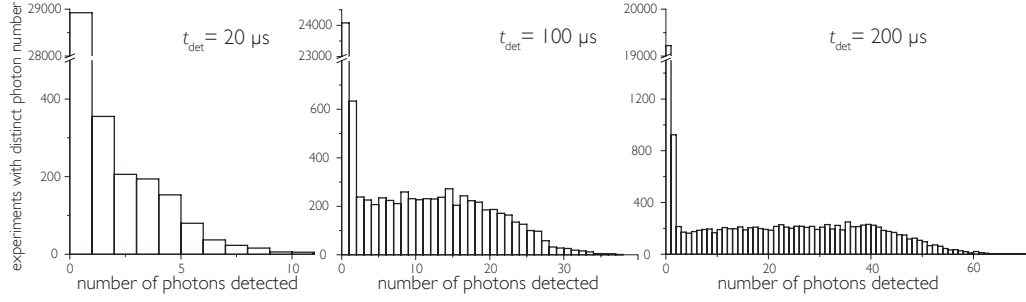


Figure 9.1. – Histograms of detected photons in dependence of the detection interval of a single ion. The number of experiments of distinct photon number is plotted versus the number of photon detected during the detection interval. The total number of experiments amounts to 30000 for each histogram. From left to right, the detection intervals amount to  $t_{\text{det}} = 20 \mu\text{s}$ ,  $100 \mu\text{s}$ , and  $200 \mu\text{s}$ , during which 4%, 20%, and 36% are off-resonantly scattered into the bright state, respectively. We deduce a leakage rate of  $\omega_{\text{leak}} \approx 2.2 \times 10^{-3} 1/\mu\text{s}$ , which is in good agreement with the theoretical predictions given in the text.

where  $C(F, F'; f, f')$  is the Clebsch-Gordon coefficient between two states  $F \rightarrow F'$  and  $m_F = f \rightarrow f'$  which is given by

$$C(F, F'; f, f') = [(2J + 1)(2J' + 1)(2F + 1)(2F' + 1)] \quad (9.4)$$

$$\times \left[ \begin{Bmatrix} L' & J' & S \\ J & L & 1 \end{Bmatrix} \begin{Bmatrix} J' & F' & I \\ F & J & 1 \end{Bmatrix} \begin{pmatrix} F & 1 & F' \\ f & q & -f' \end{pmatrix} \right]^2. \quad (9.5)$$

$\begin{Bmatrix} \end{Bmatrix}$  is the Wigner  $6J$  symbol,  $\begin{pmatrix} \end{pmatrix}$  is the Wigner  $3J$  symbol with polarisation number  $q$ . The expression is normalised, so that the cycling transition has transition strength 1. For magnesium-25 we obtain  $c_{\text{BR}} = 0.2469$ . Thus, the rate of off-resonantly scattering electrons to  $|\downarrow\rangle$  is:  $\omega_{\text{leak}} = 2.33 \times 10^{-3} 1/\mu\text{s}$ . The mean number of detected photons from an ion prepared in the dark state  $|\uparrow\rangle$  can be computed via a conditional probability distribution. One has to integrate over different decay times and sum up over the remaining detection interval, during which the ion and scatters photons obeying Poisson statistics (see [65, 70]). To summarise, the photon statistics of the  $|\uparrow\rangle$  state for longer detection intervals  $t_{\text{det}}$  is composed of a peak at zero photons plus a convolution of Poisson distributions of reduced mean value.

### 9.3. Reference histograms

We measure populations via reference histograms of states prepared with maximum fidelity. For the state  $|\downarrow\downarrow\rangle$ , we record a fluorescence histogram after Doppler cooling

## 9. State-sensitive detection

with sufficient statistics. We label the measured histogram  $s_{\downarrow\downarrow}$ . In an analogous manner, the reference curve  $s_{\uparrow\uparrow}$  for  $|\uparrow\uparrow\rangle$  is measured with a  $\pi$  pulse prior to the detection. Finally, we need a reference histogram for the state  $|\uparrow\downarrow\rangle$ , which is not directly experimentally accessible since we lack the possibility of individual ion addressing. Thus, we prepare the ions in a superposition state  $|\rightarrow\rightarrow\rangle$ , where  $|\rightarrow\rangle = 1/\sqrt{2} (|\uparrow\rangle + |\downarrow\rangle)$ . The measured histogram is denoted  $s_{\pi/2}$ . See Fig. 9.2 for experimentally recorded reference histograms for two different detection intervals. In our measurement basis this state is projected to the states  $|\downarrow\downarrow\rangle$  and  $|\uparrow\uparrow\rangle$  with probabilities  $P_{\uparrow\uparrow} = P_{\downarrow\downarrow} = 1/4$ . This implies, that this recorded basis of reference histograms is not orthogonal, but we can derive an orthogonal basis by a suitable linear combination of the reference histograms:

$$s_{\uparrow\downarrow} = 2s_{\pi/2} - \frac{1}{2}(s_{\downarrow\downarrow} + s_{\uparrow\uparrow}) . \quad (9.6)$$

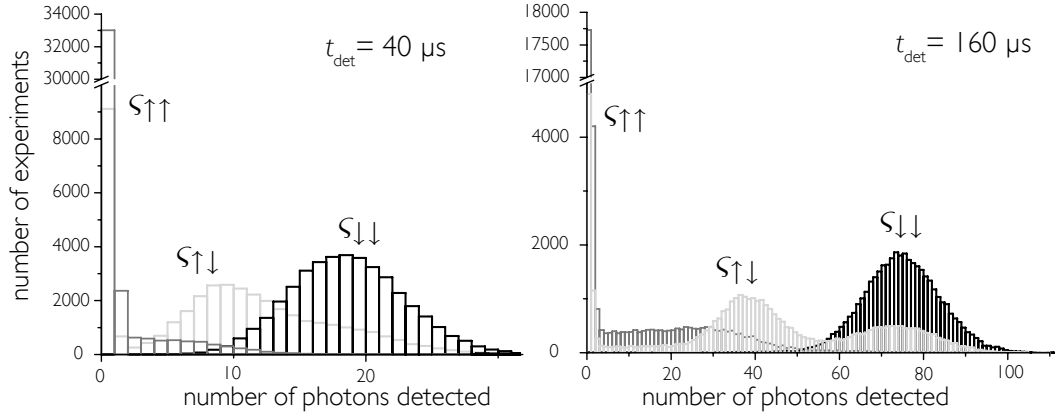


Figure 9.2. – Reference histograms for different detection intervals for two ions: The abscissa shows the number of photons detected in  $t_{\text{det}}$  and the broken ordinate shows the number of experiments out of 40000 with distinct counted photon number  $n$ . With increasing detection interval  $t_{\text{det}}$ , the overlap between the histograms diminish.

An arbitrary state of the two qubit system can in general be described by

$$|\Psi\rangle = c_{\downarrow\downarrow} |\downarrow\downarrow\rangle + c_{\downarrow\uparrow} |\downarrow\uparrow\rangle + c_{\uparrow\downarrow} |\uparrow\downarrow\rangle + c_{\uparrow\uparrow} |\uparrow\uparrow\rangle \quad (9.7)$$

and leads to a histogram to which we can fit our reference histograms and deduce the respective populations of our basis states:

$$s_{\Psi} = P_{\downarrow\downarrow} \cdot s_{\downarrow\downarrow} + P_{\uparrow\downarrow} \cdot s_{\uparrow\downarrow} + P_{\uparrow\uparrow} \cdot s_{\uparrow\uparrow} . \quad (9.8)$$

The Populations  $P_{..}$  are related to the wavefunction amplitudes as  $P_{\uparrow\uparrow} = |c_{\uparrow\uparrow}|^2$ ,  $P_{\downarrow\downarrow} = |c_{\downarrow\downarrow}|^2$  and  $P_{\uparrow\downarrow} = |c_{\uparrow\downarrow}|^2 + |c_{\downarrow\uparrow}|^2$ .

### 9.3. Reference histograms

Considerations about errors and procedures of optimising the duration of  $t_{\text{det}}$  are discussed in ref. [43]. The overlap between the histograms belonging to a state with one ion bright and states with two ions bright decreases with increasing detection interval  $t_{\text{det}}$ . However, as can be extracted from Fig. 9.2, by elongating the detection interval  $t_{\text{det}}$ , the overlap of the histograms  $\varsigma_{\downarrow\downarrow}$  and  $\varsigma_{\uparrow\downarrow}$  also increases. We find an optimum detection interval on the order of  $t_{\text{det}} = 90 \mu\text{s}$ , which lies in a wide plateau ranging from about  $40 \mu\text{s}$  to  $160 \mu\text{s}$ .

9. *State-sensitive detection*

**Part IV.**  
**Experiments**



## 10. Experiments

In section 3.4, we introduced a two-level system based on two hyperfine ground state levels of  $^{25}\text{Mg}^+$  ions and argued, that it is valid to consider this system as a spin-1/2 particle. Each ion within our Paul trap simulates a spin-1/2 system. We also introduced coherent couplings between these spin states via radiofrequency and two-photon stimulated Raman transitions (see section 3.4). In the following section 10.2, we will explicate, how these coherent couplings can be used to simulate effective magnetic fields. In chapter 8 we discussed the basics of the state-dependent optical dipole force which can be formulated in terms of a spin-spin interaction, and in chapter 9 we introduced a state sensitive detection scheme. We now have all basic ingredients and can in principle combine all these operations for the adiabatic simulation of the quantum Ising Hamiltonian. But before proceeding therewith, we want to test and optimise the operations and the experimental control (see chapter 5.1). In 2003 Diedrich Leibfried and co-workers from the ion trap group at NIST implemented a geometric phase gate [72]. We use this experiment for calibration and further introduce an experimental method for analysing entanglement of  $N$ -partite quantum systems by the help of an entanglement witness.

In addition, we want to emphasise the differences between stroboscopic algorithms used in quantum computation and the adiabatic evolution of a spin system.

### 10.1. Conditional two qubit geometric phase gate

The geometric- or Berry phase [10, 110] is an intriguing quantum mechanical feature which stayed undiscovered until 1984. It took almost 80 years after the foundations of quantum mechanics, to rigorously explain this phase, although special cases like the Aharonov-Bohm effect were known. Berry's phase arises when a state vector is parallelly displaced around a closed loop in phase space enclosing a point of degeneracy. The geometric phase of such an evolution is proportional to the area enclosed by its trajectory. The original publication regarded the evolution as adiabatic [10], but since then it has been generalised to non-adiabatic evolutions [3] and open loops. Geometric phases are not intuitive and vanish in most experiments or are negligibly small compared to other dynamical phases. That is why Berry derived the geometric phase for an adiabatic evolution, where dynamical phases are negligible.

We will now come to the description of a phase gate which makes use of the Berry

## 10. Experiments

phase. Before we move on to the mathematical description of the experiment, we will scheme the sequence of operations. For the conditional force to work properly<sup>1</sup> we have to cool the ions close to their motional ground state (see chapter 7). The trap potential has to be tuned such that the distance between the ions equals an integer multiple of the effective wavelength of the dipole force pattern, i.e. the ions experience the same phase of the pattern. We initialise the ions in the state  $|\downarrow\downarrow\rangle$  and create an electronic superposition state of the two individual ions by applying a  $\pi/2$ -pulse. The resulting superposition state can be written as  $|\rightarrow\rightarrow\rangle = 1/2(|\uparrow\uparrow\rangle + |\downarrow\uparrow\rangle + |\uparrow\downarrow\rangle + |\downarrow\downarrow\rangle)$  in our measurement basis.

Subsequently, we apply a pulse of the optical dipole force (see chapter 8) tuned near-resonant to the stretch mode of the ion crystal, i.e. at the position of the ions the walking wave pattern oscillates at a frequency close to the motional stretch mode (detuning  $\Delta_{\text{walk}} = \omega_{\text{str}} - \delta$ ). The effect of the state dependent force on the states  $|\uparrow\uparrow\rangle$  and  $|\downarrow\downarrow\rangle$  is negligible, since no differential motion is excited. The states  $|\uparrow\downarrow\rangle$  and  $|\downarrow\uparrow\rangle$  are motionally excited. Due to the detuning  $\delta$  from the stretch mode, the driving force is asynchronous. Half of the period, given by  $t = 2\pi/\delta$ , the differential motion of the ions is excited, whereas in the second half the driving force gets out of phase by more than  $180^\circ$  and the motion is decelerated. In the co-rotating frame of the stretch mode phase space the ground state wave function gets displaced. The effect of this

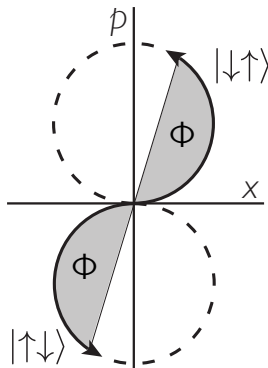


Figure 10.1. – Effect of the displacement pulse in the phase space of the co-rotating frame of the stretch mode: The plot shows the trajectory on which the two states  $|\uparrow\downarrow\rangle$  and  $|\downarrow\uparrow\rangle$  are taken through phase space. The enclosed area (shaded) corresponds to the geometric phase  $\Phi$  acquired during the evolution.

“displacement pulse” on the ions can be interpreted as a cyclic evolution in phase space, see Fig. 10.1. The amplitude  $\Omega_D$ , which corresponds to the radius of the circle in phase space, is mainly determined by the laser beam intensity of the beams generating the optical dipole force and the detuning  $\delta$ . The acquired geometric phase of the

<sup>1</sup>The ions have to be localised with respect to the force pattern, if otherwise the ions’ wave packets are smeared out over the force pattern, the dipole force does not achieve the desired effect.

### 10.1. Conditional two qubit geometric phase gate

contributions  $|\uparrow\downarrow\rangle$  and  $|\downarrow\uparrow\rangle$  reads as

$$\Phi = \left( \frac{\Omega_D}{\delta} \right)^2 (\sin(\delta t) - \delta t). \quad (10.1)$$

By choosing appropriate laser beam intensities, we can tune the acquired phase to  $\Phi = \pi/2$ . We include a spin-echo pulse (see section 6.4) in the middle of the experiment to minimise decoherence effects. A subsequent  $\pi/2$ -pulse ideally transforms<sup>2</sup> the state into a maximally entangled Schrödinger cat state [88] in our measurement basis. The experiment takes on the form of a Ramsey experiment, its pulse protocol is summarised in Fig. 10.2.

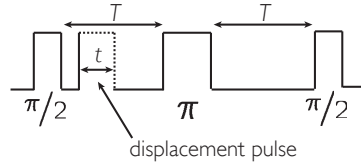


Figure 10.2. – Pulse sequence of the experiment as given in the text: A coherent displacement pulse of variable duration  $t$  is embedded in a Ramsey experiment, see section 6.4.

We continue with the mathematical description of the experiment. We begin with the system initialised close to the ground state of motion and optically pumped to  $|\downarrow\downarrow\rangle$ :

$$\Psi_{\text{ini}} = |\downarrow\downarrow\rangle |n \cong 0\rangle. \quad (10.2)$$

We apply a  $R(\pi/2, \pi/2)$  pulse (see chapter 6.4.3) which rotates both spins individually into a superposition state

$$\Psi_1 = R(\pi/2, \pi/2)\Psi_{\text{ini}} = 1/\sqrt{2} (|\uparrow\rangle + |\downarrow\rangle) \cdot 1/\sqrt{2} (|\uparrow\rangle + |\downarrow\rangle). \quad (10.3)$$

The coherent drive of the state dependent optical dipole force displaces the states  $|\uparrow\downarrow\rangle$  and  $|\downarrow\uparrow\rangle$  for a duration  $t$ ,

$$\Psi_1 \xrightarrow{\text{dipole force}} \Psi_2 = 1/2 \left[ (|\downarrow\downarrow\rangle + |\uparrow\uparrow\rangle) |n \cong 0\rangle + e^{i\Phi(t)} (|\downarrow\uparrow\rangle |\alpha(t)\rangle + |\uparrow\downarrow\rangle |-\alpha(t)\rangle) \right], \quad (10.4)$$

where  $|\alpha\rangle$  represents the coherently displaced motional state at time  $t$  and  $\Phi(t)$  is the accumulated phase. A spin-echo pulse  $R(\pi, 0)$  inverts all the spins, such that (slow) decoherence effects can be reversed within the second half of the experiment (see

<sup>2</sup>Individual qubit rotations do not alter the entanglement of the bi-partite system, it is solely rotated to a different basis.

## 10. Experiments

section 6.4). Together with the final  $R(\pi/2, \pi/2)$ -pulse the wavefunction evolves to

$$\begin{aligned} \Psi_f = R(\pi/2, \pi/2)R(\pi, 0)\Psi_2 = 1/2 \left[ (|\downarrow\downarrow\rangle + |\uparrow\uparrow\rangle) |n \cong 0\rangle \right. \\ \left. + 1/2 e^{i\Phi(t)} (|\downarrow\uparrow\rangle - |\uparrow\uparrow\rangle + |\downarrow\downarrow\rangle - |\uparrow\downarrow\rangle) |\alpha(t)\rangle \right. \\ \left. + 1/2 e^{i\Phi(t)} (|\uparrow\downarrow\rangle - |\uparrow\uparrow\rangle + |\downarrow\downarrow\rangle - |\downarrow\uparrow\rangle) |-\alpha(t)\rangle \right]. \end{aligned} \quad (10.5)$$

The corresponding fluorescence rate takes the following form [72]

$$\begin{aligned} S(t) &= S_0 [P_{\downarrow\downarrow} + 1/2 (P_{\uparrow\downarrow} + P_{\downarrow\uparrow})] \\ &= S_0 1/2 [1 + e^{-|\alpha(t)|/2} \cos(\Phi(t))], \end{aligned} \quad (10.6)$$

where

$$\alpha(t) = i \frac{\Omega_D}{\delta} (e^{-i\delta t} - 1) e^{i\phi_L}, \quad (10.7)$$

which describes a harmonic oscillator driven detuned by  $\delta$  from its resonance frequency.  $\phi_L$  denominates the phase of the displacement drive. See Fig. 10.3 for an experimental

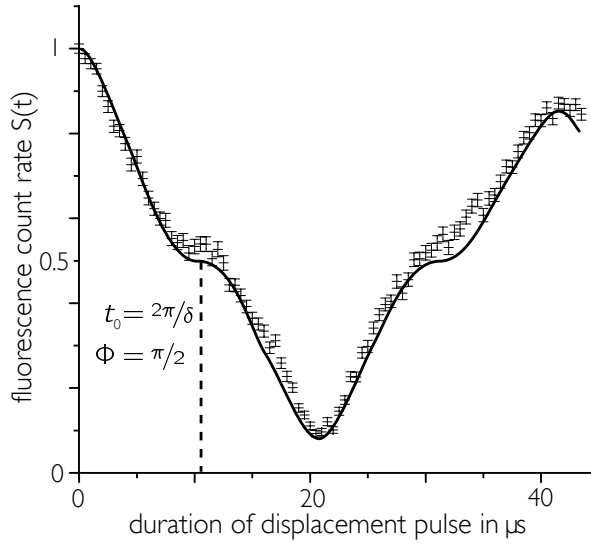


Figure 10.3. – Normalised fluorescence of two ions detected after the experimental protocol depicted in Fig. 10.2.

measurement. The beam intensities of the optical dipole force are adjusted such that the recorded geometric phase for one circle in phase space accounts to  $\Phi(t) = \pi/2$  and the coherent excitation amplitude  $\alpha(t)$  becomes close to zero:  $\alpha(t_0) \approx 0$  at  $t_0 = 2\pi/\delta$ . The gate duration amounts to  $t_0 = 10.05 \mu\text{s}$  and the detuning  $\delta$  from the motional

### 10.1. Conditional two qubit geometric phase gate

stretch mode  $\delta = 2\pi \times 99.5$  kHz. Going back to Eq. 10.5, we consider the final state  $\Psi_f$  at  $\Phi(t) = \pi/2$  and obtain

$$\Psi_f(\Phi(t) = \pi/2) = \frac{1}{\sqrt{2}} e^{-i\frac{\pi}{4}} \left( |\uparrow\uparrow\rangle + e^{i\frac{\pi}{2}} |\downarrow\downarrow\rangle \right) |0\rangle. \quad (10.8)$$

At the “gate” duration  $t_0 = 2\pi/\delta$  we have deterministically created a GHZ state.

**Experimental results** To prove the entanglement of the final state, we consider the Bell state fidelity  $\mathcal{F} = \langle \Psi | \rho | \Psi \rangle$  which has to fulfil  $\mathcal{F} > 1/2$  [109]. For the special case of a GHZ state, this is particularly simple, as the density matrix  $\rho$  only contains four non-zero entries. To determine the coherences of the density matrix, we use the parity  $\Pi(\phi) = P_{\uparrow\uparrow} + P_{\downarrow\downarrow} - (P_{\uparrow\downarrow} + P_{\downarrow\uparrow})$ , see Appendix A. This parity oscillates two times in  $2\pi$  for two-particle entanglement. Via the amplitude  $C$  of this oscillation, we can determine the coherences of the density matrix [11]. The Bell state fidelity of the deterministically

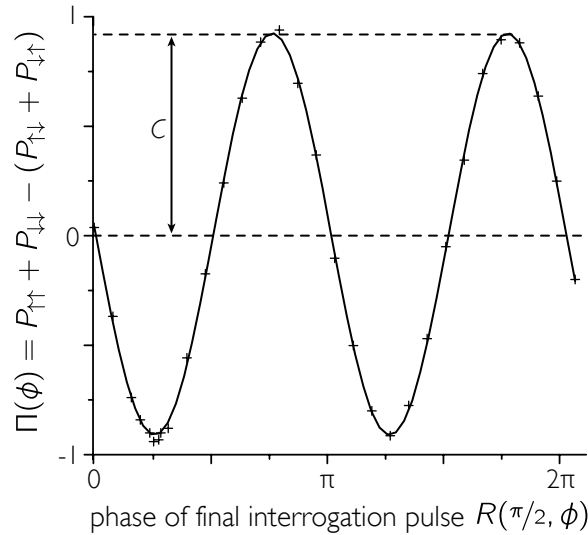


Figure 10.4. – The parity  $\Pi(\phi)$  is plotted versus the phase  $\phi$  of the interrogation pulse  $R(\pi/2, \phi)$ . It shows two oscillations within  $2\pi$ , the contrast  $C$  is determined by the best fit method and amounts to  $C = 91.7\%$ .

created entangled final state amounts to

$$\begin{aligned} \mathcal{F} &= \langle \Psi | \rho | \Psi \rangle = \frac{1}{2} (P_{\uparrow\uparrow} + P_{\downarrow\downarrow}) + |\rho_{\uparrow\downarrow}| \\ &= \frac{1}{2} (P_{\uparrow\uparrow} + P_{\downarrow\downarrow}) + \frac{C}{2} = \frac{97.2\%}{2} + \frac{91.7\%}{2} = 94.5\%. \end{aligned} \quad (10.9)$$

## 10. Experiments

The system is highly entangled, since  $\mathcal{F} \gg 1/2$ , which is the boundary for this *entanglement witness* [49, 109]. Entanglement witnesses rely on the geometrical property, that the set of separable states is convex, and provide a useful tool to prove entanglement in experiments, however, we want to point out, that they in general do not fulfil the conditions of an entanglement measure [100].

**Error considerations** The main contribution to the lacking fidelity is spontaneous emission during the displacement drive, for the used Raman intensities the estimated decrease of contrast amounts to 3 – 4%, for details see section 3.4. This error can be minimised by increasing the detuning  $\Delta_R$  of the virtual level  $|v\rangle$ . For the fluorescence data (Fig. 10.3), the finite detection duration  $t_{\text{det}} = 20 \mu\text{s}$  decreases the contrast by  $\approx 1\%$ . The remaining infidelity is due to Raman beam power fluctuations, magnetic field fluctuations and off-resonant excitation of the com-mode. Diminishing the detuning  $\delta$ , we could further reduce the latter point, however, the relative error of the detuning  $\delta$  in case of changing transition frequencies due to magnetic field fluctuations would increase. We are currently working on a refined magnetic field drift compensation circuit.

We did not intend to beat the fidelity record of this kind of gate operations [72]. We only wanted to use this experiment to calibrate our interactions. Thus, we will proceed with quantum simulation experiments after a short examination of differences between these two types of experiments.

## 10.2. Adiabatic simulation of quantum spin Hamiltonians

An envisioned universal quantum computer [35] should be able to simulate the dynamics of any quantum system. Therefore the dynamics of a quantum system has to be formulated in terms of a quantum algorithm composed out of quantum logic gates. For generic quantum algorithms, one needs a universal set of gates. For example, a single qubit (phase shifter) gate and a conditional phase gate constitute a universal set of gates. Recently the fidelity of a two qubit phase gate has been pushed to 99.3% [6]. Yet, to be able to achieve fault tolerant quantum computing it is stated [106, 4, 91], that one has to achieve gate infidelities of the order of  $10^{-3} - 10^{-5}$ . Furthermore, one has to include an overhead of 5 – 9 ancilla qubits for each logical qubit to implement error correction [117, 119, 44]. Optimistically rated, it will take another decade to achieve these conditions.

However, simulation of quantum mechanical systems can also be carried out by using an analogue quantum simulator. The idea of simulating quantum mechanical systems with different quantum mechanical systems was raised by R. Feynman [35] in 1982. In 2004 D. Porras and I. Cirac [103] proposed a scheme how to implement the simulation of quantum spin Hamiltonians in an ion trap. Quantum spin Hamiltonians describe interesting dynamics of a broad variety of solid state systems such as quantum phase transitions, or high  $T_c$ -superconductivity.

We chose the quantum Ising Hamiltonian which is the simplest quantum spin Hamiltonian, yet it shows interesting dynamics already for a chain of spins. This work is to be seen as a feasibility study for simulating the dynamics of quantum spin Hamiltonians in an ion trap. We demonstrate the basic building blocks for simulating a rich family of Hamiltonians such as the  $XY$ -model or the Heisenberg model.

During the next subsections we will adapt the idea of quantum simulations, formulated in chapter 1, to the context of simulating quantum spin Hamiltonians, discuss why it is interesting to simulate the quantum Ising model in one dimension and then proceed with the experimental implementation of the simulation with two spins.

**Spin system** The spin-1/2 to be simulated is represented by two hyperfine ground state levels of  $^{25}\text{Mg}^+$  ions spanning a two-level system (see section 3.4). Each ion simulates a single spin-1/2. To illustrate the dynamics of single spins we employ the Bloch sphere.

**Magnetic field** External magnetic fields are simulated by coherently coupling the two spin states [5, 127]. We use the spin rotation matrix  $R(\theta, \phi)$  introduced in section 6.4.3 to describe this coupling. The orientation of the effective magnetic field is governed by the variable  $\phi$  and determines the rotational axis. Experimentally we provide the coherent coupling by electromagnetic fields (TPSR transitions, see section 3.4, or directly via radiofrequency, see section 4.7). The rotational axis  $\phi$  is determined by the phase

## 10. Experiments

of the respective pulse and can be illustrated by distinct meridians of the spins on the Bloch sphere. See Fig. 10.5 for an illustration. Initialising the spin (state vector on the

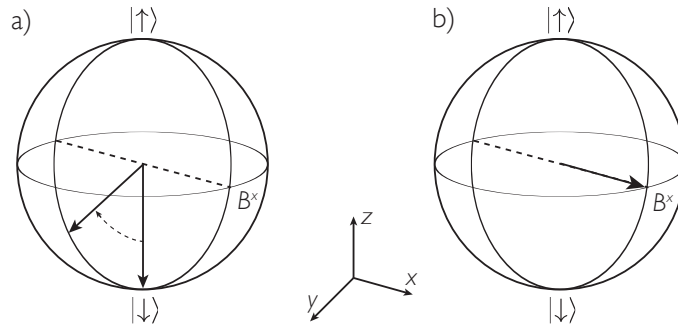


Figure 10.5. – Simulation of a magnetic field by an effective magnetic field. In a) the spin is initialised in state  $|\downarrow\rangle$  and upon applying an effective magnetic field  $B^x$ , the spin precesses about the x-axis. In b) the spin is initialised in the eigenstate of the system and remains in its orientation.

Bloch sphere) in state  $|\downarrow\rangle$ , the coherent coupling can be visualised as the precession of the spin e.g. around the x-axis. If the spin is aligned with the x-axis and we apply the same coupling, the system will not show any dynamics since it is initialised in its eigenstate.

**Spin-spin coupling** The ions in the trap are spatially separated by a distance of the order of  $4\ \mu\text{m}$  which renders any direct coupling between their spins negligible. Instead, the effect of the spin-spin interaction is evoked by the in- or decrease of Coulomb energy between the ions due to action of a state dependent optical dipole force (see chapter 8). The distance between the spins is affected conditionally on the mutual orientation of their spins.

### 10.2.1. Quantum Ising model

The well-studied classical Ising model [55] in one dimension does not show a phase transition, yet it exhibit regions where its correlation length [108] becomes very large. Interestingly, in the scaling limit (lattice spacing  $a \rightarrow 0$ ) the partition function of the classical Ising chain can be mapped to a single quantum spin, and the lattice spacing can be interpreted as an imaginary time. The transfer from one site to the next in the classical model is similar to an evolution in imaginary time [108]. The same mapping can be applied to higher dimensions, therefore the dynamics of a 1D quantum Ising model resembles the dynamics of a 2D classical spin model.

## 10.2. Adiabatic simulation of quantum spin Hamiltonians

The temperature which plays the role of the order parameter in classical models is replaced by a different coupling constant. Thermal fluctuations in classical models usually freeze out when approaching the absolute zero point of temperature, whereas pure quantum phase transitions only occur at  $T = 0$  and are driven by quantum fluctuations. Thus moving away from  $T = 0$  one will observe an interplay between thermal fluctuations and quantum fluctuations. In the following all considerations will be taken out at  $T = 0$ , in our simulation experiments thermal fluctuations are negligible.

The Hamiltonian describing the quantum Ising model on a linear chain of spins consists of two parts

$$\begin{aligned}
 H_{\text{Ising}} &= H_B + H_J \\
 &= \underbrace{-B^x \sum_i \sigma_i^x}_{\text{external magnetic field}} - \underbrace{\sum_{i>j} J_{ij} \sigma_i^z \sigma_j^z}_{\text{spin-spin coupling}}.
 \end{aligned} \tag{10.10}$$

where the index  $i$  accounts for spins residing on discrete lattice sites. The eigenstates of  $\sigma_i^z$  represent the two possible orientations of an *Ising spin* [108] in our measurement basis, we will denote these  $|\uparrow\rangle$  and  $|\downarrow\rangle$ .

The Pauli matrix  $\sigma^x$  of the first term of the Hamiltonian is off-diagonal with respect to the measurement basis, therefore it induces quantum mechanical tunnelling [108] between the spin states  $|\uparrow\rangle$  and  $|\downarrow\rangle$ . This can be understood as the action of a magnetic field oriented in  $x$ -direction interacting with each spin individually.

Neglecting the spin-spin interaction term for a moment and only considering the term  $H_B$ , representing the magnetic field ( $B^x > 0$ ,  $J_{ij} = 0$ ), we find its ground state to be all spins aligned with the external magnetic field, a paramagnetically ordered state.

The latter term  $H_J$  represents the spin-spin interaction. It is diagonal in our measurement basis and prefers a global ferromagnetic or antiferromagnetic alignment of the spins depending on the sign of the coupling matrix  $J$ . For the coupled spin system ( $B^x = 0$ ,  $|J_{ij}| > 0$ ), we have to discriminate between two scenarios:

- $J_{ij} > 0$ ,  $B^x = 0$  The spin-spin coupling is ferromagnetic, the coupling term tends to align adjacent spins in a parallel manner, the state of lowest energy or ground state of solely this term of the Hamiltonian corresponds to a superposition of the two ferromagnetic states  $c_1 |\uparrow\uparrow\uparrow \dots\rangle + c_2 |\downarrow\downarrow\downarrow \dots\rangle$ ,  $c_i \in \mathbb{C}$ ,  $\sum_i |c_i|^2 = 1$ .
- $J_{ij} < 0$ ,  $B^x = 0$  The spin-spin coupling is anti-ferromagnetic, the energetically preferred state is  $c_1 |\uparrow\downarrow\uparrow \dots\rangle + c_2 |\downarrow\uparrow\downarrow \dots\rangle$ ,  $c_i \in \mathbb{C}$ ,  $\sum_i |c_i|^2 = 1$ .

**Quantum phase transition** We begin the simulation of the spin system with zero spin-spin coupling ( $J_{ij} = 0$ ) in the ground state of the first term of the Hamiltonian

## 10. Experiments

$-B^x \sum_i \sigma_i^x$ . Thus the state is given by all spins aligned with the effective magnetic field (see Fig. 10.5). Following the adiabatic theorem [12, 60], the system will stay in its

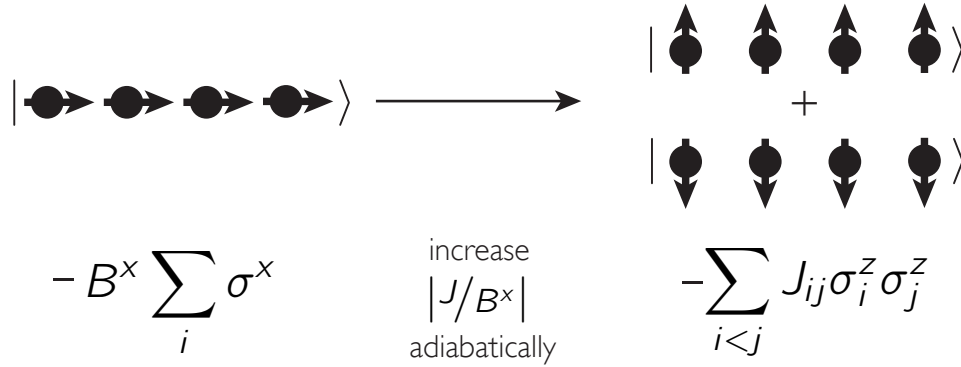


Figure 10.6. – Adiabatic evolution ferromagnet ( $J_{ij} > 0$ ): The evolution begins in the ground state of the Hamiltonian simulating the external magnetic field. All spins point along the axis of the effective magnetic field which is kept fixed all the time. Then one adiabatically increases the spin-spin coupling  $J_{ij}$ . The system evolves to the ground state of the coupled system which is of ferromagnetic order for  $J_{ij} > 0$ . Since there is no preferred direction for the spins, we end up in a coherent superposition of maximally magnetised states (normalisation omitted).

ground state when we adiabatically increase the spin-spin coupling  $J_{ij}$  of the Hamiltonian  $H_J$ . For  $|J_{ij}| \gg B^x$  the spin-spin interaction term dominates the Hamiltonian and we end up close to the ground state of  $H_J$ , which for  $J_{ij} > 0$  is given by ferromagnetic order as can be seen in Fig. 10.6. In the thermodynamic limit of infinitely many spins, we would observe a quantum phase transition between the paramagnetic phase ( $|J_{ij}| \ll B^x$ ) and the ferromagnetic phase, or antiferromagnetic phase, respectively, ( $|J_{ij}| \gg B^x$ ), taking place at a critical parameter  $|J_{ij}| \cong B^x$ .

### 10.2.2. Implementation

The experimental protocol is illustrated in Fig. 10.7, the enumeration refers to the encircled numbers within the figure.

1. We finetune the trapping potential such that  $d_{\text{inter-ion}} = 18 \times \lambda_{\text{eff}} \approx 3.56 \mu\text{m}$ . This corresponds to an axial confinement of  $\omega_z = 2\pi \times 2.14 \text{ MHz}$ . We cool two  $^{25}\text{Mg}^+$  ions to the ground state of axial motion  $\bar{n}_{\text{str}} \approx \bar{n}_{\text{com}} \approx 0.04$  and optically pump them to the state  $|\downarrow\downarrow\rangle$ .
2. We simultaneously rotate both spins into an electronic superposition state by applying a radiofrequency pulse  $R(\pi/2, \pi/2)$  acting on both ions individually (see

## 10.2. Adiabatic simulation of quantum spin Hamiltonians

section 6.4.3).

The spin system is initialised in the state  $\Psi_i = |\rightarrow\rangle^{\otimes 2} = 1/\sqrt{2}(|\uparrow\rangle + |\downarrow\rangle)^{\otimes 2}$ . This initial state  $\Psi_i$  is the eigenstate of lowest energy of the term describing the effective magnetic field  $-B^x \sum_i \sigma_i^x$ . In our measurement basis, this initial state expresses as

$$\Psi_i = 1/2(|\downarrow\downarrow\rangle + |\downarrow\uparrow\rangle + |\uparrow\downarrow\rangle + |\uparrow\uparrow\rangle). \quad (10.11)$$

The probabilities  $P_{\downarrow\downarrow}$  and  $P_{\uparrow\uparrow}$ , which represent the probability of detecting the system in state  $|\downarrow\downarrow\rangle$ , or  $|\uparrow\uparrow\rangle$ , respectively, amount to  $P_{\downarrow\downarrow} = P_{\uparrow\uparrow} = 25\%$ .

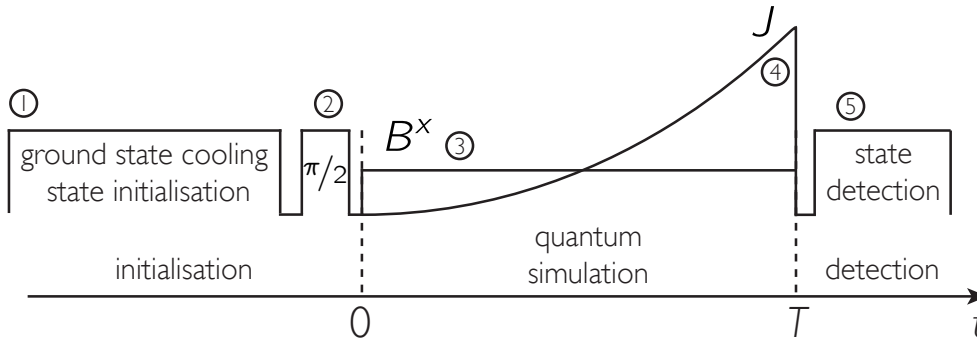


Figure 10.7. – Pulse protocol of the adiabatic simulation: During the quantum simulation, both interactions  $B^x$  and  $J$  are applied simultaneously.

3. Subsequently, we switch on the effective magnetic field  $R(\theta, 0)$ . The state vectors of both individual Bloch spheres “rotate about their pointing directions” and, therefore, remain in the eigenstate of  $H_B$ , see section 10.2. The amplitude of this effective magnetic field is given by the Rabi frequency of the equivalent transition. We deduce a related amplitude of the effective magnetic field  $B^x$  of  $2\pi \times 4.24$  kHz from a rotation period  $\theta = 2\pi$  in  $118 \mu\text{s}$ .
4. Simultaneously, we switch on and adiabatically increase the effective spin-spin interaction<sup>3</sup> starting at  $J(t=0) = 0$  to a maximum value  $|J(T)| = |J_{\text{max}}|$  at time  $t = T$  being the total duration of the simulation. The temporal shape of the adiabatic ramp is illustrated in Fig. 10.8. Ramping up the spin-spin interaction is broken up into discrete steps due to the digital nature of the DACs employed for setting the beam intensities, see Fig. 5.3. We use the walking wave pattern described in chapter 8 with the following parameters. We apply the dipole force pattern detuned by  $\delta = -2\pi \times 250$  kHz to lower frequencies of the stretch mode  $\omega_{\text{str}} = \sqrt{3}\omega_z = 2\pi \times 3.71$  MHz, so the actual frequency difference between the

<sup>3</sup>Note, that for two spins there exists only nearest neighbour interaction, hence,  $J_{ij}$  reduces to  $J_{i,i+1}$  which we refer to as  $J$  in the following

## 10. Experiments

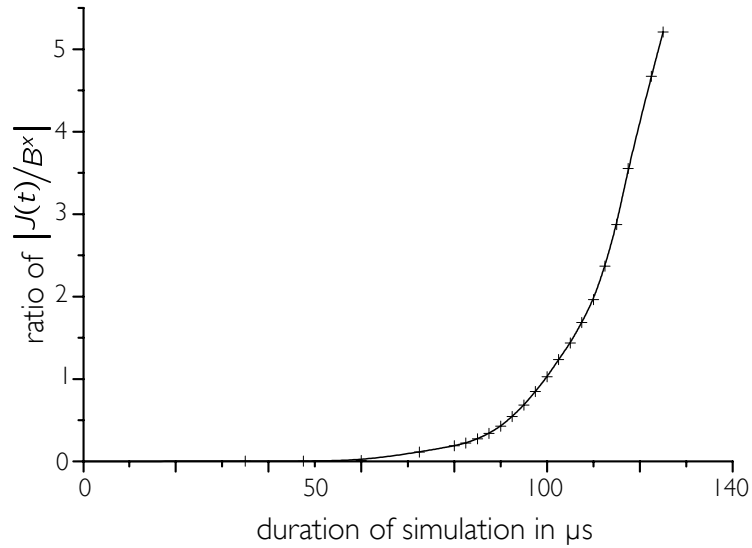


Figure 10.8. – Temporal shape of the adiabatically increasing spin-spin interaction

two Raman beams R1 and R2 amounts to  $\Delta_{\text{walk}} = \omega_{\text{stretch}} - \delta = 2\pi \times 3.45$  MHz. The maximum value  $|J_{\text{max}}|$  of the spin-spin interaction corresponds to  $|J_{\text{max}}/B^x| = 5.2$  which we achieve with Raman beam powers of 2.25 mW for each Raman beam R1 and R2, beam waists of  $45 \mu\text{m}$  and a detuning  $\Delta_R$  of the virtual level of  $\Delta_R = 2\pi \times 80$  GHz in the UV. Having reached the maximum value  $|J_{\text{max}}|$ , we switch off both the effective magnetic field and the effective spin-spin interaction concurrently.

5. Finally, we analyse the final state of the simulation via the state sensitive detection technique (see chapter 9). We repeat each experiment for the same set of parameters  $10^4$  times to obtain sufficient statistics.

**Transition from paramagnetic to ferromagnetic order** Initialising the two spins in the ground state of the Hamiltonian  $H_B$  and adiabatically increasing the spin-spin interaction  $|J|$  with  $J > 0$ , we observe a transition from the paramagnetic to a ferromagnetic configuration. Fig. 10.9 shows the population projected to ferromagnetically ordered states  $|\uparrow\uparrow\rangle$  and  $|\downarrow\downarrow\rangle$  plotted in dependence of the fraction  $|J(T)/B^x|$ . We achieve final state probabilities  $P_{\uparrow\uparrow} = P_{\downarrow\downarrow} = 49 \pm 2\%$ , which corresponds to a probability of  $P = P_{\uparrow\uparrow} + P_{\downarrow\downarrow} = 98 \pm 3\%$  of finding the system in a ferromagnetically ordered state.

## 10.2. Adiabatic simulation of quantum spin Hamiltonians

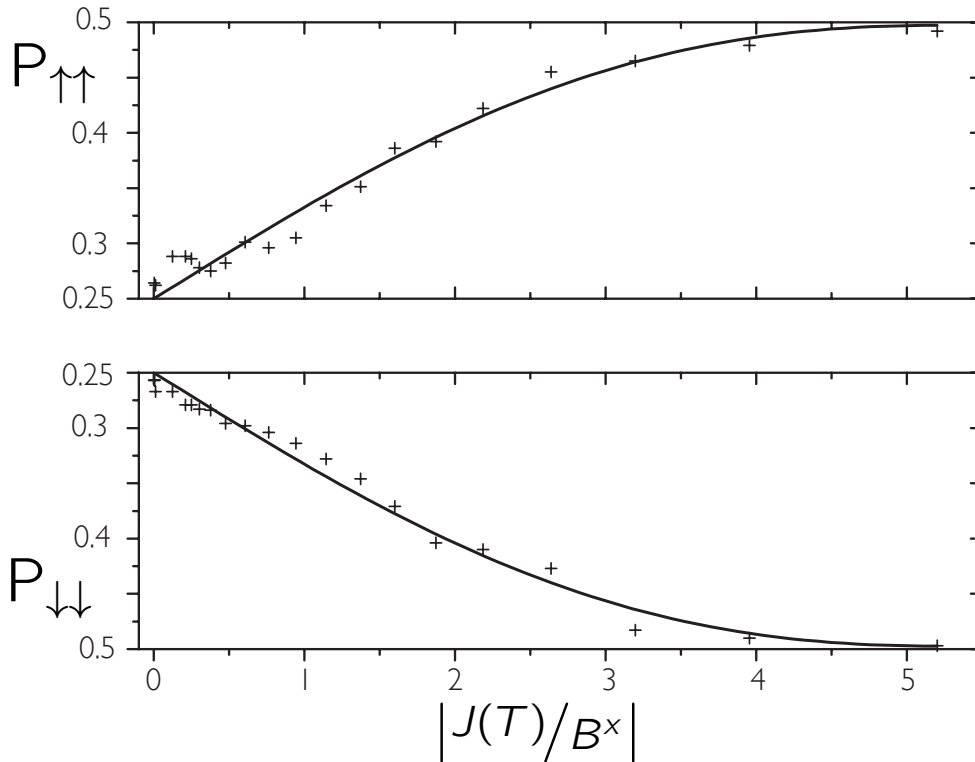


Figure 10.9. – Evolution to the ferromagnetic state: We plotted the probabilities  $P_{\cdot}$  of measuring the final state of the simulation to be  $|\downarrow\downarrow\rangle$  or  $|\uparrow\uparrow\rangle$ , respectively, in dependence of the ratio  $|J(T)/B^x|$ . For the lower plot the population of the state  $|\downarrow\downarrow\rangle$  is displayed in an inverted manner to emphasise the unbroken symmetry of the evolution. The evolution starts in the paramagnetically ordered state  $\Psi_i = 1/2 (|\uparrow\rangle + |\downarrow\rangle)^{\otimes 2}$ . Note that the initial state is projected to each of the states  $|\downarrow\downarrow\rangle$  and  $|\uparrow\uparrow\rangle$  with 25% probability. In each experiment we keep the effective magnetic field  $B^x$  fixed and adiabatically ramp up the spin-spin coupling  $J$  to the maximum value  $|J(T)/B^x|$  given by the abscissa. For  $|J_{\max}/B^x| = 5.2$  we obtain the highest populations  $P_{\uparrow\uparrow} = P_{\downarrow\downarrow} = 49 \pm 2\%$ . Each data point represents the mean value of  $10^4$  experiments. The straight lines represent a theoretic simulations of the effective Hamiltonian for the experimental parameters, see Fig. 10.13 and ref. [103].

To analyse the magnetisation of the system, we consider the ideal final state of the evolution in more detail. From the above mentioned probabilities of measuring the system in state  $|\downarrow\downarrow\rangle$  or  $|\uparrow\uparrow\rangle$ , respectively, we cannot deduce, if the final state of the system is a pure or a mixed state. If the final state was a superposition of two maximally correlated states, we would deduce a magnetisation of zero. For a

## 10. Experiments

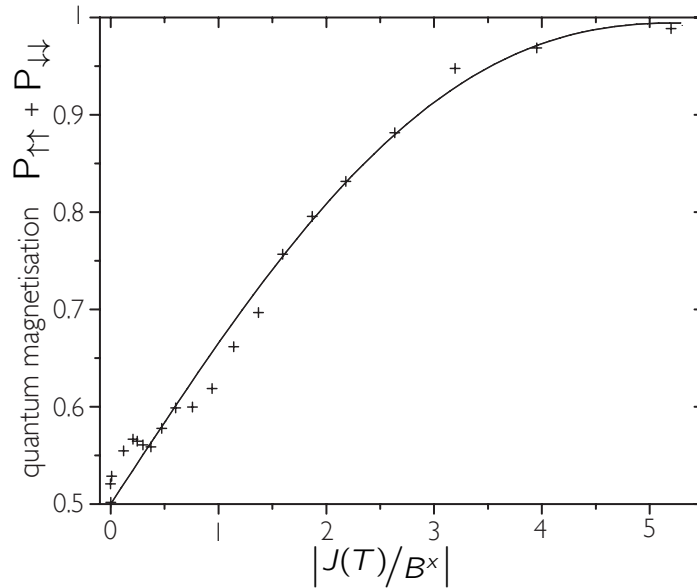


Figure 10.10. – Evolution to the ferromagnetic state: This plot represents the identical data as in Fig. 10.9 plotted in form of the quantum magnetisation  $\mathcal{M}$  defined as  $\mathcal{M} = P_{\uparrow\uparrow} + P_{\downarrow\downarrow}$ . The quantum magnetisation  $\mathcal{M}$  of the final state of the evolution amounts to  $\mathcal{M} = 98 \pm 3\%$ .

statistical mixture, the magnetisation would be 98%, however, in half of the experiments we would measure the system to be in state  $|\downarrow\downarrow\rangle$  or  $|\uparrow\uparrow\rangle$ , respectively. Thus, it is more appropriate to express the results in terms of a spin correlation or a quantum magnetisation  $\mathcal{M}$ , which we define as the sum of the probabilities of measuring the system in one of the ferromagnetic states  $\mathcal{M} = P_{\uparrow\uparrow} + P_{\downarrow\downarrow}$ , for our final state the quantum magnetisation amounts to  $\mathcal{M} = 98 \pm 3\%$ . The quantum magnetisation for the initial state of this two particle system is already 50% since  $\Psi_i = 1/2 (|\uparrow\rangle + |\downarrow\rangle)(|\uparrow\rangle + |\downarrow\rangle) = 1/2 (|\uparrow\uparrow\rangle + |\downarrow\uparrow\rangle + |\uparrow\downarrow\rangle + |\downarrow\downarrow\rangle)$  and thus  $P_{\uparrow\uparrow} = P_{\downarrow\downarrow} = 25\%$ . This high magnetisation of the initial state is related to the limited number of spins. Each additional spin reduces the the quantum magnetisation of the paramagnetic state by a factor of 2. For three particles  $P_{\uparrow\uparrow\uparrow} = P_{\downarrow\downarrow\downarrow} = 12.5\%$  and for four particles  $P_{\uparrow\uparrow\uparrow\uparrow} = P_{\downarrow\downarrow\downarrow\downarrow} = 6.25\%$ .

We can also evolve the system back from the final to the initial state by adiabatically decreasing the spin-spin interaction from its maximum value  $|J(T)/B^x| = 5.2$  down to  $|J(T)| \ll B^x$ .

**Entanglement** In the co-rotating frame, the two ferromagnetic states  $|\downarrow\downarrow\rangle$  and  $|\uparrow\uparrow\rangle$  are degenerate. Since the spin-spin interaction does not prefer any of the two ferro-

## 10.2. Adiabatic simulation of quantum spin Hamiltonians

magnetic states, the final state of the adiabatic simulation is a superposition of the two maximally magnetised states  $|\downarrow\downarrow\rangle$  and  $|\uparrow\uparrow\rangle$ . In order to prove this, we use the scheme presented in section A to verify the entanglement of the final state. The corresponding plot of the parity  $\Pi(\phi) = P_{\uparrow\uparrow} + P_{\downarrow\downarrow} - (P_{\uparrow\downarrow} + P_{\downarrow\uparrow})$  after an additional  $R(\pi/2, \phi)$  pulse of varied phase  $\phi$  is depicted in Fig. 10.11. Via the best fit method, we deduce a contrast

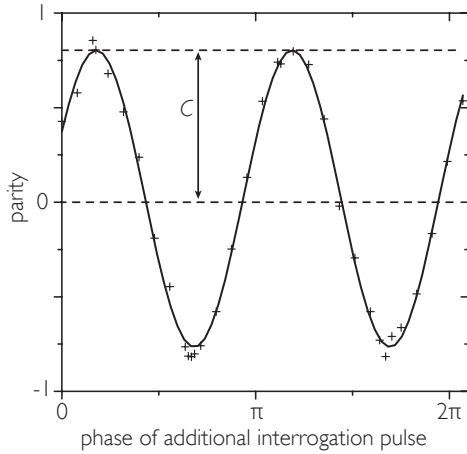


Figure 10.11. – Plot of parity versus the phase of an additional analysis pulse. Analogous to the method described in section A, we introduce a  $R(\pi/2, \phi)$ -pulse after the simulation which is varied in phase  $\phi$ . From the contrast of the parity flopping curve of  $C = 78 \pm 2\%$  and the final state populations we deduce a Bell state fidelity of the final state of the evolution of  $\mathcal{F} = 88 \pm 4\%$  (see text for details). Thus the final state of the evolution is highly entangled. Each data point represents  $10^4$  experiments.

$C$  of the data of  $C = 78 \pm 2\%$ . The related Bell state fidelity of the final state of the evolution amounts to  $\mathcal{F} = \frac{1}{2}(P_{\uparrow\uparrow} + P_{\downarrow\downarrow}) + \frac{C}{2} = 88 \pm 2\%$ . That is, the final state of the adiabatic simulation is deterministically entangled.

**Biased transition** We discussed in section 8.4, that residual differential AC-Stark shifts can lead to contributions of  $B^z\sigma^z$  in the Hamiltonian. These contributions break the degeneracy of the two spin states  $|\downarrow\downarrow\rangle$  and  $|\uparrow\uparrow\rangle$  in the co-rotating frame and the system evolves preferably to state  $|\downarrow\downarrow\rangle$  or  $|\uparrow\uparrow\rangle$ , respectively, depending on the sign of this bias field. For each experiment we carefully cancel differential AC-Stark shifts of the Raman beams (see section 6.5). Residual AC-Stark shifts can also be compensated by detuning the frequency of the effective magnetic field [101] on the order of single kHz. By deliberately introducing a bias field by introducing a differential AC-Stark shift between the Raman beams, we can imbalance the populations and end up in the final state  $\Psi_f = |\downarrow\downarrow\rangle$ . The evolution of this biased transition is shown in Fig. 10.12.

**Adiabaticity** For a strictly adiabatic evolution ( $T \rightarrow \infty$ ) the quantum magnetisation  $\mathcal{M}$  of the final state achievable by a spin-spin coupling of  $|J/B^x| = 5.2$  corresponds to [101]  $\mathcal{M} = 93.4\%$ . Shortening the simulation leads to a steeper increase of the quantum magnetisation for the evolution to the ferromagnetic state and an oscillation of the quantum magnetisation of the final state. Theoretical simulations of the effective

## 10. Experiments

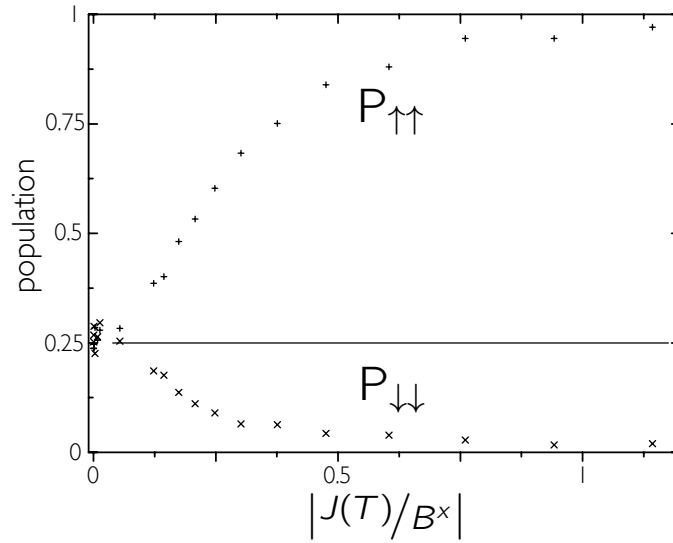


Figure 10.12. – Biased transition: Deliberately introducing a bias field by providing a differential AC-Stark shift between the Raman beams, we can imbalance the evolution such that it ends up in the final state  $\Psi_f = |\downarrow\downarrow\rangle$ .

Hamiltonian for two scenarios (strictly adiabatic evolution and not strictly adiabatic evolution) are depicted on the left hand side of Fig. 10.13. The plot shows, that the faster evolution reaches the maximal quantum magnetisation for smaller values of  $|J/B^x|$  compared to the ideally adiabatic evolution. Moreover, we are able to minimise decoherence by moving to shorter durations of the quantum simulation  $T$ . In the plot on the right hand side of Fig. 10.13, we show a fit of the simulation of the effective Hamiltonian to our measurement data. It indicates that for a larger ratio  $|J/B^x|$ , the final state quantum magnetisation  $\mathcal{M}$  slightly oscillates.

By shortening the experiment duration, we are able to demonstrate, that the final state of the simulation is an entangled state rather than a mixed state and proof, that the transition is due to quantum fluctuations and not due to thermal fluctuations or fluctuating bias fields.

Quantum phase transitions usually occur where energy levels of the ground state and an excited state cross or have an avoided crossing [131]. The finite energy gap between neighbouring levels decreases rapidly as one approaches the thermodynamic limit [17]. For  $N \rightarrow \infty$ , the energy gap at the critical point tends to zero and it becomes impossible to pass this point at finite speed without exciting the system. Thus the system will end up in a quantum superposition of states like

$$|\dots \uparrow\uparrow\downarrow\downarrow\downarrow\downarrow\uparrow\uparrow\uparrow\uparrow\downarrow\downarrow\uparrow\downarrow\downarrow \dots\rangle \quad (10.12)$$

with finite domains of spins pointing up or down and separated by kinks where the

## 10.2. Adiabatic simulation of quantum spin Hamiltonians

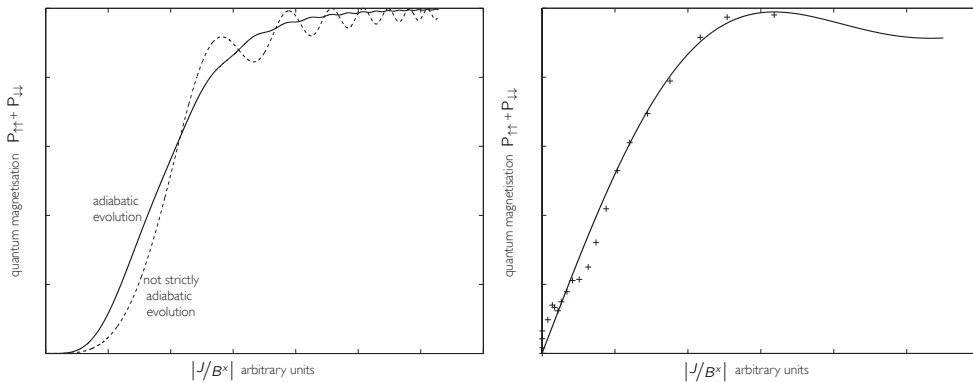


Figure 10.13. – The curves on the left hand side show theoretical simulations of the effective Hamiltonian of the quantum magnetisation in dependence of the ratio  $|J/B^x|$  for two scenarios in a qualitative way: the solid line represents a purely adiabatic evolution of the spin system, and the dashed line shows a faster evolution displaying oscillations of the quantum magnetisation.

The plot on the right hand side shows our experimental data (dots) with a theory fit (straight line) of the evolution. We reach a higher level of quantum magnetisation with our given level of spin-spin coupling  $|J/B^x| = 5.2$  as would have been the case for a purely adiabatic evolution.

polarization of spins changes its orientation [23].

**Transition from paramagnetic to antiferromagnetic order** For a spin-spin coupling  $J_{ij} < 0$  in the Hamiltonian Eq. 10.10, the ground state of the spin-spin interaction Hamiltonian  $H_J$  is given by an antiferromagnetically ordered system,

$$\Psi_f = \frac{1}{\sqrt{2}}(|\uparrow\downarrow\uparrow\downarrow \dots\rangle + |\downarrow\uparrow\downarrow\uparrow \dots\rangle). \quad (10.13)$$

Experimentally this antiferromagnetic interaction can be achieved by using the radial motional modes of the spin chain [103].

Alternatively, we can start the simulation in the excited state  $|\leftarrow\leftarrow\leftarrow \dots\rangle$  of the Hamiltonian  $H_B$  which is given by the spins oriented antiparallel to the effective magnetic field. Upon an adiabatic simulation the spin system will remain in its excited state and end up in the excited state of the Hamiltonian  $H_J$  which is given by the antiferromagnetic order.

An equally valid viewpoint of this experiment interprets the state  $|\leftarrow\leftarrow\leftarrow \dots\rangle$  as the ground state of the Hamiltonian  $-H_{\text{sing}}$ . Because the sign of all spin-spin interactions is also reversed in  $-H_{\text{sing}}$ , it is equivalent to a change of sign in the spin-spin interaction  $J$ . Actually, we do not even have to start in a different initial state, only the orientation

## 10. Experiments

of the magnetic field is inverted, i.e. the phase of the effective magnetic field is changed by  $\pi$ .

We observe final state populations  $P_{\uparrow\downarrow} + P_{\downarrow\uparrow} = 95 \pm 2\%$ . For measuring the fidelity of the preparation of the final state  $1/\sqrt{2}(|\uparrow\downarrow\rangle + |\downarrow\uparrow\rangle)$ , we project it to a ferromagnetic state by applying a  $R(\pi/2, \phi_0)$  pulse, where  $\phi_0$  can be chosen arbitrarily. This ideally rotates the antiferromagnetic state again to the ferromagnetic state

$$1/\sqrt{2}(|\uparrow\downarrow\rangle + |\downarrow\uparrow\rangle) \rightarrow 1/\sqrt{2}(|\uparrow\uparrow\rangle + |\downarrow\downarrow\rangle). \quad (10.14)$$

Then we again apply an additional  $R(\pi/2, \phi)$  pulse which is varied in phase and deduce a Bell state fidelity for the final state of  $80 \pm 4\%$ .

Ideally, the fidelity for creating the antiferromagnetically ordered state is expected to be even higher compared to the ferromagnetic state, since bias fields affect both parts of the wavefunction identically. This is closely related to the existence of decoherence free subspaces in quantum computation [62]. The lacking fidelity compared to the ferromagnetic case has its origin in the transformation from the antiferromagnetic to the ferromagnetic case. This operation reduced the quantum magnetisation of the system to  $\mathcal{M} \cong 80\%$ . We expect, that due to local gradients and therefore partial individual addressing, some population is transferred to the singlet state  $1/\sqrt{2}(|\uparrow\downarrow\rangle - |\downarrow\uparrow\rangle)$ . Being a scalar, this state remains unaffected by the applied rotation of the analysis pulse and appears as a loss of population in the states  $|\uparrow\uparrow\rangle$  and  $|\downarrow\downarrow\rangle$ .

**Excitation of motional states during the evolution** By adopting the walking wave scheme for the adiabatic evolution, there arises another parallel to the above described geometric phase gate. For the detuned driven quantum mechanical oscillator [18], the driving force is in-phase for half a period and out-of-phase for the second half of the driving period. Therefore, the motion of the ions is excited and again de-excited during one oscillation cycle of duration  $1/\delta$ , where  $\delta$  is the detuning from the respective motional mode. For the geometric phase gate, one stops the evolution after a full cycle, exactly at the origin of the evolution, where the internal and external degrees of freedom are disentangled. We would also like to adopt this scheme for the quantum simulation. We adiabatically ramp up the spin-spin interaction which makes the system undergo an evolution in phase space, it carries out circles of increasing amplitude, see Fig. 10.14. Ideally, one would stepwise increase the amplitude of the spin-spin interaction close to the point when the driving force re-phases, i.e. at the origin of phase space.

We face two constraints. First, we should not leave the Lamb-Dicke regime upon coherently exciting the ions' motion during the simulation. Thus, the individual circles should be small compared to the geometric phase gate,  $\delta_{\text{sim}} \gg \delta_{\text{gate}}$ . Second, we should not terminate the simulation, when the internal degrees of freedom are strongly entangled with the ions' motion which results in errors of the simulation [101]. Ideally, we terminate the simulation, when  $|n\rangle \cong 0$ .

### 10.3. Summary: Quantum gates versus quantum simulations

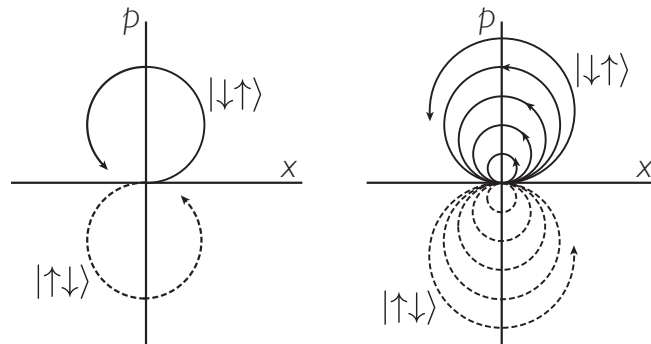


Figure 10.14. – Phase space representation of evolutions: On the left hand side the evolution of the geometric phase gate, where one stops the evolution in the origin, at minimum excitation. On the right hand side a possible realisation of an adiabatic quantum simulation. The spin-spin interaction is increased in discrete steps each time when the state vectors are at the origin of phase space. The radius of the circles represents the amplitude of the dipole force and the length of the vector from the origin to a certain point reflects the motional excitation present in the system.

### 10.3. Summary: Quantum gates versus quantum simulations

The nature of quantum gates or algorithms used for quantum computation is stroboscopic. All pulses are applied for distinct durations<sup>4</sup> without temporal overlap. Considering Fig. 10.3, we observe that the system evolves to an entangled state at the “gate” duration  $t_0 = 2\pi/\delta$ . Prolonging the displacement pulse, the system returns to an unentangled state at time  $t_1 = 4\pi/\delta$ . The displacement pulse needs to be switched off after the correct duration. This is the reason for the term *stroboscopic*.

Adiabatic simulation experiments are different. Operations or interactions are applied simultaneously, the evolution of the system is adiabatic. Once the system has evolved to its final state, it will remain in this state in spite of incessantly applying interactions.

<sup>4</sup>Recently the Innsbruck quantum computation group implemented a quantum gate using adiabatic pulse shaping [6], this is not to be confused with our work, they optimise pulse durations by switching them on and off adiabatically.

## 10. Experiments

## Conclusion and outlook

The work presented in this thesis began with setting up an ion trap apparatus suitable for quantum simulation experiments. That is, high secular frequencies for both radial and axial directions for efficient ground state cooling, and yet a low heating rate for being able to run experiments with durations of several milliseconds. This included simulations, design, and fabrication of the ion trap. We have designed a custom vacuum recipient allowing for laser access from many directions, a vacuum apparatus allowing for an UHV ( $10^{-11}$  mbar) and an optical imaging system capable of resolving single ions (down to  $1\ \mu\text{m}$ ).

To be able to manipulate and read out the state of the ions via optical transitions in the deep UV, we have designed, simulated and built laser systems consisting of infrared fibre lasers and two subsequent highly efficient second harmonic generation cavities ( $> 350\ \text{mW}$  at  $280\ \text{nm}$ ). Furthermore, we stabilised frequency and intensity of laser beams, designed and realised a coherent frequency shifting and switching apparatus and electronics to control the experiment. Repetitively, we had to replace individual defect fibre lasers by dye lasers which had to be fibre-coupled to be integrated into the existing setup.

After having successfully photoionised and loaded first ions, we optimised the parameters to be able to deterministically load and transfer single ions from the loading zone to the experimental zone. We succeeded in driving first coherent two-photon stimulated Raman transitions and used these to identify, locate and eliminate disturbing influences. Subsequently, we worked for about a whole year on resolved sideband cooling until we achieved successful ground state cooling of several ions ( $\bar{n} < 0.05$ ). Being able to prepare a two-ion system in the motional ground state, we implemented optical dipole forces to coherently excite the ions' motion and simulated spin-spin interactions. We entangled two ions via a geometrical phase gate [72] (fidelity  $> 94\%$ ) and refined the detection scheme to state-sensitively detect the states of several ions.

Finally, we demonstrated a proof-of-principle experiment on simulating quantum spin Hamiltonians using trapped ions. We simulated the smallest non-trivial quantum spin model, namely the quantum Ising model for two spins. In this simulation, two hyperfine ground levels of trapped  $^{25}\text{Mg}^+$ -ions constitute individual spins. The interaction with an external magnetic field is simulated by coherently coupling the atomic levels via laser and radiofrequency radiation. The Ising interaction is simulated using optical dipole forces, where the effective interaction is mediated by the Coulomb energy of the linear ion chain. We show the transition from a paramagnetically ordered system to a system

## 10. Experiments

of (anti-)ferromagnetic order, respectively. Moreover, we prove that this transition which is to become a quantum phase transition in the thermodynamic limit of infinitely many particles, is driven by quantum fluctuations which dominate the dynamics of such systems at the absolute zero-point of temperature rather than thermal fluctuations absent at 0 K. This is verified by the fact that the final state of our (reversible) adiabatic evolution is highly entangled and close to a Bell state.

- Perpetuating the simulation of quantum spin models, the next step which could be pursued is scaling up the number of particles and thereby observing a qualitative change of the transition curve from the smooth transition we showed for two particles to a veritable quantum phase transition for a larger number of particles. Simulations predict, that this transition for spin chains of the order 10 ions behaves like a transition close to the thermodynamic limit [101]. Thus, a veritable quantum phase transition might be observed already for a moderate number of spins. Scaling the current setup to higher numbers of ions demands a change from the axial modes of the ion crystal to the radial modes due to the fact that the dipole force pattern will not be applicable for chains of ions with varying mutual distances between the individual ions. Furthermore the ground state cooling scheme can be simplified via simultaneously addressing the radial modes. On the required modification of the laser setup we already commented in section 4.6.3.
- Other proof-of-principle experiments apart from the quantum Ising model which could be addressed include the XY-model or the Heisenberg model [103]. The Bose-Hubbard model and thus Bose-Einstein-Condensation can be simulated in an ion trap [102], or the spin-boson model [104] showing revivals of oscillations. Apart from these many-ion-simulations there are other Hamiltonians which allow for implementation in an ion trap like the simulation of quantum walks. For this experiment tossing a coin is represented by creating a superposition of internal states. This information is transferred to the vibrational modes by employing the same dipole force mechanism as employed in this thesis. After a few steps, different phase space trajectories begin to overlap and interfere which gives rise to fascinating non-classical dynamics. Or another possible experiment of completely different subject is the simulation of particle creation in the early universe [113]. For this experiment the trapping potential has to be ramped up non-adiabatically, thereby creating squeezed states of motion of one or several ions. To draw the analogy to the early universe the phonons (only appearing pairwise) can be interpreted as particle-antiparticle creation processes taking place in an inflationary expanding universe.
- On longer time-scales, one could imagine to move from the massive 3D trap to a chip design [21, 121, 116]. This transitions involves new technical challenges

### 10.3. Summary: Quantum gates versus quantum simulations

which are currently under investigation such as novel loading schemes [19] or anomalous heating effects [29] due to the proximity to electrical surfaces. Having gained experience with surface traps one can think of extending these traps to two dimensional arrays [63]. Scaling quantum simulation experiments to two dimensions exceptionally depends on the availability of high power laser sources in order to introduce sufficiently strong spin-spin interactions. This is due to the fact that for two-dimensional simulation experiments the inter-ion spacings will presumably be larger than in the reported experiments.

This dissertation summarises the work carried out between October 2004 and July 2008. In the meantime the realisation of the above mentioned quantum walk experiment has been addressed both by Tobias Schätz's group (see ref. [112]) as well as R. Blatt's group (see ref. [130]). By the latter group also the *Zitterbewegung* has been simulated in a quantum simulation experiment of the Dirac equation (see ref. [41]).

Based on my experience with single frequency high power lasers, I have been hired by Toptica, a well-known supplier of lasers for the scientific community, to follow a new approach in developing even higher narrowband laser beam powers based on Raman amplification of narrowband sources. Within the near future, these novel high power laser sources might close the whole wavelength gap between the gain regions of ytterbium (around 1060 nm) and erbium (around 1500 nm), in which no suitable gain material existed yet to build high power narrow linewidth lasers. In turn, this might pave the way for large scale quantum simulation experiments based on trapped ions.

## 10. Experiments

## A. Derivation of an entanglement witness

In general, diagnostics of entanglement in several ion systems is a difficult task and one has to perform state tomography [50] of the coupled system. For a two spin system this involves up to  $4 \times 4$  entries to be measured. However, the prepared state contains a special class of entanglement. It is called a Greenberger, Horne, Zeilinger (GHZ) state<sup>1</sup> [46, 45] or Schrödinger *cat* state. A general GHZ state reads

$$|\Psi\rangle_{\text{GHZ}} = 1/\sqrt{2} \left( |\uparrow\rangle^{\otimes N} + e^{i\phi_0} |\downarrow\rangle^{\otimes N} \right). \quad (\text{A.1})$$

The density matrix of this state solely consists of 4 non-zero entries.

Thus for measuring the entanglement of an experimentally created state, we have to measure the directly accessible populations  $P_{N\uparrow}$  and  $P_{N\downarrow}$  ( $P_{N\uparrow}$  is the probability of finding the system in state  $|\uparrow\rangle^{\otimes N}$ , see section 9) and the far off-diagonal matrix elements  $\rho_{N\uparrow\downarrow}$  expressing the coherences between the states  $|\downarrow\rangle^{\otimes N}$  and  $|\uparrow\rangle^{\otimes N}$ . The fidelity  $\mathcal{F}$  of having created a GHZ states then reads

$$\mathcal{F} = \langle \Psi | \rho | \Psi \rangle = 1/2 (P_{N\uparrow} + P_{N\downarrow}) + \rho_{N\uparrow\downarrow}. \quad (\text{A.2})$$

For measuring the coherence term  $\rho_{N\uparrow\downarrow}$  of the final state we apply an additional  $\pi/2$  interrogation pulse which we vary in phase  $\phi$ . This can be represented in form of a unitary transformation,

$$U(\phi) = \bigotimes_{i=1}^N R_i(\pi/2, \phi), \quad (\text{A.3})$$

where  $R_i$  represents the rotation matrix (see section 6.4.3) acting on spin  $i$ . The GHZ state is transformed to

$$\begin{aligned} U(\phi)\Psi_{\text{GHZ}} &= \left(\frac{1}{\sqrt{2}}\right)^{N+1} \bigotimes_{i=1}^N [ (|\downarrow\rangle - ie^{i\phi}|\uparrow\rangle) + e^{i\phi_0}(-ie^{-i\phi}|\downarrow\rangle + ie^{i\phi}|\uparrow\rangle) ] \\ &= \sum_{j=1}^{2^N} c_j |j\rangle, \end{aligned} \quad (\text{A.4})$$

---

<sup>1</sup>Strictly speaking GHZ states are defined for particle numbers  $N > 2$ , but the scheme presented here can also be applied for two particles

### A. Derivation of an entanglement witness

where the state  $|j\rangle$  takes on all possible spin orientations of  $N$  spins and the coefficients  $c_j$  are given by [70]

$$c_j = 2^{-\frac{N+1}{2}} (-ie^{i\phi})^{n_1(j)} \left[ 1 + (-1)^{n_1(j)} e^{i(\phi_0 - N\phi - N\pi/2)} \right]. \quad (\text{A.5})$$

The function  $n_1(j)$  counts the number of spins of orientation  $|\downarrow\rangle$  in  $|j\rangle$ . The probability of measuring  $k$  ions in state  $|\downarrow\rangle$  is given by

$$P_k = \sum_{\{j: n_1(j)=k\}} |c_j|^2 = 2^{-N} \binom{N}{k} \left[ 1 + (-1)^k \cos(\phi_0 - N\phi - N\pi/2) \right]. \quad (\text{A.6})$$

Using the binomial theorem we can construct the parity  $\Pi$  [70]

$$\Pi(\phi) \equiv \sum_{k=0}^N (-1)^k P_k = \cos(\phi_0 - N\phi - N\pi/2). \quad (\text{A.7})$$

The parity  $\Pi(\phi)$  oscillates  $N$  times in  $2\pi$  for  $N$  particles. The amplitude  $C$  of this oscillation equals twice [11] the matrix element  $C = 2\rho_{N\uparrow\downarrow}$ . For proving  $N$  particle entanglement of the final state the measured fidelity  $\mathcal{F}$  has to be [109]  $\mathcal{F} > 1/2$ .

## B. List of Publications

The publications marked with  $\star$  are included on the subsequent pages:

- $\star$  A. Friedenauer, H. Schmitz, J. Glueckert, D. Porras and T. Schaetz, *Simulating a quantum magnet with trapped ions*, Nature Physics **4**, 757 (2008)
- $\star$  A. Friedenauer, F. Markert, H. Schmitz, L. Petersen, S. Kahra, M. Herrmann, Th. Udem, T. W. Haensch and T. Schaetz, *High power all solid state laser system near 280 nm*, Appl. Phys. B **84**, 371 (2006)
- R. Schuetzhold, M. Uhlmann, L. Petersen, A. Friedenauer, H. Schmitz and T. Schaetz, *Analogue of cosmological particle creation in an ion trap*, Phys. Rev. Lett. **99**, 201301 (2007)
- T. Schaetz, A. Friedenauer, H. Schmitz, L. Petersen, S. Kahra, *Towards (scalable) Quantum Simulations in ion trap*, J. Mod. Opt. **54**, 2317 (2007)
- H. Schmitz, A. Friedenauer, Ch. Schneider, R. Matjeschk, M. Enderlein, T. Huber, J. Glueckert, D. Porras, *The 'arch' of simulating quantum spin systems with trapped ions*, Appl. Phys. B **95**, 195 (2009)

# Simulating a quantum magnet with trapped ions

A. FRIEDENAUER\*, H. SCHMITZ\*, J. T. GLUECKERT, D. PORRAS AND T. SCHAEZT†

Max-Planck-Institut für Quantenoptik, Hans-Kopfermann-Str. 1, D-85748 Garching, Germany

\*These authors contributed equally to this work

†e-mail: tschaetz@mpq.mpg.de

Published online: 27 July 2008; doi:10.1038/nphys1032

**To gain deeper insight into the dynamics of complex quantum systems we need a quantum leap in computer simulations. We cannot translate quantum behaviour arising from superposition states or entanglement efficiently into the classical language of conventional computers. The solution to this problem, proposed in 1982 (ref. 1), is simulating the quantum behaviour of interest in a different quantum system where the interactions can be controlled and the outcome detected sufficiently well. Here we study the building blocks for simulating quantum spin Hamiltonians with trapped ions<sup>2</sup>. We experimentally simulate the adiabatic evolution of the smallest non-trivial spin system from paramagnetic into ferromagnetic order with a quantum magnetization for two spins of 98%. We prove that the transition is not driven by thermal fluctuations but is of quantum-mechanical origin (analogous to quantum fluctuations in quantum phase transitions<sup>3</sup>). We observe a final superposition state of the two degenerate spin configurations for the ferromagnetic order ( $|\uparrow\uparrow\rangle + |\downarrow\downarrow\rangle$ ), corresponding to deterministic entanglement achieved with 88% fidelity. This method should allow for scaling to a higher number of coupled spins<sup>2</sup>, enabling implementation of simulations that are intractable on conventional computers.**

It is not possible to efficiently describe the time evolution of quantum systems on a classical device, such as a conventional computer, because their memory requirements grow exponentially with their size. For example, a classical memory would need to hold  $2^{50}$  numbers to store arbitrary quantum states of 50 spin-1/2 particles. The ability to calculate their evolution requires the derivation of a matrix of  $(2^{50})^2 = 2^{100}$  elements, already exceeding by far the capacity of state-of-the-art computers. Further, each doubling of computational power permits only one additional spin-1/2 particle to be simulated. To allow for deeper insight into quantum dynamics, we need a ‘quantum leap’ in simulation efficiency.

As proposed in ref. 1, a universal quantum computer would accomplish this step. A huge variety of possible systems are under investigation, with individual trapped ions<sup>4,5</sup> as quantum bits (qubits) being a very promising architecture. After addressing the established criteria summarized in ref. 6 on up to eight ions<sup>7,8</sup> with operational fidelities exceeding 99% (refs 7–9), there seems to be no fundamental reason why such a device would not be realizable.

Alternatively, an analogue quantum computer, much closer to the original proposal in ref. 1, might allow for a shortcut towards quantum simulations. We would like to simulate a given system by a different one described by a Hamiltonian containing all the

important features of the original system. The simulator system needs to be controlled, manipulated and measured in a sufficiently precise manner and has to be rich enough to address interesting questions about the original system. For large coupled spin systems, optical lattices might be advantageous<sup>10</sup>, whereas smaller spin systems and degenerate quantum gases might be simulated by trapped ions<sup>2,11</sup>. Instead of implementing a Hamiltonian with a universal set of gates, direct simulation of the Hamiltonian can be implemented by one (adiabatic) evolution of the initial state into the corresponding final state of interest.

Here, in a proof-of-principle experiment, we simulate the adiabatic transition from a quantum para- to a quantum (anti-)ferromagnet and illustrate the advantages of the adiabatic quantum simulation (Fig. 1). We demonstrate the individual access, via radio-frequency (r.f.) and laser fields, to all relevant parameters in the underlying Hamiltonian, representing one out of a large spectrum of quantum spin Hamiltonians.

The adiabatic quantum simulation of generic spin Hamiltonians proposed in ref. 2 can be illustrated considering a string of charged spin-1/2 particles confined in a common harmonic potential. Two electronic states of each ion simulate the two-level system of a spin-1/2 magnetic moment,  $|\uparrow\rangle$  and  $|\downarrow\rangle$ . The inter-ion distance of several micrometres renders any direct spin–spin coupling negligible. The quantum Ising Hamiltonian,

$$H_{\text{ising}} = H_B + H_J = -B_x \sum_i \sigma_i^x + \sum_{i<j} J_{ij} \sigma_i^z \sigma_j^z, \quad (1)$$

consists of two terms. The first denotes the interaction of each individual spin, represented by the Pauli operator  $\sigma_i^k$  ( $k$  can be  $x, y$  or  $z$ ), with a uniform magnetic field of amplitude proportional to  $B_x$  pointing in direction  $x$ . The second term represents the spin–spin interaction, which tries to align the spins ( $\sigma_i^z$ ) parallel or antiparallel along the  $z$  axis, depending on the sign of the interaction amplitude  $J_{ij}$ . To simulate the first term in equation (1), the eigenstates of  $\sigma_i^z$ ,  $|\uparrow\rangle_i$  and  $|\downarrow\rangle_i$ , can be coupled with an electromagnetic field. The latter is simulated by a state-dependent force<sup>12</sup>, further explained in Fig. 2.

To understand the experiment discussed below, we consider interactions between nearest neighbours only,  $J_{i,i+1} = J$ , and two extreme scenarios. For the case of  $J = 0$  and  $B_x > 0$ , the ground state of the spin system has all spins aligned with  $B_x$  along the  $x$  axis. This corresponds to the paramagnetically ordered state  $|\rightarrow\rightarrow\rightarrow\rightarrow\rangle$ , the eigenstate of the Hamiltonian  $H_B = -B_x \sum_i \sigma_i^x$  with the lowest energy.

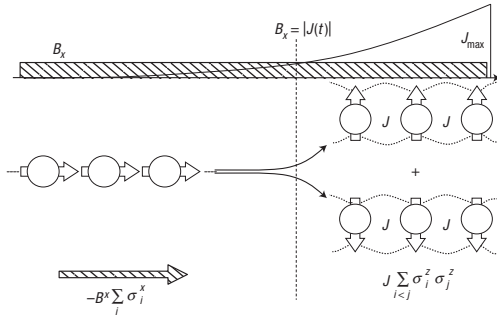


**Figure 1** Phase transition of a quantum magnet. Each ion can simulate a magnetic spin, analogous to an elementary magnet. We initialize the  $N$  spins in the paramagnetic state  $|\rightarrow \dots \rightarrow\rangle$ , the ground state of the Hamiltonian  $H_0 = -B_x(\sigma_1^x + \sigma_2^x + \dots + \sigma_N^x)$ . This is equivalent to aligning the spins parallel to the simulated magnetic field. Adding an effective spin–spin interaction  $J(t)$  (at constant  $B_x$ ) and increasing it adiabatically to  $|J_{\max}| \gg B_x$ , we expect the system to undergo a quantum phase transition into a ferromagnet, the new ground state of the system ( $J$  is symbolized as short chains, trying to keep neighbouring spins aligned). Ideally, the two possible ferromagnetic orders  $|\uparrow \uparrow \dots \uparrow\rangle$  and  $|\downarrow \downarrow \dots \downarrow\rangle$  are degenerate ground states. The spin system should evolve into the superposition state  $|\uparrow \uparrow \dots \uparrow\rangle + |\downarrow \downarrow \dots \downarrow\rangle$ , a maximally entangled ‘Schrodinger cat’ state/magnet.

For the opposite case of  $B_x = 0$  and  $J < (>)0$ , the system has an infinite number of degenerate ground states, defined by any superposition of the lowest-energy eigenstates of  $\sum_{i<j} J \sigma_i^z \sigma_j^z$ , namely  $|\uparrow \uparrow \dots \uparrow\rangle$  and  $|\downarrow \downarrow \dots \downarrow\rangle$ , which represent ferromagnetic order (or  $|\uparrow \uparrow \downarrow \dots \uparrow \uparrow \downarrow\rangle$  and  $|\downarrow \downarrow \uparrow \dots \downarrow \uparrow \downarrow\rangle$ , the antiferromagnetic order, respectively). Initializing the spin system in an eigenstate in the  $\sigma^x$  basis, starting with  $J(t=0) = 0$ ,  $B_x > 0$  and adiabatically increasing  $|J(t)|$  to  $|J_{\max}| \gg B_x$  should evolve the system from the paramagnetic order arbitrarily close to the (anti-) ferromagnetic order, as depicted in Fig. 1. A quantum phase transition is supposed to occur at  $B_x = |J|$  in the thermodynamic limit of an infinite number of spins<sup>3,13</sup>.

We experimentally demonstrate the above features on two spins as follows. We confine two  $^{25}\text{Mg}^+$  ions in a linear Paul trap<sup>14</sup> and laser-cool them to the Coulomb-crystalline phase, where the ions align along the trap axis  $a$ . The motion of the ions along this axis  $a$  can be described in the basis of normal modes. The in-phase mode oscillates at a frequency  $\omega_{\text{com}}/2\pi = 2.1$  MHz, whereas the out-of-phase mode has  $\omega_{\text{stretch}}/2\pi = \sqrt{3}\omega_{\text{com}}/2\pi = 3.7$  MHz.

In our implementations we define the  $^2S_{1/2}$  hyperfine ground states as  $|\downarrow\rangle \equiv |F=3; m_f=3\rangle$  and  $|\uparrow\rangle \equiv |F=2; m_f=2\rangle$ , which are separated by  $\omega_0/2\pi \simeq 1.7$  GHz. An external magnetic field  $B$  (different from the simulated magnetic field in equation (1)) of 5.5 G orients the magnetization axis for the projection  $\hbar m_f$  of each ion’s angular momentum  $F$ . In this field adjacent Zeeman sublevels of the  $F=3$  and 2 manifolds are split by 2.7 MHz per level.

We coherently couple the states  $|\downarrow\rangle$  and  $|\uparrow\rangle$  with a resonant r.f. field at  $\omega_0$  to implement single spin rotations<sup>14–16</sup>

$$R(\Theta, \phi) = \cos(\Theta/2)I - i\sin(\Theta/2)\cos\phi\sigma^x - i\sin(\Theta/2)\sin\phi\sigma^y, \quad (2)$$

where  $I$  is the identity operator,  $\sigma^x$  and  $\sigma^y$  denote the Pauli spin matrices acting on  $|\uparrow\rangle_i$  and  $|\downarrow\rangle_i$ ,  $\Theta/2 = B_x t/\hbar$  is proportional to

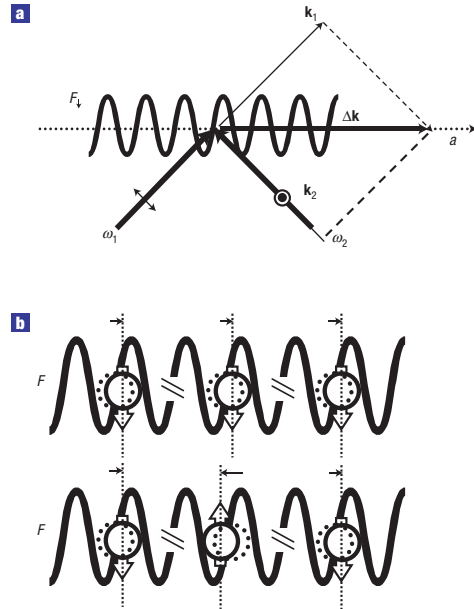


**Figure 2** Simulating the quantum magnet. **a**, Two perpendicular polarized laser beams of frequencies  $\omega_1$  and  $\omega_2$  induce a state-dependent optical-dipole force  $F_1 = -(3/2)F_1$  by the a.c. Stark shift (here, only  $F_1$  is depicted). The wavevector difference  $\Delta\mathbf{k} = \mathbf{k}_2 - \mathbf{k}_1$  points along the trap axis  $a$ . **b**, For a standing wave  $\omega_1 = \omega_2$ , the force conditionally changes the distance between neighbouring spins, simulating a spin–spin interaction<sup>2</sup> ( $F_1$ ,  $F_2$ ) symbolized by the arrow to the right (left). Only if all spins are aligned (top) does the distance between the spins (that is, between the ions) remain unchanged. Therefore, the total Coulomb energy of the spin system is not increased, defining ferromagnetic order, the quantum magnet, to be the ground state. For  $\omega_1 \neq \omega_2$ , the sinusoidal force pattern can be seen as a wave moving along the trap axis  $a$  pushing or pulling the ions repeatedly at a frequency  $\omega_1 - \omega_2$ . We chose  $\omega_1 - \omega_2$  close to the resonance frequency of the ions oscillating out of phase (stretch mode). The energies of different spin chains now depend on the coupling of the spin state to the stretch mode. Energy can be coupled efficiently into the state with different spin orientations (bottom, for example), defining the unaffected upper case as a ground state<sup>8</sup>. The interpretation in terms of an effective spin–spin interaction is further described in the Methods section.

the duration  $t$  of the rotation and  $\phi$  is the phase of the r.f. oscillation defining the axis of rotation in the  $x$ – $y$  plane of the Bloch sphere<sup>15</sup>.

We provide the effective spin–spin interaction by a state-dependent optical-dipole force<sup>12,16,17</sup>. The relative amplitudes  $F_1 = -(3/2)F_2$  are due to a.c. Stark shifts induced by two laser beams at a wavelength  $\lambda$  of 280 nm, perpendicular in direction and polarization, with their wavevector difference pointing along the trap axis  $a$ . They are detuned 80 GHz blue of the  $^2P_{3/2}$  excited state, with intensities allowing for  $|J/\hbar|$  as large as  $2\pi \times 22.1$  kHz. We use a walking-wave force-pattern by detuning the two laser frequencies by  $2\pi \times 3.45$  MHz =  $\omega_{\text{stretch}} + \delta$ , with  $\delta = -2\pi \times 250$  kHz. This choice avoids several technical problems of the original proposal<sup>2</sup> (see the Methods section), while at the same time resonantly enhancing the effective spin–spin interaction by a factor of  $|\omega_{\text{stretch}}/\delta| = 14.8$  compared with the

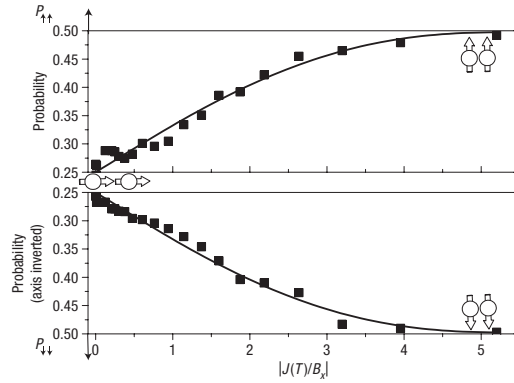


**Figure 3** Quantum magnetization of the spin system. We initialize the spins in the paramagnetic state  $|\rightarrow\rangle|\rightarrow\rangle \equiv (|\uparrow\rangle + |\downarrow\rangle)(|\uparrow\rangle + |\downarrow\rangle) = |\uparrow\uparrow\rangle + |\uparrow\downarrow\rangle + |\downarrow\uparrow\rangle + |\downarrow\downarrow\rangle$ , the ground state of the Hamiltonian  $H_0 = -B_x(\sigma_1^z + \sigma_2^z)$ . A measurement of this superposition state will already project into both  $|\uparrow\uparrow\rangle$  and  $|\downarrow\downarrow\rangle$ , each with a probability of 0.25. After applying  $B_x$ , we adiabatically increase the effective spin–spin interaction from  $J(t=0) = 0$  to  $J(T)$ . State-sensitive fluorescence detection enables us to distinguish the final states  $|\uparrow\uparrow\rangle$ ,  $|\downarrow\downarrow\rangle$ ,  $|\uparrow\downarrow\rangle$  or  $|\downarrow\uparrow\rangle$ . Averaging over  $10^4$  experiments provides us with the probability distributions  $P_{\uparrow\uparrow}$  (two ions fluoresce),  $P_{\uparrow\downarrow}$  (no ion fluoresces) and  $P_{\downarrow\downarrow}$  (one ion fluoresces). We repeat the measurement for increasing ratios  $|J(T)/B_x|$ . The experimental results for the two ferromagnetic contributions  $P_{\uparrow\uparrow}$  and  $P_{\downarrow\downarrow}$  are depicted as squares. Solid lines are the result of a calculation of the evolution of the effective spin system induced by  $B_x$  and  $J(t)$ . For  $|J(T)/B_x| \ll 1$ , the paramagnetic order is preserved. For  $|J(T)/B_x| \gg 1$ , the spins undergo a transition into the ferromagnetic order, the ground state of the Hamiltonian  $H_f = J_{\max}\sigma_1^z\sigma_2^z$ , with a related quantum magnetization  $M = P_{\uparrow\uparrow} + P_{\downarrow\downarrow} \geq 98 \pm 2\%$ . Note that we invert the ordinate of the lower frame to emphasize the unbroken symmetry of the evolution.

standing-wave case<sup>18</sup>. The enhancement is induced by the fact that the walking wave is closer to resonance (detuned only by  $\delta$ ) with the vibrational mode compared with the standing wave (detuned by  $\omega_{\text{stretch}}$ ).

After laser cooling we initialize the quantum simulator by optical pumping<sup>19</sup> to the state  $|\downarrow\rangle|\downarrow\rangle|n \approx 0\rangle$ . We rotate both spins in a superposition state via an  $R(\pi/2, -\pi/2)$  pulse (see equation (2)) on the r.f. transition to initialize the state  $|\Psi_i\rangle = |\rightarrow\rangle|\rightarrow\rangle|n \approx 0\rangle$ . Note that the paramagnetic state  $|\rightarrow\rangle|\rightarrow\rangle \equiv (|\uparrow\rangle + |\downarrow\rangle)(|\uparrow\rangle + |\downarrow\rangle) = |\uparrow\uparrow\rangle + |\uparrow\downarrow\rangle + |\downarrow\uparrow\rangle + |\downarrow\downarrow\rangle$  has a 25% probability to be projected into either  $|\uparrow\uparrow\rangle$  or  $|\downarrow\downarrow\rangle$  (normalization factors are suppressed throughout).

We simulate the effective magnetic field by continuously applying an r.f. field with phase  $\phi = 0$  and an amplitude such that it corresponds to a single qubit rotation  $R(\Theta, 0)$  with full rotation period  $\Theta = 2\pi$  in  $118 \mu\text{s}$  and deduce  $B_x/\hbar = 2\pi \times 4.24 \text{ kHz}$ . Precise control of the phase  $\phi$  of the r.f. oscillator relative to the initialization pulse enables alignment of  $B_x$  parallel to the spins along the  $x$  axis in the equatorial plane of the Bloch sphere, ensuring that  $|\Psi_i\rangle$  is an eigenstate of this effective magnetic field.

At the same time, we switch on the effective spin–spin interaction  $J(t)$  ( $t \in [0; T]$ ) and increase its amplitude adiabatically up to  $J(T)$  within 50 steps of  $2.5 \mu\text{s}$  each. At time  $T$ , we switch off the interactions and analyse the final state of the two spins via the state-sensitive detection described below. In a sequence of experiments at constant  $B_x$  we increase  $J_{\max}$  and

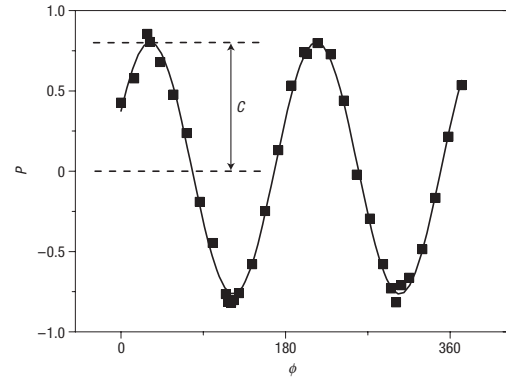


**Figure 4** Entanglement of the quantum magnet. Measurement of the parity  $P = P_{\uparrow\downarrow} + P_{\downarrow\uparrow} - (P_{\uparrow\uparrow} + P_{\downarrow\downarrow})$  of the final ferromagnetic state after the simulation reached  $|J_{\max}/B_x| = 5.2$ . As we vary the phase  $\phi$  of a subsequent analysis pulse  $R(\pi/2, \phi)$ , the parity of the two spins oscillates as  $C \cos(2\phi)$ . Together with the final-state populations  $P_{\uparrow\downarrow}$  and  $P_{\downarrow\uparrow}$  depicted in Fig. 3, we can deduce the fidelity  $F = |\langle \Psi_{\text{final}} | \downarrow\downarrow + \uparrow\uparrow \rangle|^2 = 1/2(P_{\uparrow\downarrow} + P_{\downarrow\uparrow}) + C/2 = 88 \pm 3\%$  for the final superposition state  $|\uparrow\uparrow\rangle + |\downarrow\downarrow\rangle$ , a maximally entangled state, highlighting the quantum nature of this transition. We find qualitatively comparable results for the antiferromagnetic case  $|\uparrow\downarrow\rangle + |\downarrow\uparrow\rangle$ . Each data point represents an average over  $10^4$  experiments.

therefore  $|J(T)/B_x|$ . Finally we reach the maximal amplitude  $|J(t = 125 \mu\text{s})/B_x| = |J_{\max}/B_x| = 5.2$  (see the Methods section) and achieve a quantum magnetization  $M$ , the probability of being in a state with ferromagnetic order, of  $M = P_{\uparrow\downarrow} + P_{\downarrow\uparrow} = 98\% \pm 2\%$ .

After the adiabatic evolution described above, we project the final spin state into the  $\sigma^z$  measurement basis by a laser beam tuned resonantly to the  $|\downarrow\rangle \leftrightarrow {}^2P_{3/2}(F = 4; m_f = 4)$  cycling transition<sup>16</sup>. An ion in state  $|\downarrow\rangle$  fluoresces brightly, leading to the detection of an average of 40 photons during a  $160 \mu\text{s}$  detection period with our photomultiplier tube. In contrast, an ion in state  $|\uparrow\rangle$  remains close to dark (on average six photons). We repeat each experiment for the same set of parameters  $10^4$  times and derive the probabilities  $P_{\uparrow\downarrow}$ ,  $P_{\downarrow\uparrow}$  and  $P_{\uparrow\uparrow}$  for the final state being projected into state  $|\downarrow\downarrow\rangle$ ,  $|\uparrow\uparrow\rangle$  and  $(|\downarrow\uparrow\rangle$  or  $|\uparrow\downarrow\rangle)$ , respectively (further described in the Methods section).

In our experiment we can detect both ferromagnetic contributions,  $P_{\uparrow\downarrow}$  and  $P_{\downarrow\uparrow}$ , separately. Any imperfection in the simulation acting as a bias field  $B_z$  along the  $z$  axis would energetically prefer one of the ferromagnetic states over the other and therefore unbalance their contributions to the final state. We carefully cancel all bias fields (see the Methods section), to balance the populations  $P_{\uparrow\downarrow}$  and  $P_{\downarrow\uparrow}$  as can be seen in Fig. 3. The results are in good agreement with theoretical predictions for our experiment, shown as solid lines. We expect the final state to be a coherent superposition of the two ferromagnetic states  $|\uparrow\uparrow\rangle + |\downarrow\downarrow\rangle$ —a maximally entangled Bell state. To quantify the experimentally reached coherence we measure the parity<sup>20</sup>  $P = P_{\uparrow\downarrow} + P_{\downarrow\uparrow} - (P_{\uparrow\uparrow} + P_{\downarrow\downarrow})$  after applying an additional  $R(\pi/2, \phi)$  pulse to both ions after  $J_{\max}$  is reached, with a variable r.f. phase  $\phi$  relative to the r.f. field simulating  $B_x$ . The measured data shown in Fig. 4 have a component that oscillates as  $C \cos(2\phi)$ , where  $|C|/2$  characterizes the coherences between the  $|\uparrow\uparrow\rangle$  and the  $|\downarrow\downarrow\rangle$  components in the final state  $|\Psi_{\text{final}}\rangle$  produced. Deducing a contrast

$C$  of  $78 \pm 2\%$  from the best fit we derive the Bell-state fidelity<sup>20</sup>  $F = |\langle \Psi_{\text{final}} | \downarrow\downarrow + \uparrow\uparrow \rangle|^2 = 1/2(P_{\downarrow\downarrow} + P_{\uparrow\uparrow}) + C/2$  of  $88 \pm 3\%$ .

We also simulate the adiabatic evolution of a system not initialized in the ground state of the initial Hamiltonian. In particular, we prepare the paramagnetic eigenstate  $|\leftarrow \leftarrow\rangle = (|\downarrow\rangle - |\uparrow\rangle)(|\downarrow\rangle - |\uparrow\rangle)$ , with the spins aligned antiparallel with respect to the simulated magnetic field via an  $R(\pi/2, \pi/2)$  r.f. initialization pulse. The adiabatic evolution should preserve the spin system in its excited state, leading now into the antiferromagnetic order  $|\uparrow\downarrow\rangle + |\downarrow\uparrow\rangle$ . After evolution to  $J = J_{\text{max}}$  we find  $P_{\downarrow\uparrow} + P_{\uparrow\downarrow} \geq 95 \pm 2\%$ . To investigate the coherence between the  $|\uparrow\downarrow\rangle$  and the  $|\downarrow\uparrow\rangle$  components, we first rotate the state via an additional  $R(\pi/2, 0)$  pulse, which would ideally take  $|\uparrow\downarrow\rangle + |\downarrow\uparrow\rangle \rightarrow |\uparrow\uparrow\rangle + |\downarrow\downarrow\rangle$ , followed by the measurement of the parity as explained above. We deduce the fidelity of the antiferromagnetic entangled state  $F = |\langle \Psi_{\text{final}} | \downarrow\uparrow + \uparrow\downarrow \rangle|^2 = 1/2(P_{\downarrow\uparrow} + P_{\uparrow\downarrow}) + C/2 = 80 \pm 4\%$ .

An equally valid viewpoint of this experiment interprets  $|\leftarrow \leftarrow\rangle$  as the ground state of the Hamiltonian  $-H_{\text{Ising}}$ . Because the sign of all spin–spin interactions is also reversed in  $-H_{\text{Ising}}$ , it is equivalent to a change of sign in the spin–spin interaction  $J$ .

The entanglement of the final states confirms that the transition from paramagnetic to (anti-) ferromagnetic order is not caused by thermal fluctuations driving thermal phase transitions. The evolution is coherent and quantum mechanical, the coherent equivalent to the so-called quantum fluctuations<sup>3,13</sup> driving quantum phase transitions in the thermodynamic limit. In this picture, tunnelling processes<sup>13</sup> induced by  $B_x$  couple the degenerate (in the rotating frame) states  $|\uparrow\rangle_i$  and  $|\downarrow\rangle_i$  with an amplitude proportional to  $(|B_x/J|)$ . In a simplified picture for  $N$  spins, the amplitude for the tunnelling process between  $\Psi_{N\uparrow} = |\uparrow\uparrow\dots\uparrow\rangle$  and  $\Psi_{N\downarrow} = |\downarrow\downarrow\dots\downarrow\rangle$  is proportional to  $(|B_x/J|)^N$ , because all  $N$  spins must be flipped. In the thermodynamic limit ( $N \rightarrow \infty$ ), the system is predicted to undergo a quantum phase transition at  $|J| = B_x$ . At values  $|J| > B_x$ , the tunnelling between  $\Psi_{\infty\uparrow}$  and  $\Psi_{\infty\downarrow}$  is completely suppressed. In our case of a finite system,  $\Psi_{2\uparrow}$  and  $\Psi_{2\downarrow}$  remain coupled and the sharp quantum phase transition is smoothed into a gradual change from paramagnetic to (anti-) ferromagnetic order.

In conclusion, we have demonstrated the feasibility of simple quantum simulations in an ion trap by implementing the Hamiltonian of a quantum magnet undergoing a robust transition from a paramagnetic to an entangled ferromagnetic or antiferromagnetic order. Although our system is currently too small to solve classically intractable problems, it uses an approach that is complementary to a universal quantum computer in a way that can become advantageous as the approach is scaled to larger systems. Our scheme does not rely on the use of sequences of quantum gates, thus scaling to a higher number of ions can be simpler, because it only requires inducing the same overall spin-dependent optical force on all the ions<sup>2</sup>. Furthermore, the desired outcome might not be affected by decoherence as drastically as typical quantum algorithms, because a continuous loss of quantum fidelity might not completely spoil the outcome of the experiment.

For example, the coherence of a Greenberger–Horne–Zeilinger-like state  $|\uparrow\uparrow\dots\uparrow\rangle + |\downarrow\downarrow\dots\downarrow\rangle$  might be completely lost, but still the output of the quantum simulation describes correctly the ground state in a solid-state system, where spontaneous symmetry breaking implies ferromagnetic ordering randomly along one of two antiparallel orientations. In contrast, universal quantum computation will almost certainly require involved subalgorithms for error correction<sup>5</sup>. Decoherence in the simulator might even mimic the influence of the natural environment<sup>21</sup> of the studied system if we judiciously construct our simulation (for example, the decoherence we mainly observe in our demonstration implements a dephasing environment).

Despite technical challenges, we expect that this work is the start to extensive experimental research of complex many-body phases with trapped-ion systems. Linear trapping set-ups may be used for the quantum simulation of quantum dynamics beyond the ground state, where chains of 30 spins would already enable us to outperform current simulations with classical computers. We may also adapt our scheme to new ion-trapping technologies<sup>22</sup>. For example, a modest scaling to systems of  $20 \times 20$  spins in two dimensions would yield insight into open problems in solid-state physics, for example related to spin frustration. This could pave the way to address a broad range of fundamental issues in condensed-matter physics that are intractable with exact numerical methods, such as spin liquids in triangular lattices, suspected to be closely related to phases of high-temperature superconductors<sup>23</sup>.

## METHODS

### STATE-DEPENDENT OPTICAL-DIPOLE FORCE

An effective (Ising) spin–spin interaction was proposed to be implemented via magnetic field gradients<sup>24</sup>. It was suggested to use state-dependent optical-dipole forces<sup>2,11,17</sup> displacing the spin state  $|S\rangle$  ( $S$  either  $\downarrow$  or  $\uparrow$ ) in phase space by an amount that depends on  $|S\rangle$ . The area swept in phase space changes the state to  $e^{i\phi(S)}|S\rangle$ . The phase  $\phi(S)$  can be broken down into single-spin terms proportional to  $\sigma_i^z$  and apparent spin–spin interactions proportional to  $\sigma_i^z \sigma_j^z$  and thus gives rise to the desired simulation of spin–spin interactions<sup>25</sup>. It can also lead to single-spin phases that simulate the unwanted contribution of a common bias field  $B_z \sigma^z$  in the Hamiltonian that will result in an imbalance of the probabilities  $P_{\downarrow\downarrow}$  and  $P_{\uparrow\uparrow}$ . To achieve a balanced probability distribution as depicted in Fig. 3, we have to carefully compensate these single-spin phases. To this end we compensate the residual a.c. Stark shifts of the individual laser beams by carefully choosing the direction and polarization of the beams<sup>12</sup> and also compensate for the imbalance caused by single-spin phases via a detuning of the order of several kilohertz of the r.f. transition relative to  $\omega_0$ . Furthermore, the ions have to be separated by an integer multiple of the effective wavelength  $\lambda_{\text{eff}} = \lambda/\sqrt{2}$ ; in our implementation  $18\lambda_{\text{eff}} \approx 3.6 \mu\text{m}$ , requiring the control of the axial trapping frequency to better than 100 Hz.

To minimize the errors of our simulation, we have to keep the motional excitation small enough during the evolution to enable the system to be described within the Lamb–Dicke regime<sup>16</sup> (ideally  $\bar{n} \times \eta^2 \ll 1$ ). The Lamb–Dicke factor  $\eta$  can be interpreted as the ratio between the width of the ground-state wavefunction of the ion and  $\lambda_{\text{eff}}/2\pi$  (for our parameters  $\eta \approx 0.25$ ).

In addition, we have to return the system close to its motional ground state at the end of the simulation to minimize the errors due to residual spin–motion coupling<sup>2</sup> causing entanglement between the spin states and the motional degrees of freedom. To fulfil the first condition, we detune the two laser beams far enough from resonantly exciting the motional modes. Adjusting the detuning  $\delta = -(\omega_{\text{stretch}} - (\omega_1 - \omega_2)) = -2\pi \times 250 \text{ kHz}$  red of the stretch-mode frequency reduces the motional excitation during one step of the evolution and on average to  $\bar{n} \approx 1$ . Finally terminating the evolution after the system returned into its motional ground state<sup>17</sup>, it ideally completely cancels the simulation errors discussed in ref. 2, allowing for the measured contrast of the parity oscillations depicted in Fig. 4.

### STATE-SENSITIVE DETECTION

For two spins, the integrated fluorescence signal does not enable us to distinguish between two ( $|\downarrow\uparrow\rangle$  and  $|\uparrow\downarrow\rangle$ ) of the four possible spin configurations. In addition, the number of detected photons for each of the three distinguishable configurations fluctuates from experiment to experiment according to Poissonian statistics and therefore can be determined only with limited accuracy. For the data reported, we repeated each experiment  $10^4$  times and fitted the resulting photon-number distribution to the weighted sum of three reference distributions to derive  $P_{\downarrow\downarrow}$ ,  $P_{\uparrow\uparrow}$  and  $P_{\downarrow\uparrow} + P_{\uparrow\downarrow}$ .

### ADIABATIC EVOLUTION

We achieve the best fidelities for the reported transitions at a duration of the simulation of  $T = 125 \mu\text{s}$  at a  $B_x$  of  $2\pi \times 4.24 \text{ kHz}$ . We are not strictly in the adiabatic limit, where for  $T \rightarrow \infty$  the final ratio  $|J_{\text{max}}/B_x| = 5.2$  allows for a maximum quantum magnetization of 93.4%. The robustness of the coupling scheme used enables us to minimize decoherence effects and even to

enhance the final quantum magnetization to 98% by reducing the duration of the simulation.

In addition, technical factors related to the specific nonlinear performance of the r.f. attenuator used to control  $J(t)$  led to its evolution being linear in time to up to  $J(t = 50 \mu\text{s}) = 5 \times 10^{-4} J_{\text{max}}$ , continued by  $J(t) \sim (e^{\alpha t} - \beta)^2$  best fitted by  $\alpha = 26 \times 10^3 \text{ s}^{-1}$  and  $\beta = 4$ . So far we have not improved the fidelities by evolving or terminating  $J(t)$  or  $B_x$  in a more adiabatic way.

Received 27 March 2008; accepted 25 June 2008; published 27 July 2008.

#### References

1. Feynman, R. P. Simulating physics with computers. *Int. J. Theor. Phys.* **21**, 467–488 (1982).
2. Porras, D. & Cirac, J. I. Effective quantum spin systems with trapped ions. *Phys. Rev. Lett.* **92**, 207901 (2004).
3. Sachdev, S. *Quantum Phase Transitions* (Cambridge Univ. Press, Cambridge, 1999).
4. [http://qist.lanl.gov/qcomp\\_map.shtml](http://qist.lanl.gov/qcomp_map.shtml).
5. Nielsen, M. & Chuang, I. *Quantum Computation and Quantum Information* (Cambridge Univ. Press, Cambridge, 2000).
6. DiVincenzo, D. P. in *Scalable Quantum Computation* (eds Braunstein, S. L., Lo, H. K. & Kok, P.) 1–13 (Wiley, New York, 2001).
7. Leibfried, D. *et al.* Creation of a six-atom ‘Schrödinger cat’ state. *Nature* **438**, 639–642 (2005).
8. Häffner, H. *et al.* Scalable multiparticle entanglement of trapped ions. *Nature* **438**, 643–646 (2005).
9. Benhelm, J., Kirchmair, G., Roos, C. F. & Blatt, R. Towards fault-tolerant quantum computing with trapped ions. *Nature Phys.* **4**, 463–466 (2008).
10. Greiner, M., Mandel, O., Esslinger, T., Haensch, T. W. & Bloch, I. Quantum phase transition from a superfluid to a Mott insulator in a gas of ultracold atoms. *Nature* **415**, 39–44 (2002).
11. Porras, D. & Cirac, J. I. Bose–Einstein condensation and strong-correlation behaviour of phonons in ion traps. *Phys. Rev. Lett.* **93**, 263602 (2004).
12. Wineland, D. J. *et al.* Quantum information processing with trapped ions. *Phil. Trans. R. Soc. Lond. A* **361**, 1349–1361 (2003).
13. Sachdev, S. Quantum criticality: Competing ground states in low dimensions. *Science* **288**, 475–480 (2000).
14. Schaetz, T., Friedenauer, A., Schmitz, H., Petersen, L. & Kahra, S. Towards (scalable) quantum simulations in ion traps. *J. Mod. Opt.* **54**, 2317–2325 (2007).
15. Allen, L. & Eberly, J. H. *Optical Resonance and Two-Level Atoms* (Dover, New York, 1987).
16. Wineland, D. J. *et al.* Experimental issues in coherent quantum-state manipulation of trapped atomic ions. *J. Res. Natl Inst. Stand. Technol.* **103**, 259–328 (1998).
17. Leibfried, D. *et al.* Experimental demonstration of a robust, high fidelity geometric two ion-qubit phase gate. *Nature* **422**, 412–415 (2003).
18. Porras, D. & Cirac, J. I. Quantum manipulation of trapped ions in two dimensional Coulomb crystals. Preprint at <<http://arxiv.org/abs/quant-ph/0601148v3>> (2006).
19. King, B. E. *et al.* Cooling the collective motion of trapped ions to initialize a quantum register. *Phys. Rev. Lett.* **81**, 1525–1528 (1998).
20. Sackett, C. A. *et al.* Experimental entanglement of four particles. *Nature* **404**, 256–259 (2000).
21. Lloyd, S. Universal quantum simulators. *Science* **273**, 1073–1078 (1996).
22. Chaverini, J. & Lybarger, W. E. Jr. Laserless trapped-ion quantum simulations without spontaneous scattering using microtrap arrays. *Phys. Rev. A* **77**, 022324 (2008).
23. Orestein, J. & Millis, A. J. Advances in the physics of high- $T_c$  superconductivity. *Science* **288**, 468–474 (2000).
24. Wunderlich, C. *Laser Physics at the Limit* 261–273 (Springer, Heidelberg, 2002).
25. Wang, X., Sorensen, K. & Molmer, A. Multitbit gates for quantum computing. *Phys. Rev. Lett.* **86**, 3907–3910 (2001).

#### Acknowledgements

This work was supported by the Emmy-Noether Programme of the German Research Foundation (DFG, grant No SCHA 973/1-2) the MPQ Garching, the DFG Cluster of Excellence Munich—Centre for Advanced Photonics and the European project SCALA. We thank D. Leibfried for his input and I. Cirac and G. Rempe for comments and support. We thank D. Moehring for reading and improving the manuscript.

#### Author information

Reprints and permission information is available online at <http://npg.nature.com/reprintsandpermissions>. Correspondence and requests for materials should be addressed to T.S.

A. FRIEDENAUER<sup>1,✉,\*</sup>  
F. MARKERT<sup>1,\*,\*\*</sup>  
H. SCHMITZ<sup>1</sup>  
L. PETERSEN<sup>1</sup>  
S. KAHRA<sup>1</sup>  
M. HERRMANN<sup>1</sup>  
TH. UDEM<sup>1,2</sup>  
T.W. HÄNSCH<sup>1,2</sup>  
T. SCHÄTZ<sup>1</sup>

## High power all solid state laser system near 280 nm

<sup>1</sup> Max-Planck-Institut für Quantenoptik, Hans-Kopfermann-Str. 1, 85748 Garching, Germany  
<sup>2</sup> Ludwigs-Maximilians-Universität München, Schellingstr. 4, 80799 München, Germany

Received: 20 March 2006

Published online: 23 May 2006 • © Springer-Verlag 2006

**ABSTRACT** We present a stable high power all solid state laser system emitting 1-W of continuous wave laser radiation at a wavelength of 559 nm or 275 mW near 280 nm. The system consists of a commercial 2-W fiber laser with a line width of less than 200 kHz at 1118 nm and two home-built subsequent second harmonic generation external ring cavities using LBO and BBO crystals, respectively. The system is designed to act as a detection and cooling laser for trapped  $Mg^+$  ions.

**PACS** 03.67.Lx; 32.80.Qk; 42.60.By; 42.79.Nv

### 1 Introduction

The fact that the laser apparatus for experiments with trapped light ions ( $Be^+$ ,  $Mg^+$ ) is very complex and expensive is one of the main obstacles for scaling up to larger multi-beam experiments. Due to the development of high power fiber laser systems with superb beam quality and low maintenance combined with efficient frequency quadruplers, this kind of experiment comes closer into consideration as these systems cost a fraction of the formerly used dye and related pump lasers. The laser source we present in this paper is actually used to detect and cool trapped  $Mg^+$  ions driving the transitions from the ground state  $3S_{1/2}$  to the  $3P_{1/2}$  or  $3P_{3/2}$  levels at approximately 280 nm.

### 2 Laser system

Acting as fundamental beam source, we use a commercially available 2-W ytterbium fiber laser at 1118 nm with a line width smaller than 200 kHz

built by Koheras. The fiber laser consists of a fiber master oscillator and a power amplifier pigtailed by a non-polarization-maintaining fiber with an FC/APC connector. The laser is tunable both by temperature for slow tuning and by a piezo-controlled optical path length of the fiber allowing for a total scan range of 80 GHz with a bandwidth of 20 kHz at 1118 nm. We double the frequency of the laser output in the infrared (IR) twice by two subsequent second harmonic generation (SHG) cavities. We use 10 mW of the second-harmonic beam at 559 nm to implement polarization spectroscopy [1, 2] to stabilize the laser frequency to an appropriate iodine transition (R(53)28-3 at 559.271 nm) using the piezo of the laser. In addition to the power of 2 W at the wavelength of 1118 nm, the fiber laser emits 1.2 W of broadband amplified spontaneous emission (ASE) peaked between 1060 nm and 1100 nm. After switching on the power amplifier the laser undergoes polarization drifts which fall off exponentially in time. After about two

hours the output polarization reaches a steady state provided that the non-polarization-maintaining fiber is fixed in position. We control the polarization of the beam coming from the single-mode fiber by quarter- and half-wave plates. We reduce the amount of retroreflected light into the laser by an optical isolator, which is designed for a wavelength of 1064 nm and transmits approximately 90% of the incident power at 1118 nm (isolation  $\approx 30$  dB) and half of the unpolarized ASE power, ending up with 1.8 W of pump power for the first SHG cavity. Since the ASE is not resonant with the cavity mode, it is filtered out by the optical resonator. We retrieve the incoupling efficiency by subtracting the ASE power from the total power. We mode match the pump beam into the first SHG cavity using two lenses, one of these being a fiber collimator with a variable distance between the end of the fiber and the lens.

### 3 SHG cavities

Frequency-doubling efficiencies up to 85% have been reported [3, 4] using type II phase matching in KTP crystals at wavelengths of 1060 or 1080 nm. Unfortunately, there is no possible non-critical type II phase match (NCPM) in KTP at 1118 nm [7]. Potentially usable crystals for doubling 1118 nm include potassium niobate (KNB, effective nonlinearity  $d_{\text{eff}} = -12.1$  pm/V), lithium niobate (LNB,  $d_{\text{eff}} = -4.4$  pm/V) or lithium triborate (LBO,  $d_{\text{eff}} = 0.84$  pm/V). Although the niobate crystals have higher effective nonlinearities, the main advantage of LBO is its very high optical quality, high damage threshold and its moder-

✉ Fax: +49-89-32905-200, E-mail: axel.friedenauer@mpq.mpg.de

\*Both A. Friedenauer and F. Markert contributed to this work equal parts.

\*\*Present address: Johannes-Gutenberg-Universität Mainz, Staudinger Weg 7, 55128 Mainz, Germany

ate NCPM temperature of 89 °C compared to 351 °C for KNB and 219 °C for MgO:LNB, which would be suitable for high-power applications.

For the first SHG cavity we use non-critically phase-matched, type I,  $\alpha$ -cut lithium triborate (LBO) which is antireflective coated both for the fundamental and for the harmonic waves. The cutting angles of the crystal are  $\theta = 90^\circ$ ,  $\varphi = 0^\circ$ ; therefore, we obtain a round non-astigmatic green beam out of the cavity which can be coupled into the next cavity via two spherical lenses. The 18-mm-long crystal is placed inside an oven temperature controlled to within 20 mK. Theory predicts a phase-matching temperature of 89 °C, but we found optimum harmonic generation at 94 °C that might be due to improper heat contact between the copper oven and the crystal despite a thin indium foil in between. The crystal is placed in the smaller focus of a folded ring cavity (see Fig. 1). The cavity has a small folding angle of 10° (full angle between incident and reflected beams) at both focusing mirrors to minimize astigma-

tism. The total length of the ring cavity is 400 mm to ensure a large free spectral range (FSR = 750 MHz) and therefore a large resonance width of the longitudinal cavity modes.

As an input coupler we use a plane mirror with a reflectivity of  $R = 97.5\%$  for the fundamental (M1, antireflective (AR) coated on the outside of the cavity) to impedance match the losses inside the cavity. The second mirror, highly reflective (M2,  $R > 99.98\%$ ), is mounted on a small stacked piezo with high resonance frequency (Thorlabs model AE020304D04,  $\nu_{\text{res}} \approx 18$  kHz loaded). We glued the piezo to a disk made of lead to absorb vibrations and reduce the resonance frequency of the mirror mount. The dimension of this mirror is very small, allowing for a high servo bandwidth ( $3 \times 3 \times 2$  mm<sup>3</sup>). Furthermore, two curved mirrors of focal length  $f = 25$  mm are used, one of them highly reflective at the fundamental (M3,  $R > 99.98\%$ ), the other acting as an output coupler highly reflective at the fundamental (M4,  $R > 99.9\%$ ) and highly transmissive at the harmonic

wavelength ( $T > 95\%$ ). The output coupler is shaped as a ‘zero lens’ and AR coated for the harmonic on the convex side. We modeled the cavity including linear and conversion losses of the crystal and reflection losses of the mirrors to determine the optimum crystal length of 18 mm. We derived the optimum focus inside the crystal from calculations following Boyd–Kleinman theory [5] to be 27.3- $\mu\text{m}$  beam waist ( $1/e^2$  of the intensity) and adjusted the distance between the curved mirrors to match this value at the plateau of the stability region (geometric distance between focusing mirrors M3 and M4:  $d = 62$  mm). For stabilizing the length of the cavity we use the polarization-locking scheme of [6]. We obtain 1 W of green output power at 559 nm. For long-term operation, one can increase the stability of the system by further tilting the input polarization with respect to the crystal axis, sacrificing some output power for a stronger error signal. In this way we obtain a stable output power of 950 mW, corresponding to a conversion efficiency of the LBO resonator of larger than 52.7%. We stress that we give the available output power relative to the laser power in front of the cavity rather than correcting for coupling efficiency, Fresnel losses and output coupler loss.

The output of the first cavity is coupled into an astigmatism-compensated second cavity based on a Brewster-cut BBO crystal, which we heat to approximately 50 °C in order to prevent water from condensing on the hygroscopic, polished surfaces of the crystal. The BBO crystal ( $4 \times 4 \times 10$  mm<sup>3</sup>) is mounted on a rotational and a linear translation stage which preserves distances and angles between the crystal and the focusing mirrors. Again, calculations following Boyd–Kleinman theory are carried out leading to an ideal focus of 19.4  $\mu\text{m}$ . Mode matching the incoupling beam to the mode of the second SHG cavity is performed by two lenses mounted on 3D translational stages to ease realigning. The layout of the second cavity is similar to the first, differing only in the reflectivities of the mirrors and the folding angle of the cavity at both mirrors (full angle 27.4°) to compensate for the astigmatism caused by the Brewster-cut BBO crystal. We implemented this cavity using mirrors (M2', M3') with  $R > 99.93\%$  and the

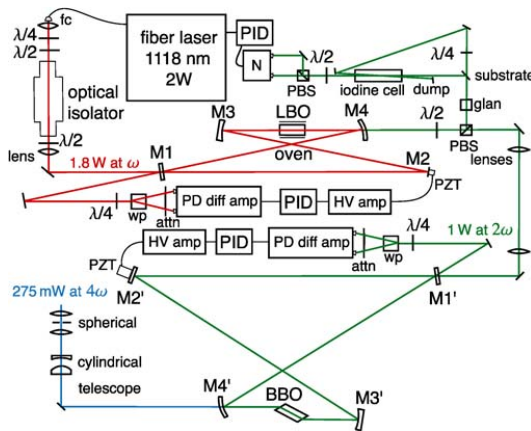


**FIGURE 1** Optical setup of the laser system. The light coming from the fiber laser is collimated by the fiber collimator (fc) and passes the optical isolator after polarization adjustment by quarter- and half-wave plates ( $\lambda/4$  and  $\lambda/2$ ). After passing another half-wave plate the beam is mode matched (lens) into the LBO cavity consisting of mirrors M1, M2, M3 and M4. The light reflected at M1 passes a quarter-wave plate and a Wollaston prism (wp), is attenuated (attn) and falls on a photodiode (PD) differential amplifier. That signal goes to a proportional-integral-derivative (PID) servo and after amplification (HV amp) is fed to the piezo (PZT) on which the mirror M2 is mounted. The second-harmonic beam generated in the LBO crystal leaves the cavity via the output coupler M4 and 10 mW are separated from the beam for the iodine lock using a half-wave plate and a polarizing beam splitter (PBS). With this beam we implement polarization spectroscopy [2] using a Glan laser polarizer (glan) and a New Focus Nirvana photodetector (N). The larger part traversing the PBS is mode matched in the BBO cavity consisting of mirrors M1', M2', M3' and M4' using two mode-matching lenses. The generation of the error signal is identical to the first cavity. The ultraviolet beam generated in the BBO crystal leaves the cavity via M4' and is projected into a Gaussian TEM<sub>00</sub> mode and collimated with the help of cylindrical and spherical telescopes. The whole setup fits on a breadboard measuring 90 × 30 cm<sup>2</sup> and is moveable

	LBO cavity	BBO cavity
Highly reflective (HR) mirrors fundamental	99.98%	99.93%
Output coupler HR fund.	99.9%	99.8%
Input coupler fund.	97.5%	98.4%
Distance between focusing mirrors	62 mm	59.4 mm
Total cavity length	400 mm	470 mm
Full folding angle	10°	27.4°
Incoupling power	1.80 W	0.95 W
Output power	0.95 W	0.275 W
Doubling efficiency	52.7%	28.9%

TABLE 1 Mirror reflectivities, measures and technical data of the SHG cavities

output coupler (M4')  $R > 99.8\%$  at 560 nm and  $T > 94\%$  at 280 nm. We project 95% of the astigmatic beam exiting the second cavity into a Gaussian TEM00 mode using a cylindrical telescope and collimate the beam using a spherical cleaning telescope. We end up with 275 mW of ultraviolet output power. Measures, mirror reflectivities and efficiencies of both cavities are summarized in Table 1.

#### 4 Resonances

We discovered a 14-GHz-broad frequency region between 1118.409 nm and 1118.339 nm where we observe the following: when scanning the cavity length in one direction the transmission fringes are broadened while by scanning it backwards the fringes are narrowed. We were not able to lock the cavity in this frequency domain. We reproduced this phenomenon using several lasers, cavities and crystals. We note that all crystals were bought from the same crystal manufacturer (Crystals of Siberia). This frequency domain (quadrupled to the ultraviolet) does not overlap with the resonant transitions of  $Mg^{+}$  isotopes from the ground state  $3S_{1/2}$  to the  $3P_{1/2}$  or  $3P_{3/2}$  levels. But, it imposes restric-

tions for two-photon stimulated Raman transitions via detuned levels. It seems as if the index of refraction of the crystal changes with light intensity in the crystal. Previously, resonances of OH groups in LBO crystals have been found [8] with a comparable width however at different wavelengths than observed here.

#### 5 Stability

We observe fluctuations in the ultraviolet (UV) output power within 2% deviation from the mean value. Furthermore, on microsecond time scales we notice regular drops of the UV output power smaller than 4%. Drops larger than 7% appear less than once a minute. In addition, we discover a sensitivity to long-term temperature drifts of the environment which resulted in oscillations as large as 10% of the output power as the temperature changed by 2 K, but we were able to reduce these drifts to 5% by proper thermal isolation of the crystal oven. The other problem is that the output polarization of the laser changes as the heat sink of the power amplifier of the fiber laser changes in temperature. Thus, the beam which is no longer parallel polarized with respect to the input polarizer of the

optical isolator is not completely transmitted through the optical isolator. One has to manually adjust the output polarization of the fiber with the help of the quarter- and the half-wave plates to retrieve optimum transmission through the optical isolator. One solution to this issue could be an active stabilization of the temperature of the heat sink of the laser with the help of a Peltier element.

#### 6 Conclusion

In summary, we presented a laser system consisting of a commercial ytterbium fiber laser and two subsequent external second harmonic generation ring cavities with an output power of 275 mW near 280 nm. This corresponds to an overall conversion efficiency of 15.2%.

**ACKNOWLEDGEMENTS** We thank Ove Poulsen, Jim Bergquist and Dietrich Leibfried for their genuine input and triggering ideas. We gratefully acknowledge financial support by the Deutsche Forschungsgemeinschaft and the Max-Planck-Institut für Quantenoptik.

#### REFERENCES

- 1 C. Wieman, T.W. Hänsch, Phys. Rev. Lett. **36**, 1170 (1976)
- 2 C.P. Pearman, C.S. Adams, S.G. Cox, P.F. Griffin, D.A. Smith, I.G. Hughes, J. Phys. B **35**, 5141 (2002)
- 3 R. Paschotta, K. Fiedler, P. Kürz, R. Henking, S. Schiller, J. Mlynek, Opt. Lett. **19**, 1325 (1994)
- 4 Z.Y. Ou, S.F. Pereira, E.S. Polzik, H.J. Kimble, Opt. Lett. **17**, 640 (1992)
- 5 G.D. Boyd, D.A. Kleinman, J. Appl. Phys. **39**, 3597 (1968)
- 6 T.W. Hänsch, B. Couillaud, Opt. Commun. **35**, 441 (1980)
- 7 All crystal data taken from SNLO program by Sandia National Laboratories
- 8 L. Kovács, K. Polgár, A. Péter, R. Capelletti, Mikrochim. Acta Suppl. **14**, 523 (1997)

*B. List of Publications*

## Bibliography

- [1] M. Abramowitz and I. A. Stegun, *Handbook of Mathematical Functions*, Dover, New York, 1972.
- [2] M. Acton, K. A. Brickman, P. C. Haljan, P. J. Lee, L. Deslauriers, and C. Monroe, *Near-perfect simultaneous measurement of a qubit register*, *Quantum Inf. Comput.* **6** (2006), 465.
- [3] Y. Aharonov and J. Anandan, *Phase change during a cyclic quantum evolution*, *Phys. Rev. Lett.* **58** (1987), no. 16, 1593.
- [4] P. Aliferis, D. Gottesman, and J. Preskill, *Accuracy threshold for postselected quantum computation*, *Quantum Inf. Comput.* **8** (2008), 181.
- [5] L. Allen and J. H. Eberly, *Optical resonance and two-level atoms*, Dover, New York, 1987.
- [6] J. Benhelm, G. Kirchmair, C. F. Roos, and R. Blatt, *Towards fault-tolerant quantum computing with trapped ions*, *Nature Physics* **4** (2008), 463.
- [7] P. Benioff, *The computer as a physical system: A microscopic quantum mechanical hamiltonian model of computers as represented by turing machines*, *J. Stat. Phys.* **22** (1980), no. 5, 563.
- [8] ———, *Quantum mechanical models of turing machines that dissipate no energy*, *Phys. Rev. Lett.* **48** (1982), no. 23, 1581.
- [9] D. J. Berkeland, J. D. Miller, J. C. Bergquist, W. M. Itano, and D. J. Wineland, *Minimization of ion micromotion in a paul trap*, *J. Appl. Phys.* **83** (1998), no. 10, 5025.
- [10] M. V. Berry, *Quantal phase factors accompanying adiabatic changes*, *Proc. R. Soc. London Ser. A* **392** (1984), 45.
- [11] J. J. Bollinger, W. M. Itano, D. J. Wineland, and D. J. Heinzen, *Optimal frequency measurements with maximally correlated states*, *Phys. Rev. A* **54** (1996), R4649.
- [12] M. Born and V. Fock, *Beweis des Adiabatensatzes*, *Z. Phys. A* **51** (1928), 165.

## Bibliography

- [13] B. Boulanger, I. Rousseau, J. P. Fève, M. Maglione, B. Ménaert, and G. Marnier, *Optical Studies of Laser-Induced Gray-Tracking in KTP*, IEEE J. Quantum Electron. **35** (1999), no. 3, 281.
- [14] G.D Boyd and D.A. Kleinman, *Parametric interaction of focused gaussian light beams*, J. Appl. Phys. **39** (1968), no. 8, 3597.
- [15] G.K. Brennen, C.M. Caves, P.S. Jessen, and I.H. Deutsch, *Quantum logic gates in optical lattices*, Phys. Rev. Lett. **82** (1998), no. 5, 1060.
- [16] G. Burkard, D. Loss, and D. P. DiVincenzo, *Coupled quantum dots as quantum gates*, Phys. Rev. B **59** (1999), no. 3, 2070.
- [17] A. C. M. Carollo and J. K. Pachos, *Geometric phases and criticality in spin-chain systems*, Phys. Rev. Lett. **95** (2005), 157203.
- [18] P. Carruthers and M. M. Nieto, *Coherent states and the forced quantum oscillator*, Am. J. Phys. **7** (1965), 537.
- [19] M. Cetina, A. Grier, J. Campbell, I. Chuang, and V. Vuletić, *Bright source of cold ions for surface-electrode traps*, Phys. Rev. A **76** (2007), 041401.
- [20] J. Chiaverini, J. Britton, D. Leibfried, E. Knill, M.D Barrett, R.B. Blakestad, W.M. Itano, J.D. Jost, C. Langer, R. Ozeri, T. Schaetz, and D.J. Wineland, *Implementation of the semiclassical quantum fourier transform in a scalable system*, Science **308** (2005), 997.
- [21] J. Chiaverini and W.E. Lybarger, *Laserless trapped-ion quantum simulations without spontaneous scattering using microtrap arrays*, Phys. Rev. A **77** (2008), 022324.
- [22] I. Chiorescu, Y. Nakamura, C. J. Harmans, and J. E. Mooij, *Coherent quantum dynamics of a superconducting flux qubit*, Science **299** (2003), 1869.
- [23] L. Cincio, J. Dziarmaga, M. M. Rams, and W. H. Zurek, *Entropy of entanglement and correlations induced by a quench: Dynamics of a quantum phase transition in the quantum ising model*, Phys. Rev. A **75** (2007), no. 052321.
- [24] J.I. Cirac and P. Zoller, *Quantum computations with cold trapped ions*, Phys. Rev. Lett. **74** (1995), no. 20, 4091.
- [25] \_\_\_\_\_, *A scalable quantum computer with ions in an array of microtraps*, Nature **404** (2000), 579.

- [26] J. Dalibard and C. Cohen-Tannoudji, *Dressed-atom approach to atomic motion in laser light: the dipole force revisited*, J. Opt. Soc. Am. B **2** (1985), no. 11, 1707.
- [27] H. G. Dehmelt, *Paramagnetic resonance reorientation of atoms and ions aligned by electron impact*, Phys. Rev. **103** (1962), 1125.
- [28] X. L. Deng, D. Porras, and J. I. Cirac, *Effective spin quantum phases in systems of trapped ions*, Phys. Rev. A **72** (2005), 063407.
- [29] L. Deslauriers, S. Olmschenk, D. Stick, W. K. Hensinger, J. Sterk, and C. Monroe, *Scaling and suppression of anomalous heating in ion traps*, Phys. Rev. Lett. **97** (2006), 103007.
- [30] D. P. DiVincenzo, *The physical implementation of quantum computation. in scalable quantum computation*, Wiley, 2001.
- [31] E. A. Donley, T. P. Heavner, F. Levi, M. O. Tataw, and S. R. Jefferts, *Double-pass acousto-optic modulator system*, Rev. Sci. Instr. **76** (2005), 063112.
- [32] G. W. F. Drake (ed.), *Handbook of atomic, molecular and optical physics*, Springer Verlag Heidelberg, 2006.
- [33] S. Earnshaw, *On the nature of the molecular forces which regulate the constitution of the luminiferous ether*, Trans. Camb. Phil. Soc. **7** (1842), 97.
- [34] J. Eschner, G. Morigi, F. Schmidt-Kaler, and R. Blatt, *Laser cooling of trapped ions*, J. Opt. Soc. Am. B **20** (2003), 1003.
- [35] R.P. Feynman, *Simulating physics with computers*, Int. J. Theo. Phys. **21** (1982), 467.
- [36] R.P. Feynman, F.L. Vernon, and R.W. Hellwarth, *Geometrical representation of the schrödinger equation for solving maser problems*, J. Appl. Phys. **28** (1957), 49.
- [37] A. Friedenauer, F. Markert, H. Schmitz, L. Petersen, S. Kahra, M. Herrmann, Th. Udem, T.W. Hänsch, and T. Schaetz, *High power all solid state laser system near 280 nm*, Appl. Phys. B **84** (2006), 371.
- [38] A. Friedenauer, H. Schmitz, J. T. Glückert, D. Porras, and T. Schätz, *Simulating a quantum magnet with trapped ions*, Nature Physics **4** (2008), 757.
- [39] Y. Furukawa, K. Kitamura, A. Alexandrowski, R. K. Route, M. M. Fejer, and G. Foulon, *Green-induced infrared absorption in MgO doped LiNbO<sub>3</sub>*, Appl. Phys. Lett. **78** (2001), no. 14, 1970.

## Bibliography

- [40] J. J. García-Ripoll, E. Solano, and M. A. Martin-Delgado, *Quantum simulation of anderson and kondo lattices with superconducting qubits*, Phys. Rev. B **77** (2008), 024522.
- [41] R. Gerritsma, G. Kirchmair, F. Zähringer, E. Solano, R. Blatt, and C. F. Roos, *Quantum simulation of the dirac equation*, Nature **463** (2009), 68.
- [42] P. K. Ghosh, *Ion traps*, Oxford science publications, 1995.
- [43] J. T. Glückert, *Master's thesis, LMU München*, 2008.
- [44] D. Gottesman, *Stabilizer codes and quantum error correction*, Ph.D. thesis, Caltech, 1997.
- [45] D. M. Greenberger, M. A. Horne, A. Shimony, and A. Zeilinger, *Bell's theorem without inequalities*, Am. J. Phys. **58** (1990), no. 12, 1131.
- [46] D. M. Greenberger, M. A. Horne, and A. Zeilinger, *Going beyond bell's theorem*, Kluwer Academic, Dordrecht, The Netherlands, 1989.
- [47] M. Greiner, O. Mandel, T. Esslinger, T.W. Hänsch, and I. Bloch, *Quantum phase transition from a superfluid to a mott insulator in a gas of ultracold atoms*, Nature **415** (2002), 39–44.
- [48] L. K. Grover, *A fast quantum mechanical algorithm for database search*, Proceedings of the twenty-eighth annual ACM symposium on Theory of computing, 1996, p. 212.
- [49] O. Gühne and G. Tóth, *Entanglement detection*, Physics Reports **474** (2009), 1.
- [50] H. Häffner, W. Hänsel, C.F. Roos, J. Benhelm, D. Chek al kar, M. Chwalla, T. Körber, U.D. Rapol, M. Riebe, P.O. Schmidt, C. Becher, O. Gühne, W. Dür, and R. Blatt, *Scalable multiparticle entanglement of trapped ions*, Nature **438** (2005), 643–646.
- [51] J. L. Hall, *External laser stabilization*, Laser Physics at the Limits, Springer Verlag Heidelberg, 2001.
- [52] T.W. Hänsch and B. Couillaud, *Laser frequency stabilization by polarization spectroscopy of a reflecting reference cavity*, Opt. Commun. **35** (1980), no. 3, 441.
- [53] T.W. Hänsch and A. Schawlow, *Cooling of gases by laser radiation*, Opt. Commun. **13** (1975), 68.
- [54] W. Happer, *Optical pumping*, Rev. Mod. Phys. **44** (1972), no. 2, 169–249.

- [55] E. Ising, *Beitrag zur theorie des ferromagnetismus*, Z. Phys. **31** (1925), 253.
- [56] D.F.V. James, *Quantum dynamics of cold trapped ions with application to quantum computation*, Appl. Phys. B **66** (1998), 181.
- [57] E. T. Jaynes and F. W. Cummings, *Comparison of quantum and semiclassical radiation theories with application to the beam maser*, Proc. IEEE **51** (1963), 89.
- [58] S. R. Jefferts, C. Monroe, E. W. Bell, and D. J. Wineland, *Coaxial-resonator-driven RF (Paul) trap for strong confinement*, Phys. Rev. A **51** (1995), no. 3112.
- [59] S. Jørgensen, M. Drewsen, and R. Kosloff, *Intensity and wavelength control of a single molecule reaction: Simulation of photodissociation of cold-trapped  $mgh^+$* , J. Chem. Phys. **123** (2005), 094302.
- [60] T. Kato, *On the adiabatic theorem of quantum mechanics*, J. Phys. Soc. Jap. **5** (1950), 435.
- [61] D. Kielpinski, *Entanglement and decoherence in a trapped-ion quantum register*, Ph.D. thesis, U Colorado, 2001.
- [62] D. Kielpinski, V. Meyer, M. A. Rowe, C. A. Sackett, W. M. Itano, C. Monroe, and D. J. Wineland, *A decoherence-free quantum memory using trapped ions*, Science **9** (2001), 1013.
- [63] D. Kielpinski, C. Monroe, and D. J. Wineland, *Architecture for a large-scale ion-trap quantum computer*, Nature **417** (2002), 709.
- [64] B. E. King, C. S. Wood, C. J. Myatt, Q. A. Turchette, D. Leibfried, W. M. Itano, C. Monroe, and D. J. Wineland, *Cooling the collective motion of trapped ions to initialize a quantum register*, Phys. Rev. Lett. **81** (1998), no. 7, 1525.
- [65] B.E. King, *Quantum state engineering and information processing with trapped ions*, Ph.D. thesis, U Colorado, 1999.
- [66] Y. Kong, W. Zhang, X. Chen, J. Xu, and G. Zhang,  *$oh^-$  absorption spectra of pure lithium niobate crystals*, J. Phys.: Condens. Matter **11** (1999), 2139.
- [67] L. Kovács, K. Polgár, Á. Péter, and R. Capelletti, *Ftir spectroscopy of  $oh^-$  ions in borate single crystals*, Mikrochim. Acta Suppl. **14** (1997), 523.
- [68] J. Labaziewicz, Y. Ge, P. Antohi, D. Leibbrandt, K. R. Brown, and I. L. Chuang, *Suppression of heating rates in cryogenic surface-electrode ion traps*, Phys. Rev. Lett. **100** (2008), 013001.

## Bibliography

- [69] Sandia National Laboratories, *SNLO software*, 2005.
- [70] C. Langer, *High fidelity quantum information processing with trapped ions*, Ph.D. thesis, U Colorado, 2006.
- [71] D. Leibfried, R. Blatt, C. Monroe, and D.J. Wineland, *Quantum dynamics of single trapped ions*, Rev. Mod. Phys. **75** (2003), 281.
- [72] D. Leibfried, B. DeMarco, V. Meyer, D. Lucas, M. Barrett, J. Britton, W.M. Itano, B. Jelenkovic, C. Langer, T. Rosenband, and D.J. Wineland, *Experimental demonstration of a robust, high-fidelity geometric two ion-qubit phase gate*, Nature **422** (2003), 412–415.
- [73] D. Leibfried, E. Knill, S. Seidelin, and et al., *Creation of a six-atom schrödinger cat state*, Nature **438** (2005), no. 1, 639.
- [74] S. Lloyd, *Universal quantum simulators*, Science **273** (1996), 1073.
- [75] D. Loss and D. P. DiVincenzo, *Quantum computation with quantum dots*, Phys. Rev. A **57** (1998), no. 1, 120.
- [76] R. Loudon, *The quantum theory of light*, Oxford University Press, 1983.
- [77] D. N. Madsen, S. Balslev, M. Drewsen, N. Kjærgaard, Z. Videsen, and J.W. Thomsen, *Measurements on photo-ionization of  $3s3p\ ^1P_1$  magnesium atoms*, J. Phys. B **33** (2000), 4981.
- [78] F. G. Major, V. N. Gheorge, and G. Werth, *Charged particle traps*, Springer Verlag Heidelberg, 2005.
- [79] Y. Makhlin, G. Schön, and A. Shnirman, *Quantum-state engineering with josephson-junction devices*, Rev. Mod. Phys. **73** (2001), 357.
- [80] O. Mandel, *Entanglement with quantum gates in an optical lattice*, Ph.D. thesis, LMU München, 2005.
- [81] I. Manek-Hönninger, J. Boulet, T. Cardinal, F. Guillen, S. Ermeneux, M. Podgorski, R. Bello Doua, and F. Salin, *Photodarkening and photobleaching of an ytterbium-doped silica double-clad lma fiber*, Opt. Expr. **15** (2007), 1606.
- [82] K. E. Mattsson, S. N. Knudsen, B. Cadier, and T. Robin, *Photodarkening in ytterbium co-doped silica material*, 2008.
- [83] P. Maunz, T. Puppe, I. Schuster, N. Syassen, P. W. H. Pinkse, and G. Rempe, *Cavity cooling of a single atom*, Nature **428** (2004), 50.

- [84] H. J. Metcalf and P. van der Straten, *Laser cooling and trapping*, Springer, 1999.
- [85] P. Meystre and S. Murray, *Elements of Quantum Optics*, Springer Verlag Heidelberg, 1991.
- [86] C. Monroe, D. M. Meekhof, B. E. King, W. M. Itano, and D. J. Wineland, *Demonstration of a fundamental quantum logic gate*, Phys. Rev. Lett. **75** (1995), no. 25, 4714.
- [87] C. Monroe, D. M. Meekhof, B. E. King, S. R. Jefferts, W. M. Itano, and D. J. Wineland, *Resolved-sideband raman cooling of a bound atom to the 3d zero-point energy*, Phys. Rev. Lett. **75** (1995), no. 22, 4011–4014.
- [88] C. Monroe, D. M. Meekhof, B. E. King, and D. J. Wineland, *A “schrödinger cat” superposition state of an atom*, Science **272** (1996), 1131.
- [89] G. Morigi, J. Eschner, J. I. Cirac, and P. Zoller, *Laser cooling of two trapped ions: Sideband cooling beyond the lamb-dicke limit*, Phys. Rev. A **59** (1999), no. 5, 3797.
- [90] W. Nagourney, J. Sandberg, and H. Dehmelt, *Shelved optical electron amplifier: Observation of quantum jumps*, Phys. Rev. Lett. **56** (1986), no. 26, 2797.
- [91] M. Nielsen and I. Chuang, *Quantum computation and quantum informtion*, Cambridge University Press, 2000.
- [92] D. N. Nikogosyan, *Beta barium borate*, Appl. Phys. A **52** (1991), 359.
- [93] ———, *Lithium triborate*, Appl. Phys. A **58** (1994), 181.
- [94] J. Orestein and A. J. Millis, *Advances in the Physics of High- $T_c$  Superconductivity*, Science **288** (2000), 468.
- [95] Z.Y. Ou, S.F. Pereira, E.S. Polzik, and H.J. Kimble, *85% efficiency for cw frequency doubling from 1.08 to 0.54 micrometer*, Opt. Lett. **17** (1992), no. 9, 640.
- [96] R. Ozeri, C. Langer, J. D. Jost, B. DeMarco, A. Ben-Kish, B. R. Blakestad, J. Britton, J. Chiaverini, W. M. Itano, D. B. Hume, D. Leibfried, T. Rosenband, P. O. Schmidt, and D. J. Wineland, *Hyperfine coherence in the presence of spontaneous photon scattering*, Phys. Rev. Lett. **95** (2005), 030403.
- [97] R. Paschotta, P. Kuerz, R. Henking, S. Schiller, and J. Mlynek, *82% Efficient continuous-wave frequency doubling of 1.06 micrometer with a monolithic MgO:LiNbO3 resonator*, Opt. Lett. **19** (1994), no. 17, 1325.

## Bibliography

- [98] W. Paul, O. Osberghaus, and E. Fischer, *Ein Ionenkäfig*, Forschungsber. Wirtsch. Verkehrsminist. Nordrhein-Westfalen **415** (1958).
- [99] L. Petersen, *Quantum simulations in ion traps*, Master's thesis, LMU München, 2006.
- [100] M. B. Plenio and S. Virmani, *An introduction to entanglement measures*, Quant. Inf. Comp. **7** (2007), 1.
- [101] D. Porras, *private communication*, 2008.
- [102] D. Porras and J.I. Cirac, *Bose-einstein condensation and strong-correlation behaviour of phonons in ion traps*, Phys. Rev. Lett. **93** (2004), 263602.
- [103] \_\_\_\_\_, *Effective quantum spin systems with trapped ions*, Phys. Rev. Lett. **92** (2004), 207901.
- [104] D. Porras, F. Marquardt, J. von Delft, and J. I. Cirac, *Mesoscopic Spin-Boson Models of Trapped Ions*, ArXiv e-prints **710** (2007).
- [105] N. F. Ramsey, *Molecular beams*, Oxford University Press, 1963.
- [106] R. Raussendorf and J. Harrington, *Fault-tolerant quantum computation with high threshold in two dimensions*, Phys. Rev. Lett. **98** (2007), 190504.
- [107] C. F. Roos, *Controlling the quantum state of trapped ions*, Ph.D. thesis, U Innsbruck, 2000.
- [108] S. Sachdev, *Quantum phase transitions*, Cambridge University Press, 1999.
- [109] C.A. Sackett, D. Kielpinski, B.E. King, C. Langer, V. Meyer, C.J. Myatt, M. Rowe, Q.A. Turchette, W.M. Itano, D. J. Wineland, and C. Monroe, *Experimental entanglement of four particles*, Nature **404** (2000), 256.
- [110] J. J. Sakurai, *Modern quantum mechanics*, Prentice Hall, 1993.
- [111] H. Schmitz, *Dissertation*, LMU München, 2010.
- [112] H. Schmitz, R. Matjeschk, Ch. Schneider, J. Glückert, M. Enderlein, T. Huber, and T. Schätz, *The quantum walk of a trapped ion in phase space*, Phys. Rev. Lett. **103** (2009), 090504.
- [113] R. Schützhold, M. Uhlmann, L. Petersen, H. Schmitz, A. Friedenauer, and T. Schätz, *Analogue of cosmological particle creation in an ion trap*, Phys. Rev. Lett. **99** (2007), no. 20, 201301.

- [114] F. Schwabl, *Quantenmechanik*, Springer Verlag Heidelberg, 2004.
- [115] M. O. Scully and M. S. Zubairy, *Quantum optics*, Cambridge University Press, 1997.
- [116] S. Seidelin, J. Chiaverini, R. Reichle, J. J. Bollinger, D. Leibfried, J. Britton, J. H. Wesenberg, R. B. Blakestad, R. J. Epstein, D. B. Hume, W. M. Itano, J. D. Jost, C. Langer, R. Ozeri, N. Shiga, and D. J. Wineland, *Microfabricated surface-electrode ion trap for scalable quantum information processing*, Phys. Rev. Lett. **96** (2006), 253003.
- [117] P. W. Shor, *Fault-tolerant quantum computation*, IEEE Press, 1996.
- [118] Peter W. Shor, *Polynomial-time algorithms for prime factorization and discrete logarithms on a quantum computer*, SIAM Journal on Computing **26** (1997), no. 5, 1484.
- [119] A. M. Steane, *Efficient fault-tolerant quantum computing*, Nature **399** (1999), 124.
- [120] A. Steinbach, M. Rauner, F.C. Cruz, and J.C. Bergquist, *Cw second harmonic generation with elliptical gaussian beams*, Opt. Commun. **123** (1996), 207.
- [121] D. Stick, W. K. Hensinger, S. Olmschenk, M. J. Madsen, K. Schwab, and C. Monroe, *Ion trap in a semiconductor chip*, Nature Physics **2** (2006), 36.
- [122] Toptica Photonics AG, *Iodine Spec 4 software*.
- [123] Q. A. Turchette, C. J. Hood, W. Lange, H. Mabuchi, and H. J. Kimble, *Measurement of conditional phase shifts for quantum logic*, Phys. Rev. Lett. **75** (1995), no. 25, 4710.
- [124] Q. A. Turchette, D. Kielpinski, B. E. King, D. Leibfried, D. M. Meekhof, C. J. Myatt, M. A. Rowe, C. A. Sackett, C. S. Wood, W. M. Itano, C. Monroe, and D. J. Wineland, *Heating of trapped ions from the quantum ground state*, Phys. Rev. A **61** (2000), 063418.
- [125] D. J. Wineland and H. Dehmelt, *Proposed  $10^{14}\delta\nu < \nu$  laser fluorescence spectroscopy on  $ti^+$  mono-ion oscillator iii*, Bull. Am. Phys. Soc. **20** (1975), 637.
- [126] D. J. Wineland and W. M. Itano, *Laser cooling of atoms*, Phys. Rev. A **20** (1979), no. 4, 1521.
- [127] D. J. Wineland, C. Monroe, W.M. Itano, D. Leibfried, B.E. King, and D.M. Meekhof, *Experimental issues in coherent quantum-state manipulation of trapped atomic ions*, J. Res. Natl. Inst. Stand. Technol. **103** (1998), no. 3, 259.

- [128] D.J. Wineland, M. Barrett, J. Britton, J. Chiaverini, B.L. DeMarco, W.M. Itano, B.M. Jelenkovic, C. Langer, D. Leibfried, V. Meyer, T. Rosenband, and T. Schaetz, *Quantum information processing with trapped ions*, Phil. Trans. Royal Soc. London A **361** (2003), 1349–1361.
- [129] S. T. Yang, C. C. Pohalski, E. K. Gustafson, R. L. Byer, R. S. Feigelson, R. J. Raymakers, and R. K. Route, *6.5-w, 532-nm radiation by cw resonant external-cavity second-harmonic generation of an 18-w nd:yag laser in lib3o5*, Opt. Lett. **16** (1991), no. 19, 1493.
- [130] F. Zähringer, G. Kirchmair, R. Gerritsma, E. Solano, R. Blatt, and C. F. Roos, *Realization of a quantum walk with one and two trapped ions*, arXiv:quant-ph/0911.1876 (2009).
- [131] S.-L. Zhu, *Scaling of geometric phases close to the quantum phase transition in the xy spin chain*, Phys. Rev. Lett. **96** (2006), 077206.

# Danksagung

Zuallererst gebührt mein Dank meinem Betreuer Tobias Schätz für das entgegengebrachte Vertrauen, die offene Tür bei sämtlichen Problemen, die freundschaftliche Atmosphäre, die gemeinsamen Mittagessen, bei denen die Probleme der Welt, jedoch explizit nicht der Physik, gelöst wurden. Speziell hervorzuheben wäre auch noch Dein Wagemut, mit zwei 'Theoretikern' ein Experiment dieser Komplexität aufzubauen und die unvergesslichen Gruppenbergtouren.

Zu ganz besonderem Dank bin ich Hector Schmitz verpflichtet, meinem Doktoranden-Kollegen von der ersten Stunde an. Nicht zuletzt dank Deines unstillbaren Basteleifers, haben wir es geschafft, sämtliche Probleme aus dem Wege zu räumen, besonders zu erwähnen die Mikrobewegungskompensationsorgien. Ohne Deine große Erfahrung mit elektronischen Schaltungen aller Art und das aus-dem-Boden-stampfen unserer umfangreichen Experiment-Steuerungssoftware wäre es unmöglich gewesen, dieses Experiment in so kurzer Zeit durchzuführen.

Lutz Petersen, der nicht nur durch seine bunten Pullover Farbe in den Laboralltag gebracht hat. Deine Programmierkünste, die Du sowohl bei der Kamerasoftware als auch bei der Paulbox, durch die diese erst ihr wahres Potential entfalten konnte, unter Beweis gestellt hast, waren unersetzlich für das Experiment.

Jan Glückert für unzählige nächtliche Parameter-Optimierungs-Orgien inklusive zum zehnten Mal Ionen nachladen, wenn wieder mal ein Ion dunkel wurde.

Den Dunkelionspezialisten Steffen Kahra und Günther Leschhorn, die nicht nur durch Prätzen und kaputtes Schuhwerk den Alltag aufgeheitert haben. Christian Schneider, der mir durch diverse  $\text{T}_{\text{E}}\text{X}$ -Tricks bei der Gestaltung meiner Arbeit behilflich war. Maximilian Herrmann für viele hilfreiche Denkanstöße, den Rempe-Jungs für die freundliche Einbindung unserer Gruppe. Diego Porras für viele Diskussionen über die zugrundeliegende Theorie. Arnold Steyer, der mechanischen rechten Hand der Gruppe, der nachdem wir ihn seiner Solitärlethargie entrissen hatten, jeden Spezialauftrag in keiner Zeit erledigte. Helmut Brückner, der bei jeder Art elektronischer Probleme immer ein offenes Ohr hatte, Tom Wiesmeier für die Hilfsbereitschaft beim Elektronikplatinen ätzen und fräsen. Desweiteren den Werkstattmitarbeitern für ihre exzellente Arbeit.

Ein ganz besonderes Dankeschön außerdem allen, die sich bei der Konstruktion meines genialen Doktorhuts engagiert haben.

Meiner Familie, die mich auf allen meinen Wegen unterstützt hat, und nicht zuletzt Laura, die mir in stressigen Phasen immer den Rücken freigehalten hat.



# Curriculum Vitae

Axel Friedenauer

---

## Persönliche Daten

Axel Friedenauer  
Trappentreustr. 19  
80339 München  
Geboren am 17.08.1977 in Stuttgart

---

## Schulbildung

1984–1988      Grundschule Ilsfeld  
1988–1997      Justinus-Kerner-Gymnasium Heilbronn  
06/1997        Abitur am JKG Heilbronn  
                  Robert Mayer Preis der Stadt Heilbronn für herausragende  
                  naturwissenschaftliche Leistungen  
08/1997–09/1998 Zivildienst im chirurgischen OP im Krankenhaus Heilbronn

---

## Studium

10/1998–07/2004 Studium der Physik an der Universität Heidelberg  
08/2001–10/2001 Praktikum an der Thammasat University Bangkok, Thailand  
03/2002–08/2002 Masterarbeit an der Universität Uppsala, Schweden  
                  Thema: Noncyclic geometric quantum computation  
07/2003–06/2004 externe Diplomarbeit an der Universität Potsdam  
                  Thema: Verschränkung beim FRET  
10/2004–06/2008 Doktorarbeit am Max-Planck-Institut für Quantenoptik  
                  Thema: Simulation von Quanten-Spin-Systemen in einer  
                  Ionenfalle  
04/2005–09/2006 Praktikumsbetreuung an der LMU München

---

## Beruflicher Werdegang

07/2008–heute    Laser-Entwicklung bei der Firma Toptica Photonics AG

---

## Sprachen

Deutsch	Muttersprache
Englisch	fließend
Französisch	gut
Russisch	Grundkenntnisse

---

## Veröffentlichungen

- A. Friedenauer, H. Schmitz, J. Glueckert, D. Porras and T. Schaetz, *Simulating a quantum magnet with trapped ions*, Nature Physics **4**, 757 (2008)
- A. Friedenauer, F. Markert, H. Schmitz, L. Petersen, S. Kahra, M. Herrmann, Th. Udem, T. W. Haensch and T. Schaetz, *High power all solid state laser system near 280 nm*, Appl. Phys. B **84**, 371 (2006)
- R. Schuetzhold, M. Uhlmann, L. Petersen, A. Friedenauer, H. Schmitz and T. Schaetz, *Analogue of cosmological particle creation in an ion trap*, Phys. Rev. Lett. **99**, 201301 (2007)
- T. Schaetz, A. Friedenauer, H. Schmitz, L. Petersen, S. Kahra, *Towards (scalable) Quantum Simulations in ion trap*, J. Mod. Opt. **54**, 2317 (2007)
- H. Schmitz, A. Friedenauer, Ch. Schneider, R. Matjeschk, M. Enderlein, T. Huber, J. Glueckert, D. Porras, *The 'arch' of simulating quantum spin systems with trapped ions*, Appl. Phys. B **95**, 195 (2009)
- A. Friedenauer, E. Sjöqvist: *Noncyclic geometric quantum computation*; Phys. Rev. A **67**, 024303 (2003)

München, 7. Juni 2010  
Axel Friedenauer